Complex light fields in polarisation state tomography and atomic spectroscopy

Mustafa A. Al Khafaji

Submitted in fulfilment of the requirements for the degree of
Doctor of Philosophy

to the

School of Physics and Astronomy
College of Science and Engineering
University of Glasgow

July 2024

Abstract

While the output beams from laser systems are usually homogeneously polarised, the increasing interest in recent years to shape light with a spatially varying polarisation profile, the like of vector and Poincaré beams, has prompted developments of amplitude and phase modulators, the likes of digital micromirror devices (DMDs), spatial light modulators (SLMs), and vector vortex plates (VVP), offering unprecedented control and flexibility in shaping complex light fields. In this work, we provide a detailed description of beam shaping techniques, with an emphasis on generation methods for experimental applications, as a means to evaluate the performance of our single-shot polarimeter utilising a set of unbiased generalised measurements for full polarisation state reconstruction of the light field.

Our research extends to interactions of light fields with rubidium vapours, utilising coherent laser diodes with several megahertz of frequency tunability, housed within external cavities, for use in applications of atomic spectroscopy and with particular interest in polarisation spectroscopy (polspec). This spectroscopic technique, consisting of an optically pumped and magnetically shielded atomic medium, provides a high-resolution Doppler-free signal for use in laser frequency stabilisation. In this work, we combine this technique with our understanding of vector beam generation and detection to introduce a Doppler-free spectroscopic technique utilising a spatially varying probing signal to measure the magneto-optical effects in the region near resonance. This novel spatially resolved approach could allow for a new kind of modulation-free, perhaps one-shot measurement of laser frequency with applications in laser stabilisation for quantum technology.

A Letter to the Reader

It was always my objective to write this thesis in a language that a graduate or perhaps even an undergraduate student with a fundamental understanding of various physics-based concepts could pick up and comprehend, offering them an insight into the world of experimental optics. Whether I managed to achieve my objective is an entirely different matter, subject to the judgement of our dear readers. However, to aid me in my quest, I have included many figures illustrating the various ideas and phenomena we will encounter in this thesis. Additionally, I have opted to expand as much as possible on any calculations or descriptions I believe could be challenging for the reader to understand. Finally, I have included many footnotes scattered throughout this work, providing further explanations where I deem necessary, that otherwise do not fit in the main body of the thesis.

I would like to state that this document is the product of over four years of work and, at times, might read more like a journal, where I share my knowledge and experiences with the occasional story, offering the reader a glimpse into my time as a PhD student at the University of Glasgow. Additionally, I would like to emphasise that despite me being the sole author of this thesis, it is without a doubt the result of the combined effort of many of those I had the privilege of working with and learning from throughout the years, and to acknowledge their contributions, I write this thesis in the third person.

Before we start, I would like to briefly state that the notation used in this thesis will be defined as we go along; however, we conform to the norm found in literature where bold letters appearing in equations refer to vector quantities. Additionally, the majority of the schematics of experimental setups were created using the ComponentLibrary package developed by Alexander Franzen, which can be found in [1].

Acknowledgement

The past four and a half years have been some of the most interesting years of my life, filled with a variety of challenges both personally and academically. However, I remain eternally grateful for having the opportunity to meet and work with so many wonderful people along the way.

I would like to extend my gratitude to Sarah Croke for her role as my second supervisor and her continued support during our POVM work and beyond. Additionally, I want to thank Sebastião Pádua and Claire Marie Cisowski for teaching me the basics of experimental optics and for the many fun moments we had working together in the lab during our time on the POVM project.

I would like to thank all of the members of the Optics group past and present who provided a welcoming and friendly environment for my academic development, in particular Amy McWilliam and Sphinx Svensson, for sharing an office and a lab space with me for the past three years. Additionally, I would like to extend my gratitude to Richard Aguiar Maduro, who, despite joining as I was leaving, provided a great deal of assistance in my final days, helping with running the experiment and gathering data, all while blasting hashashin music in the lab[1].

Furthermore, I want to thank Jinwen Wang, who taught me the basics of experimental atom optics, and Harry Jimbrown for helping me adjust to my life in Glasgow. I most definitely missed our daily lunches and the many fun conversations we had along the way.

However, none of what I achieved during my time as a PhD student would have been possible without my supervisor, Sonja Franke-Arnold, who provided vital guidance and displayed incredible patience in dealing with my shenanigans and who, over the course of the past four and a half years, has been nothing but supportive. I thank you and count myself beyond lucky to have been your student.

I would like to thank Fraunhofer CAP for their funding and continued support during my time as a PhD student and for allowing me access to their facilities, equipment, and expertise. Additionally, I would like to thank Loyd McKnight and Christopher Carson for their supervision; Craig Hunter and Rachel Elvin for their eagerness to help; Charikleia Troullinou, Mateusz Mrozowski, and Jan Simon Hennig for being wonderful lab partners; and Jack Thomas for providing assistance in the lab, which often leads to fun conversations on an array of topics; and for imparting some of his electronics knowledge to me.

However, I can say with utmost confidence that without the help I received from Adam Selyem over the years, who took an active role in my supervision from the very beginning, always

[1] Shoutout to the Eagle.

making time to provide guidance and support, occasionally at the expense of his own time, completing this PhD would have been nothing but an ambitious undertaking. For his role as my supervisor and mentor, I am eternally grateful.

Finally, none of this would have been possible without the direct support of my friends and family, and especially my parents, who, over the years, continued to support me without question, sacrificing so much along the way. To you all, I say thank you, and to them, I say,

شكرا جزيلا لتضحياتكم على مدا السنين.

Declaration of Authorship

I hereby declare the work presented in this thesis to be my own, carried out under the supervision of Prof. Sonja Franke-Arnold at the University of Glasgow and Dr. Adam Selyem at the Fraunhofer Centre for Applied Photonics between January 2020 and July 2024, with the exception of references made to the work of others, and has not been presented to another institution or organisation for a degree of any kind.

Mustafa A. Al Khafaji

List of Publications

The following is a list of papers where I am either the first author or have co-authored during my PhD.

[1] **Al Khafaji, M. A.**, Cisowski, C. M., Jimbrown, H., Croke, S., Pádua, S., & Franke-Arnold, S. "Single-shot characterization of vector beams by generalized measurements." *Optics Express* Vol. 30, Issue 13, p. 22396, (2022).

[2] Wang, J., Chen, Y., **Al Khafaji, M. A.**, Svensson, S. J., Yang, X., Wang, C., Gao, H., Cisowski, C. M., & Franke-Arnold, S. "Exploring the ellipticity dependency on vector helical Ince-Gaussian beams and their focusing properties." *Optics Express*, Vol. 30, Issue 14, p. 24497, (2022).

[3] Wang, J., Svensson, S. J., Clark, T. W., Chen, Y., **Al Khafaji, M. A.**, Gao, H., Westerberg, N., & Franke-Arnold, S. "Measuring the Optical Concurrence of Vector Beams with an Atomic-State Interferometer." *Physical Review Letters*, Vol. 132, Issue 19, (2024).

[4] McWilliam, A., **Al Khafaji, M. A.**, Svensson, S. J., Pádua, S., & Franke-Arnold, S.. "Dynamic Mueller matrix polarimetry using generalized measurements." *Optics Express* Vol. 32, Issue 12, p. 21909, (2024).

Contents

List of Figures

List of abbreviations

Below is a list of all abbreviations used throughout this thesis in alphabetical order.

^{85}Rb	Rubidium-85
^{87}Rb	Rubidium-87
AOM	Acousto-optic modulator
BEC	Bose-Einstein condensate
CCD	Charge Coupled Device
CMOS	Complementary Metal-Oxide-Semiconductor
Cam	Camera
CW	Continuous wave
DAQ	Data Acquisition
DBR	Dstributed Bragg reflectors
DLP	Digital light processing
DMD	Digital micromirror device
ECDL	External cavity diode laser
FC	Fibre collimator
FI	Faraday isolator
FSR	Free spectral range
FWHM	Full width at half maximum
GR	Gear ratio
HG	Hermite-Gaussian
HWP	Half waveplate
HeNe	Helium-Neon laser
IA	Instrumentation amplifier
LD	Laser diode
LG	Laguerre-Gaussian
MIC-POVM	Minimum informationally complete positive operator valued measure
ND	Neutral density
NIR	Near infrared
NPBS	Non-polarising beam splitter
OAM	Orbital angular momentum
Op-Amps	Operation amplifier
PBS	Polarising beam splitter
PD	photodiode
PDE	Partial differential equation
PM-SMF	Polarisation maintaining single-mode fibre
POVM	Positive operator valued measure

PZT	piezoelectric transducer
Polspec	Polarisation spectroscopy
Pot	potentiometer
QP	Quartz plates
QWP	Quarter waveplate
RF	Radio frequency
Rb	Rubidum vapour
SLM	Spatial light modulator
Satspec	Saturated absorption spectroscopy
Spatpolspec	Spatial polarisation spectroscopy
VCA	Voltage control attenuator
VCO	Voltage control oscillator
VCSEL	Vertical cavity surface emitting laser
VVP	Vector vortex plate
WBS	Wollaston beam splitter
pol	Polariser
qubit	Quantum bit

Introduction

Light could very well be mankind's oldest field of study, dating back to the civilisations of the ancient world [2, 3]. However, over the centuries, humanity's understanding of the nature of light rapidly developed, leading to many great scientific discoveries and the development of the electromagnetic theory [4]. Perhaps the most notable achievement in recent years is the process of light amplification via stimulated emission of radiation (L.A.S.E.R.), theoretically proposed by Albert Einstein in 1916 [5] and later implemented experimentally by Theodore Maiman in 1960 [6], offering access to the first monochromatic and coherently light source in the visible spectrum. Over the years, great strides have been made in the development of laser technologies, giving birth to powerful and versatile systems (like the Ti:Sapphire [7]), providing extensive control over the tuning frequency of coherent electromagnetic radiation ideal for a variety of applications ranging from chemical analysis [8] to gas sensing [9, 10] and even more fundamental research in atomic physics [11], utilising electromagnetic interaction detectors the likes of cameras and photodiodes to obtain information on the behaviour of the system.

However, the majority of these devices are concerned with the spatial structure of light (i.e. intensity and colour), perhaps as a consequence of the human eye's ability to register information about these parameters from its surroundings. Another property of light encoded into its spatial structure is the phase, which has implications for coherent light sources (i.e. light sources with a stable phase relationship between different points in space or time), leading to interference effects. Additionally, it contributes to the spatial structure of transverse modes of propagation, such as Gaussian beams (see Section 1.5 for more information). This spatial phase should not be confused with the phase difference between orthogonal polarisation components, which determines the polarisation state of the light field. Polarisation provides an additional degree of freedom for the light, representing the orientation of the light field oscillation, an interesting optical property that plays a central role in our research here in the optics group at the University of Glasgow, as will be evident in the coming chapters.

In Part I of this thesis, we heavily focus on building a solid understanding of the properties of light, with an interest in the generation and manipulation of beams with varying polarisation structures for experimental use. In Chapter 1, we introduce the electric field in the paraxial approximation as a solution to Maxwell's equations and develop an understanding of light polarisation using different mathematical and graphical representations before discussing various techniques for manipulation of polarisation structures. Finally, we conclude our introductory section on polarisation by examining experimental techniques for the detection of light polarisation utilising Stokes tomography. In the remainder of the chapter, we introduce different transverse modes of propagation, called Gaussian modes, as solutions to the Helmholtz equation. The energy content of these Gaussian modes is bound within a finite space, making them realistic solutions to physically realisable light fields in an experimental setting.

In Chapter 2, we focus on ideas of beam manipulation, discussing reflection of light and the Jones matrix of mirrors, along with imaging of beam profiles and the focusing of Gaussian modes.

We then briefly mention the concepts of birefringence and dichroism, two very important properties for understanding the manipulation of light amplitude and polarisation profile, with a recurring theme in later chapters of this thesis. We finally conclude the chapter by introducing digital micromirror devices (DMD) and vector vortex plates (VVP), two methods for the generation of vector beams we extensively use in our experiments. The DMD is a dynamic binary amplitude modulator, utilising holograms for generation and manipulation of complex vector fields, while a VVP offers static generation of vector beams via birefringent effects. The way they work will be thoroughly discussed in this chapter.

Finally, we arrive at the last chapter in Part I, which details our work realising a single-shot polarimeter with generalised measurements. In Chapter 3, we combine all the knowledge we have accumulated so far, and working with our collaborators, we investigate an alternative method of polarisation detection using a unique experimental configuration. In this setup, the incoming beam is projected onto a set of unbiased projection operators, forming a positive operator value measure (POVM), which entails a reduction in the required measurements for polarisation state reconstruction from six with Stokes tomography down to just four. This chapter goes into extensive detail on the background of generalised measurements and our POVM states before introducing the experimental realisation, then discussing our results in comparison to Stokes tomography and theory before concluding with an introduction to the subsequent work that followed, building on our initial investigation.

In Part II of this thesis, we shift our focus to the interaction of light with matter, with a great interest in observing and quantifying the magneto-optical effects around resonance experienced by vector vortex beams interacting with rubidium vapour. In Chapter 4, we build our understanding of how light interacts with matter, introducing the atomic structure of rubidium and discussing the processes of light emission and absorption, leading to the simple two-level system of matter-light interaction described by the Bloch equations. We then explore the conditions leading to the Doppler broadening effects observed experimentally, before discussing various pumping schemes of light with different polarisation structures and the conditions required to drive them. Finally, we introduce the rate equations of multilevel systems and observe the effect of the two circular polarisation structures on the population of the atomic states.

The quantised nature of atomic energy levels necessitates the matching of the transition energy to the photon frequency for excitations to occur, requiring precise control over the laser frequency. Which is why in Chapter 5 we provide a detailed description of our homemade frequency-tunable external cavity diode lasers (ECDL), constructed from a laser diode and a grating in what is commonly referred to as the enhanced Littrow configuration. We then introduce Doppler free spectroscopy as the method for error signal generation for laser frequency stabilisation, followed by exploring the use of acousto-optic modulators (AOM) as a means for laser frequency control, before finally concluding with a brief investigation into the effects of power broadening on transition linewidth across varying ratios of pump and probe powers in saturated absorption spectroscopy (satspec). This investigation helped us understand the ideal power settings to generate an optimal Doppler-free signal.

Chapter 6 marks the last chapter in this thesis, combining all the concepts encountered in both parts to realise an experimental configuration of Doppler free spectroscopy utilising a vector probe beam. We first introduce the necessary theoretical concepts required for the modelling of our system, starting with the derivation of the electric susceptibility, which we use to compute the complex refractive index and obtain an expression for the absorption and dispersion coefficients of the light field. We then introduce a method for calculating the optical density based on the Beer-Lambert law and use it to estimate the number of atoms that interact with our light field.

The next section introduces the Faraday effect, a magneto-optical effect causing a rotation of the plane of linear polarisation as a consequence of external magnetic fields, which plays an important role in our experiment. As a starting point and to lay the groundwork for our research, we thoroughly investigate a polarisation spectroscopy (polspec) setup, utilising an optically pumped medium housed in a magnetically shielded cell, permitting a component of the earth's magnetic field to enter the vapour cell along the beam propagation direction, driving atomic transitions with circularly polarised light $\sigma_{\pm}$. The induced circular birefringence and dichroism in the medium give rise to preferential absorption and dispersion of the light field, which are necessary for the generation of the polspec signal. In the last section of this chapter, we provide a detailed description of all changes to the initial polspec setup to realise an experimental configuration for spatial polarisation spectroscopy (spatpolspec). In this work, we investigate the interaction of vector vortex light with rubidium vapour at room temperature, with the intention of establishing a pattern between variations to the spatial structure of the output beam and the frequency of the light source, in the hopes of laying the groundwork for the development of a new method of modulation-free, perhaps one-shot measurement of a spatially varying frequency signal for laser locking purposes. This section provides extensive descriptions of our experimental findings and analysis techniques before concluding with a comparison between our results and those generated with a numerical model.

PART I

LIGHT, POLARISATION AND POLARIMETRY

Chapter 1

The electromagnetic wave and polarisation

1.1 Introduction

Maxwell's equations and the Lorentz force provide a complete picture of the classical behaviour of electromagnetic radiation. Following the literature in [2, 12], we develop a mathematical understanding of the wave nature of electromagnetic radiation, starting with the electric wave solution of Maxwell's equations, leading to the development of a quantitative description of light polarisation before finally introducing and examining the characteristics of transverse modes of propagation.

1.2 Light the classical wave

In their most general differential form, ***Maxwell's equations*** in the presence of matter and charge are given by,

$$\nabla \cdot \mathbf{D} = \rho, \tag{1.2.1}$$

$$\nabla \cdot \mathbf{B} = 0, \tag{1.2.2}$$

$$\nabla \times \mathbf{E} = -\frac{\partial \mathbf{B}}{\partial t}, \tag{1.2.3}$$

$$\nabla \times \mathbf{H} = \mathbf{J} + \frac{\partial \mathbf{D}}{\partial t}, \tag{1.2.4}$$

where $\mathbf{E}$ and $\mathbf{H}$ are the electric and magnetic fields, respectively, $\mathbf{D}$ the electric displacement, $\mathbf{B}$ the magnetic flux density, ρ the charge density, $\mathbf{J}$ the current density, and t the time. In Cartesian coordinates, the nabla or del operator is given by $\nabla = (\frac{\partial}{\partial x}\hat{\mathbf{e}}_\mathbf{x} + \frac{\partial}{\partial y}\hat{\mathbf{e}}_\mathbf{y} + \frac{\partial}{\partial z}\hat{\mathbf{e}}_\mathbf{z})$, where $\{\hat{\mathbf{e}}_\mathbf{x}, \hat{\mathbf{e}}_\mathbf{y}, \hat{\mathbf{e}}_\mathbf{z}\}$ are basis vectors[1]. The electric displacement $\mathbf{D}$ (sometimes called the electric flux density) shares the following relationship with the electric field $\mathbf{E}$,

$$\mathbf{D} = \varepsilon_0 \mathbf{E} + \mathbf{P} = \varepsilon \mathbf{E}, \tag{1.2.5}$$

[1]The operations $\nabla \cdot \mathbf{A}$ and $\nabla \times \mathbf{A}$ are known as the divergence and the curl of $\mathbf{A}$, arising from taking the dot $(\cdot)$ and cross $(\times)$ product of $\mathbf{A}$ respectively. These are localised quantities, where the divergence measures the tendency of a field to behave as a point source and the curl the infinitesimal rotation of the vector field.

where $\mathbf{P}$ is the polarisation density, ε is the permittivity, a measure of the polarisability of a medium, given by $\varepsilon = \varepsilon_r \varepsilon_0$, where ε_r is the relative permittivity unique to the medium and ε_0 is the permittivity of free space. Generally, any polarisation is induced by the $\mathbf{E}$-field; however, certain dielectric materials can be manufactured with permanent polarisation, whose effects are characterised by the $\mathbf{P}$-field. In a similar fashion, the magnetic field $\mathbf{H}$ and the magnetic flux density $\mathbf{B}$ share the following relation,

$$\mathbf{B} = \mu_0 \mathbf{H} + \mathbf{M} = \mu \mathbf{H}, \tag{1.2.6}$$

where $\mathbf{M}$ is the magnetisation density and μ is the permeability, a measure of the magnetisation of a medium, given by $\mu = \mu_r \mu_0$, where μ_r is the relative permeability and μ_0 is the permeability of free space. Any external contribution to the $\mathbf{B}$-field is accounted for by the $\mathbf{M}$-field; a prime example of such contributions are ferromagnetic materials with permanent magnetisation.

To derive an equation for the propagation of the electric field $\mathbf{E}$, we assume our light field is propagating in vacuum ($\varepsilon_r = \mu_r = 1$) in the absence of any charges ($\rho = \mathbf{J} = 0$) or external fields ($\mathbf{P} = \mathbf{M} = 0$). These assumptions help significantly reduce the complexity of Maxwell's equations to the vacuum state equations,

$$\nabla \cdot \mathbf{E} = 0, \tag{1.2.7}$$

$$\nabla \cdot \mathbf{B} = 0, \tag{1.2.8}$$

$$\nabla \times \mathbf{E} = -\frac{\partial \mathbf{B}}{\partial t}, \tag{1.2.9}$$

$$\nabla \times \mathbf{B} = \mu_0 \varepsilon_0 \frac{\partial \mathbf{E}}{\partial t}. \tag{1.2.10}$$

To derive an equation for the Electric field $\mathbf{E}$, we take the curl of Eqn. 1.2.9,

$$\nabla \times (\nabla \times \mathbf{E}) = -\frac{\partial (\nabla \times \mathbf{B})}{\partial t}, \tag{1.2.11}$$

using the vector identity $\nabla \times (\nabla \times \mathbf{E}) = \nabla(\nabla \cdot \mathbf{E}) - \nabla^2 \mathbf{E}$, and substituting in Eqn. 1.2.7 and Eqn. 1.2.10 into Eqn. 1.2.11, we end up with,

$$\nabla^2 \mathbf{E} = \mu_0 \varepsilon_0 \frac{\partial^2 E}{\partial t^2}. \tag{1.2.12}$$

The product of the permeability and susceptibility $\mu_0 \varepsilon_0$ are related to the speed of light c by $c = 1/\sqrt{\mu_0 \varepsilon_0} \approx 3.00 \times 10^8 \mathrm{ms}^{-1}$. Substituting this into Eqn. 1.2.12, we obtain the common form of the equation found in literature,

$$\nabla^2 \mathbf{E} = \frac{1}{c^2} \frac{\partial^2 E}{\partial t^2}. \tag{1.2.13}$$

The above equation is known as the ***wave equation*** of $\mathbf{E}$, a second-order partial differential equation (PDE) with a series of analytic solutions. Luckily, these solutions can be easily calculated using the separation of variables method, where the simplest solution is given by the ***plane wave solution***,

$$\mathbf{E}(\mathbf{r}, t) = E_{0\mathbf{r}} \exp\big[i(\mathbf{k} \cdot \mathbf{r} - \omega t + \phi)\big] \hat{\mathbf{e}}_r, \tag{1.2.14}$$

where $\mathbf{r} = \{x, y, z\}$ and t are the spatial and temporal coordinates respectively, $E_{0\mathbf{r}}$ is the amplitude, ω is the angular frequency defined as $\omega = 2\pi\nu$, where ν is the wave frequency and $\mathbf{k}$ the wave vector, pointing in the direction of wave propagation and perpendicular to surfaces of constant phase, as illustrated in Fig. 1.1a. Mathematically, they represent minima and maxima in the wave oscillation profile and are locally perceived as flat planes by the propagating wave, separated by the wavelength λ, as shown by the red and blue surfaces in Fig. 1.1b respectively. We define the magnitude of the wave vector as $|\mathbf{k}| = 2\pi/\lambda$, where λ is the wavelength. Here ϕ is the phase offset (defined as the phase at $\mathbf{r} = t = 0$), where $i = \sqrt{-1}$ is the imaginary number, and the basis vectors $\hat{\mathbf{e}}_r$ describe the oscillation of the $\mathbf{E}$-field in the specified direction plane.

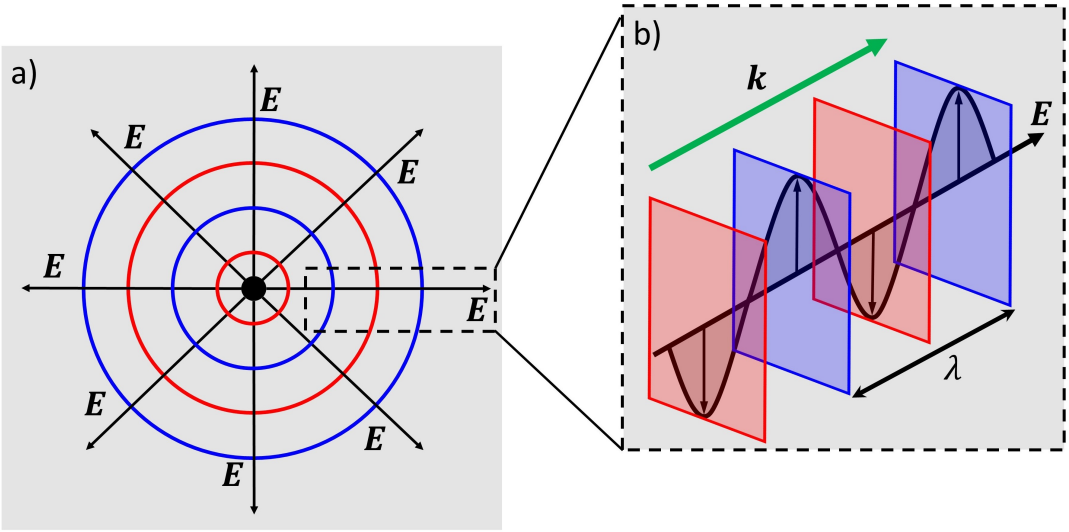

Figure 1.1: Surfaces of constant phase corresponding to the wave minima (red) and maxima (blue). a) An illustration of a point source producing electric fields propagating in all directions along circles representing surfaces of constant phase. b) A close-up of the phase surfaces, where locally these surfaces are flat planes separated by the wavelength λ. The $\mathbf{E}$-wave propagates in the direction of the $\mathbf{k}$ vector, highlighted by the green arrow.

It is worth mentioning that Maxwell's equations can be solved in a similar fashion to derive an equation for the propagation of the $\mathbf{B}$-field[2], however, magnetic field contributions are not considered in the first part of this thesis[3], but plays a crucial role in our experiment with matter-light interaction, as we shall see in the later chapters of this thesis.

1.3 Polarisation

1.3.1 A quantitative description

In the previous section, we derived an expression for the propagation of the electric field from Maxwell's theory. The orientation (or oscillation) of the propagating wave defined by the unit vector $\hat{\mathbf{e}}_r$ in Eqn. 1.2.14 quantifies a key property of the electric field, namely the polarisation.

[2]Note in some literature, the magnetic flux density $\mathbf{B}$ is sometimes called the magnetic field. Generally it is a labelling choice; however, under certain conditions (i.e. $\mathbf{M} = 0$), they are interchangeable.

[3]Since the $\mathbf{B}$-field is orthogonal to the electric field, $\mathbf{E}$, it is of no consequence to us; however, the two quantities share a straightforward relationship given by the Lorentz force $F = q(\mathbf{E} + v \times \mathbf{B})$, where q is the elemental charge and v is the particle velocity.

Given that any linear superposition of plane waves is also a solution to the wave equation 1.2.13, the electric field for a wave propagating in the z-direction is given by,

$$\begin{aligned}\mathbf{E}(z,t) &= \frac{1}{\sqrt{2}}(E_{0x}e^{i(kz-\omega t+\phi_x)}\hat{\mathbf{e}}_x + E_{0y}e^{i(kz-\omega t+\phi_y)}\hat{\mathbf{e}}_y) \\ &= \frac{1}{\sqrt{2}}(E_{0x}e^{i\phi_x}\hat{\mathbf{e}}_x + E_{0y}e^{i\phi_y}\hat{\mathbf{e}}_y)e^{i(kz-\omega t)},\end{aligned} \tag{1.3.1}$$

where $\hat{\mathbf{e}}_x$ and $\hat{\mathbf{e}}_y$ are basis vectors indicating wave oscillations along the x and y directions, respectively. In terms of the electric field, we define the beam intensity as follows,

$$\mathbf{I}(z,t) = \left|\mathbf{E}(z,t)\right|^2 = \mathbf{E}(z,t)\mathbf{E}^*(z,t), \tag{1.3.2}$$

where $\mathbf{E}^*(z,t)$ denotes the complex conjugate of $\mathbf{E}(z,t)$. The superimposed electric field amplitudes, along with the phase difference between the two, can generate an infinite number of polarisation possibilities. However, there are special cases of the electric field orientation, as a consequence of certain conditions obeyed by the amplitude E_{0x}, E_{0y} and phase components ϕ_x, ϕ_y, that generated useful polarisation structures. The wave represented by Eqn. 1.3.1 depicts a polarisation structure commonly known as ***elliptically polarised***[4]. Fully polarised beams are always elliptical; however, there are two special cases of elliptical polarisation with unique and simplified structures, known as linearly and circularly polarised. Let us consider the simplest polarisation case, assuming the y-component of the wave does not exist (i.e. $E_{0y} = 0$), we denote the **E**-field of a wave oscillating in the x-direction, propagating along z by,

$$\mathbf{E}(z,t) = \frac{1}{\sqrt{2}}E_{0x}e^{i\phi_x}e^{i(kz-\omega t)}\hat{\mathbf{e}}_x \equiv \hat{H}. \tag{1.3.3}$$

In literature, this electric field orientation is a form of linear polarisation called ***horizontally polarised*** ($\hat{H}$). Now we consider another special case of linear polarisation that requires equal amplitude and phase between the polarisation components: $E_{0x} = E_{0y} = E_0$ and $\phi_x = \phi_y = \phi$,

$$\mathbf{E}(z,t) = \frac{1}{\sqrt{2}}E_0(\hat{\mathbf{e}}_x + \hat{\mathbf{e}}_y)e^{i\phi}e^{i(kz-\omega t)} \equiv \hat{D}. \tag{1.3.4}$$

This type of polarisation is knowns as ***diagonally polarised*** ($\hat{D}$), on account of the equal amplitudes between the two polarisation components, ensuring the oscillation is occurring at 45° with respect to the horizontal. In the case where the electric field amplitudes are not equal (i.e. $E_{0x} \neq E_{0y}$), the polarisation angle θ is given by $\theta = \tan^{-1}(E_{0y}/E_{0x})$, as illustrated in Fig. 1.2a. Pure linearly polarised light has no ellipticity, and any linear polarisation structure formed by superimposing the two polarisation components along x and y must have a phase shift equal to a multiple of π (i.e. $\phi_y - \phi_x = n\pi$, where $n \in \mathbb{Z}$)[5]. Conversely, elliptically polarised light exhibits variations in the electric field oscillation, where the amplitude and phase of one (or both) of the polarisation components change throughout propagation, tracing an ellipse in space as seen in Fig. 1.2b. When discussing phase variations of the light field, we usually refer to the relative phase between the two polarisation components and can express Eqn. 1.3.1 as,

[4]The name stems from the wave tracing the shape of an ellipse along the $x-y$ plane while propagating along z. More will be discussed in Section 1.3.3.

[5]Where $\mathbb{Z}$ is the set of all integers.

$$\mathbf{E}(z,t) = \frac{1}{\sqrt{2}}(E_{0x}\hat{\mathbf{e}}_x + E_{0y}e^{i\Delta\phi}\hat{\mathbf{e}}_y)e^{i(kz-\omega t)}, \tag{1.3.5}$$

where we have introduced the relative phase $\Delta\phi = \phi_y - \phi_x$. In this formalism, the horizontal phase ϕ_x now has a global term that we choose to ignore[6]. For the special case where an elliptically polarised beam obeys the equal amplitudes condition (i.e. $E_{0x} = E_{0y} = E_0$) and the two polarisation components possess a phase difference of $\Delta\phi = n\pi/2$ where $n \in \mathbb{Z}$, the beam will trace out a perfect circle in the $x-y$ plane while propagating along z and hence is said to be circularly polarised. If we consider a phase shift of $-\pi/2$ between the two polarisation components, the electric field is given by,

$$\mathbf{E}(z,t) = \frac{1}{\sqrt{2}}E_0(\hat{\mathbf{e}}_x - i\hat{\mathbf{e}}_y)e^{i(kz-\omega t)} \equiv \hat{R}, \tag{1.3.6}$$

where such a polarisation structure is known as ***right-hand circularly polarised*** ($\hat{R}$). The handedness of the polarisation rotation is a consequence of the phase sign.

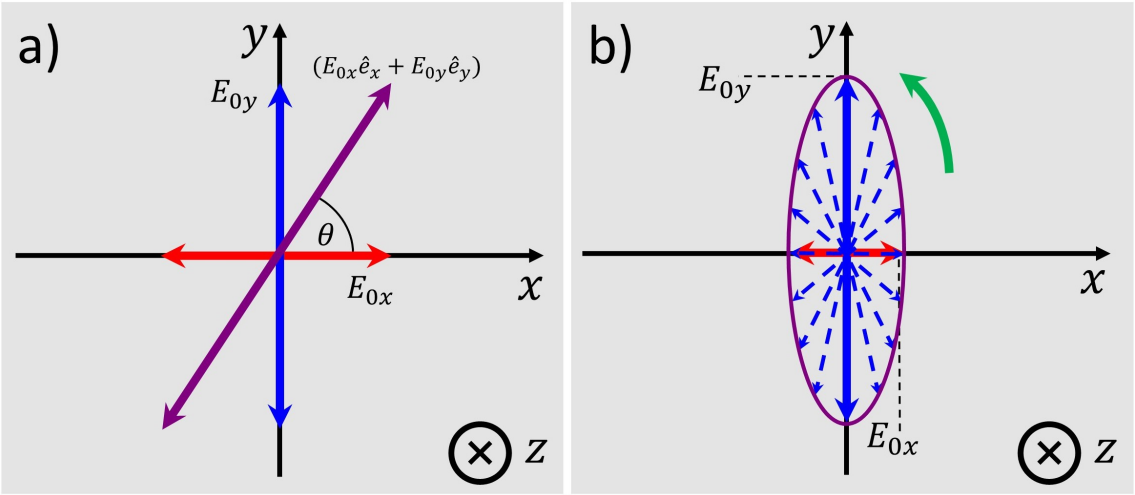

Figure 1.2: General linear and elliptical polarisation states, both propagating along the z-direction (into the page)[7]. The double-sided arrows indicate the oscillation across the plane. Blue indicates polarisation along y, red is polarisation along x, and purple is a superposition of both. a) Linear polarisation given by the angle θ. b) elliptical polarisation with a spatially varying vertical component as a consequence of a complex phase i and unequal amplitudes along the x and y directions. The curved green arrow indicates the rotation direction.

The special cases of linearly and elliptical polarisation described in Eqns. 1.3.3, 1.3.4 and 1.3.6 all possess orthogonal polarisation states called ***vertical*** ($\hat{V}$), ***anti-diagonal*** ($\hat{A}$) and ***left-hand circular*** ($\hat{L}$) polarisation, respectively, creating a total of six polarisation states. The table below provides a summary of the conditions for the relative phase $\Delta\phi$ and amplitudes E_{0x}, E_{0y} that must be obeyed to generate the special polarisation states.

[6]Experimentally, we measure intensities given by Eqn. 1.3.2, where any global phase terms disappear in the absolute square value. However, the effect of global phases become important for interferometric setups (more in Chapter 3), but generally we are forgiven for ignoring these phases in our electric field formalism.

[7]In literature, a circle with a dot indicates an arrow tip where the axis points out of the page, while a circle with an "x" indicates the back of the arrow where the axis points into the page.

Amplitude condition	phase condition	$\mathbf{E}(z,t)$	Polarisation type
$E_{0y} = 0$	———————	$E_{0x}e^{i\phi_x}\hat{\mathbf{e}}_x$	Horizontal, $\hat{H}$
$E_{0x} = 0$	———————	$E_{0y}e^{i\phi_y}\hat{\mathbf{e}}_y$	Vertical, $\hat{V}$
$E_{0x} = E_{0y} = E_0$	$\Delta\phi = 2n\pi$	$E_0(\hat{\mathbf{e}}_x + \hat{\mathbf{e}}_y)$	Diagonal, $\hat{D}$
$E_{0x} = E_{0y} = E_0$	$\Delta\phi = (2n+1)\pi$	$E_0(\hat{\mathbf{e}}_x - \hat{\mathbf{e}}_y)$	Anti-diagonal, $\hat{A}$
$E_{0x} = E_{0y} = E_0$	$\Delta\phi = (2n-\frac{1}{2})\pi$	$E_0(\hat{\mathbf{e}}_x - i\hat{\mathbf{e}}_y)$	Right-hand circular, $\hat{R}$
$E_{0x} = E_{0y} = E_0$	$\Delta\phi = (2n+\frac{1}{2})\pi$	$E_0(\hat{\mathbf{e}}_x + i\hat{\mathbf{e}}_y)$	Left-hand circular, $\hat{L}$

Table 1.1: Summary of the amplitude and phase conditions to generate the six unique polarisation structures. Here n is an integer (i.e. $n \in \mathbb{Z}$), where $\mathbb{Z}$ refers to the set of all integers. Note we only state the polarisation term of the electric field $\mathbf{E}(z,t)$; the propagation term $e^{i(kz-\omega t)}$ is implied.

Note that superimposing multiple elliptical polarisation profiles can generate a linearly polarised output beam and vice versa. Generally speaking, the sign of the diagonal or anti-diagonal and right or left circular polarisation basis is subject to the chosen frame of reference. In this thesis, we define the polarisation along the beam propagation. However, it is important to consider the frame of reference when recording images using image sensors like complementary metal-oxide semiconductors (CMOS) or charge-coupled devices (CCD), as the recorded image might not agree with the defined coordinate frame of the polarisation states. These six orthogonal polarisation states form what is known as the Stokes basis and are mutually unbiased in their measurement[8] and are graphically represented in Fig. 1.3 below.

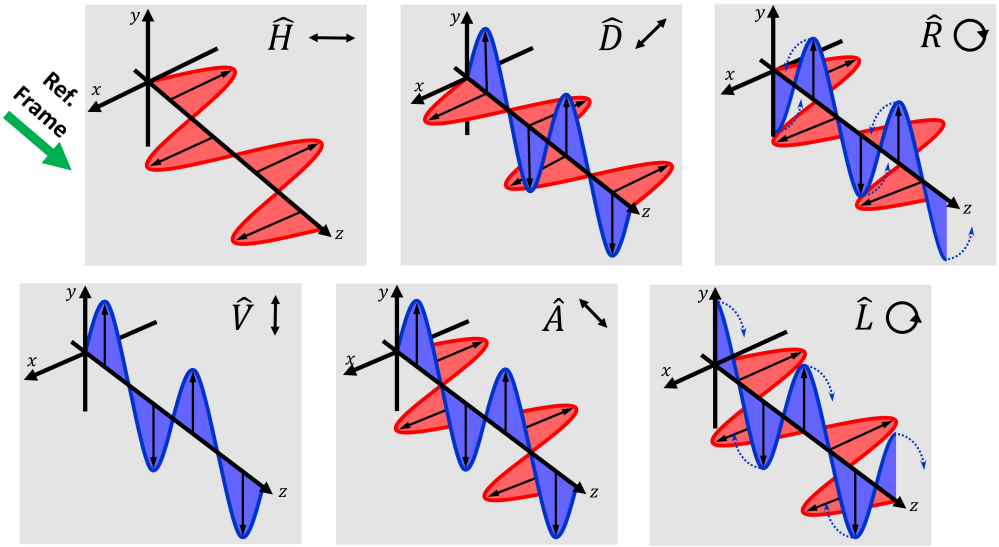

Figure 1.3: Electric field oscillation of the six unique polarisation structures of the Stokes basis. From top left to bottom right, the polarisation is: horizontal, diagonal, right-left circular, vertical, anti-diagonal, and left-hand circular. The waves are propagating with respect to the frame of reference indicated by the green arrow.

[8]The idea of bias in the reconstruction of input states will be extensively explored in a later chapter of this thesis.

1.3.2 Formalism and manipulation

So far, we have described the oscillating nature of electromagnetic waves and associated the orientation of the oscillation with different polarisation states. There are some well-known mathematical formalism that deal with polarisation descriptions and the interaction of light with optics throughout propagation. The most common representations are Jones calculus and Mueller calculus. In this section, we make use of the Jones formalism, taking advantage of its simplified nature to describe the manipulation of the polarisation state. Since the plane-wave solution is assumed, we only concern ourselves with the transverse polarisation profile, mathematically characterised by a 2×1 vector as follows,

$$\mathbf{E} = \begin{pmatrix} E_x \\ E_y \end{pmatrix} = \begin{pmatrix} E_{0x} e^{i\phi_x} \\ E_{0y} e^{i\phi_y} \end{pmatrix} = \begin{pmatrix} E_{0x} \\ E_{0y} e^{i\Delta\phi} \end{pmatrix}, \tag{1.3.7}$$

where in the last expression we once again consider the phase difference between the two polarisation components $\Delta\phi = \phi_y - \phi_x$, ignoring any global phase terms. When compared with Eqn. 1.3.5, we consider the polarisation of the beam at a fixed point in space and time (we choose the origin for simplicity, i.e. $z = t = 0$). This vector is known as the ***Jones vector***. Once again, the intensity is given by the modulus squared of the electric field $|\mathbf{E}|^2$, as follows,

$$I = \mathbf{E}^*\mathbf{E} = \begin{pmatrix} E_x & E_y \end{pmatrix} \begin{pmatrix} E_x \\ E_y \end{pmatrix} = |E_x|^2 + \left|E_y\right|^2, \tag{1.3.8}$$

where $\mathbf{E}^*$ denotes the complex conjugate of the electric field $\mathbf{E}$. Note E_x and E_y are the horizontal and vertical components of the electric field from Eqn. 1.3.7 respectively[9]. In the plane wave solution, the electric field in the direction of propagation is zero ($E_z = 0$)[10], however, this does not imply the longitudinal polarisation component (along the z-direction) does not exist. In fact, longitudinal polarisation has been a subject of study in previous literature in experiments utilising strong focusing techniques [13–15]. Nevertheless, such focusing techniques are beyond the scope of this thesis[11], and we only concern ourselves with the transverse polarisation profile (x, y directions) of the electric field. It is important to note that Jones notation only works with fully polarised light. To represent the polarisation basis, we require our vectors to be normalised. In order to achieve this, we demand that the intensity in Eqn. 1.3.8 equals 1. Some Jones vectors that meet this requirement are,

$$\hat{H} = \begin{pmatrix} 1 \\ 0 \end{pmatrix}, \qquad \hat{V} = \begin{pmatrix} 0 \\ 1 \end{pmatrix}. \tag{1.3.9}$$

These are the Jones vector representations of the horizontal and vertical polarisation states, respectively. Now if we consider a superimposed state, similar to the ones in Table 1.1, by using

[9] Some literature prefers E_h and E_v instead; however, they both denote the same quantities.

[10] We easily observe this by substituting Eqn. 1.2.14 into Eqn. 1.2.7 and obtain $\mathbf{k} \cdot \mathbf{E} = 0$, stating the electric field does not exist in the direction or propagation.

[11] The paraxial theory we developed for the electric field relies on small angles with the optical axis. However, strong focusing involves large angles, which violates our initial assumption.

Eqn. 1.3.9 we can construct an expression for the diagonal polarisation state, $\hat{D} = c(1\ \ 1)^T$, where c is a normalisation constant. Now we check to see if the vector $\hat{D}$ is indeed normalised by substituting it into Eqn. 1.3.8 and setting $I = 1$ once more. Doing so gives us a value for the normalisation constant $c = 1/\sqrt{2}$. By extending this treatment to all the polarisation states in Table 1.1, we obtain an expression for the normalised Jones vectors of the six different polarisations,

$$\begin{aligned} \hat{H} &= \begin{pmatrix} 1 \\ 0 \end{pmatrix}, & \hat{V} &= \begin{pmatrix} 0 \\ 1 \end{pmatrix}, \\ \hat{D} &= \frac{1}{\sqrt{2}} \begin{pmatrix} 1 \\ 1 \end{pmatrix}, & \hat{A} &= \frac{1}{\sqrt{2}} \begin{pmatrix} 1 \\ -1 \end{pmatrix}, \\ \hat{L} &= \frac{1}{\sqrt{2}} \begin{pmatrix} 1 \\ i \end{pmatrix}, & \hat{R} &= \frac{1}{\sqrt{2}} \begin{pmatrix} 1 \\ -i \end{pmatrix}, \end{aligned} \tag{1.3.10}$$

where the imaginary number i indicates a phase shift of $\pi/2$. Two waves are said to be orthogonal if their state of polarisation, represented by the complex amplitudes $\mathbf{E}_1$ and $\mathbf{E}_2$, obeys [16],

$$\mathbf{E}_1 \cdot \mathbf{E}_2^* = 0. \tag{1.3.11}$$

From Eqns. 1.3.10, it is much easier to see that any combination of horizontal/vertical, diagonal/anti-diagonal, and left-circular/right-circular are indeed orthogonal to one another, obeying the condition in Eqn. 1.3.11 $\hat{H} \cdot \hat{V} = \hat{D} \cdot \hat{A} = \hat{R} \cdot \hat{L} = 0$ and confirming their unbiased nature in polarisation state reconstruction.

Any optical element acting on the electric field throughout propagation can be represented by a 2×2 matrix called the ***Jones matrix***, $\mathbf{J}_M$. These matrices are considered transformation matrices that produce an output Jones vector $\mathbf{E}_{out}$ via the standard rules of matrix multiplication (i.e. $\mathbf{E}_{out} = \mathbf{J}_M \mathbf{E}_{in}$). Optical elements that manipulate beam polarisation are called ***polarisation optics***; the most common are polarisers and phase retarders. A polariser is a dichroic element (see Section 2.4 for more information) that works by absorbing (or reflecting) the light perpendicular to its transmission axis, which is useful in reducing the beam intensity. Their Jones matrix is given by [17],

$$\mathbf{J}'_{pol} = \begin{pmatrix} T_x & 0 \\ 0 & T_y \end{pmatrix}, \tag{1.3.12}$$

where T_x and T_y are the transmitted light along the horizontal, x and vertical, y axes, respectively. In this notation, a 100% light transmission corresponds to $T_{x,y} = 1$, while 0% of the light being transmitted is denoted by $T_{x,y} = 0$. In an experimental setting, one can use a rotation mount (like a Thorlabs RSP1/M) to rotate the transmission axis of the polariser, hence affecting the transmission coefficients from Eqn. 1.3.12. Mathematically, this rotation is given by the transformation,

$$\mathbf{J}_{pol} = \mathbf{R}(-\theta)\mathbf{J}'_{pol}\mathbf{R}(\theta), \tag{1.3.13}$$

where $R(\theta)$ is called the rotation matrix and given by,

$$\mathbf{R}(\theta) = \begin{pmatrix} \cos(\theta) & \sin(\theta) \\ -\sin(\theta) & \cos(\theta) \end{pmatrix}, \tag{1.3.14}$$

with the angle θ made with respect to the horizontal axis. Inserting the rotation matrix and Eqn. 1.3.12 into Eqn. 1.3.13 yields,

$$\mathbf{J}_{pol} = \begin{pmatrix} T_x \cos^2\theta + T_y \sin^2\theta & (T_x - T_y)\sin(\theta)\cos(\theta) \\ (T_x - T_y)\sin(\theta)\cos(\theta) & T_x \sin^2\theta + T_y \cos^2\theta \end{pmatrix}. \tag{1.3.15}$$

For an ideal polariser with the transmission axis oriented flat along the x-axis, we expect maximum transmission along the horizontal with no transmitted light in the vertical (i.e. $T_x = 1$ and $T_y = 0$). This simplifies the Jones matrix into the following,

$$\mathbf{J}_{pol} = \begin{pmatrix} \cos^2\theta & \sin(\theta)\cos(\theta) \\ \sin(\theta)\cos(\theta) & \sin^2\theta \end{pmatrix}, \tag{1.3.16}$$

where θ is the polariser angle with respect to the horizontal axis. We see from the Jones matrix above that we expect maximum transmission of horizontally polarised light when $\theta = 0$, and similarly for vertically polarised light when $\theta = \pi/2$. Unfortunately, this simplified ideal matrix is not an accurate representation of polariser behaviour in an experimental environment. In reality, the polariser's ability to absorb light perpendicular to its transmission axis is given in terms of an ***extinction ratio***.

This extinction ratio is determined by certain parameters (e.g. the material the polariser is manufactured from) and is defined as the ratio of maximum to minimum transmission. Ideally, a very high extinction ratio is desirable for all polarisation optics, especially for tomography purposes (more in Section 1.4), and achieving it requires a careful selection of the right materials. Most conventional polarisers are polymer-based; the ones available for our work at 780nm consist of a dichroic film inside N-BK7 glass and offer an extinction ratio of $> 400:1$ (Thorlabs LPNIRE100-B). Their low extinction ratio hinders their ability to effectively absorb unwanted polarisation structures, especially for higher-intensity beams, which is why they are best avoided in a tomography setup. However, a nano-particle polariser covering our wavelength of interest can offer an extinction ratio of up to $> 100,000:1$, sufficient to behave more like the perfect polariser represented by Eqn. 1.3.16, with much less polarisation cross-talk.

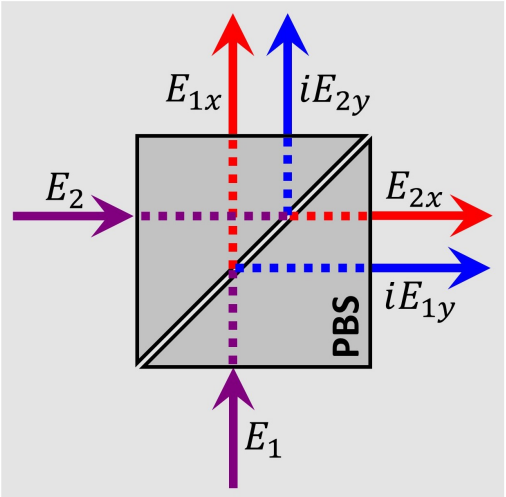

Figure 1.4: A polarising beam splitting cube. The cube transmits $\hat{H}$ while reflecting $\hat{V}$ with an added phase.

There are types of polarisation optics that work via reflection, where an incident beam is instead split into its two orthogonal polarisation states, with one of the components being transmitted while

the other is reflected. An example of such an optical element is a polarising beam splitter (PBS)[12]. Generally, they come in the form of a thinly coated piece of glass (commonly named economy PBS) or otherwise a cube made of two prisms bound together with cement and dielectrically coated at the hypotenuse, introducing a birefringence (see section 2.4) in the medium, enabling the transmission of a horizontally polarised beam while reflecting any vertically polarised light. Similar to polarisers, PBS also have extinction ratios governing their performance. In fact, some specific laser line PBS offer high enough extinction ratios that could replace a polariser for tomography purposes. Mathematically, a PBS cube is described by the following Jones matrices,

$$\mathbf{J}_{pbs}^{T} = \begin{pmatrix} 1 & 0 \\ 0 & 0 \end{pmatrix}, \qquad \mathbf{J}_{pbs}^{R} = \begin{pmatrix} 0 & 0 \\ 0 & i \end{pmatrix}, \tag{1.3.17}$$

where $\mathbf{J}_{pbs}^{T}$ and $\mathbf{J}_{pbs}^{R}$ are the transmission and reflection matrix of the PBS, respectively, and i is the imaginary number. From the equation above, we expect horizontally polarised light to transmit through the PBS and vertically polarised light to reflect off the PBS, picking up an additional $\pi/2$ phase, as shown in Fig. 1.4. Despite the usefulness of polarisers and PBS, they work by manipulating the intensity or beam paths, respectively; however, the polarisation output remains fixed. Instead, we use waveplates to manipulate the polarisation without changing the beam intensity. Waveplates, or phase retarders, are birefringent materials that possess fast and slow axes and are usually made of some form of crystal or polymer[13]. As the name suggests, a polarisation component oriented with respect to the fast axis of the waveplate will propagate faster than its orthogonal polarisation component, introducing a phase delay between the two and changing the polarisation of the beam. This delay is given by [2],

$$\Delta\psi = \frac{2\pi d\Delta n}{\lambda_0}, \tag{1.3.18}$$

where d is the waveplate thickness, λ_0 is the light wavelength in vacuum, and Δn is the difference between the refractive index of the material along the slow and fast axes, $\Delta n = n_{slow} - n_{fast}$. The angle of $\Delta\psi$ is given in radians. We can implement a similar treatment to the matrix in Eqn. 1.3.12 to derive an expression for a general linear phase retarder. For a phase plate with an angle θ along the x-axis, where the Jones matrix is given by [17, 18],

$$\mathbf{J}_{LPR} = e^{\frac{i\delta}{2}} \begin{pmatrix} \cos^2\theta + e^{-i\delta}\sin^2\theta & (1-e^{-i\delta})\sin(\theta)\cos(\theta) \\ (1-e^{-i\delta})\sin(\theta)\cos(\theta) & \sin^2\theta + e^{-i\delta}\cos^2\theta \end{pmatrix}, \tag{1.3.19}$$

where δ is the relative phase difference between the fast and slow axes of the retarder. Typically, there are two different types of linear waveplates: a half-wave plate and a quarter waveplate (sometimes abbreviated as HWP, or $\lambda/2$ and QWP, or $\lambda/4$ respectively).

A HWP works by introducing a π phase shift between the polarisation components, equivalent to

[12]The most common PBS are ones that split the beam into the $\hat{H}$ and $\hat{V}$ components; however, they can be manufactured to split the beam into other orthogonal components like $\hat{R}$ and $\hat{L}$.

[13]An interesting consequence of the chosen waveplate material is the deviation angle to the beam path. Our quartz waveplates (Thorlabs WPH10M) deviate the beam path by an angle of < 10 arc-seconds, 30 times smaller than a similar polymer-based waveplate (Thorlabs WPH10E series), with a deviation angle of < 5 arc-minutes. These angles are negligibly small in free-space beam propagation but are sufficient to misalign any beams collimated through a pinhole or fibre.

a rotation in the polarisation structure of 2θ, with an additional change in handedness experienced by elliptical and circularly polarised light (i.e. right-hand circular light becomes left-hand circular after propagating through the HWP). The Jones vector for a HWP is given by,

$$\mathbf{J}_{HWP} = e^{\frac{i\pi}{2}} \begin{pmatrix} \cos(2\theta) & \sin(2\theta) \\ \sin(2\theta) & -\cos(2\theta) \end{pmatrix}. \tag{1.3.20}$$

In a similar fashion, a QWP introduces a $\pi/2$ phase shift between the polarisation components. A linearly polarised light propagating through a QWP with its axes oriented at 45° will generate a circularly polarised output beam. The reverse is also true, as the QWP will undo any circularity in the beam profile, turning a right or left-hand circular input into a linearly polarised output. However, in the case where a linear input beam is not at 45° relative to the waveplate axes, the output beam is expected to be elliptically polarised. A QWP has the following Jones matrix,

$$\mathbf{J}_{QWP} = e^{\frac{i\pi}{4}} \begin{pmatrix} \cos^2\theta - i\sin^2\theta & (1+i)\sin(\theta)\cos(\theta) \\ (1+i)\sin(\theta)\cos(\theta) & \sin^2\theta - i\cos^2\theta \end{pmatrix}. \tag{1.3.21}$$

Incidentally, there are different kinds of phase retarders called vector vortex plates, more commonly known as q-plates. These q-plates can generate vector beams from linear input light, making them ideal replacements for complicated beam-shaping methods. A beam that contains multiple polarisation structures in its transverse profile is known as ***vector beams*** or a ***complex light field***. These beams are a recurring theme in this thesis, where the techniques for their generation and manipulation will be discussed in the following sections.

1.3.3 Polarisation ellipse and the Poincaré sphere

Until now, we have primarily considered the mathematical representation of polarisation in the context of Jones calculus. However, there is a graphical representation based on the ellipse equation of the electric field that provides a useful visual illustration of light polarisation. Following the theory in [2, 17], an ellipse not aligned with the horizontal axis is defined by the equation,

$$\left(\frac{E_x}{E_{0x}}\right)^2 + \left(\frac{E_y}{E_{0y}}\right)^2 - \frac{2E_xE_y}{E_{0x}E_{0y}}\cos(\Delta\phi) = \sin^2(\Delta\phi), \tag{1.3.22}$$

where $\Delta\phi = \phi_y - \phi_x$ and the propagation terms all cancel out. Since this ellipse equation refers to the behaviour of the electric field, the equation is known as the polarisation ellipse. As previously stated, all polarisation is elliptical in nature, where linear and circular are merely special forms of elliptically polarised light. This makes Eqn. 1.3.22 sufficient to provide a visual description of any polarisation type we desire. We can express the polarisation ellipse in terms of two angles, namely the ellipse orientation angle ψ and ellipticity angle χ given by,

$$\begin{aligned} \tan(2\psi) &= \frac{2E_{0x}E_{0y}}{E_{0x}^2 - E_{0y}^2}\cos(\Delta\phi) \\ \sin(2\chi) &= \frac{2E_{0x}E_{0y}}{E_{0x}^2 + E_{0y}^2}\sin(\Delta\phi), \end{aligned} \tag{1.3.23}$$

where $0 \leq \psi \leq \pi$ and $0 \leq \chi \leq \pi/2$. For any polarisation type, we can estimate the shape of the ellipse using Eqns. 1.3.23, as illustrated in Fig. 1.5a. For example, consider some polarised beam with a diagonal element (i.e. it could be $\hat{D}$ or $\hat{A}$), and recall from Table 1.1 that the electric field amplitudes and the phase difference are given by $E_{0x} = E_{0y} = E_0$ and $\Delta\phi = n\pi$ for $n \in \mathbb{Z}$, respectively[14]. Inserting these values into Eqns. 1.3.23 yields,

$$\begin{aligned} \tan(2\psi) \to \infty \quad &\implies \quad \therefore \ \psi = \pm\frac{\pi}{4} \\ \sin(2\chi) = \sin(n\pi) \quad &\implies \quad \therefore \ \chi = 0. \end{aligned} \tag{1.3.24}$$

Here we obtained the ellipticity and inclination angle for both diagonal and anti-diagonal elements, where the ellipticity is zero for both as expected (since linear polarisation has no ellipticity). This is illustrated in Fig. 1.5b, by the purple diagonal ellipse (i.e. straight line) of the $\hat{D}$ polarisation state. We apply the same treatment for circularly polarised light, where once again the electric field amplitudes are equal (i.e. $E_{0x} = E_{0y} = E_0$), but the phase difference is now $\Delta\phi = (2n+1)\pi/2$, where n is once again an integer (i.e. $n \in \mathbb{Z}$)[15]. By inserting these values into Eqns. 1.3.23 we have,

$$\begin{aligned} \tan(2\psi) \to \infty \quad &\implies \quad \therefore \ \psi = \pm\frac{\pi}{4} \\ \sin(2\chi) = \sin\left(\frac{(2n+1)\pi}{2}\right) \quad &\implies \quad \therefore \ \chi = \frac{(2n+1)\pi}{4}. \end{aligned} \tag{1.3.25}$$

Once again, these are the orientation and ellipticity angles, where the even and odd values of n correspond to the left and right circular polarised components, respectively, illustrated as a red circle in Fig. 1.5b below[16].

We can re-write the angles in Eqns. 1.3.23 in a pure trigonometric form by introducing the angle $\tan(\sigma) = E_{0y}/E_{0x}$ (as seen in the inset of Fig. 1.5). By calculating the double angles of the sine and cosine of σ, we get,

$$\begin{aligned} \sin(2\sigma) &= \frac{2E_{0x}E_{0y}}{E_{0x}^2 + E_{0y}^2} \\ \cos(2\sigma) &= \frac{E_{0x}^2 - E_{0y}^2}{E_{0x}^2 + E_{0y}^2}, \end{aligned} \tag{1.3.26}$$

where we use Eqns. 1.3.26 to get the expression,

$$\tan(2\sigma) = \frac{\sin(2\sigma)}{\cos(2\sigma)} = \frac{2E_{0x}E_{0y}}{E_{0x}^2 - E_{0y}^2}, \tag{1.3.27}$$

and finally express the orientation angle ψ and ellipticity χ in a more compact form given by,

$$\begin{aligned} \tan(2\psi) &= \tan(2\sigma)\cos(\Delta\phi) \\ \sin(2\chi) &= \sin(2\sigma)\sin(\Delta\phi). \end{aligned} \tag{1.3.28}$$

[14] The phase term is slightly different since both diagonal and anti-diagonal components are being considered.
[15] Once again, this is a general phase expression for both right and left circular polarised.
[16] The handedness is not considered here, but are opposite for the respective circular components.

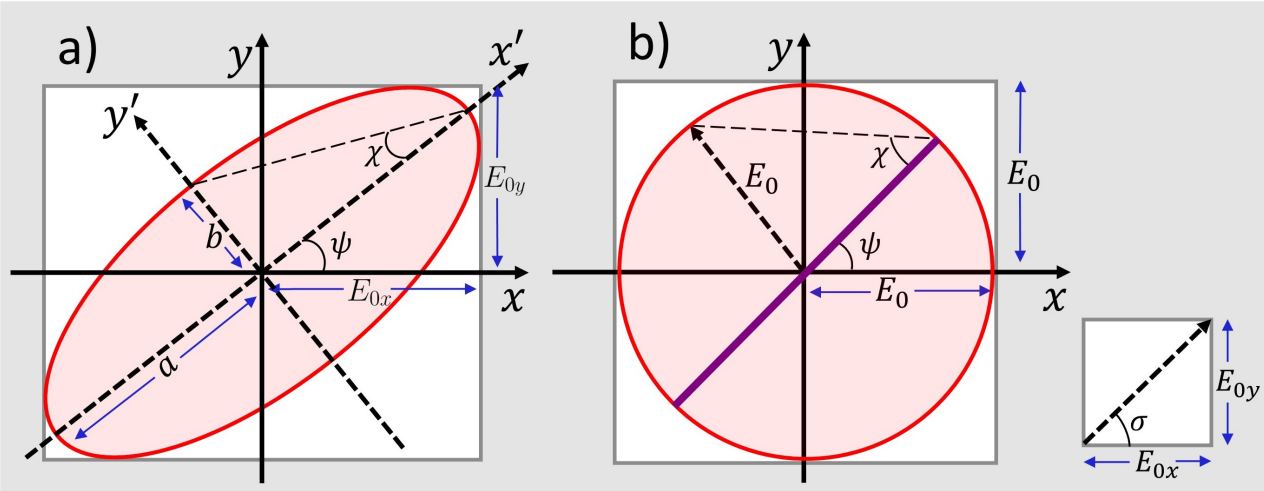

Figure 1.5: Polarisation ellipse of different polarisation states. a) A general polarisation ellipse. b) Polarisation ellipse for a diagonal and circular state, represented by the purple line and red circle, respectively. The inset defines the angle σ between the amplitude of the two polarisation components E_{0x} and E_{0y} used to obtain a purely trigonometric expression for Eqns. 1.3.23.

Although Jones calculus is a useful mathematical tool to represent the polarisation profiles of light propagating through optical elements or other media, it is limited to describing fully polarised light only. In the case where a beam is partially polarised[17] or unpolarised[18], the Jones formalism breaks down, failing to accurately characterise such beams. The ***Stokes vector*** offers a more general mathematical description, useful to characterise any possible polarisation state. The Stokes vector is defined as,

$$\mathbf{S} = \begin{pmatrix} S_0 & S_1 & S_2 & S_3 \end{pmatrix}^T, \tag{1.3.29}$$

where the ^{T} corresponds to the transpose and the quantities S_0, S_1, S_2, S_3 are known as the Stokes parameters. Often in literature, one might find the Stoke parameters denoted by I, Q, U, V, respectively; however, throughout this thesis, we use the former notation. Once again, this vector follows the simple rules of matrix multiplication, where optical elements are denoted by 4×4 matrices known as ***Mueller matrices***[19]. To populate the Stokes vector, we associate each parameter with the intensity measurements for a set of two orthogonal polarisation bases, giving the Stokes parameters the following values for purely polarised light,

$$\begin{aligned} S_0 &= I_H + I_V = I_D + I_A = I_R + I_L \\ S_1 &= I_H - I_V \\ S_2 &= I_D - I_A \\ S_3 &= I_R - I_L. \end{aligned} \tag{1.3.30}$$

[17] A light wave with both polarised and unpolarised components.
[18] A wave with arbitrary polarisation at any given spacial or temporal position.
[19] Mueller matrices of various optical elements can be found in [2, 17, 18] and many other suitable optics textbooks.

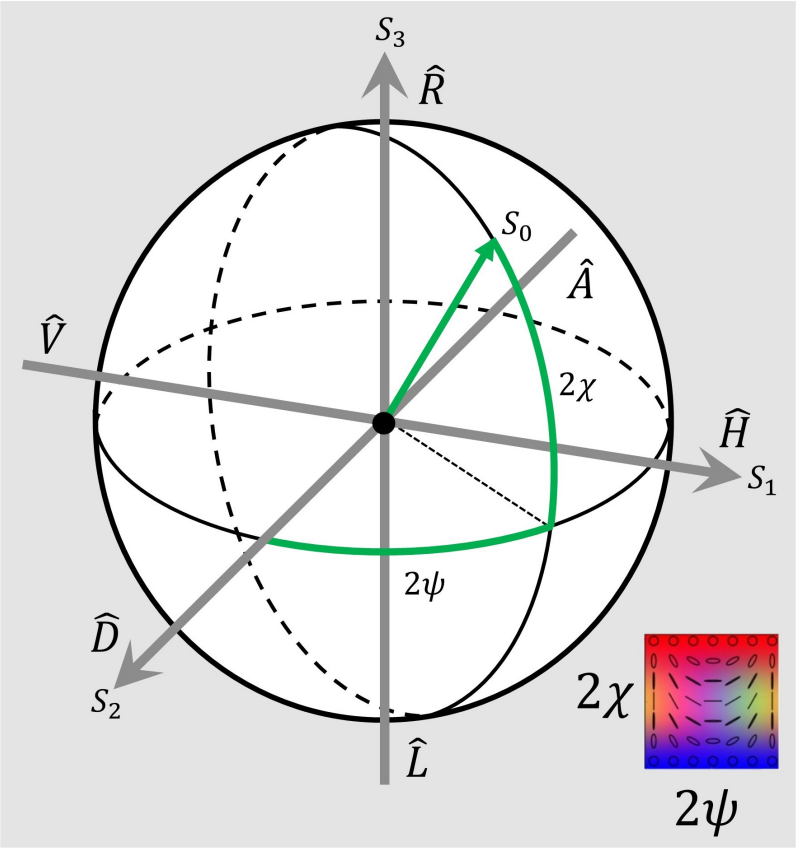

Figure 1.6: The Poincare sphere depicts the three axes associated with the six polarisation states. The green arrow is a vector of a pure state on the sphere surface with a magnitude of S_0, positioned at an angle given by the polarisation ellipse orientation ψ and ellipticity χ. The inset is a colour mapping of the ellipse angles to the sphere surface.

These parameters satisfy the relation $S_0^2 \geq S_1^2 + S_2^2 + S_3^2$. From this description, we define S_0 as the total intensity of the beam, calculated from the sum of any two orthogonal polarisation states. Here S_1 is the degree of horizontality or verticality; S_2 is the degree of diagonality present in the beam; and S_3 is the degree of circularity in the beam polarisation profile. We relate the Stokes parameters to the amplitudes of the electric fields in the basis given by Eqn. 1.3.7 as follows,

$$\begin{aligned} S_0 &= E_x E_x^* + E_y E_y^* \\ S_1 &= E_x E_x^* - E_y E_y^* \\ S_2 &= E_x E_y^* + E_x^* E_y \\ S_3 &= i(E_x E_y^* + E_x^* E_y), \end{aligned} \tag{1.3.31}$$

where i is the imaginary number and E_x^*, E_y^* denotes the complex conjugate of E_x, E_y, respectively. See [19] for a more in-depth description of formalism conversion between Stokes and Jones notations. The polarisation state denoted by the Stokes parameters can be graphically represented as a vector pointing from the centre of a unit sphere called the ***Poincaré sphere***. From Fig. 1.6, we observe that in this representation, all linear polarisation states occupy the sphere equator, while circular polarised light is positioned at the poles. If we choose to normalise the Stokes parameters by setting $S_0 = 1$, the vector of pure polarisation states obeying the relation $\sqrt{S_1^2 + S_2^2 + S_3^2} = 1$ sits on the sphere surface, while partial polarisation states occupy the internals of the sphere (i.e. $\sqrt{S_1^2 + S_2^2 + S_3^2} < 1$). Unlike a sphere in a three-dimensional real space $\mathbb{R}^3$, the Poincaré sphere contains both orthogonal polarisation bases on the same axes, where a change to the orthogonal polarisation state constitutes an orientation angle shift given by $\psi = \pi/2$. Note that one has the freedom to orient the sphere however desired. As shown in Fig. 1.6, we can express the parameters

of the normalised Stokes vector in terms of the ellipse orientation angle ψ and ellipticity χ,

$$\begin{aligned} S_1 &= S_0 \sin(2\psi)\cos(2\chi) \\ S_2 &= S_0 \cos(2\psi)\cos(2\chi) \\ S_3 &= S_0 \sin(2\chi), \end{aligned} \tag{1.3.32}$$

where, by rearranging, we derive expressions for ψ, χ in terms of the Stokes parameters,

$$\begin{aligned} \tan(2\psi) &= \frac{S_1}{S_2} \\ \sin(2\chi) &= \frac{S_3}{S_0}. \end{aligned} \tag{1.3.33}$$

When generating polarisation plots for experimental data, we use a colour scheme (as seen from the inset of Fig. 1.6) to provide a continuous mapping of the orientation angle ψ and ellipticity χ to the sphere surface. We demonstrate our colour scheme for the polarisation plots of the six Stokes basis in Fig. 1.7 below.

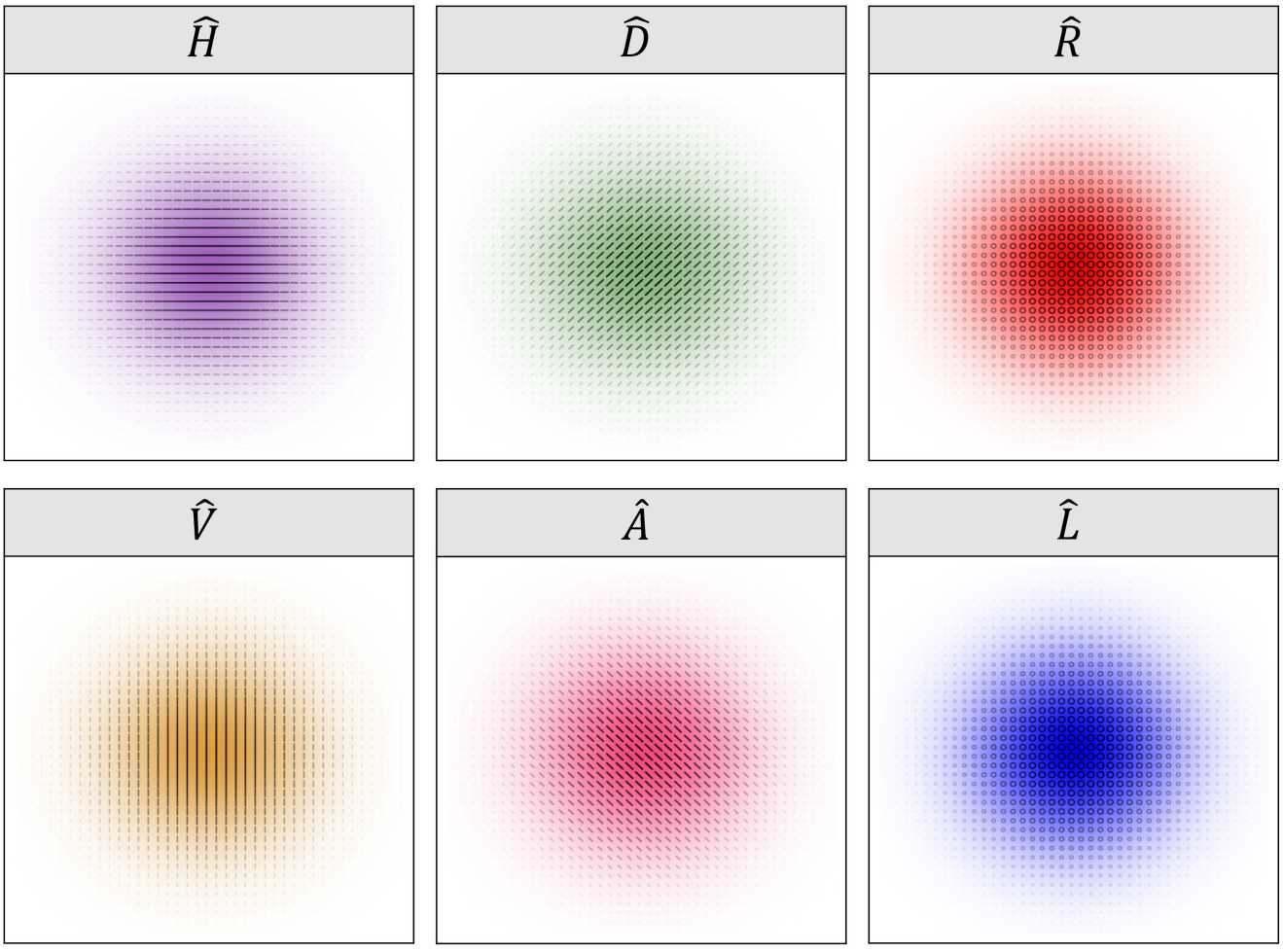

Figure 1.7: Polarisation plots of the six Stokes bases. These plots depict the polarisation ellipse in black, with the Poincaré sphere colour scheme in the background, modulated in opacity according to the beam intensity.

1.4 Stokes tomography and polarisation detection

This section provides an overview of the Stokes tomography procedure used to determine light polarisation. Tomography is the name given to a method frequently used in medical imaging that creates a final image by combining multiple images together, using electromagnetic radiation to capture various sections of an object or medium. In the context of ***Stokes tomography***, we produce six intensity images of the incoming beam projected along the six polarisation states given by Eqns. 1.3.10 and use these to reconstruct the full polarisation state of the light field using Eqns. 1.3.30.

It is possible to generate the polarisation information by projecting the incoming light onto only four different polarisation states[20], where a simple example of such a scheme is projecting the beam onto the polarisation basis: $\hat{H}, \hat{V}, \hat{D}$, and $\hat{L}$ (In Chapter 3, we revisit this idea to present our work investigating a four-state tomography scheme with a unique experimental setup). These measurements are sufficient to calculate the Stokes parameters using Eqns. 1.3.30. However, such a scheme is considered biassed in its polarisation state reconstruction, using only a quarter of the Poincaré sphere (as illustrated in the red outline of Fig. 1.8). In this example, we are estimating the reconstruction of the $\hat{A}$ and $\hat{R}$ states solely based on the information gathered from projections made on the other states, assuming an equal reconstruction probability with their orthogonal basis states (i.e. $\hat{D}$ and $\hat{L}$, respectively). In reality, especially in a laboratory setting where noise and losses are a common occurrence, such an assumption will generate errors in the reconstruction of the polarisation profile. For this reason, Stokes tomography is done with overcomplete measurements across all six polarisation bases.

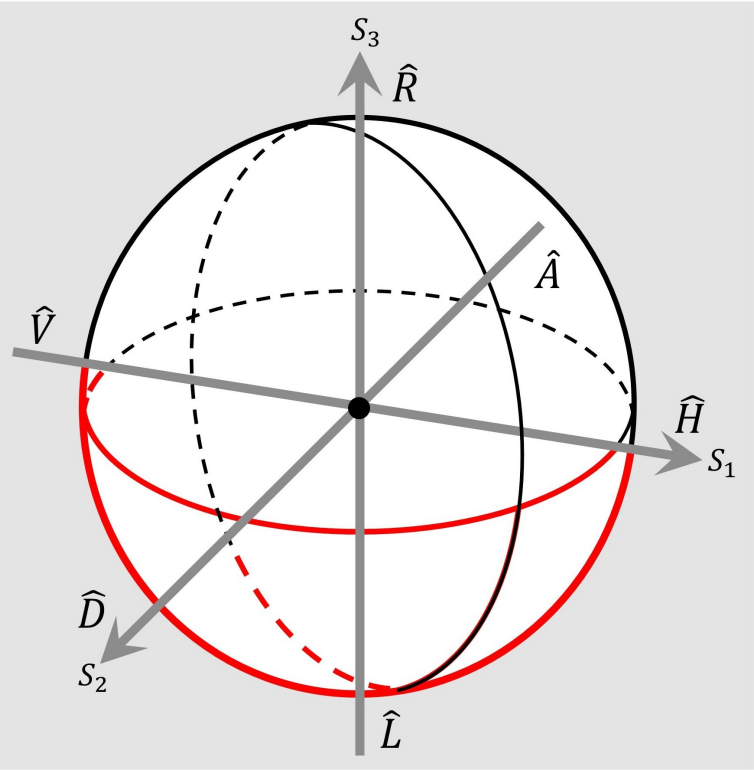

Figure 1.8: Region of the Poincaré sphere used when performing four-state tomography with the polarisation basis: $\hat{H}, \hat{V}, \hat{D}, \hat{L}$. In this scheme, only a quarter of the sphere is in use.

There are two different methods to calculate the Stokes parameters in an experiment. The first method requires only two optical elements, namely a polariser (Pol) and a quarter wave

[20]Four projection measurements is the minimum number of required measurements, more will be discussed in Chapter 3.

plate (QWP), along with a detector. The process consists of two steps, where we perform the measurements for the linear and circular polarisation separately. Ironically, before we can use our tomography setup, we must first calibrate the system with a light source of a known polarisation structure. In our experiments, we use a vertically polarised light beam for our calibration[21] and although any light polarisation can be used, this might further complicate the calibration process. If we assume we have a light source of arbitrary polarisation structure, then a simple PBS placed along the beam propagation direction will generate $\hat{H}$ and $\hat{V}$ in the transmitted and reflected arms of the PBS, respectively, which we can use to calibrate our waveplates[22].

We begin the Stokes tomography calibration by inserting a polariser into the beam path and adjusting the transmission angle, once again aiming to minimise the light incident on the camera[23]. This corresponds to the polariser transmission axis (θ) aligned with the x-axis (i.e. $\theta = 0$). Although the QWP is not yet needed, it is best to calibrate it at the beginning while the vertically polarised light is still in use. The process is the same; we insert the QWP into the beam path before the polariser (as shown in Fig. 1.9a) and rotate its fast axis angle (ϕ) until the beam intensity on the camera is minimised (corresponding to $\phi = 0$)[24]. Once the QWP is calibrated, we remove it from the setup for now.

Polarisation	QWP (ϕ)	Pol (θ)
$\hat{H}$	Not placed	0°
$\hat{D}$	Not placed	45°
$\hat{V}$	Not placed	90°
$\hat{A}$	Not placed	135°
$\hat{R}$	90°	45°
$\hat{L}$	90°	135°

Table 1.2: Table of transmission and fast axis angles for the polariser (θ) and quarter wave plate (ϕ), respectively, to generate the corresponding polarisation states with Stokes tomography.

The system is now ready to perform the measurements. For any input polarisation state, we perform the measurements by taking a camera image with the polariser angle (θ) orientated according to the angles in Table 1.2. These correspond to the measurements for all linear polarisation states (i.e. $\{H, D, V, A\}$). The next step is inserting the QWP into the beam path after the polariser to perform the measurements for the circular polarisation states (see Fig. 1.9a). For the circular states, we need to adjust both the angles of the polariser (θ) and the QWP (ϕ). These angles can once again be found in Table 1.2. Note that the choice of angles to generate $\hat{R}$ and $\hat{L}$ is not unique, as there are other combinations of ϕ, θ that can perform the same projections. Using the six polarisation state measurement images generated from the classical method, we calculate the Stokes parameters with the help of Eqns. 1.3.30 and construct the Stokes vector of the input polarisation beam.

[21] The choice to use vertical light is deeply rooted in our eyes ability to better differentiate absence of light from changes in brightness. This is more relevant when using a CCD or CMOS than a powermeter, which was the case for us most of the time.

[22] In this case, one might ask, how do we know this beam is actually vertical, given that we deduce the polarisation of the light field based on the behaviour of the PBS? The short answer is we can't; however, at some point you have to trust something; otherwise, if we could generate any polarisation structure reliably, then there would be no need to perform polarisation state tomography.

[23] If a PBS is used instead, the comment regarding the transmission angle can be ignored.

[24] If the fast and slow axis are mixed up, then $\hat{R}$ will be generated when $\hat{L}$ is expected and vice versa.

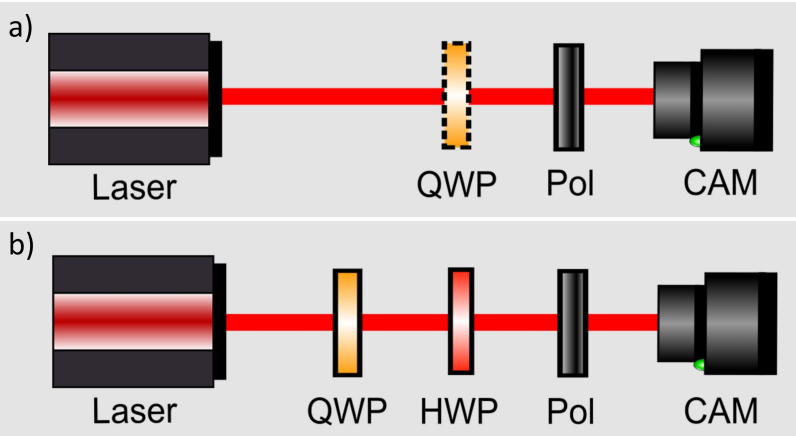

Figure 1.9: Stokes polarisation measurement schemes. a) A classical polarisation tomography setup, utilising a polariser (Pol) and a quarter wave plate (QWP). The dashed outlines of the QWP indicate its removal for parts of the measurement process. b) A modified setup for Stokes tomography that includes an extra half-wave plate (HWP), where all necessary optics are needed for the measurement procedure.

Although classical Stokes tomography is simple to implement, for a large number of polarisation measurements[25], having to remove the QWP on a regular basis can get very tiresome and could potentially impede the data collection process. For this reason, we use an altered Stokes tomography method that includes an additional half-waveplate (HWP) but does not require the constant removal of any of the optical elements to perform the measurements, as illustrated in Fig. 1.9b.

Similar to the previous case, we calibrate the system with a vertically polarised beam, minimising the beam incident on the camera for all three optical elements, beginning with the polariser and working backwards. Once the polariser transmission axis is optimised for horizontal light, it is fixed throughout the procedure. In this scheme, we change the angle of the QWP (α) and HWP (β) to generate the polarisation measurements. We proceed to calibrate the HWP and QWP in that order, respectively, as demonstrated in Fig. 1.9b. Once calibration is complete, we perform Stokes measurements according to the angles in Table 1.3, where the Stokes parameters are once again calculated using Eqns. 1.3.30. It is worth mentioning that in the modified Stokes method, the polariser can be replaced with a polarising beam splitter (PBS), requiring no calibration[26].

Polarisation	QWP (α)	HWP (β)
$\hat{H}$	0°	0°
$\hat{D}$	22.5°	0°
$\hat{V}$	45°	0°
$\hat{A}$	67.5°	0°
$\hat{R}$	67.5°	45°
$\hat{L}$	22.5°	45°

Table 1.3: Table of fast axis angles for the QWP (α) and HWP (β) to generate the six polarisation states using the altered Stokes measurement method.

One advantage of not having to remove any of the optics in the altered Stokes tomography is the ability to automate the measurement process, where the waveplate rotation is done sequentially. The waveplate is placed in a 3D-printed rotation mount controlled by a 12V stepping motor. The stepping motor is connected to a commercial stepping motor control board, controlled by an Arduino[27] linked to our experimental computer. This system can generate the six measurement images in under 10 seconds; however, the time between each captured image can be slightly sped up or slowed down within reason[28]. By observing the rotation

[25] An example is calculating the Mueller matrix of optical elements. See [19] for more information.

[26] Generally, it is best to use the polariser or PBS available with the largest extinction ratio for a more accurate polarisation measurement.

[27] More information on the Arduino pin configuration can be found in [20].

[28] Sufficient time should be given for the programme to capture an image before instructing the plates to rotate, which is a minimum of a few seconds. Therefore, there is a limitation for how short the time between image captures can be, but no limitations for extending the length of time in between.

mount, we deduce that the stepping motor produced around 508 steps for a full 2π rotation, resulting in a ratio of approximately 1.41 steps per degree. The rotation mount was designed by Ermes Toninelli back when he was at the University of Glasgow, and the individual components are shown in Fig. 1.10.

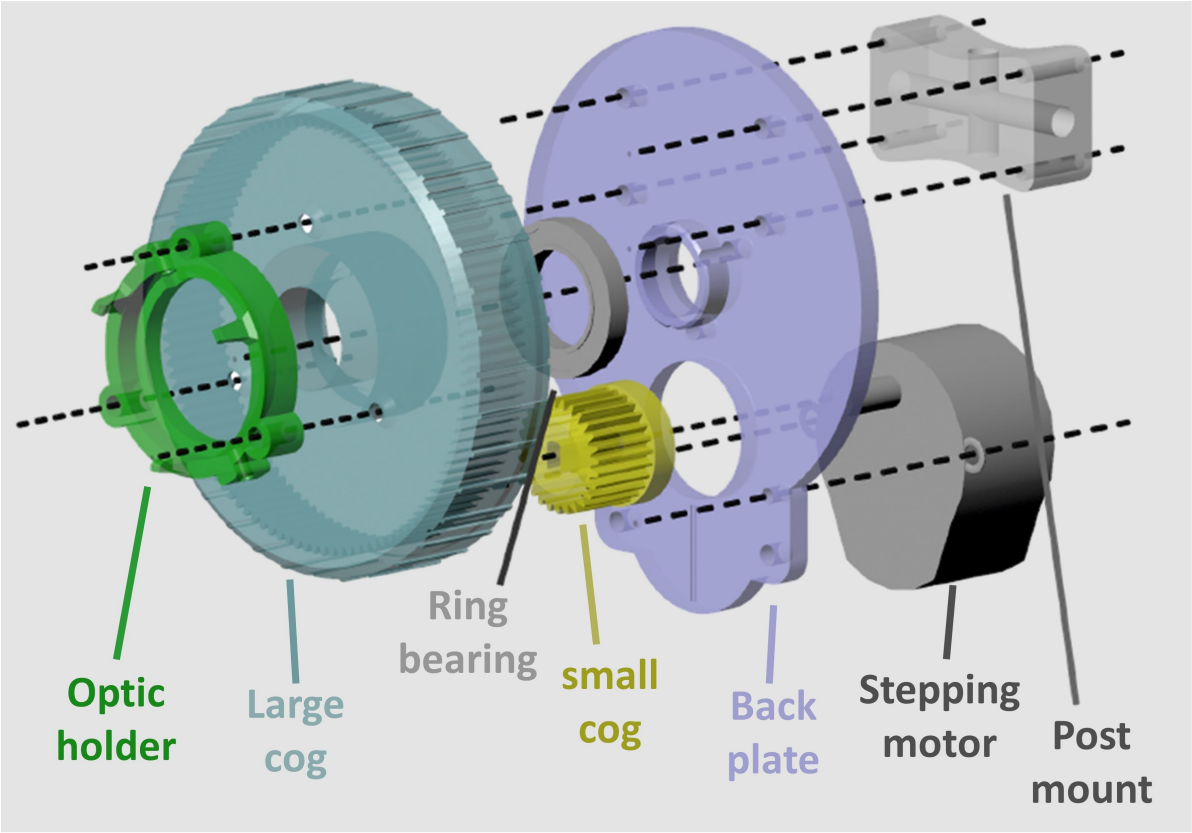

Figure 1.10: The five 3D-printed components of the waveplate automated rotation mount. A 1-inch-mounted optic is screwed into the optics holder (green), mounted on a large cog (cyan). The ring teeth on the large cog are connected to the small cog (yellow) operated by the stepping motor (grey). A ring bearing (grey) is placed in the central region of the large cog, securing it in place to the back plate (purple). Finally, a post mount (light grey) is screwed into the back plate, where a standard Thorlabs 1/2-inch post is attached via an M6 grub screw. The different parts are secured together with M3 screws, as illustrated by the dashed black lines. Image taken from [20].

There is no doubt the rotating waveplate from Fig. 1.10 is an amazing tool for Stokes tomography, especially when a large number of measurements are required. However, there are some features that could definitely be improved upon. The design itself is too bulky and, at times, could prove challenging to some of the motors we used in the past. Additionally, the optics holder (green from Fig. 1.10) is screwed in place to the large cog (cyan from Fig. 1.10) from the cog's side and secured by washers placed in the three holes of the optics holder. At times, the screw head can obstruct the motion of the small cog (yellow from Fig. 1.10), causing the rotating mechanism to jam and ruin the waveplate calibration. One way of potentially solving this problem is by adjusting the height of the small cog without sacrificing too much of the contact between the gears. Additionally, there are far too many teeth in both gear structures, which forces them to be very fine in construction. What essentially determines the rotation steps is the gear ratio (GR), given by $GR = N_{large}/N_{small}$ [21], where N_{large} is the number of teeth in the large gear and N_{small} is the number of teeth in the small gear. By adjusting the number of teeth, one can maintain the number

of steps for a full rotation while enlarging the teeth, providing better gear traction and ease of 3D printing[29]. Finally, the code to operate the rotating waveplates shifts the direction of motion of the gear rotation for the different Stokes measurements. The teeth on the gears are typically smaller than the root clearance (space between the teeth) to prevent the gears from becoming stuck. When the gears stop rotating, their teeth are in contact. However, if the gears were to rotate in the other direction, the gap between the teeth and clearance would result in a lost motion, known as gear backlash. Over time, the accumulation of gear backlash misaligns the rotating waveplates, where recalibration is required. Unfortunately, these changes could not be implemented due to time constraints.

1.5 Gaussian modes

1.5.1 The Helmholtz equation

Gaussian modes are a family of solutions to the time-independent wave equation with unique properties appealing for experimental use. The transverse amplitude distribution of many lasers, some propagation modes of optical fibres, and even Fabry–Pérot cavities with spherical mirrors possess a Gaussian amplitude distribution [22][30]. Additionally, they play a key role in our light shaping techniques to generate vector vortex and Poincaré beams. In this section, we explore different families of Gaussian modes, their mathematical form, physical properties, and spatial structures. In literature, the time-independent wave equation is commonly known as the Helmholtz equation. To derive the Helmholtz equation, consider the wave equation of the electric field given by Eqn. 1.2.13,

$$\left(\nabla^2 - \frac{1}{c^2}\frac{\partial^2}{\partial t^2}\right)\mathbf{E}(\mathbf{r},t) = 0, \tag{1.5.1}$$

where recall that $\mathbf{r} = \{x, y, z\}$ and t are the spatial and temporal coordinates, respectively. We can decompose $\mathbf{E}(\mathbf{r},t)$ into two functions of its two variables as,

$$\mathbf{E}(\mathbf{r},t) = E(\mathbf{r})T(t). \tag{1.5.2}$$

This technique, commonly known as separation of variables, is a simple method of solving partial differential equations (PDE) that possesses a series of analytic solutions[31]. By substituting Eqn. 1.5.2 into the wave equation above we are left with,

$$\begin{aligned}\left(\nabla^2 - \frac{1}{c^2}\frac{\partial^2}{\partial t^2}\right)E(\mathbf{r})T(t) &= 0 \\ \frac{\nabla^2 E(\mathbf{r})}{E(\mathbf{r})} &= \frac{1}{c^2}\frac{\mathrm{d}^2T(t)}{\mathrm{d}t^2}\frac{1}{T(t)}.\end{aligned} \tag{1.5.3}$$

Since the function $T(t)$ depends only on time, the derivative transforms from a partial into a

[29]Note 3D printing of fine structures requires a printer with a higher resolution. Testing the printer's capabilities with a resolution test piece is recommended before committing to a print job.

[30]Its worth mentioning that many diode lasers do not have a Gaussian intensity distribution.

[31]Not every PDE has analytic solutions. However, some of the most well-known with analytic solutions are the wave equation, the heat equation, and Laplace's equation.

total derivative. Observe how the left-hand side of Eqn. 1.5.3 above depends solely on $\mathbf{r}$, while the right-hand side only depends on t. When two equations that depend on two entirely different variables are equal, there is only one possible solution; they must both be constant. By that logic,

$$\frac{\nabla^2 E(\mathbf{r})}{E(\mathbf{r})} = \frac{1}{c^2}\frac{\mathrm{d}^2 T(t)}{\mathrm{d}t^2}\frac{1}{T(t)} = -k^2, \tag{1.5.4}$$

where $-k^2$ is a constant[32], leaving us with two equations,

$$\left(\nabla^2 + k^2\right) E(\mathbf{r}) = 0 \tag{1.5.5}$$

$$\frac{\mathrm{d}^2 T(t)}{\mathrm{d}t^2} - \omega^2 T(t) = 0, \tag{1.5.6}$$

that are functions of the spatial and temporal coordinates of the propagating wave, respectively. Here, $\omega = ck$ is the angular frequency, and k is now the wave number. We are interested in the spatial properties of the wave as given by Eqn. 1.5.5, which is a scalar form of the wave equation, known as the ***Helmholtz equation***. For a monochromatic wave propagating along the z-direction, assuming the paraxial wave approximation (i.e. the wave angle θ with respect to the optical axis is very small, such that $\sin(\theta) \approx \theta$), the electric field has the form [23][24][33],

$$E(\mathbf{r}) = u(\mathbf{r})e^{-ikz}, \tag{1.5.7}$$

where $u(\mathbf{r})$ is the complex amplitude and i the imaginary unit. By substituting Eqn. 1.5.7 into Eqn. 1.5.5 we have,

$$\begin{gathered}\left(\nabla^2 + k^2\right) u(\mathbf{r})e^{-ikz} = 0 \\ \left(\nabla\perp^2 + \frac{\partial^2}{\partial z^2}\right)\left[u(\mathbf{r})e^{-ikz}\right] + k^2 u(\mathbf{r})e^{-ikz} = 0 \\ \nabla_\perp^2 u(\mathbf{r})e^{-ikz} + \frac{\partial^2 u(\mathbf{r})}{\partial z^2} + 2ik\frac{\partial u(\mathbf{r})}{\partial z}e^{-ikz} = 0,\end{gathered} \tag{1.5.8}$$

where $\nabla_\perp$ is the transverse del operator given by $\nabla_\perp = (\partial^2/\partial x^2 + \partial^2/\partial y^2)$. In the paraxial approximation, the wave is assumed to have slow variations in the propagation direction $\left(\text{i.e. } \left|\frac{\partial^2 u(\mathbf{r})}{\partial z^2}\right| \ll \left|k\frac{\partial u(\mathbf{r})}{\partial z}\right|\right)$ [23, 25]. Incorporating this condition into Eqn. 1.5.8 above, we derive an expression for the paraxial Helmholtz equation,

$$\nabla\perp^2 u(\mathbf{r}) - 2ik\frac{\partial u(\mathbf{r})}{\partial z} = 0. \tag{1.5.9}$$

Once again, this equation has analytic solutions, some of which will be discussed in the following sections.

[32] The constant $-k^2$ is a choice of convenience.

[33] Note that in order to solve such a second-order PDE correctly, you must first determine whether the differential equations possess a solution for the three cases where k is positive, zero, or negative. A procedure that a lecturer in my undergraduate days at the University of Hertfordshire likened to "death by a thousand cuts." In spite of the remark, the calculation is not difficult, merely tedious.

1.5.2 Finite energy solution

The problem with the plane wave solution of the **E**-field wave equation given by Eqn. 1.2.14 is the lack of physical restrictions on the wave. This solution states the wave still maintains a transverse oscillation, even if the transverse space extends to infinity, making it a highly unrealistic solution. In a physical sense, the energy content of the wave has to be bound within a finite space, and tends to zero as the space extends to infinity (i.e. $E_{0\mathbf{r}} \to 0$ as $x, y \to \pm\infty$). The most common solution that satisfies this condition is the Gaussian beam [22, 26],

$$u(\mathbf{r}) = \underbrace{\frac{w_0}{w(z)} \exp\left[-\frac{(x^2+y^2)}{w(z)^2}\right]}_{\text{wave amplitude}} \underbrace{\exp\left[-ik\frac{(x^2+y^2)}{2R(z)}\right]}_{\text{paraxial term}} \underbrace{\exp\left[i\phi(z)\right]}_{\text{phase}}, \tag{1.5.10}$$

where,

$$\begin{cases} w(z) = w_0\sqrt{1+\left(\dfrac{z}{z_R}\right)^2}, & \text{beam radius} \quad (1.5.11) \\ z_R = \dfrac{\pi w_0^2}{\lambda}, & \text{Rayleigh range} \quad (1.5.12) \\ R(z) = z\left[1+\left(\dfrac{z_R}{z}\right)^2\right], & \text{radius of curvature} \quad (1.5.13) \\ \phi(z) = \arctan\left(\dfrac{z}{z_R}\right). & \text{Gouy phase} \quad (1.5.14) \end{cases}$$

Here $w(z)$ is the beam width in the transverse profile (or beam spot size), describing the distance where the field amplitude falls to $1/e$ (i.e. $\sim 36.8\%$) of its maximum value. Additionally, the dependence of the beam radius on the distance along the z-direction, is a clear indication that the beam size varies throughout propagation. At $z = 0$, the beam radius reduces to the waist w_0, a point where a Gaussian beam converges to or diverges from as a consequence of diffraction effects (or focusing) and when the beam radius has reached its minimum. The Rayleigh range describes the distance when the beam cross-sectional area doubles in size, occurring when the beam radius $w(z)$ is $\sqrt{2}$ the beam waist w_0[34]. The Gouy phase accounts for variations in the phase profile of the wave at the beam waist (see Section 1.5.4 for more information).

The bound nature of the Gaussian wave gives rise to curved surfaces of constant phase. The wavefront of a Gaussian beam approaches the behaviour of the plane wave solution illustrated in Fig. 1.1 at the beam waist; however, they are generally parabolic surfaces influenced by the radius of curvature $R(z)$. From Eqn. 1.5.13, we observe the dependence of the curvature on the beam waist, suggesting curvier wave fronts are expected for smaller waists and the absence of any curvature at zero and infinity (as $R(z) \to \infty$). To obtain the expression for the propagating Gaussian wave, we substitute Eqn. 1.5.10 into Eqn. 1.5.7 to recover an expression of the Gaussian electric field in radial coordinates, propagating along the z-direction,

$$E(r,z) = \frac{w_0}{w(z)} \exp\left[-\frac{r^2}{w(z)^2}\right] \exp\left[-ik\left(\frac{r^2}{2R(z)} + z\right)\right] \exp\left[i\phi(z)\right], \tag{1.5.15}$$

[34] Incidentally, it is also the distance beyond which the beam divergence becomes linear.

where $\mathbf{r} = \{x, y, z\} = \{r, z\}$ and r is the radial coordinate[35]. The beauty of the Gaussian wave is that the beam profile remains a Gaussian distribution (also called normal distribution) throughout propagation through transparent optical elements in the absence of aberrations (i.e. polariser, PBS, lenses, waveplates, etc.), where the beam radius $w(z)$ is the only quantity expected to vary as the wave travels. We obtain an expression for the intensity profile of the Gaussian wave by inserting Eqn. 1.5.15 into Eqn. 1.3.2,

$$I(r, z) = \left(\frac{w_0}{w(z)}\right)^2 \exp\left[-\frac{2r^2}{w(z)^2}\right]. \tag{1.5.16}$$

The intensity profile of a Gaussian beam is expected to peak at the beam centre (as shown in Fig. 1.11); however, the beam radius $w(z)$ now describes the distance where the intensity falls to $1/e^2$ or 13.5% its highest value.

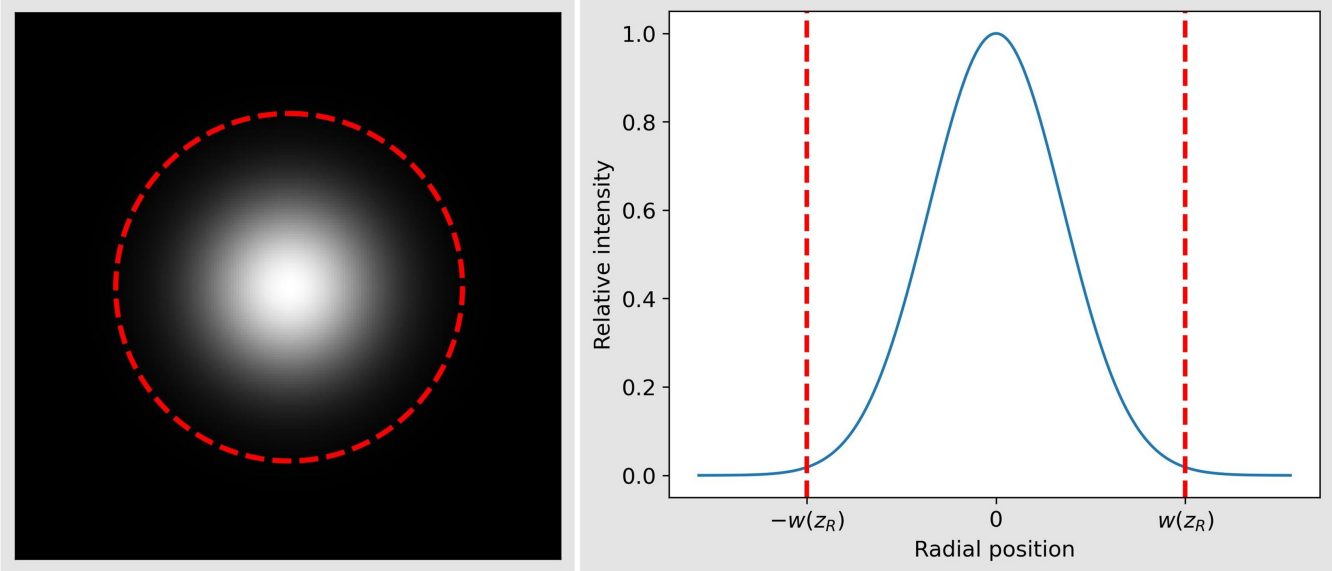

Figure 1.11: Gaussian beam intensity profile in free space (left image) and as a function of the radial position (right graph). The dotted line highlights the beam radius at the Rayleigh range z_R.

1.5.3 Higher order modes

The proposed solution to the paraxial Helmholtz in Eqn. 1.5.9 was motivated by our desire to find a realistic solution with finite energy content along the transverse profile. The outcome shown in Eqn. 1.5.10 pertains to the lowest order among a set of solutions that comply with this constraint. However, there are other solutions to the paraxial Helmholtz equation that yield sets of complete transverse higher-order propagation modes with unique spatial structures that are easy to calculate and use to express any light field as a linear combination of their respective modes. In this section, we introduce some of these higher-order modes and explore their key properties. The two most common families of higher-order modes are the Hermite-Gaussian (HG) and Laguerre-Gaussian (LG) modes. The electric field amplitudes of the HG and LG modes are respectively given below,

[35]For interested readers, a full derivation of the Gaussian beam profile can be found in [23].

$$\mathrm{HG}_{nm}(x,y,z) = \frac{w_0}{w(z)} \exp\left[-\frac{(x^2+y^2)}{w(z)^2}\right] H_n\left(\frac{\sqrt{2}x}{w(z)}\right) H_m\left(\frac{\sqrt{2}y}{w(z)}\right) \times \exp\left[-ik\left(\frac{(x^2+y^2))}{2R(z)} + z\right)\right] \exp\left[i(1+N)\phi(z)\right], \tag{1.5.17}$$

$$\mathrm{LG}_p^l(r,\psi,z) = K_p^l \frac{w_0}{w(z)} \left(\frac{r\sqrt{2}}{w(z)}\right)^{|l|} \exp\left[-\frac{r^2}{w(z)^2}\right] L_p^{|l|}\left(\frac{2r^2}{w(z)^2}\right) \exp\left[-il\psi\right] \times \exp\left[-ik\left(\frac{r^2}{2R(z)} + z\right)\right] \exp\left[i(1+N)\phi(z)\right], \tag{1.5.18}$$

where n and m are the horizontal and vertical mode indices of HG beams, while l and p are the azimuthal and radial mode numbers of LG modes, where $\{n,m,p\} \in \mathbb{Z}^+$ and l is an integer (i.e. $l \in \mathbb{Z}$)[36]. $H_i(x)$ are the Hermite polynomials, $L_p^{|l|}(x)$ are the generalised Lauguerre polynomials, and N is the mode number. It is worth mentioning that these HG and LG modes are orthonormal in nature, and therefore we expect the inner product of any two high-order modes with different indices in the same set to equal zero. The $\exp[-il\psi]$ term from Eqn. 1.5.18 denotes the azimuthal phase of LG mode, which corresponds to the number of full $(0 \to 2\pi)$ phases found in the beam profile as a multiple of l. Here K_p^l is a normalisation constant in cylindrical coordinates given by [27][37],

$$K_p^l = \sqrt{\frac{(2p)!}{\pi(p+|l|)!}} \to \int d\psi \int r dr \left|\mathrm{LG}_p^l(r,\phi,z)\right|^2 = 1, \tag{1.5.19}$$

where $x!$ denotes the factorial of x. In both HG and LG mode equations, we introduce the variable N. This quantity is known as the mode number, given by $N = n+m$ for HG modes and $N = |l|+2p$ for LG modes, and plays an important role in variation to the beam profile as a consequence of the Gouy phase. All other quantities in Eqn. 1.5.17 and Eqn. 1.5.18 remain the same as before. We can calculate the intensities of the higher-order modes using Eqn. 1.3.2, to obtain,

$$I_{\mathrm{HG}_{nm}}(x,y,z) = \left[\frac{w_0}{w(z)} H_n\left(\frac{\sqrt{2}x}{w(z)}\right) H_m\left(\frac{\sqrt{2}y}{w(z)}\right)\right]^2 \exp\left[-\frac{2(x^2+y^2)}{w(z)^2}\right], \tag{1.5.20}$$

$$I_{\mathrm{LG}_p^l}(r,\psi,z) = \left[K_p^l \frac{w_0}{w(z)} \left(\frac{r\sqrt{2}}{w(z)}\right)^{|l|} L_p^{|l|}\left(\frac{2r^2}{w(z)^2}\right)\right]^2 \exp\left[-\frac{2r^2}{w(z)^2}\right]. \tag{1.5.21}$$

The underlying cubic symmetry in the intensity profile of the HG modes (as seen in Fig. 1.12, makes the Cartesian coordinate system a suitable choice to represent HG modes. Similarly, LG modes are expressed in cylindrical coordinates since they possess cylindrical symmetry, as seen in

[36] Here $\mathbb{Z}$ is the set of all integers, and $\mathbb{Z}^+$ is the set of positive integers.

[37] The general form of the normalisation integral is, $\int d\psi \int r dr LG_{p_1}^{l_1}(r,\phi,z) LG_{p_2}^{l_2}(r,\phi,z) = \delta_{p_1,p_2}\delta_{l_1 l_2}$, where δ is the Kronecker delta.

Fig. 1.13. We note that regions of zero intensity correspond to sharp changes in the phase profile, as seen in almost all HG modes (except HG_{00}) in Fig. 1.12 and all LG modes with $p > 0$ in Fig. 1.13.

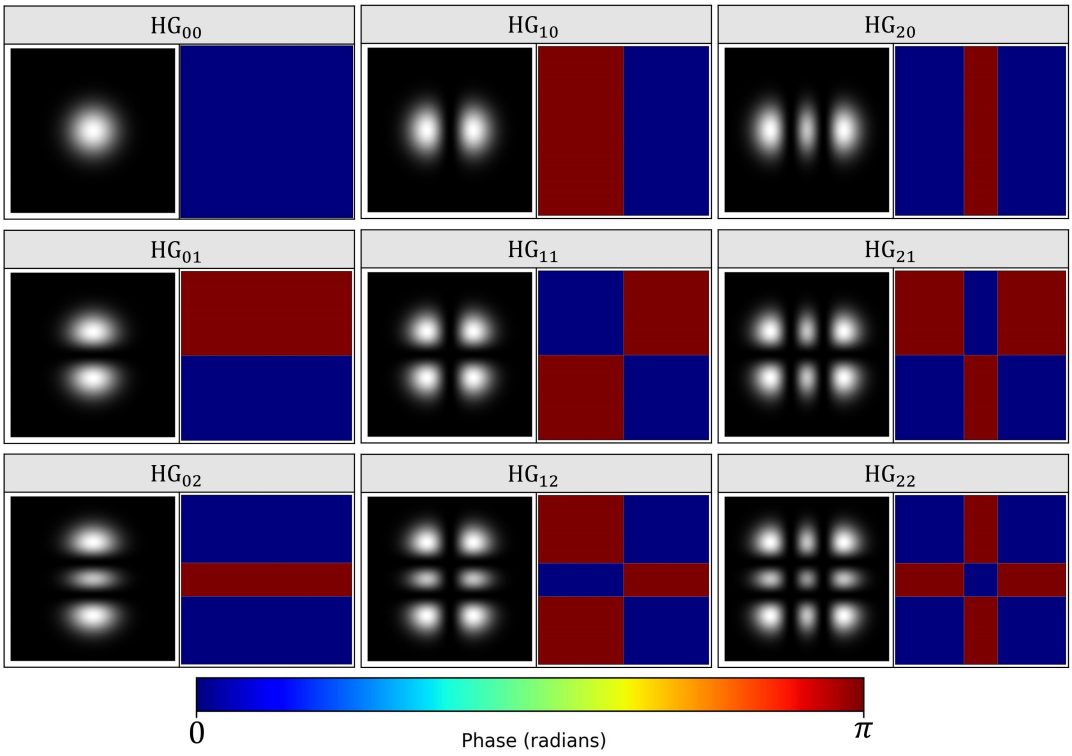

Figure 1.12: Spatial intensity structure and phase profile of Hermite-Gaussian modes with different index values.

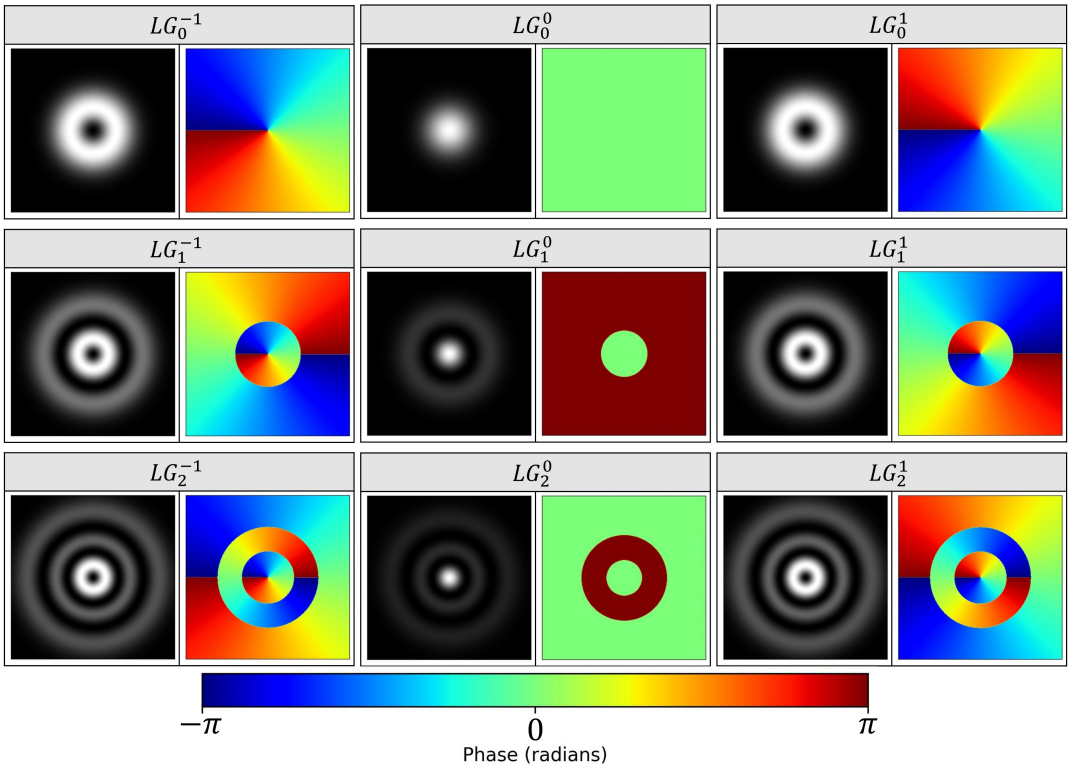

Figure 1.13: Spatial intensity structure and phase profile of Laguerre-Gaussian modes with different index values. For LG modes with $l < 0$, the phase is inverted when compared to modes with $l > 0$.

We have previously stated that HG and LG modes form what is known as a complete set of transverse modes. The implications are that they can be used to generate any desired beam shape by superimposing multiple different modes from within the specific HG or LG set in the paraxial approximation. When comparing their equations to Eqn. 1.5.15, we observe changes to the amplitude and phase (for LG modes) structures; however, the paraxial and propagation terms are identical, suggesting that higher-order modes remain transverse modes of propagation and only amplitude variations are expected throughout propagation. Interestingly, for the cases where $n = m = p = l = 0$, both HG and LG modes reduce to the lowest-order finite energy solution given by the Gaussian electric field of Eqn. 1.5.15.

Although the azimuthal index of the LG solution is an intrinsic property of the wave, its phase-dominated nature makes it challenging to determine without a specialised experimental configuration. The majority of classical experimental work relies on intensity measurements, where the azimuthal index l affects the Laguerre polynomial of the wave amplitude as seen in Eqn. 1.5.21. Unfortunately the emerging spatial pattern does not possess any distinct structures to differentiate the different values of the azimuthal index by eye, as demonstrated in Fig. 1.14 below[38].

An interesting property of LG modes closely associated with the azimuthal index is their ability to carry orbital angular momentum [28–30], as a consequence of the helical geometry of their phase fronts, introduced by the $\exp[-il\psi]$ term from Eqn. 1.5.18. This quantity is usually conserved as the beam interacts with different mediums and does not depend on the beam polarisation (unlike spin angular momentum (SAM), which is a polarisation effect found in elliptical or circular polarised light). Note that the number of helical wave fronts and their handedness depend on the magnitude and sign of l. The interest in understanding the OAM structure of LG modes is responsible for the development of experimental techniques to accurately determine the azimuthal profile of LG modes [31–33].

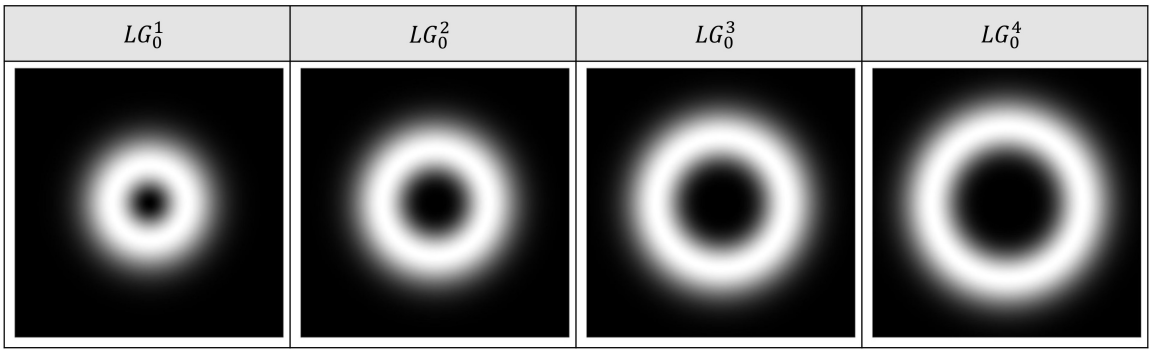

Figure 1.14: Intensity profile of LG modes with varying azimuthal profile.

There are other higher-order modes besides the two discussed in this section. The Ince-Gaussian (IG) beams [34, 35] represent another set of full higher-order modes, with an elliptical symmetry and a slightly more complex spatial and phase structure. The mathematical expression describing their complex amplitude contains the Ince polynomials, similar to the other higher-order modes; however, these polynomials assume different forms for even and odd modes.

1.5.4 Propagation of Gaussian modes

We have stated that Gaussian modes undergo variations in both the beam diameter and the phase profile throughout propagating, as observed from Eqn. 1.5.11 and Eqn. 1.5.13. These changes are

[38] Here it is easy to see there is a difference between the beams, however without the information labelling the beam type, determining the value of l is a guess at best.

observed in the spatial intensity and phase profiles respectively of the light field when considering different modes of propagation across varying distances. In this section, we will take a quick look at these changes to the beam properties to improve our understanding of Gaussian mode behaviour.

To understand Gaussian mode propagation, we must first understand the Gouy phase. This effect was first observed by Louis Georges Gouy in 1890, where the curved structure of the Gaussian wave fronts constitutes a reduction in the phase shift of the Gaussian beam in comparison to a plane wave. This reduction corresponds to a larger distance between the wave fronts (i.e. an increase in the wavelength), and hence an increase in the local phase velocity at a constant frequency. An alternative explanation proposed by [36] states the bound nature of the Gaussian modes to the transverse spatial profile through the focus, introduces a distribution in the transverse momentum profile as a consequence of the Heisenberg uncertainty principle. This distribution results in an additional change to the longitudinal wave vector, where the net sum of all wave vector contributions is the Gouy phase. We investigate changes to the beam radius and phase structure for different test beams in both HG and LG modes, illustrated in Fig. 1.15 and Fig. 1.16, respectively.

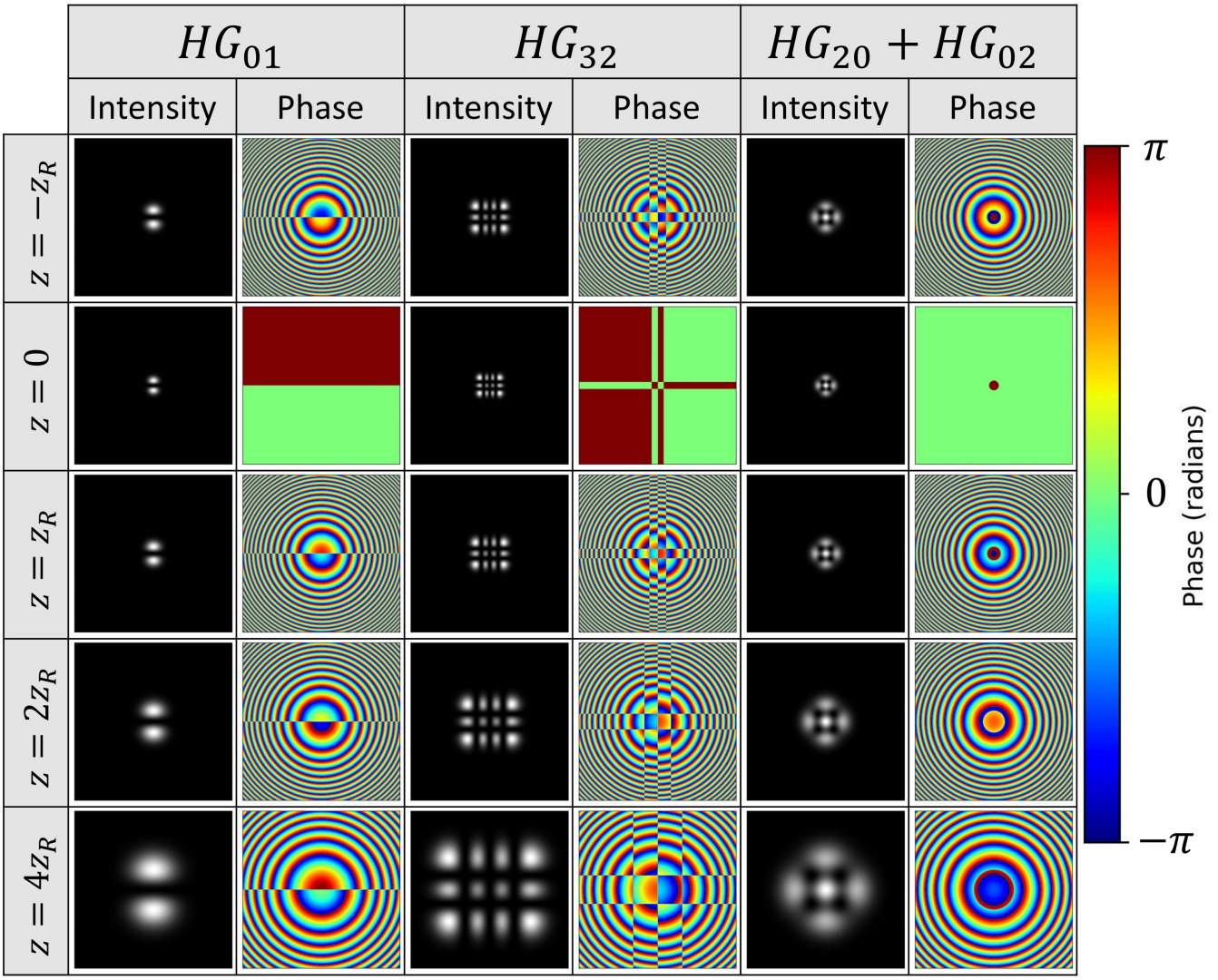

Figure 1.15: Intensity and phase patterns of the three HG test modes, HG_{10}, HG_{32} and the superposition mode $HG_{20} + HG_{02}$ as a function of propagation distance.

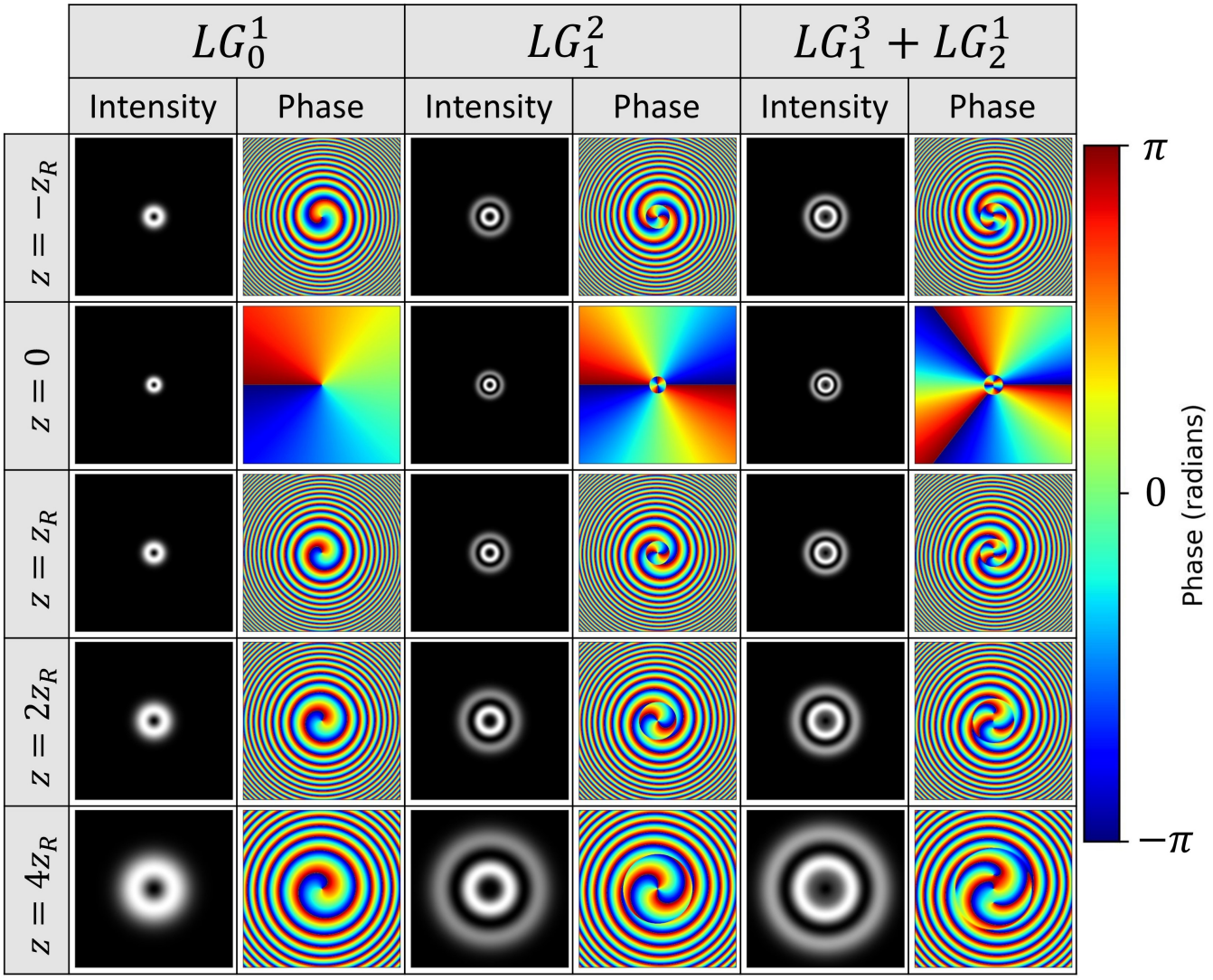

Figure 1.16: Intensity and phase patterns of the three LG test modes, LG_0^1, LG_1^2 and the superposition mode $LG_1^3 + LG_1^2$ as a function of propagation distance.

As expected from Gaussian modes, the beam intensity profiles are identical at the Rayleigh ranges, $z = -z_R, z_R$, and continue to increase in size with increasing distance. However, at the point where $z = 0$ (i.e. when the beam radius reduces to the beam waist), the Gaussian modes behave like plane waves, where the intensity profile is the smallest in size.

For the Gouy phase, we observe that the clockwise and anti-clockwise nature of the rotation pattern depends on the propagation direction[39], where the central phase pattern is also seen to expand with longer propagation distances. Note that the last row of Fig. 1.15 and Fig. 1.16 are examples of the superposition of multiple higher-order modes with identical mode numbers, implying a similar Gouy phase rotation between the two.

1.6 Summary

In this chapter, we introduced the paraxial solution of the electric field wave equation derived from Maxwell's equations. We discussed the concept of polarisation, introducing a formalism in terms of

[39]Not to be confused with the $-l$ modes of LG beams from Fig. 1.13, where the handedness of the phase map has reversed (i.e. clockwise: red for l, while blue for $-l$ when viewed from the $-x$-axis).

Jones, Stokes, and the polarisation ellipse, and explored techniques for polarisation measurements using Stokes tomography. We introduced the Gaussian mode as the lowest-order realistic solution to the time-independent wave equation, otherwise known as the Helmholtz equation, in the paraxial approximation and briefly discussed its properties. Finally, we introduced some higher-order transverse propagation modes, saw examples of their spatial and phase profiles, and discussed their unique properties throughout propagation.

Chapter 2

Manipulating light fields

2.1 Introduction

By now, we have developed a good understanding of propagating light fields, first in terms of a plane wave solution of Maxwell's equations and then as finite energy transverse modes of propagation of the Helmholtz equation. Not only do Gaussian modes provide a realistic representation of electric field oscillations, they are also the fundamental modes (i.e. lowest order modes) of optical resonators [37, 38]. Since light amplification via stimulated emission of radiation (LASER) involves a pumped medium sandwiched between a highly reflective back facet and an output coupler, forming an optical cavity, it is no surprise that output beams from most laser sources possess a Gaussian intensity distribution profile. However, experiments that involve the generation and use of vector light fields require some form of preparation and a great deal of beam manipulation. These can range from simple redirection and magnification of the light field to slightly more complex procedures involving diffraction of the beam with dynamic devices.

2.2 Reflection

Reflection is perhaps the most commonly observed property of light, experienced on a daily basis with the widespread use of mirrors, which are abundantly found in a laboratory setting, proving to be an extremely useful tool for beam redirection and are key components of experimental techniques such as interferometers and spectroscopy configurations. We aim to develop an understanding of their effects on the propagating beam for efficient experimental use.

Light reflecting off a mirror obeys the law of reflection. This law simply states that the angle of the beam at the plane of incidence (ϕ) with respect to the mirror normal ($\hat{n}$) is equal to the beam angle at the reflection plane (θ) leaving the mirror surface (i.e. $\phi = \theta$). An interesting consequence of beam reflection is the introduction of a phase shift between the two polarisation components of the electric field. Since the tilt of the surface mirror can affect either the horizontal or vertical component of the light polarisation, the polarisation is usually considered with respect to the orientation of the incident plane. For an incoming beam with an electric field oscillation perpendicular to the normal of the incident plane, the polarisation is said to be s-polarised[1], and when parallel to the normal, the polarisation is p-polarised[2], as illustrated by the blue arrows in Fig. 2.1. However, one can select a coordinate system that maps the s and p polarisations to the

[1] Which comes from the German word senkrecht, meaning perpendicular.
[2] Which again comes from the German word parallel (which also happens to be the same word in English).

horizontal and vertical polarisation structures and vice versa, where in our example, s maps to the horizontal ($s \mapsto x$) and p maps to the vertical ($p \mapsto y$)[3].

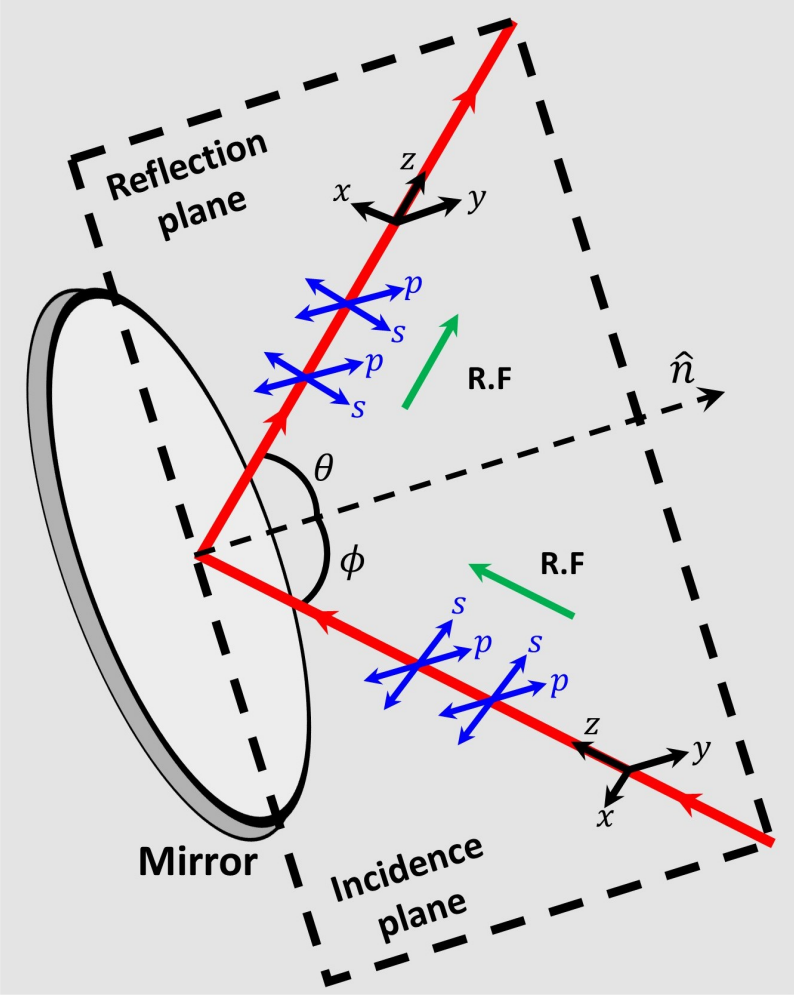

Figure 2.1: Reflection off a mirror surface, showing a propagating beam with s and p polarisation structures, incident on the mirror surface with an angle ϕ, reflected at an angle θ relative to the mirror normal $\hat{n}$. When mapping the s and p polarisations to the Cartesian coordinate system, the horizontal polarisation experiences a phase shift of π when viewed from the reference frame (R.F.) indicated by the green arrows.

When considering a beam propagating along the reference frame (R.F.) given by the green arrows in Fig. 2.1, we notice the p-polarised light maintains its orientation; however, the s-polarised light picks up an additional phase shift of π, which, when mapped to the horizontal polarisation structure, is equivalent to the transformation given by $x \longrightarrow -x$. In addition to this phase shift, the reflected wave will experience variations in the electric field amplitude of the two polarisation components, the magnitude of which depends on some parameters. These are the refractive index of the medium surrounding the mirror[4], the tilt angle of the mirror surface, the orientation angle of the incident beam, and even the refractive index of the reflector itself[5]. Following the formalism described in [39, 40], the Jones matrix of a general reflector is given by,

$$\mathbf{J}_R = \begin{pmatrix} \rho_s & 0 \\ 0 & \rho_p \end{pmatrix}, \tag{2.2.1}$$

[3]Note that in this example we are considering a fully polarised light field with both horizontal and vertical components incident on the mirror surface.

[4]Which is only relevant if the mirror is submerged in a fluid.

[5]Which is only significant when dealing with partially reflective mirrors.

where the entries of the matrix are given by $\rho_s = (p_R - p_M)/(p_R + p_M)$ and $\rho_p = (q_R - q_M)/(q_R + q_M)$, for $p = \nu\cos(\phi)$ and $q = \nu^{-1}\cos(\phi)$. Here ϕ is the light propagation angle (see Fig. 2.1) and $\nu = \sqrt{\varepsilon/\mu}$, where ε and μ are the electric permittivity and magnetic permeability, respectively[6]. The subscripts R and M refer to the reflector and medium it is currently embedded in, respectively. Consider a simple example of a planar mirror, with a beam incident on the normal of the mirror surface (i.e. $\phi = \theta = 0$ from Fig. 2.1), we calculate ρ_s and ρ_p to be,

$$\begin{aligned} \rho_s &= \frac{1-\sigma}{1+\sigma} \\ \rho_p &= \frac{\sigma-1}{\sigma+1}, \end{aligned} \tag{2.2.2}$$

where $\sigma = \nu_M/\nu_R$. Substituting Eqns. 2.2.2 into Eqn. 2.2.1, we obtain the expression,

$$\mathbf{J}_R = \frac{\sigma-1}{\sigma+1}\begin{pmatrix} -1 & 0 \\ 0 & 1 \end{pmatrix}. \tag{2.2.3}$$

Since the absolute refractive index n is related to the permittivity and permeability by $n = \sqrt{\varepsilon\mu} = \sqrt{\varepsilon_r\varepsilon_0\mu_r\mu_0}$ [2], we obtain an expression of σ in terms of the refractive index given by $\sigma = \varepsilon_M n_R/\varepsilon_R n_M$, where ε_M and ε_R are the relative permittivity for the reflector and medium, respectively. For a mirror sitting in air or vacuum[7] (i.e. $\varepsilon_M = n_M = 1$), we re-write Eqn. 2.2.3 as,

$$\mathbf{J}_R = \frac{n_R - \varepsilon_R}{n_R + \varepsilon_R}\begin{pmatrix} -1 & 0 \\ 0 & 1 \end{pmatrix}. \tag{2.2.4}$$

The refractive index gives a measure of the degree of light refraction through a medium; however, no light should be transmitted through a reflective surface[8]. Assuming a perfect mirror, the refractive index should be infinite. From this analysis, we see that if $n_R \to \infty$, then $(n_R - \varepsilon_R)/(n_R + \varepsilon_R) \to 1$, which gives the final Jones matrix for a perfect mirror,

$$\mathbf{J}_R = \begin{pmatrix} -1 & 0 \\ 0 & 1 \end{pmatrix}. \tag{2.2.5}$$

We opted to derive the Jones matrix for the simplest case of a planar mirror; however, Eqn. 2.2.1 can be used to calculate a matrix expression for any type of reflector placed within any medium at any desired orientation angle (of both reflector and medium). From Eqn. 2.2.5, we observe that the beam reflected off the mirror surface picks up a π phase shift in the horizontal polarisation components (i.e. $\{x, y, z\} \to \{-x, y, z\}$). If we consider the example of a right-hand circular beam, $\hat{R}$ reflecting off a mirror, we get,

[6] Recall from Section 1.2 that $\varepsilon = \varepsilon_r\varepsilon_0$, while $\mu = \mu_r\mu_0$.
[7] Note that air has a slightly larger refractive index than vacuum, but can be approximated to 1.
[8] This is only true for a perfect reflector, which does not physically exist.

$$\mathbf{J}_R\hat{R} = \begin{pmatrix} -1 & 0 \\ 0 & 1 \end{pmatrix} \begin{pmatrix} 1 \\ -1j \end{pmatrix} = - \begin{pmatrix} 1 \\ 1j \end{pmatrix}, \tag{2.2.6}$$

where the minus sign in the equation above corresponds to the rotation of the polarisation plane, constituting a change in handedness of the propagating wave polarisation. In this case, the right-hand circular polarisation turns into a left-hand circular polarisation. This concept extends to the diagonal or anti-diagonal polarisation states; however, we note that the use of another mirror will undo the change in handedness, reverting the polarisation structure to its initial state. Note that a similar formalism to Eqn. 2.2.1 in terms of the Muller matrix can be found in [41].

In some experimental situations, there is a need for greater control over the beam's spatial position. One example is the alignment through a pinhole or an optical fibre, where a deviation of a few micrometres can completely block the beam path. By implementing a two-mirror system, we are able to effectively control the beam position and deviation angle for precision alignment.

By adjusting the tilt angles of the first mirror α_x, α_y as seen in Fig. 2.2, we are able to control the beam position in the near field along the $x-y$ plane, while changes in the tilt angles of the second mirror β_x, β_y correspond to angular deviation in the far field along the horizontal and vertical, respectively. It is generally recommended to define a fixed beam path before employing the two-mirror system for fine-tune alignment. This is simply done by first adjusting the beam height and horizontal position, and then the deviation angle. Once the beam maintains a constant position in the $x-y$ plane, the system is aligned. The desired optical element (i.e. pinhole or fibre) is then introduced to the beam path, where both mirror angles are scanned in order to maximise the beam's output power, indicating optimal alignment.

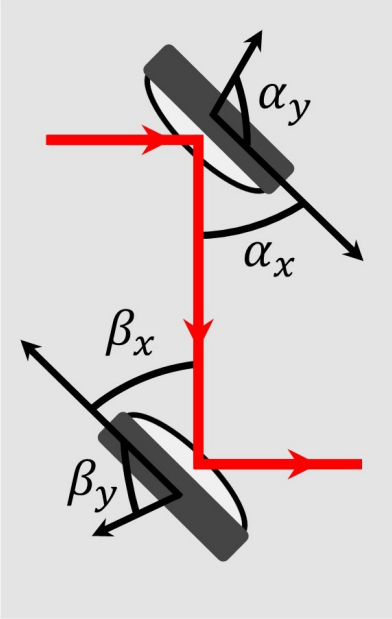

Figure 2.2: A two mirror system. The tilt angles α_x and α_y of the first mirror control the beam position and height, respectively. However, the tilt angles of the second mirror β_x and β_y control the beam angle in the far field, along the horizontal and vertical, respectively.

We note that most of our mirrors are made from glass with a dielectric coating for the desired wavelength. These mirrors are optimised for beams incident on the mirror surface at angles of 45° and 0°, where purely polarised states experience little change to their polarisation structure. However, in cases where such incident angles are not possible due to a lack of sufficient space on the optical bench, the use of metal-coated mirrors like gold or silver will minimise the aberrations on the beam polarisation profile.

2.3 Focusing and imaging

When one thinks of imaging, the concept of optical planes is what normally comes to mind. Lenses are refractive elements whose behaviour is usually visualised with ray diagrams, a convenient graphical tool depicting beam propagation during the imaging process. An example of such a diagram can be found in Fig. 2.3. In the simplest case, a lens transfers the optical field from the object to the image plane (see Fig. 2.3a). Mathematically, the focusing behaviour of a lens is akin to

taking the Fourier transform of the object plane at a distance d_o before the lens to the focal point f after the lens, which is mathematically similar to considering the light propagating to infinity[9]. This transformation obeys the Gaussian form of the lens equation $1/d_o + 1/d_i = 1/f$, where d_i is the image distance from the lens centre. Note that the beam size and position at the image plane after focusing effects vary depending on a few parameters, such as lens type, beam size, lens focal length, and beam position on the lens surface. Although variations in these parameters produce different results, the lens preserves the intensity value of the light field, at the cost of the spatial beam structure. An appropriate application for a single-lens system is focusing into a photodiode (PD) for a better spectroscopy signal (As will be seen in our polspec experiment in Section 6.5)[10].

If we introduce a second lens positioned where the focal lengths of the two lenses coincide, as shown in Fig. 2.3b, we create what is commonly known as a telescope system. In terms of the Fourier transform, the second lens will undo the effects of the first lens, introducing another Fourier transform and restoring the spatial intensity profile of the beam up to a magnification factor[11]. This magnification is derived from the Gaussian lens equation and is given by the ratio of the focal lengths of the two lenses, $M = f'/f$.

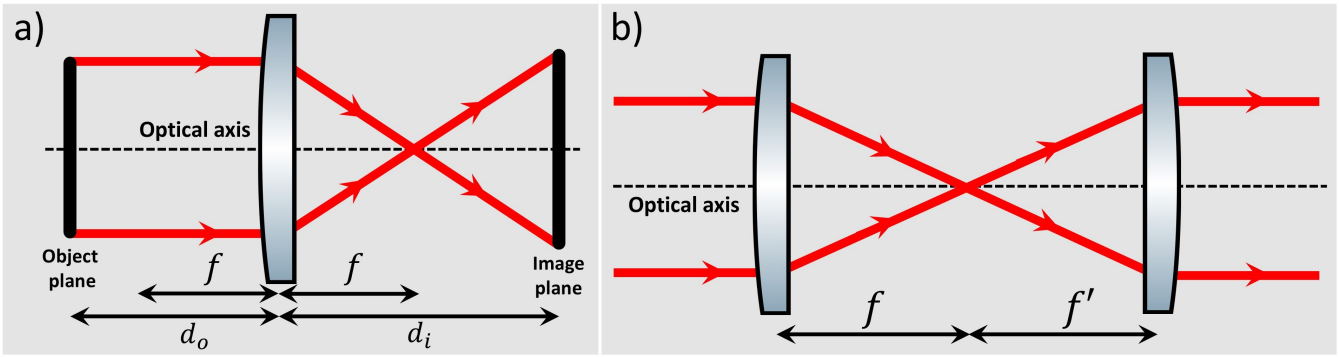

Figure 2.3: Lens ray-tracing diagrams. a) Single lens focusing of a beam from the object to the image planes, where d_o and d_i are the object and image distances from the lens centre. b) A telescope system focusing light parallel to the optical axis, utilising two lenses with focal lengths f and f'.

In the most common lens types, aberrations are quite noticeable and observed in the curved spherical surface of the lens, resulting in beam focusing either before or after the lens focal point. The issue is that a spherical surface is not the correct geometry for a lens, but it provides a relatively decent approximation in the centre, close to the optical axis. However, incident light rays further away from the optical axis are refracted at a greater angle off the lens surface and experience greater aberrations as a consequence of tighter focusing. By centralising the lens along the beam path, we can significantly reduce aberration effects experienced by the beam; however, replacing spherical lenses with aspherical lenses eliminates these aberrations.

Although the rays in Fig. 2.3 provide a useful tool for understanding imaging, in reality, light fields obey a slightly different focusing geometry. In the case of Gaussian modes, the beam is not focused on a single point as seen in Fig. 2.3, but instead follows a hyperbolic shape, where the

[9]Up to a scaling factor.

[10]Photodiodes work by converting incident photons into electric current and do not care about the spatial structure of the beam. On occasions where the PD chip is smaller than the beam size, focusing the beam can boost the detected signal.

[11]This second Fourier transform introduces a global phase, however since experimentally we are concerned with intensity measurements, outside of interferometric setups this phase can be ignored.

beam at the lens focus is known as the Gaussian beam waist w_0 (see Fig. 2.4a), and the divergence angle, ϕ in the far field approximation conforms to the expression [42],

$$\phi = \frac{\lambda}{\pi w_0}, \tag{2.3.1}$$

where λ is the wavelength. Although one must consider the type and focal length of the lens when imaging, the size of the beam waist from focusing is determined by the diameter and wavelength of the transverse mode of propagation. Larger transverse modes of propagation will yield a smaller beam waist w_0 for the same focusing lens, compared to modes with a smaller spatial structure. This can be explained since the Fourier transform of a Gaussian function is also a Gaussian function up to a scaling factor proportional to the inverse of the beam radius (i.e. $\propto 1/w(z)$). This nets a tighter focusing for a beam with a large radius, however a beam with a small spatial structure (i.e. $w(z) > 1$) passing through a lens experiences a magnification in the beam profile throughout propagation. Incidentally, we observe from Eqn. 2.3.1 that Gaussian modes with a smaller beam waist w_0 produce a larger divergence angle, while larger beam waists produce a more collimated beam throughout propagation.

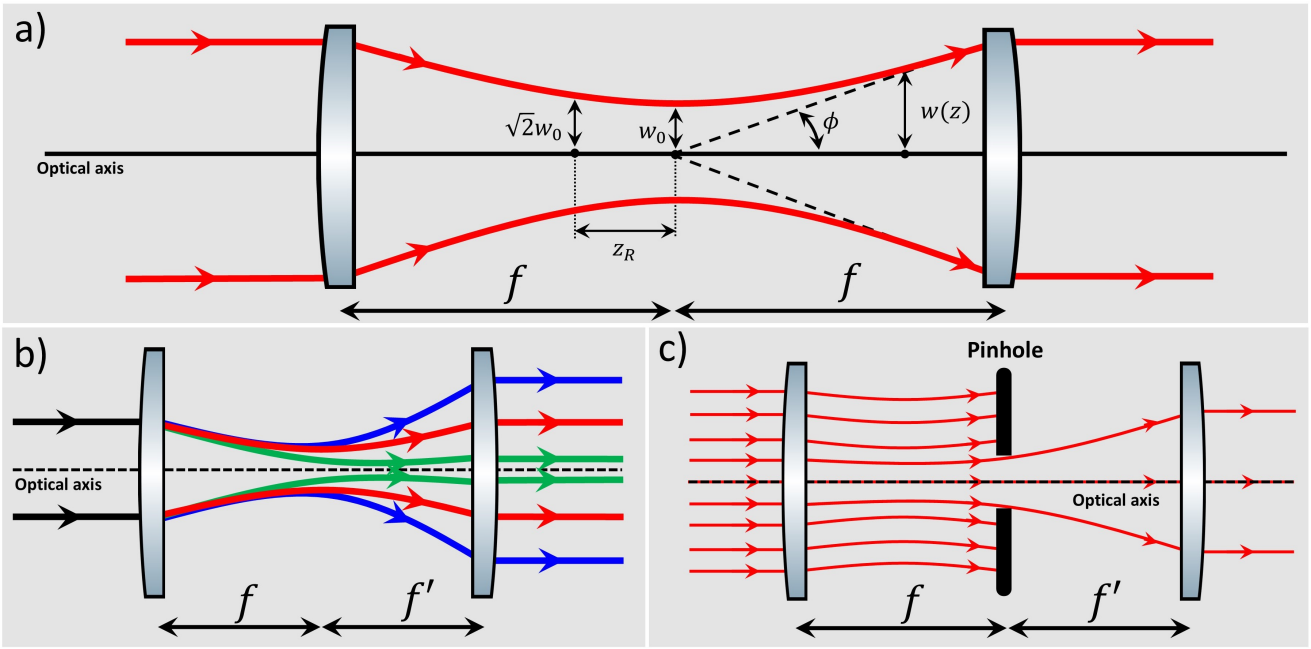

Figure 2.4: Imaging of Gaussian modes. a) Effect of a telescope system with identical lenses on Gaussian modes. b) A telescope system with lenses of varying focal length. In the three cases, the blue beam is magnified ($f < f'$), the green beam is demagnified ($f > f'$), and the red beam is left unchanged ($f = f'$). c) Focusing of a Gaussian mode with an iris placed between the lens foci for beam shape adjustment.

Although a telescope is recognised for magnification, a two-lens system can be used to demagnify the beam, as shown in Fig. 2.4b. In this example, the beam incident (black) enters the lens of focal length f, converging the beam at the beam waist w_0 before diverging towards the second lens with focal length f' for collimation. In the case where $f < f'$ the beam is magnified (blue); if $f = f'$, the beam experiences no changes in size from the two lenses (red)[12] and if $f > f'$ we are left with

[12]Although Gaussian modes will experience changes in size throughout propagation since the diameter $w(z)$ is a function of distance (see Section 1.5.2).

a demagnified output beam (green).

Occasionally, one might find themselves using a laser system whose beam output possesses a distorted spatial structure. In the past, I have used external cavity diode lasers (ECDL)[13] with a hole in the central region of the Gaussian profile, which made experiments difficult to perform. A convenient method of cleaning the beam profile in favour of a more uniformly distributed beam output is using an iris or pinhole placed within the telescope system at the focus of the two lenses (i.e. at the beam waist w_0), as illustrated in Fig. 2.4c. Unfortunately, we are trading optical power for a better beam shape since the pinhole will block about $50\% - 80\%$ of the incident beam[14]. In this configuration, the magnification is no longer calculated via the ratio of the lens foci and is instead determined by the iris aperture and the collimation lens, whereas the first lens determines the portion of the discarded light via focusing at the waist.

A final comment regarding imaging is that elliptically shaped beam profiles propagating through a lens will experience astigmatism. By definition, astigmatism refers to the focusing of the transverse profiles of two orthogonal intensities onto different focusing planes. Unfortunately, ordinary lenses cannot compensate for this effect, but a cylindrical lens focusing only on a single plane of the light field can restore the Gaussian beam shape of the propagating wave[15].

2.4 Light interaction concepts: Birefringence and dichroism

In experiments utilising complex light fields, a variety of optical elements with dichroic or birefrengent properties are employed, enabling the manipulation of the amplitude and polarisation profiles of the light field. These properties even play a key role in our experiments with matter-light interaction and will be extensively discussed in Chapter 6. In line with the literature in [2], our goal is to gain a thorough understanding of these ideas and their application in experiments.

A polariser is considered the most basic static optical element that operates via ***dichroism***, defined as the selective absorption of certain polarisation states subject to the transmission axis of the polariser. The simplest model describing this behaviour is the wire grid polariser. Consider a simple wire grid polariser, where the grid is made of parallel conducting wires as shown in Fig. 2.5. The polarisation components of the incident electromagnetic wave can be decomposed into their orthogonal states (E_x and E_y), where we choose the grid orientation to be parallel to E_y but perpendicular to E_x. A common misperception regarding the wire grid image is that the horizontal component E_x of the electric field is absorbed entirely, while the vertical component E_y propagates through the wire's gaps. In reality, the energy from E_y is transferred to the electrons in the wire, exciting them and generating a current flow. These electrons then de-excite and re-radiate the energy in the form of waves proapgating in both directions of the polariser. The incident wave interacts with the reradiated wave in the forward direction, destructively interfering and preventing the transmission of E_y. The light re-radiated in the backward direction appears as a back reflection from the polariser surface. Since the electrons are not free to move in the perpendicular direction, the polarisation component E_x in this direction remains unattenuated as it propagates through. Note that even though the majority of polarisers used in experiments nowadays are based on polymers or nanoparticles, they behave similarly to a wire grid polariser.

[13] We will discuss ECDLs in more depth in Section 5.2.

[14] Generally, the size of the pinhole determines the number of modes allowed through. A larger pinhole allows more modes to propagate through, which is not ideal for a beam with a very distorted spatial structure.

[15] Whether the x or y axes are to be focused is subject to the beam's initial shape (i.e. rotating the cylindrical lens will alternate between focusing the intensity profiles of the x and y components).

Polarisation anisotropy is a natural characteristic of many materials with dichroic properties; in the polariser's case, it corresponds to the preferential absorption of one of the orthogonal polarisation components over the other. This anisotropy can be induced by stress (for example, in glass cavities) or external magnetic fields (i.e. polarisation spectroscopy (polspec)) and even applies to materials with birefringent properties. ***Birefringence*** is the optical property where a material possesses two different refractive indices for the orthogonal polarisation components, resulting in different propagation velocities through the material and introducing a phase shift between the two. Wave retarders are a good example of optics utilising birefringent materials with a polymer or crystalline structure (like quartz), carefully manufactured with the right thickness to introduce in the most common cases a half or quarter wavelength phase shift (π and $\pi/2$, respectively), which translates to a change in the polarisation structure of the light field (Revisit Section 1.3 for more information).

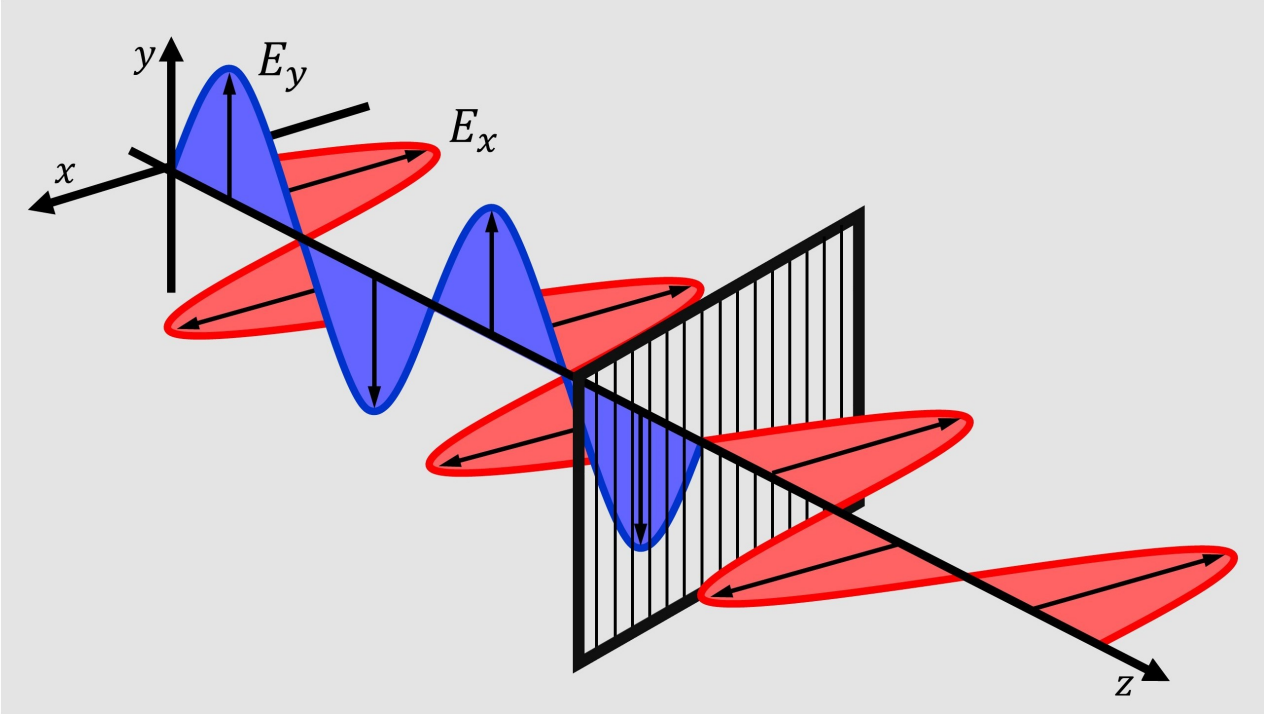

Figure 2.5: EM wave propagating through a wire polariser orientated parallel to E_y and perpendicular to E_x.

2.5 Generating structured beams

The concept of a beam with a spatially variant polarisation structure dates back to the early 1970s [43]; however, throughout the years, there has been an increasing interest in exploring the properties and applications of vector beams in both the classical and quantum domains [44–47]. The majority of our experiments at the University of Glasgow's optics group make use of complex vector structures generated using several different methods, classified as either passive or active generation. In the passive approach, static optical elements are used to create predetermined sets of vector vortex modes, utilising the birefringent and dichroic properties of their material, the likes of vector vortex plates [48–50], and metasurface materials [51–53]. In other static methods, the generation of vector beams is a result of geometric effects, an example of which is given by the glass cone [54–56]. Meanwhile, active generation methods make use of complex beam-shaping holograms

to alter the polarisation structure of the light field via amplitude and phase modulation. Usually, these methods involve using a spatial light modulator (SLM) [57–60] or a digital micromirror device (DMD) [61–66]. These devices are not limited to any particular finite-order spatial mode and are very useful tools for the generation of arbitrary vector beams. In this section, we focus primarily on the construction of a vector beam using a DMD and vector vortex plates; however, we will very briefly touch on SLM beam generation.

2.5.1 Digital Micromirror Devices (DMD)

A digital micromirror device (DMD) consists of tiny, micrometre-sized diamond-shaped mirrors individually mounted and arranged on a 2D array, capable of tilted movement across the $x - y$ plane. This mirror array creates a mask, modulating the amplitude of the incident wave, where the tilts of the individual mirrors act like a binary switch. When the switch is ON, the mirror reflects the beam along the desired path, and when the switch is OFF, the light is deflected away from the path. These devices utilise digital light processing (DLP), a technology developed by Texas Instruments capable of producing a high-resolution video output, utilising the fast modulation rate (up to 25kHz) for use in overhead projectors.

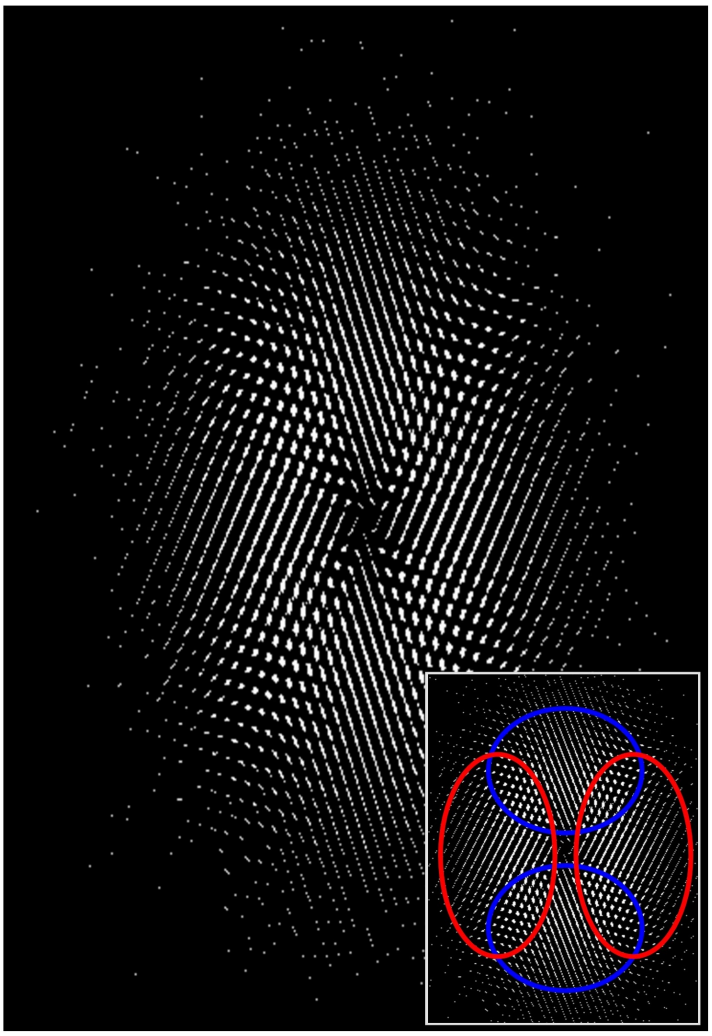

Figure 2.6: An example of a numerically generated multiplexed hologram projected on the DMD chip. The inset highlights the region of the hologram responsible for individual shaping the horizontal (red) and vertical (blue) polarisation components in the desired reflection order.

The amplitude modulation characteristic of DMDs allows the simultaneous manipulation of light beams with different polarisation structures by superimposing two orthogonal polarisation states. Unfortunately, the limited size of the DMD chip makes adjacent hologram placement difficult; however, the solution comes in the form of hologram multiplexing. This technique loads two overlapped numerically generated holograms, of the desired transverse propagation modes, occupying different regions on the DMD mirror array (see Fig. 2.6 for an example), which independently shapes the two polarisation profiles of the incident light field, diffracting them into many different mode orders. For example, the region of the hologram highlighted in red in the inset of Fig. 2.6 is used to shape the spatial structure of the horizontally polarised light, while the blue region of the hologram will shape the vertical beam. The first-order modes generated from the DMD output are then superimposed using the DMD steering controls to produce the desired vector beams. The role of the steering control is to shift the position of the first-order (or any desired-order) beams reflected off the DMD chip, which is achieved by adjusting

the tilt angle of the pixels in the mirror array for the section of the hologram corresponding to each polarisation structure (e.g. to shift the diffraction pattern of the horizontally polarised beam, the tilt angle of the pixels in the red region of the inset in Fig. 2.6 will have to be adjusted accordingly).

The experimental configuration is quite simple and illustrated in Fig. 2.7. We first prepare the laser beam by diagonalising the polarisation using a HWP and passing it through a Wollaston beam splitter (WBS)[16]. The prism separates the polarisation structure of the incoming beam into the horizontal and vertical components, with a slight angle between the two depending on the cube material. A telescope system (L_1 and L_2 in Fig. 2.7) is employed to focus the two polarisation components onto the DMD chip (being able to magnify or demagnify the beam is an added bonus) to apply the hologram transformation to the light field[17]. Interestingly, the ability to modify the beam magnification could be used to overfill the DMD chip to generate an output beam with a more uniform intensity distribution. Alternatively, the beam size could be demagnified to fit the hologram size to increase the output light intensity. Once the desired spatial structure is generated with the appropriate hologram, the beam is projected onto the image plane located at the iris with a lens L_3, where the first-order diffraction modes are overlapped, as illustrated in Fig. 2.8. The unwanted modes are blocked by the iris, and the beam is then collimated with a second lens L_4. For more information on the preparation and generation of vector light using a DMD, see [20, 61].

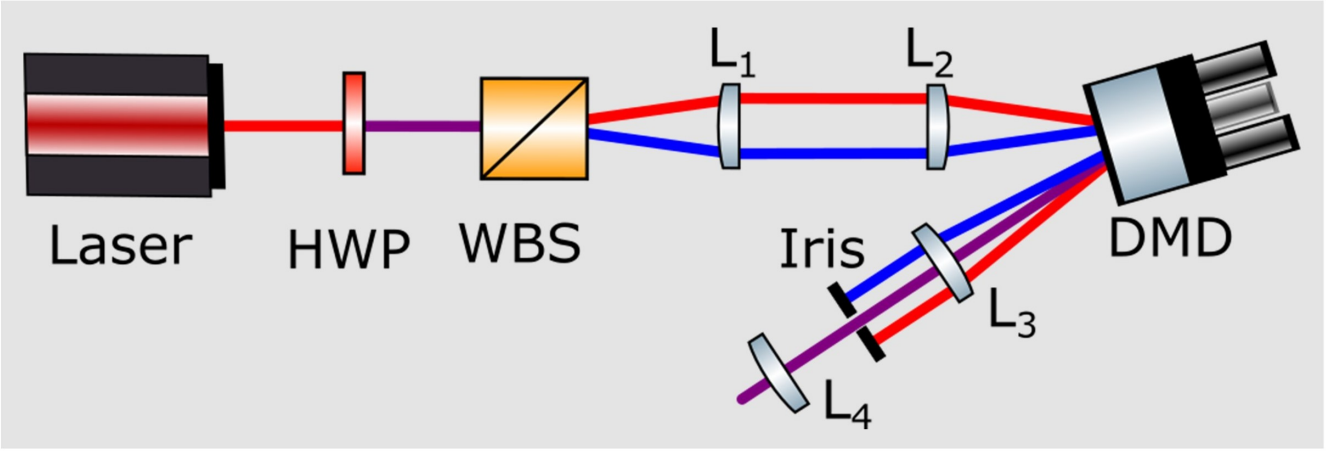

Figure 2.7: Experimental configuration used to generate a vector beam with a DMD.

Note that since the DMD is a binary modulator affecting the light amplitude, the majority of the beam intensity is lost in the diffraction process, leaving us with around 10% of the initial beam power. This makes DMDs very inefficient and unsuitable for applications requiring high optical powers. Additionally, many of the generated modes are often deflected at large angles, even beyond the confines of the optical table, posing a potential laser safety hazard if not appropriately contained.

[16] Which is also called a Wollaston prism.

[17] The main idea is to have both beams incident on the region of the DMD chip where the hologram is being projected. There could be other ways to experimentally implement this (e.g. orthogonal beams entering a PBS or maybe a birefringent microscope slide); however, using a WBS and a telescope system provides an elegant solution to focusing the beam components with the bonus of being able to adjust the beam size.

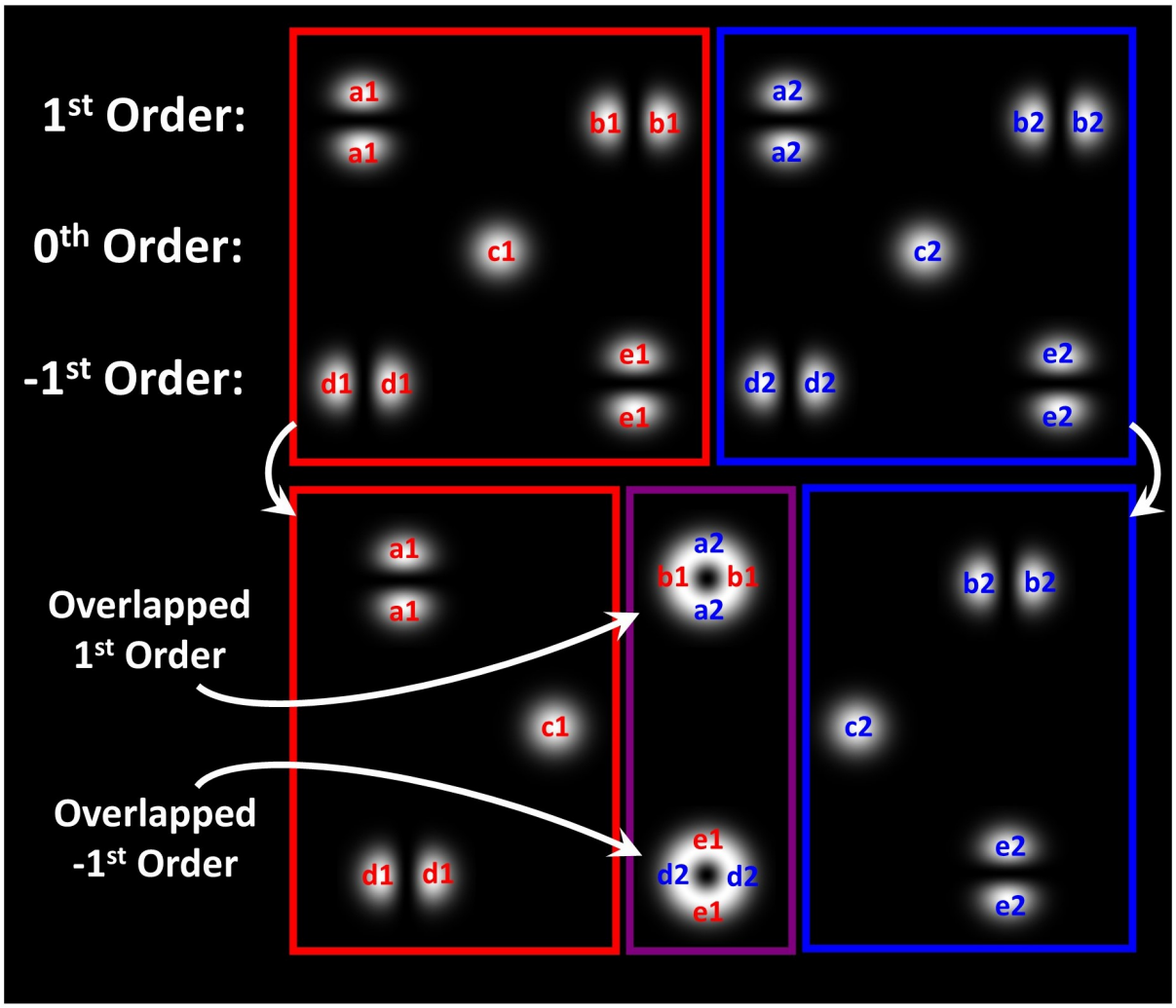

Figure 2.8: The DMD diffracts the $\hat{H}$ (red) and $\hat{V}$ (blue) polarisation components of the incident beam to generate diffraction modes according to the hologram profile. The first-order modes are overlapped (i.e. in this example, the horizontal b1 mode, along with the vertical a2 mode for the first order and the horizontal e1 mode, along with the vertical d2 mode for the minus first order) using the DMD steering control to generate the vector beam output (purple). Note that we generally use the superimposed 1^{st} order modes; however, the -1^{st} can be used, accounting for the phase shift.

A final comment on vector beam generation with a DMD. Since both polarisation components are incident on the hologram chip as illustrated in Fig. 2.7, changing the DMD settings responsible for generating the transverse propagation mode for one of the polarisation components will also affect some of the output mode orders of the other polarisation state reflected off the DMD chip. However, the two regions of the hologram previously state to individually shape the polarisation components (from the inset of Fig. 2.6) of the desired reflected orders (first orders in our case) do work as advertised, since the two beams are spatially separated by the WBS even when focused onto the DMD with the L_2 lens[18]. This means that their reflected modes will remain spatially separated, becoming increasingly noticeable with the propagation distance of the beams. However, by diverging the beams using a lens (i.e. L_3 from Fig. 2.7), we can further resolve the position of

[18]If the two polarisation components were perfectly overlapped, their reflected modes would also be perfectly overlapped (i.e. the modes with the same letters in Fig. 2.8), making generation of vector beams impossible.

the mode orders, projecting the beams onto the far field, which allows for an easier selection of the mode orders. This enables us to manually overlap the desired output modes to generate our structured beams, as illustrated in Fig. 2.8. Therefore, the two regions of the hologram indicated in the inset of Fig. 2.6 do indeed shape the two polarisation components individually, but only in the far field after selecting the desired reflected modes.

2.5.2 Vector Vortex plates (q-plates)

A vortex retarder is a static birefringent optical element made from liquid crystal polymer with a unique and interesting fast axis geometry. From Section 1.3.2, we established that a HWP works by introducing a π shift to the polarisation component aligned with the fast axis of the retarder, where a waveplate rotation of θ corresponds to a polarisation change of 2θ. In this case, the fast axis points in the same direction, affecting all regions of the incident beam uniformly. In a general sense, we can think of a q-plate having varying localised fast axis orientations, analogous to an array of half-waveplates set at different rotation angles. This effect introduces different phase shifts across the beam polarisation profile. Additionally, the q-plate works by introducing an orbital angular momentum $\pm l$ to the right and left circular polarisation components, respectively, similar to LG modes. In terms of the Jones matrix, a vortex plate is given by [48, 67],

$$\mathbf{J}_{qp} = \begin{pmatrix} \cos(2\theta) & \sin(2\theta) \\ \sin(2\theta) & -\cos(2\theta) \end{pmatrix}, \tag{2.5.1}$$

where $\theta = q\phi + \delta$, here ϕ is the azimuthal angle[19] and δ is the orientation of the q-plate fast axis when $\phi = 0$. These retarders are generally characterised by an order q, related to the LG mode number by $l = 2q$, and represent how many $(0 \to 2\pi)$ phase shifts appear within the q-plate profile (i.e. for a $q = 1$ plate, we have $l = 2$ and expect the phase structure $(0 \to 2\pi)$ to appear twice in the retarder profile)[20]. Since any polarisation state can be expressed as a superposition of two orthogonal polarisation bases, a horizontally polarised state in the circular basis is given by,

$$\hat{H} = \frac{1}{\sqrt{2}} \left(\hat{\sigma}_- + \hat{\sigma}_+ \right), \tag{2.5.2}$$

where $\hat{\sigma}_\pm$ are the left and right circular components, respectively[21]. Under the action of the q-plate, the electric field in Eqn. 2.5.2 experiences a phase change given by,

$$\mathbf{J}_{qp}\hat{H} = \frac{1}{\sqrt{2}} \left(e^{il\phi}\hat{\sigma}_- + e^{-il\phi}\hat{\sigma}_+ \right). \tag{2.5.3}$$

Although the individual circular components of the equation above possess some orbital angular momentum, the net OAM of the whole beam is zero, which is always true for a linearly polarised input beam. In the case of a circular input beam propagating through a q-plate, $\mathbf{J}_{qp}\hat{\sigma}_\pm = e^{\mp il\phi}\hat{\sigma}_\pm$, we maintain the polarisation structure but introduce OAM to the light field. Depending on the

[19] The azimuthal angle describes the position on the equator of the Poincaré sphere, extending from 0 to 2π, identical to the orientation angle ψ described in Section 1.3.3.

[20] Do not confuse this with the number of the same polarisation states appearing within a $(0 \to 2\pi)$ cycle. Since polarisation is $\pi/2$ cyclic with respect to θ, we expect to see 4 of the same polarisation structures in a $(0 \to 2\pi)$ cycle for a $q = 1$ waveplate.

[21] Here we adopted an atom optics notation for circular polarised light.

fast axis orientation of the q-plate, different polarisation structures can be generated from the same polarisation input, so Eqn. 2.5.3 can describe a radial or azimuthal polarisation structure (see Fig. 2.9 for reference).

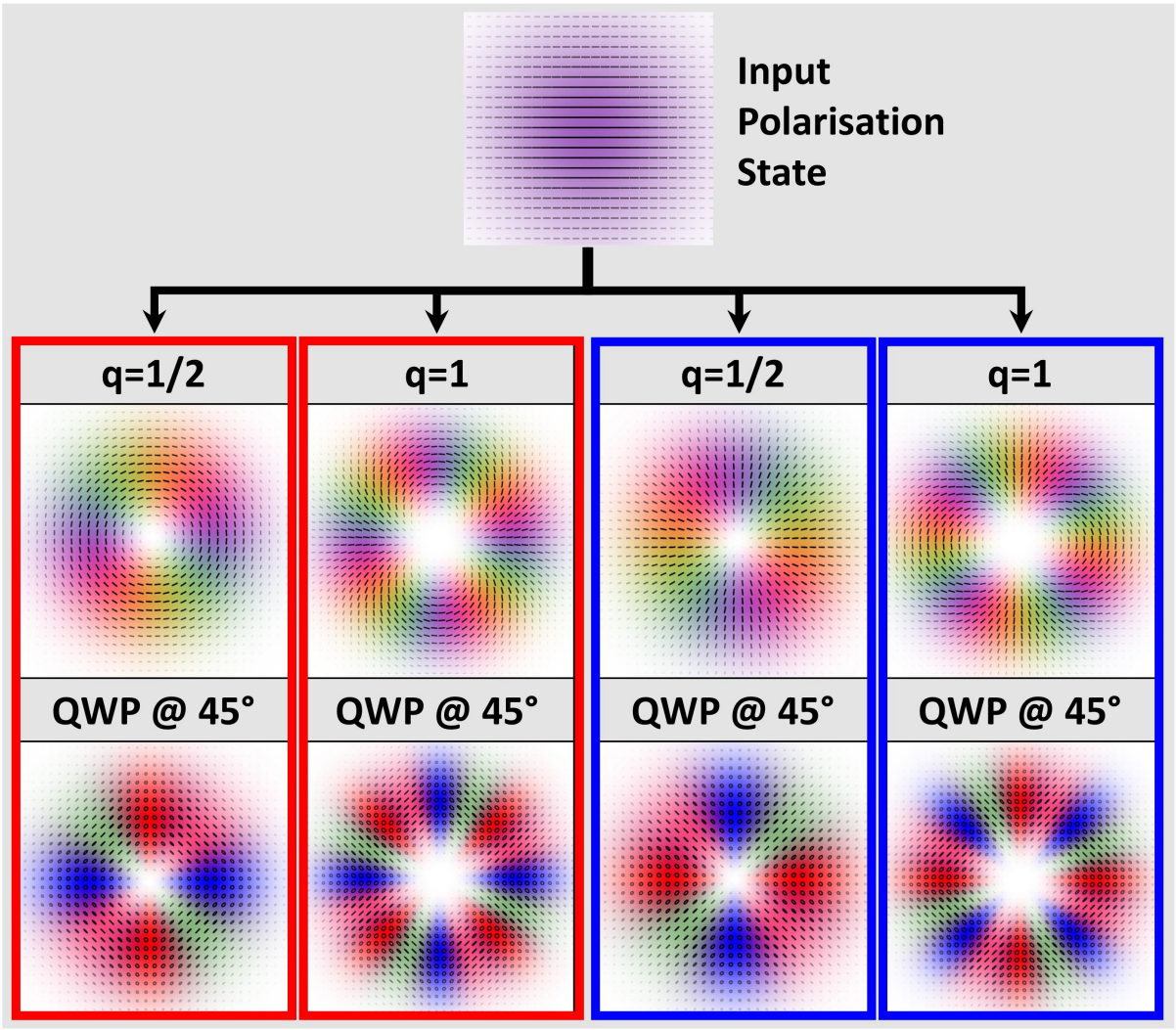

Figure 2.9: Polarisation profiles of a horizontally polarised input beam through a $q = 1/2$ and $q = 1$ vortex retarder (top rows), incident on a QWP at 45° (bottom rows). The beams in red indicate a q-plate fast axis aligned parallel with the horizontal input state, while the beams in blue indicate a fast axis at 45° to the horizontal.

Unlike active vector beam generation methods that require extensive preparation, q-plates only require simple alignment of the vortex to the beam centre (see Fig. 2.10). Additionally, they do not suffer from excessive intensity loss (like DMDs do), are incredibly efficient ($> 97\%$)[22] and relatively cheap, making them ideal for structured light generation, even for applications requiring high optical intensities (they can handle intensities up to 5W/cm)[23]. The downside is they can only generate a very limited number of transverse propagation modes; however, the generation of hybrid polarisation structures is possible with additional polarisation optics, as illustrated in the bottom row of Fig. 2.9.

[22]Value taken from [68].
[23]These values are calculated at 810nm and taken from [68].

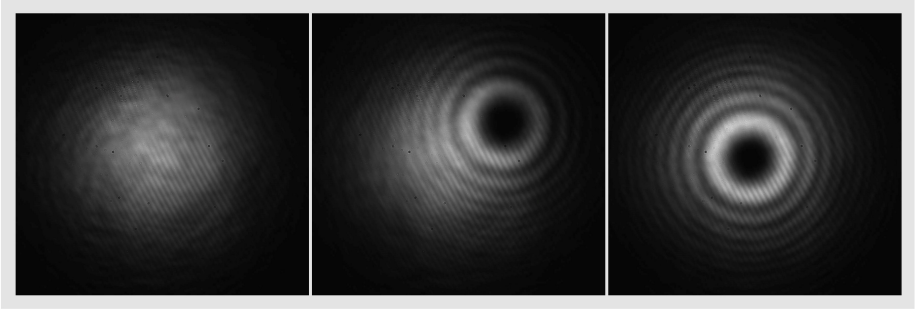

Figure 2.10: Alignment of a q-plate vortex to the beam profile. Usually these plates are housed in an XY mount (like the Thorlabs LM1XY/M) for ease of alignment.

2.5.3 A brief overview of Spatial Light Modulators (SLM)

Working in a lab where the construction of structured light is essential for our research has the benefit of exposing us to alternative techniques for complex light field generation used by other members of the group. With the exception of Ryan Hawley's experiment generating vector beams with a Fresnel cone [55][24], the most common methods of vector beam generation in our labs utilise DMDs, q-plates, and SLMs. For completeness, we provide a brief overview of SLMs.

Spatial light modulators (SLMs), which are active generation elements akin to DMDs, are composed of numerous tiny birefringent liquid crystals arranged in pixel format in between the SLM front glass panel and a reflective surface. By applying a voltage, the orientation of the liquid crystals can be controlled. Unlike DMDs, the spatial modulation of the light field is done via phase-based holograms instead of binary amplitude holograms, offering a significant increase in the efficiency of the shaped beam since only desired spatial modes are produced (for more information on experimental implementations of SLM for vector beam generation, see [20, 69, 70]).

Despite the control and flexibility offered by SLMs, there are several factors that should be considered prior to investing in or experimentally integrating an SLM. In most reflective SLMs, the back mirror is usually wavelength-coated, which restricts the kind of lasers that can be used with them. Actually, I seem to recall that Amy McWilliam, a member of our group, was investigating Zernike mode generation with an SLM using a 633nm He-Ne laser; however, the SLM mirror was coated for 780nm near-infrared (NIR) light. The experiment became challenging to conduct as a result of destructive interference in the beam pattern, which was resolved when a 795nm laser source was introduced to the setup.

Although SLMs are excellent beam shaping tools, they are much slower than DMDs (only 60Hz frame rate) and very expensive when compared to other beam shaping equipment (the cheapest SLM is easily >£10000, while the cheapest DMD is a few £100). Additionally, the crystal geometry only works with a single type of polarisation input, usually horizontal or vertical, making the experimental configuration for vector beam generation slightly more complicated.

2.6 Summary

This chapter covered the fundamental experimental ideas of light manipulation using mirror reflections and lens imaging, emphasising their effects on the light wave. We briefly discussed the ideas of birefringence and dichoism in relation to polarisation optics. Lastly, we explored a few methods for complex vector beam generation, examining their characteristics and limitations.

[24] Sadly I didn't have much overlap with Ryan, as he was finishing when I was just starting.

Chapter 3

A Single-shot polarimeter with generalised measurements

3.1 Outline

This chapter reports the work published in [71], involving members of the University of Glasgow's optics and quantum theory groups and Sebastião Pádua, a visiting researcher from the Universidade Federal de Minas Gerais (Brazil), who spent over two years with us here at the University of Glasgow before departing. In this work, C.M. Cisowski and myself optimised the experimental configuration, took and analysed the data, H. Jimbrown was involved in the data gathering and analysis during the early days of the project, S. Pádua built the initial setup and, together with S. Crooke, overseen the theoretical analysis, and S. Franke-Arnold conceived and led the work.

3.2 Introduction

In Section 1.3, we introduced the concept of light polarisation, a key property of optical beams that has an effect on the propagation and refraction of light fields, providing an additional degree of freedom (alongside the spatial and path degrees of freedom) useful for classical and quantum communications alike. While output beams from laser systems are usually homogeneously polarised (typically linearly polarised), there has been an increasing interest in recent years to shape light with spatially varying polarisation profiles, like vector vortex beams [72–76], Poincaré beams [77–81] and even special Poincaré beams called skyrmion beams [82–84]. An interesting feature of these vector beams is their non-separable relation between the spatial degree of freedom and the polarisation [85, 86], a quantity that can be inferred from the concurrence [61, 87, 88] and has interesting applications in quantum communication [89–91] memories [92], cryptography [93] and other quantum inspired concepts [94–99].

Additionally, polarisation plays a key role in a variety of metrological applications, including but not limited to material stress analysis [100, 101], biological microscopy and the pharmaceuticals [102, 103], and ellipsometry [71, 104, 105]. In those areas, the optical activity [105–109] is the quantity of interest, where a beam of well-known polarisation experiences a modification in the polarisation structure after propagating through a medium, providing a quantitative description of the sample's response to different polarisation profiles. This makes an accurate determination of the spatially dependent polarisation structure a vital task in both classical and quantum optics [110, 111].

One can represent the polarisation degree of freedom with a two-dimensional Hilbert space, ideal for a quantum bit (qubit) realisation[1]. A state on the Hilbert space of dimension d demands d^2 number of measurements for state reconstruction [112]. The tomography of the local polarisation structure, occupying the Hilbert space of dimension $d = 2$, requires a minimum of four measurements, which can be associated with the four parameters of the Stokes vector [113–117]. Most commonly, these parameters are determined from overcomplete measurements via projection on a set of mutually unbiased and orthogonal basis states[2], where the beam intensity is recorded for the horizontal, vertical, diagonal, anti-diagonal, right and left hand circular polarisation states (see Section 1.4 for more information).

Alternatively, one can use generalised measurements [118–120] with a different set of projection operators to perform full tomography of quantum states with a minimum number of required measurements [121–125]. These operators can be chosen to form what is called a minimum informationally complete positive operator value measure (MIC-POVM)[3] [126–128], which results in a reduction from the overcomplete six measurements used in Stokes tomography into a set of four unbiased measurements spanning the entirety of the Hilbert space, advantageous for polarisation tomography. The key benefits are a reduction in required time when performing sequential measurements or an increase in efficiency when performing simultaneous measurements, ideal for applications of low-intensity beams or even single photon emission. In previous literature, experiments utilising MIC-POVMs for quantum state tomography have only been implemented for homogeneously polarised light so far [129].

In this chapter, we explore our work published in [71], where we demonstrate an experimental setup of spatially resolved MIC-POVMs for vector beam reconstruction. Throughout this section, we introduce the relevant theory and explore an experimental configuration utilising an interferometer, coupling the polarisation degree of freedom to the path (or linear momentum) degree of freedom via a series of polarising beam splitters, and performing a unitary operation in the extended state space of the path and polarisation degrees of freedom. We associate the POVM elements with four different outputs of our interferometer, used to obtain the spatially resolved polarisation information using generalised measurements with the desired POVM states. We test our setup with a number of vector beams generated using a digital micromirror device (DMD) [61, 66, 130, 131], drawing a comparison between our system's performance and spatially resolved measurements from conventional Stokes tomography [61, 87, 132, 133]. We conclude by introducing the subsequent work inspired by our initial experiment and exploring potential applications for such a one-shot polarimeter for any beam characterisation.

3.3 The photon state

Recall from Section 1.3.3, we classify the polarisation of a classical light beam (or a photon's quantum state) using a vector with four parameters called the Stokes vector,

[1] The Hilbert space is a vector space equipped with an inner product, used to represent the state of a quantum system.

[2] A set of projection measurements is considered unbias if they cover the entire Hilbert space. The idea of unbias measurements will be a recurring theme throughout this chapter.

[3] We define these operators when discussing generalised measurements in Section 3.4.

$$\mathbf{S} = \begin{pmatrix} S_0 \\ S_1 \\ S_2 \\ S_3 \end{pmatrix} = \begin{pmatrix} I_H + I_V \\ I_H - I_V \\ I_D - I_A \\ I_R - I_L \end{pmatrix}, \tag{3.3.1}$$

where I_i, for $i \in \{H, V, D, A, R, L\}$ are the intensity measurements projected onto the six different polarisation basis occupying the Poincaré sphere (found in Section 1.3.3). We define a normalised Stokes vector with respect to the total intensity S_0 as follows,

$$\mathbf{S}^N = \frac{1}{S_0}\begin{pmatrix} S_0 \\ S_1 \\ S_2 \\ S_3 \end{pmatrix} = \begin{pmatrix} 1 \\ S_1/S_0 \\ S_2/S_0 \\ S_3/S_0 \end{pmatrix} = \begin{pmatrix} 1 \\ S_1^N \\ S_2^N \\ S_3^N \end{pmatrix}, \tag{3.3.2}$$

where S_1^N, S_2^N, S_3^N form the reduced Stokes vectors. A single Stokes vector is sufficient to describe the polarisation of a homogeneous beam; however, vector beams with changing polarisation structures, like vector vortex or Poincaré beams, are represented by a varying Stokes vector as a function of the transverse position of the beam $\mathbf{S}(\mathbf{r}_\perp)$, where $\perp = (x, y)$, due to their non-homogeneity. By adopting a quantum language, we defining the light beam in the paraxial approximation (or the photon wavefunction) as,

$$|\psi\rangle = |u_H\rangle|H\rangle + e^{i\phi}|u_V\rangle|V\rangle, \tag{3.3.3}$$

where $|H\rangle$ and $|V\rangle$ are the orthonormal horizontal and vertical polarisation states, respectively, and ϕ is the relative phase between the two states[4]. Here $|u_H\rangle$ and $|u_V\rangle$ constitute the associated horizontal and vertical transverse spatial states, respectively[5]. By projecting the transverse position ($\mathbf{r}_\perp$) on the light beam state from Eqn. 3.3.3, we can obtain an expression of the beam's local polarisation profile as follows,

$$|\psi(\mathbf{r}_\perp)\rangle = \langle \mathbf{r}_\perp|\psi\rangle = u_H(\mathbf{r}_\perp)|H\rangle + e^{i\phi}u_V(\mathbf{r}_\perp)|V\rangle, \tag{3.3.4}$$

where $u_j(\mathbf{r}_\perp) = \langle \mathbf{r}_\perp|u_j\rangle$ for $j \in \{H, V\}$ are the complex amplitudes of the light transverse profile $|u_j\rangle$. We use this quantum language to draw the connection between the experimental realisation of the single-shot four-state polarimeter and quantum tomography, describing the polarisation measurements of our system as elements of a POVM set.

[4]This notation is known as Dirac's bra-ket notation and will be explained at the beginning of the next section.

[5]Note that there are no restrictions or requirements that force these two spatial states to be orthogonal or normalised. In fact, if one desires to shape a beam while maintaining a homogeneous polarisation output, these spatial modes could end up being identical.

3.4 Generalised measurements

Understanding the concept of a generalised measurement is a vital step to understanding the theoretical model of our experiment. Any observable of a quantum system can be associated with a Hermitian operator, where extracting any information requires the performance of a measurement. By following the literature in [118–120, 134], we develop a mathematical understanding of the nature of generalised measurements and their usefulness. Consider a Hermitian operator $\hat{A}$ with a complete set of eigenstates $|A_n\rangle$ and eigenvalues a_n,

$$\hat{A}|A_n\rangle = a_n|A_n\rangle. \tag{3.4.1}$$

By definition, a Hermitian operator is an operator that is its own Hermitian conjugate (i.e. conjugate transpose). These operators denote a physical quantity measurable from the quantum system, an example being position, momentum, energy, etc. In this chapter, we adopt Dirac's quantum bra-ket notation, where the ket $|A_n\rangle$, denotes a state in a quantum system; however, mathematically, it represents a simple vector, obeying the axioms of vector space (see chapter 3 of [135] or any suitable linear algebra textbook). In a similar manner, the bra $\langle A_m|$, represents the Hermitian conjugate of $|A_m\rangle$, such that $\langle A_m|A_n\rangle = \delta_{mn}$ is analogous to the inner (or dot) product, where δ_{mn} is the Kronecker delta. The Kronecker delta has the property that $\delta_{mn} = 1$ if $m = n$; otherwise, $\delta_{mn} = 0$. The von Neumann definition states that performing a measurement of $\hat{A}$ will give one of the eigenvalues a_n as the output, where the probability of finding any of these eigenvalues is given by,

$$P(a_n) = \left|\langle A_n|\psi\rangle\right|^2, \tag{3.4.2}$$

where $|\psi\rangle$ is the state of the system prior to performing the measurement. So far, we have considered only pure states (i.e. a state given by a vector (or ket)); however, one might come across mixed states, defined as a collection of pure states in a quantum system. These mixed states are useful in representing states that are difficult to untangle (an example is the two-level atomic transition system, more in Section 4.3), usually denoted in terms of a density operator $\hat{\rho}$. We define the density operator as,

$$\hat{\rho} = \sum_m w_m |A_m\rangle\langle A_m|, \tag{3.4.3}$$

where w_m is the probability of occupying the state. Note that Eqn. 3.4.3 reduces to $\hat{\rho} = |A_m\rangle\langle A_m|$ for pure states[6], since the probability of the measurement equates to unity. From Eqn. 3.4.2 and recalling that $\left|\langle A_n|\psi\rangle\right|^2 = \langle A_n|\psi\rangle\langle A_n|\psi\rangle^\dagger$, we obtain an expression of the measurement probability in terms of the density operator,

$$P(a_n) = \langle A_n|\hat{\rho}|A_n\rangle = \mathrm{Tr}\big(\hat{\rho}|A_n\rangle\langle A_n|\big), \tag{3.4.4}$$

where the second expression above is a consequence of using the identity operator $\mathbb{I} = \sum_n |A_n\rangle\langle A_n|$ and the trace identity of operators $\mathrm{Tr}(\hat{B}) = \sum_i \langle\phi_i|\hat{B}|\phi_i\rangle$. The system is left in the eigenstate $|A_n\rangle$ after the measurement, provided the outcome of the measurement is the eigenvalue a_n. This remains true if the measurement is repeated in quick successions[7]. It is useful to introduce the

[6] Note in this formalism $|A_m\rangle\langle A_m|$ is akin to the outer product of the two vectors $|A_m\rangle$ and $\langle A_m|$, the result of which is a matrix.

[7] Since the state is being collapsed sufficiently quickly before the system had time to evolve.

projectors $\hat{P}_n = |A_n\rangle\langle A_n|$ so that Eqn. 3.4.4 becomes,

$$P(a_n) = \langle \hat{P}_n \rangle = \mathrm{Tr}\Big(\hat{\rho}\hat{P}_n\Big), \tag{3.4.5}$$

where $\langle \hat{P}_n \rangle$ is known as the expectation value of the operator $\hat{P}_n$. By now, we have established that the probability of measuring a specific outcome in the von Neumann model is given by Eqn. 3.4.5, where we project onto a single or multiple orthonormal states. The properties of these projectors are summarised in the table below,

1) They are Hermitian operators $\hat{P}_n = \hat{P}_n^\dagger$
2) They are positive $\hat{P}_n \geq 0$
3) They sum to unity (i.e. are complete) $\sum_n \hat{P}_n = \hat{\mathbb{I}}$
4) They are orthonormal $\hat{P}_n\hat{P}_m = \hat{P}_m\delta_{mn}$

Table 3.1: Properties of projection operators.

Here $\hat{\mathbb{I}}$ is the identity operator. The first three conditions in the list above denote physical restrictions imposed on the projector. The projectors represent observables; therefore, naturally, they are Hermitian by construction. They are probability measurements that require them to be positive and must sum to unity for all possible measurements since they form a complete set. However, the fourth condition is not strictly necessary for a measurement, and the formalism for generalised measurement in fact drops this constriction. Interestingly, the Stokes polarisation measurements discussed in Section 1.4 could be considered multiple von Neumann measurements carried out sequentially across different sets of orthogonal polarisation bases. Since the wave is complex by nature[8] the projection of the transverse electric field profile onto a set of two orthogonal bases states (e.g. $\hat{H}$ and $\hat{V}$) by themselves is insufficient to reconstruct the polarisation state of the beam as the projections failed to recover the phase information of the light field. Therefore, additional projections onto a set of different orthogonal bases states (i.e. $\hat{D}$ and $\hat{A}$ along with $\hat{R}$ and $\hat{L}$) are required for full polarisation state reconstruction.

In a noisy world where ideal experimental measurements are difficult to achieve, designing a measurement system that includes any effects of ambient noise is desirable. Consider a device that determines whether the polarisation of a single photon is horizontal or vertical. In the ideal measurement system, the projectors are given by,

$$\begin{aligned} \hat{P}_H &= |H\rangle\langle H| \\ \hat{P}_V &= |V\rangle\langle V|. \end{aligned} \tag{3.4.6}$$

We define the probability of measuring the two polarisation states as,

$$\begin{aligned} P(H) &= (1-p)\,\mathrm{Tr}\Big(\hat{\rho}\hat{P}_H\Big) + p\,\mathrm{Tr}\Big(\hat{\rho}\hat{P}_V\Big) \\ P(V) &= (1-p)\,\mathrm{Tr}\Big(\hat{\rho}\hat{P}_V\Big) + p\,\mathrm{Tr}\Big(\hat{\rho}\hat{P}_H\Big), \end{aligned} \tag{3.4.7}$$

[8] With a real amplitude and a complex phase term.

where we incorporate the error or noise in the system as the probability of measuring the wrong state denoted by p. To break it down, we established that the projectors are given by Eqn. 3.4.5, so for a prepared state $|H\rangle$, the ideal measurement probability should be 1; however, the detector now also has the probability of incorrectly measuring the state $|V\rangle$, given by p, therefore our new probability of measuring $|H\rangle$ is now $(1-p)$, in order to satisfy the unity condition. We can rewrite these probability operators in a form similar to 3.4.5,

$$\begin{aligned} P(H) &= \mathrm{Tr}(\hat{\rho}\hat{\pi}_H) \\ P(V) &= \mathrm{Tr}(\hat{\rho}\hat{\pi}_V), \end{aligned} \tag{3.4.8}$$

where we introduce a new set of probability operators given by,

$$\begin{aligned} \hat{\pi}_H &= (1-p)\hat{P}_H + p\hat{P}_V \\ \hat{\pi}_V &= (1-p)\hat{P}_V + p\hat{P}_H. \end{aligned} \tag{3.4.9}$$

These new projectors are not orthonormal and only satisfy the following conditions,

1) They are Hermitian operators $\hat{\pi}_n = \hat{\pi}_n^\dagger$
2) They are positive $\hat{\pi}_n \geq 0$
3) They sum to unity (i.e. are complete) $\sum_u \hat{\pi}_n = \hat{\mathbb{I}}$

Table 3.2: Properties of probability operators.

By dropping the fourth condition, we are able to generalise our measurement system with a set of operators $\{\hat{\pi}_m\}$, expressing the measurement probability of a system with respect to the density operator $\hat{\rho}$ as follows,

$$P(m) = \mathrm{Tr}(\hat{\rho}\hat{\pi}_m). \tag{3.4.10}$$

It follows that the product of such two such operators is calculated as,

$$\begin{aligned} \hat{\pi}_m\hat{\pi}_n &= [(1-p)\hat{P}_m + p\hat{P}_n][(1-p)\hat{P}_n + p\hat{P}_m] \\ &= (1-p)^2|A_m\rangle\langle A_n|\delta_{mn} + p^2|A_m\rangle\langle A_n|\delta_{mn} \\ &\qquad + p(1-p)(|A_m\rangle\langle A_m| + |A_n\rangle\langle A_n|) \\ \therefore\ \hat{\pi}_m\hat{\pi}_n &= \left\{ \begin{array}{ll} \hat{\mathbb{I}} & \text{if } m = n \\ p(1-p)\hat{\mathbb{I}} & \text{if } m \neq n \end{array} \right\}, \end{aligned} \tag{3.4.11}$$

where δ_{mn} is the Kronecker delta. Calculating the outcome of any generalised measurement requires a set of operators that describe the measurements, ideally a single operator for each measurement. These operators are named probability operator measures, usually abbreviated as POM, or alternatively, positive operator valued measures, or POVM for short. In the context of polarisation

state tomography, the benefit of dropping the orthonormality condition is to minimise the number of required measurements to fully describe the polarisation state of the light field. For example, Stokes tomography requires a total of 36 projection measurements for unbiased state reconstruction; however, employing the POVM operators constitutes a reduction down to 16 measurements instead[9].

Additionally, by dropping the orthonormality condition, the number of probability operators can exceed the dimension of the state space, while the orthogonal nature of projectors prevents them from ever exceeding the state space dimension[10]. Any set of POVM elements that satisfy the conditions in Table 3.2 are potential measurements, and the outcome of any measurement can be expressed as an element of the POVM set [118, 136]. A consequence of these conditions is the existence of an optimal, informationally complete set of measurement operators capable of describing any quantum state. By finding these operators, we know that a physical realisation of them exists and aim to experimentally implement them in the laboratory to construct an optimal polarisation state tomography polarimeter.

3.5 The POVM elements and instrumentation matrix

A specific form of generalised measurements of interest is the symmetric informationally complete POVM, abbreviated as SIC-POVM [126]. These POVM are deemed ***informationally complete*** due to their ability to completely determine the quantum state of an object from the carried out measurement [137–140] and their ***symmetric*** nature comes from their equal pairwise overlap between the different POVM elements[11]. Maximising the efficiency in determining the input quantum state requires the POVM elements to be positive multiples of projectors onto pure states, where each element of the POVM is a unique vector in the complex space $\mathbb{C}^d$, where d denotes the dimensions of the space. Such a set of POVM has d^2 elements of the form $\hat{\pi}_i = \frac{1}{d}|\phi_i\rangle\langle\phi_i|$ and satisfy the following,

$$\left|\langle\phi_i|\phi_j\rangle\right|^2 = \frac{d\delta_{ij}}{d+1}, \tag{3.5.1}$$

where δ_{ij} is the Kronecker delta. In the space of the Poincaré or Bloch sphere (i.e. $d = 2$), the POVM set $\{|\phi_i\rangle\}$ forms the vertices of a tetrahedron, as demonstrated in Fig. 3.1. These states are equidistant and symmetric in their distribution, negating any bias in the reconstruction of quantum states and therefore providing the same reconstruction fidelity for any input state [119]. In our work, we chose the POVM set introduced by [121],

$$\begin{aligned} |\phi_1\rangle &= a|H\rangle + b|V\rangle, & |\phi_2\rangle &= a|H\rangle - b|V\rangle, \\ |\phi_3\rangle &= b|H\rangle + ia|V\rangle, & |\phi_4\rangle &= b|H\rangle - ia|V\rangle, \end{aligned} \tag{3.5.2}$$

where $a = \sqrt{\frac{1}{2} + \frac{1}{2\sqrt{3}}}$ and $b = \sqrt{\frac{1}{2} - \frac{1}{2\sqrt{3}}}$. An extensive derivation of the POVM state coefficients a and b can be found in Appendix A of [121].

[9] In fact, the incorporation of ambient noise into the measurement system is an added advantage, and the reduction in the number of required measurements to map the polarisation state of a beam is the fundamental reason to use POVM for polarisation state tomography.

[10] Ironically, this is the opposite of what we want.

[11] Which means the pairwise inner product of any two SIC-POVM elements in the same set will always be equal.

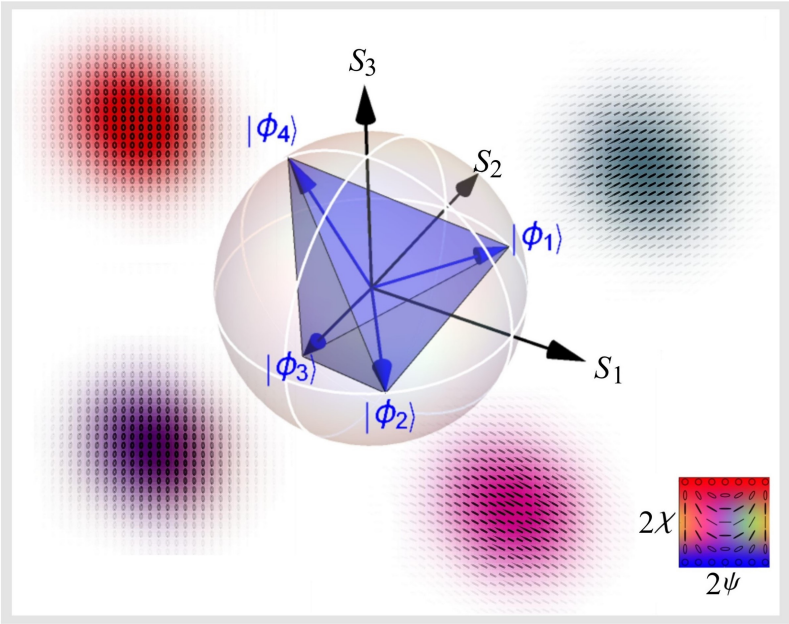

Figure 3.1: The tetrahedron formed from the POVM states $|\phi_1\rangle, |\phi_2\rangle, |\phi_3\rangle, |\phi_4\rangle$ in the Poincaré sphere. The polarisation ellipse is plotted in black, while the background colour, modulated in opacity relative to the beam intensity, maps the orientation ψ and ellipticity χ of the polarisation ellipse to the surface of the Poincaré sphere for all pixels or super-pixels, as shown in the inset. Figure taken from [71].

To perform a measurement on a set of non-orthogonal POVM states, we enlarge the Hilbert space of the input state by introducing an ancilla[12], forming a Naimark extension of the measurement [118][120]. By choosing the path degree of freedom in common with previous literature [119][121][129], we consider the photon described by Eqn. 3.3.3 having the choice of propagating along two directions, determined by the photon's linear momentum $|k_\mu\rangle$ along the paths $\mu = \alpha, \beta$, such that the extended basis of the photon state is given by $\{|H\rangle \otimes |k_\mu\rangle, |V\rangle \otimes |k_\mu\rangle\}$. We implement the desired POVM states by performing a projection measurement P, after applying the relevant unitary operation U to the extended state, as illustrated in Fig. 3.2. See Appendix A for the derivation of the Naimark extension of the POVM states, following the example in [121].

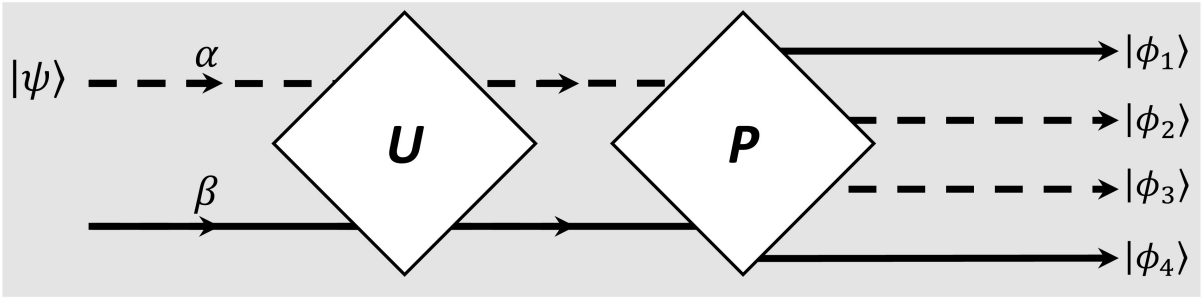

Figure 3.2: Schematic of the POVM measurement scheme. The input polarisation state $|\psi\rangle$ enters through path α, where the realisation of the additionally path β allows extension to the state space for the implementation of a four outcome measurement system. The unitary operation acts on both the path and polarisation degrees of freedom before the final projection P in the extended space constructs the POVM elements $|\phi\rangle_i$.

Experimentally we measure the intensity profile of the spatially resolved beam, in the form of a normalised intensity vector, with each entry corresponding to the intensity profile incident on a specific detector given by,

$$\mathbf{I}^N = \frac{1}{I_t}\begin{pmatrix} I_1 & I_2 & I_3 & I_4 \end{pmatrix}^T, \tag{3.5.3}$$

[12]Which is an auxiliary state.

where I_j, for $j \in \{1,2,3,4\}$, is the intensity measurement at the interferometer[13] output corresponding to the respective POVM state $\{|\phi_1\rangle, |\phi_2\rangle, |\phi_3\rangle, |\phi_4\rangle\}$ and $I_t = \sum_{j=1}^{4} I_j$ is the total intensity across all four detectors. These four intensity measurements are just enough to reconstruct the polarisation structure of any input beam. Similar to Eqn. 3.4.2, we define the expectation value our POVM states as,

$$P_j = \langle\psi|\hat{\pi}_j|\psi\rangle, \tag{3.5.4}$$

where we can re-write the measurement probability as seen in Eqn. 3.4.4 in terms of the density operator and relate it to the normalised detector intensity I_j^N as,

$$P_j = \mathrm{Tr}\big(\hat{\pi}_j\hat{\rho}\big) = I_j^N. \tag{3.5.5}$$

Note that the intensity at each detector is normalised by the total intensity calculated from the sum of all intensities across all four detectors (i.e. $I_j^N = I_j / \sum_j I_j$). We can express the density operator in terms of the Stokes vector as follows [113],

$$\hat{\rho} = \frac{1}{2}\sum_{i=0}^{3} S_i\hat{\sigma}_i, \tag{3.5.6}$$

where $\hat{\sigma}_0 = \mathbb{I}$, is the 2×2 identity operator and $\hat{\sigma}_j$, for $j \in \{1,2,3\}$ are the Pauli matrices given by,

$$\hat{\sigma}_1 = \begin{pmatrix} 0 & 1 \\ 1 & 0 \end{pmatrix}, \quad \hat{\sigma}_2 = \begin{pmatrix} 0 & -i \\ i & 0 \end{pmatrix}, \quad \hat{\sigma}_3 = \begin{pmatrix} 1 & 0 \\ 0 & -1 \end{pmatrix}, \tag{3.5.7}$$

where $i = \sqrt{-1}$ is the imaginary number. Combining Eqn. 3.3.2 and the Pauli matrices from Eqn. 3.5.7 into Eqn. 3.5.6, we derive an expression for the density operator in terms of the normalised Stokes vectors,

$$\hat{\rho} = \frac{1}{2}\begin{pmatrix} 1+S_3^N & S_1^N - iS_2^N \\ S_1^N + iS_2^N & 1 - S_3^N, \end{pmatrix}, \tag{3.5.8}$$

and finally obtain the matrix relationship,

$$\mathbf{I}^N = \Pi \cdot \mathbf{S}^N, \tag{3.5.9}$$

where Π is a 4×4 matrix known as the ***instrumetation matrix*** [121][141]. By taking the inverse of the instrumentation matrix, we obtain an expression for the normalised Stokes vector $\mathbf{S}^N = \Pi^{-1}\cdot\mathbf{I}^N$, to calculate a spatially dependent Stokes value for every transverse position along the azimuthal profile $\mathbf{r}_\perp$, from the spatially dependent intensity images of the four POVM elements taken from our detector measurements. An example of an ideal instrumentation matrix for a loss-less polarimeter setup is,

[13]By definition, an interferometer is a technique of superimposing multiple beams into a single output, usually utilising a birefringent optical element. Interferometry is a core concept in this project and will be explored further in the next section when we discuss the experimental implementation of the POVM setup.

$$\Pi = \frac{1}{4}\begin{pmatrix} 1 & \sqrt{\frac{1}{3}} & \sqrt{\frac{2}{3}} & 0 \\ 1 & \sqrt{\frac{1}{3}} & -\sqrt{\frac{2}{3}} & 0 \\ 1 & -\sqrt{\frac{1}{3}} & 0 & -\sqrt{\frac{2}{3}} \\ 1 & -\sqrt{\frac{1}{3}} & 0 & \sqrt{\frac{2}{3}}, \end{pmatrix}, \tag{3.5.10}$$

where the row entries of the instrumentation matrix represent the Stokes vector of the individual POVM elements $|\phi_i\rangle$. In the next section, we demonstrate a possible experimental setup to realise this instrumentation matrix using a configuration of conventional optics and a Mach-Zehnder interferometer.

3.6 Experimental realisation

In this section, we demonstrate a possible experimental configuration for a spatially dependent POVM measurement system, as outlined in Fig. 3.3. The POVM measurements correspond to the homogeneous polarisation states in [121]; however, we introduce beams with spatially varying polarisation profiles as an input to our polarimeter.

Using the technique in [61], we generate different vector beams of the form given by Eqn. 3.3.3, using a digital micromirror device (DMD). A beam from a Helium-Neon laser (HeNe) is incident on a half-waveplate (HWP), diagonalising the beam polarisation, which is separated into the horizontal and vertical components with equal intensities via a Wollaston beam splitter (WBS). A telescope system (formed by L_1 and L_2) is then constructed to focus the two polarisation components onto the DMD chip, where a multiplexed hologram is loaded to generate the desired beam (see Section 2.5.1 for more information), independently shaping their phase and amplitude profiles. The DMD diffracts the incoming beam into different spatial modes, where the two spatially shaped polarisation components are superimposed in their first diffraction order and spatially selected via an iris. The iris is positioned in between another telescope system (formed by L_3 and L_4) that ensures the output beam leaving the DMD is both collimated and magnified accordingly (see panel with green border in Fig. 3.3). In the setup, we introduce a flip mirror (FM), which directs the beam into either our POVM tomography setup or a conventional Stokes polarimetry configuration, as indicated by the panel with the blue and red borders in Fig. 3.3, respectively. Note that throughout the experiment, we make use of gold-plated mirrors instead of coated dielectric mirrors to minimise any unwanted polarisation changes after reflection. Following the description in [116], we perform full Stokes tomography via a sequence of intensity measurements of the beam's azimuthal profile $I_i(\mathbf{r}_\perp)$, where $i \in \{H, V, D, A, R, L\}$, using a rotating quarter waveplate (QWP) and half waveplate (HWP) and a static Polariser[14] (Pol) and recording the beam image with a CMOS camera (Thorlabs DCC1645C). More information on Stokes tomography can be found in Section 1.4. The purpose of the Stokes measurements is to provide a measure of the performance of our POVM setup.

[14] A polarising beam splitter can also be used instead.

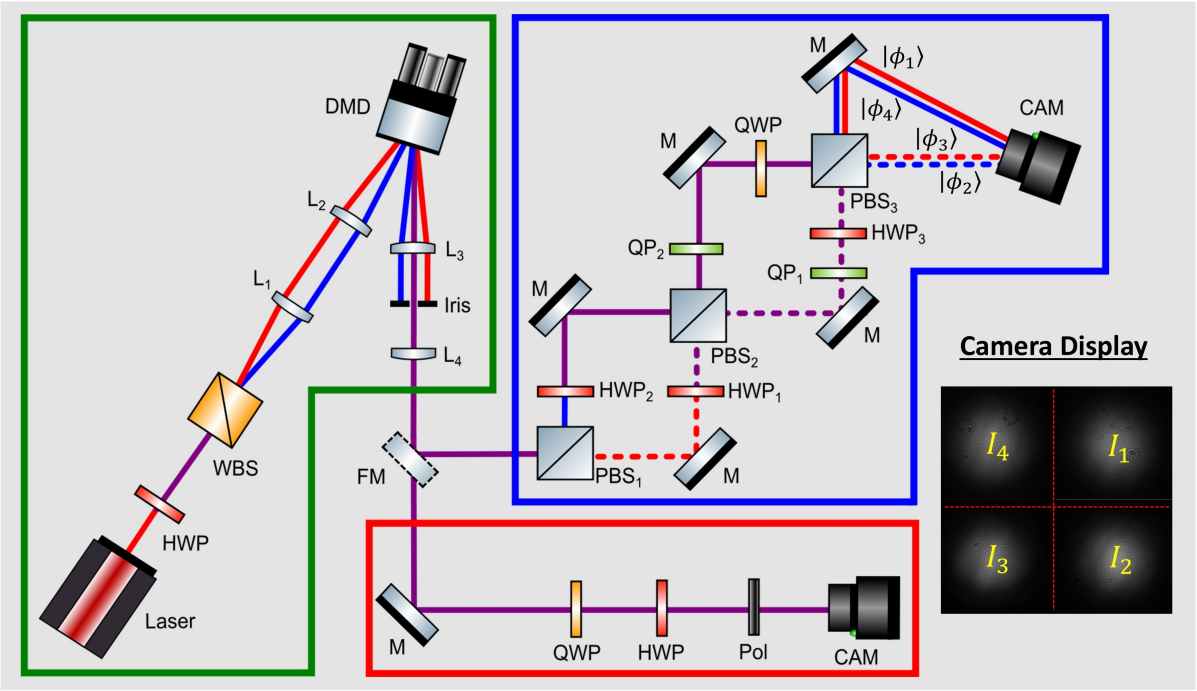

Figure 3.3: The experimental setup for our spatially dependent POVM tomography. The beam colours indicate different polarisations, where $\hat{H}$ is red, $\hat{V}$ is blue, and purple is some mixed state of the two. We denote the interferometer arms between PBS_1 and PBS_3 by the dashed and solid lines indicating the paths α and β, respectively. The setups consist of half waveplates (HWP), quarter waveplates (QWP), quartz plates (QP), a polariser (Pol), lenses (L), polarising beam splitters (PBS), a Wollaston beam splitter (WBS), mirrors (M), and a flip mirror (FM). The inset is the displayed camera image with the four quadrants of the POVM measurements. We note the camera incident angle of states $|\phi_1\rangle$ and $|\phi_4\rangle$ is exaggerated for clarity and is around 0.1 radians in reality.

Recall that the state entering our POVM measuring scheme, given by Eqn. 3.3.3 is entering our polarimeter through the path labelled α as illustrated in Fig. 3.2, giving the following extension state,

$$|\psi\rangle \otimes |k_\alpha\rangle = (|u_H\rangle|H\rangle + e^{i\phi}|u_V\rangle|V\rangle) \otimes |k_\alpha\rangle. \tag{3.6.1}$$

Here we will summarise how we experimentally implement the ideal instrumentation matrix denoted by Eqn. 3.5.10. The first polarising beam splitter (PBS_1 from Fig. 3.3) sends the horizontally or vertically polarised light along the path α or β, correlating the transverse spatial and polarisation degrees of freedom to the degree of freedom along the longitudinal path, $|u_H\rangle \otimes |H\rangle \otimes |k_\alpha\rangle + e^{i\phi}|u_V\rangle \otimes |V\rangle \otimes |k_\beta\rangle$, emphasising the implementation of the required Naimark extension. Note that the current state has the form of a Greenberger-Horne-Zeilinger (GHZ) state [142], where our classical state is correlated across the three degrees of freedom, namely polarisation, spatial (phase and intensity), and path. The beam then propagates through a Mach-Zehnder interferometer, containing the half waveplates HWP_1 and HWP_2, in the two arms, followed by PBS_2. These waveplates control the polarisation ratio of $\hat{H} : \hat{V}$ in both arms, forming what is known as a partially polarising beam splitter (PPBS) [121][143] (see Fig. 3.4a). A PPBS is an unusual optical element that Sebastião Pádua jokingly described as a bad PBS; however, when compared to commercially available optics, he is not entirely wrong. A PPBS works by transmitting a specific percentage of the incident horizontally polarised light T_H while reflecting the remainder of the horizontal beam R_H. The same is also true for a vertically polarised beam, where we describe the

transmission and reflection ratios by T_V and R_V, respectively (see Fig. 3.4b). Generally, there is an underlying symmetry given by $T_H = R_V$ and $R_H = T_V$. In our system, these ratios are given by a and b from Eqns. 3.5.2. The state transformation induced by the waveplates (HWP_1, HWP_2, HWP_3, and the QWP) in the extended basis system $\{|H\rangle \otimes |k_\mu\rangle, |V\rangle \otimes |k_\mu\rangle\}$, for $\mu = \alpha, \beta$, can be expressed as,

$$\begin{aligned}
|H\rangle \otimes |k_\alpha\rangle &\longrightarrow \left[-\frac{ia}{\sqrt{2}}(|H\rangle + |V\rangle) \otimes |k_\alpha\rangle - \frac{ib}{\sqrt{2}}(|H\rangle - i|V\rangle) \otimes |k_\beta\rangle\right] e^{i\phi_\alpha} \\
|V\rangle \otimes |k_\alpha\rangle &\longrightarrow \left[\frac{ib}{\sqrt{2}}(|H\rangle - |V\rangle) \otimes |k_\alpha\rangle - \frac{a}{\sqrt{2}}(|H\rangle + i|V\rangle) \otimes |k_\beta\rangle\right] e^{i\phi_\beta} \\
|H\rangle \otimes |k_\beta\rangle &\longrightarrow \left[\frac{a}{\sqrt{2}}(|H\rangle - |V\rangle) \otimes |k_\alpha\rangle + \frac{b}{\sqrt{2}}(-i|H\rangle + |V\rangle) \otimes |k_\beta\rangle\right] e^{i\phi_\beta} \\
|V\rangle \otimes |k_\beta\rangle &\longrightarrow \left[-\frac{b}{\sqrt{2}}(|H\rangle + |V\rangle) \otimes |k_\alpha\rangle + \frac{a}{\sqrt{2}}(|H\rangle - i|V\rangle) \otimes |k_\beta\rangle\right] e^{i\phi_\alpha},
\end{aligned} \tag{3.6.2}$$

where the rotation angles θ_j of HWP_j for $(j = 1, 2)$ are set such that $a = \sin 2\theta_1 = 2\cos 2\theta_2$ and $b = \sin 2\theta_2 = 2\cos 2\theta_1$, where a and b are the same coefficients in Eqn. 3.5.2. Effectively, the ratio of the two polarisation component amplitudes $\hat{H} : \hat{V}$ becomes $a : b$ along the path α and along the path β they take the form $b : a$, which is experimentally confirmed via power metre measurements of the beam intensity ratios.

Prior to the beam leaving PBS_3, a change in the polarisation components is experienced to generate the POVM states via rotation of the set optics[15]. The fast axis of HWP_3 along path α is rotated by 67.5° with respect to the polarisation direction along the horizontal, preparing the states $|\phi_1\rangle$ and $|\phi_2\rangle$. Meanwhile, the fast axis of the QWP in path β is set to 45°, preparing the $|\phi_3\rangle$ and $|\phi_4\rangle$ states. The phase terms ϕ_μ, for $(\mu = \alpha, \beta)$ expressed in Eqn. 3.6.2, are a consequence of the optical path length experiences by the beam from the two arms of the Mach-Zehnder interferometer. We use a set of quartz plates, QP_1 and QP_2, tilted along their vertical axis to independently cancel the phase difference experienced by the beam. These plates play a key role in calibrating our system and will be further discussed next.

Once the beams reach PBS_3, the projection measurement is performed, as indicated in Fig. 3.2 by P, separating the states $|\phi_1\rangle$ and $|\phi_2\rangle$ from path α and $|\phi_3\rangle$ and $|\phi_4\rangle$ coming from path β. We use an additional mirror to redirect the states emerging from PBS_3 (as shown in Fig. 3.3) to obtain a single-shot image of the

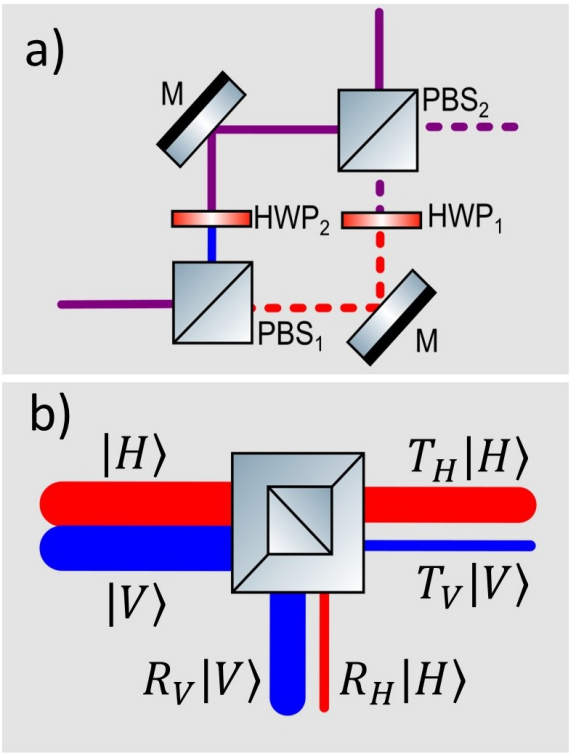

Figure 3.4: Partially polarising beam splitters (PPBS). a) Our experimental implementation of a PPBS. b) A PPBS intensity splitting ratio, depicted by the line thickness. Here T_j and R_j for $j \in \{H, V\}$ are the transmission and reflection ratios for the horizontal (red) and vertical (blue) polarisation structures. Note that purple represents a superposition of the two.

[15]Note that PBS_3 does not act as the closure of another interferometer but is used for convenience to split both components along the α and β paths independently into their $\hat{H}$ and $\hat{V}$ components.

intensity profile of the POVM elements in different quadrants of the CMOS camera, as demonstrated in the inset of Fig. 3.3. We confirm that Eqns. 3.6.2 experience the unitary transformation identical to the required unitary transformation matrix U expressed in Fig. 3.2, where further detail is given in Appendix A.

To obtain a quantitative assessment of our POVM tomograpy, we compare the ideal instrumentation matrix from Eqn. 3.5.10 with an experimental instrumentation matrix calculated from our system. Recall that the instrumentation matrix links the normalised intensities $\mathbf{I}^N$ measured by our detector with the normalised Stokes vector $\mathbf{S}^N$ of the input beam, as shown in Eqn. 3.5.9. By inverting this equation, we obtain an expression of the instrumentation matrix Π, which we can use to determine the behaviour of our POVM system[16]. The simplest way to do so, is to record the intensities $\mathbf{I}^N$ of the generated POVM elements as the input states, passing through our POVM measurement system[17], as illustrated in the top row of Fig. 3.5. Any changes experienced by the input beam as it propagates through our setup will be reflected as minor deviations in the value of the experimental instrumentation matrix Π_{exp}, in comparison to the ideal matrix presented by Eqn. 3.5.10. One such matrix is given by,

$$\Pi_{exp} = \frac{1}{4}\begin{pmatrix} 1.05 & 0.77\sqrt{\frac{1}{3}} & 1.10\sqrt{\frac{2}{3}} & 0.05 \\ 1.02 & 1.21\sqrt{\frac{1}{3}} & -0.88\sqrt{\frac{2}{3}} & -0.04 \\ 1.06 & -1.24\sqrt{\frac{1}{3}} & -0.01 & -0.93\sqrt{\frac{2}{3}} \\ 0.88 & -0.74\sqrt{\frac{1}{3}} & -0.03 & 0.89\sqrt{\frac{2}{3}}, \end{pmatrix}. \tag{3.6.3}$$

Here we implement a notation highlighting the deviation of the experimental values from the values of the ideal instrument matrix. The blue shading represents values expected to be 1, while the red shading represents values that should be 0 when compared to the ideal case of the instrument matrix Π from Eqn. 3.5.10. Note that as long as the instrument matrix allows an invertible mapping from the POVM elements to the parameterised states via the Stokes vectors, then tomography can be performed. We attribute the deviations recorded from the experimental instrument matrix as consequences of the system calibration, where a well-calibrated system is expected to produce a more ideal instrument matrix. Below we discuss a method to optimise our experimental configuration.

3.6.1 Polarimeter calibration

A crucial step prior to running the experiment is to calibrate the interferometer. This important step helps eliminate any unwanted phase shifts with the use of the quartz plates, QP_1 and QP_2. We follow the same technique demonstrated in [121], where a number of homogenously polarised beams are utilised for the calibration. However, unlike vector beams, homogenously polarised beams are smaller by construction. Therefore, to achieve a stable interferometric configuration, phase shift cancellation across the extended beam profile is required, which significantly increases

[16]Calculating the experimental instrumentation matrix requires 16 entries. A minimum of four input beams are needed, where we represent their Stokes vectors as columns in a 4×4 Stokes matrix. Similarly, the intensities measured from our POVM polarimeter are also written in terms of a 4×4 intensity matrix. These two matrices are used to calculate the experimental instrument matrix.

[17]Note these intensity measurements are derived from global values, averaged over the intensity across the whole camera. However given the homogeneity of the beam profiles, a photodiode could be used to obtain these intensity measurements.

the experimental difficulty[18]. A prominent disadvantage of the Mach-Zehnder interferometer is its sensitivity to independent phase shifts across the two arms, resulting in mandatory frequent realignment of the system. This prompted calibration measurements to be performed prior to and after data runs to ensure continued stability.

Using our DMD setup with a suitable set of multiplexed holograms, we are able to generate the homogeneously polarised POVM states $|\phi_i\rangle$ described in Eqns. 3.5.2, along with a set of orthogonal states $|\overline{\phi_i}\rangle$ to our POVM elements,

$$\begin{aligned} |\overline{\phi_1}\rangle &= b|H\rangle - a|V\rangle, & |\overline{\phi_2}\rangle &= b|H\rangle + a|V\rangle, \\ |\overline{\phi_3}\rangle &= a|H\rangle - ib|V\rangle, & |\overline{\phi_4}\rangle &= a|H\rangle + ib|V\rangle. \end{aligned} \tag{3.6.4}$$

A perfectly calibrated system should display no intensity, $I_i = 0$ for the respective orthogonal state $|\overline{\phi_i}\rangle$, for $i \in \{1, 2, 3, 4\}$ in the measurement channel corresponding to ϕ_i, while maintaining an equal intensity distribution among all other quadrants on the camera. Conversely, light prepared in the POVM state $|\phi_i\rangle$ will display maximum intensity in the corresponding detector quadrant I_i, as the state is projected onto itself, while a lower but equal intensity is expected for all other POVM element projections. This expected uniform intensity distribution among the other POVM elements is an interesting consequence of the required equidistant formalism of the POVM basis vectors described in the previous section[19]. We adjust both QP_1 and QP_2 iteratively while generating the orthogonal states to achieve the desired calibration. Fig. 3.5 shows an experimental measurement after system calibration of the POVM $|\phi_i\rangle$ and orthogonal $|\overline{\phi_i}\rangle$ states, conforming to the desired outcome, however displaying a small discrepancy in the equal intensity distribution expected from a perfectly calibrated polarimeter, indicating some phase imbalances are still present in our system.

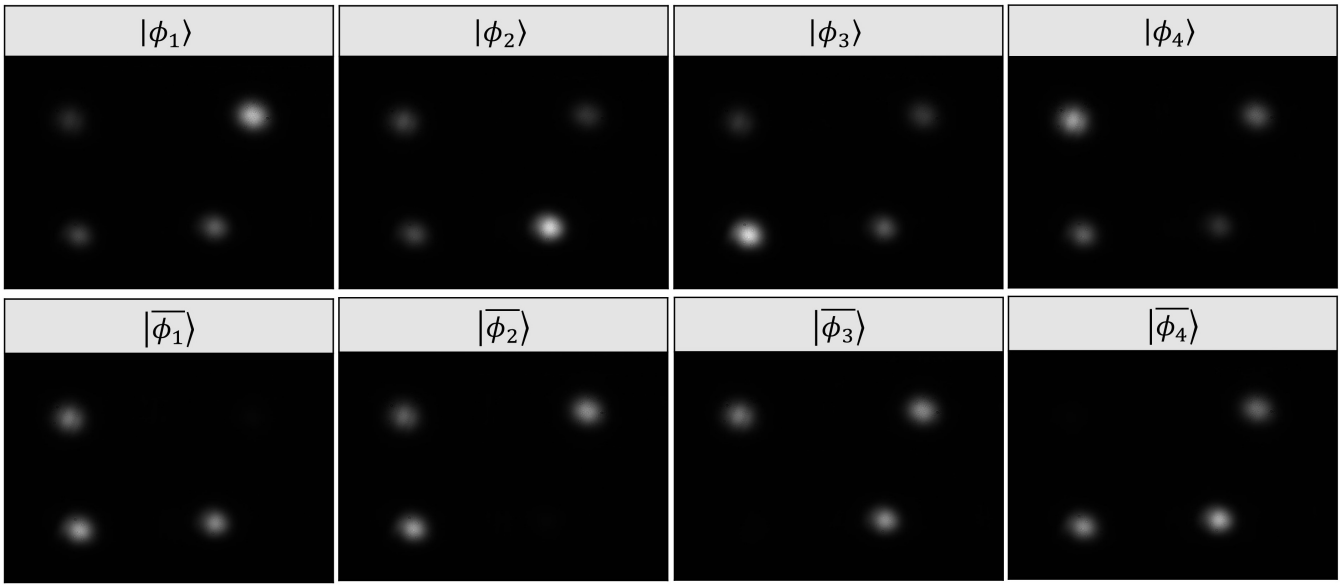

Figure 3.5: Intensity images I_i, for $I_i \in \{1, 2, 3, 4\}$ taken with a camera of the generated POVM states $|\phi_i\rangle$ and their orthogonal states $|\overline{\phi_i}\rangle$ used for calibration of the POVM setup.

[18] Our test beams have been expanded to the desired resolution by the DMD and although their size can be adjusted to match the waist of the homogeneous beams, this comes at a cost of resolution loss. However the real problem is that transverse coherence of the beam profile is more important for the correct identification of spatially resolved beams, making our system sensitive to transverse dephasing effects (i.e. different parts of the beam propagating at different lengths) that are not seen in homogeneous beams.

[19] For the POVM measurement system, this is the definition of unbiased state reconstruction.

Note that the discrepancy between the calculated instrumentation matrix from Eqn. 3.6.3 and the theoretical case presented in Eqn. 3.5.10, factoring in system calibration, implies the experimental setup is projecting onto slightly different POVM elements than the desired MIC-POVM states $|\phi_i\rangle$.

The susceptible nature of the Mach-Zehnder interferometers to vibrational noise makes active phase compensation difficult to maintain during the data collection process. We assume the imperfect phase shift between the two arms of the interferometer contributes to the primary source of error in the deviation of our experimental instrument matrix values. However, we can attribute the imbalance in optical activity along the beam paths or any inhomogeneity along the azimuthal beam profile as potential sources of errors to consider. The effect of the latter is evaluated by considering a spatially resolved experimental instrumentation matrix $\Pi(r_\perp)$ for superpixel segments of the transverse position of the POVM intensity images[20]. The average for such a matrix is given by,

$$\Pi(r_\perp) = \frac{1}{4}\begin{pmatrix} 1.27 & 0.82\sqrt{\frac{1}{3}} & 0.98\sqrt{\frac{2}{3}} & 0.24 \\ 0.99 & 0.87\sqrt{\frac{1}{3}} & -0.81\sqrt{\frac{2}{3}} & -0.12 \\ 0.76 & -0.95\sqrt{\frac{1}{3}} & -0.07 & -0.66\sqrt{\frac{2}{3}} \\ 0.98 & -0.74\sqrt{\frac{1}{3}} & -0.07 & 0.78\sqrt{\frac{2}{3}}, \end{pmatrix}. \tag{3.6.5}$$

Overall, this instrument matrix possessed some entries that were nearer to the ideal matrix value; however, there were more entries that deviated from the theoretical instrument matrix Π when compared to the experimental matrix Π_{exp} calculated in Eqn. 3.6.3. Once again, the blue-shaded numbers are expected to be 1, while the red-shaded numbers are expected to be 0 when compared to the ideal instrument matrix Π from Eqn. 3.5.10. Even after the beam images are cropped accordingly, a large number of dark pixels still remain where we calculate the instrumentation matrix before averaging. This potentially serves as a significant source of error in the final averaged matrix. Since calculating the matrix from Eqn. 3.6.5 is computationally taxing and provides no improvements to the measurement fidelity, we opt to use the experimental instrument matrix from Eqn. 3.6.3 to assess the performance of our POVM setup instead.

3.7 Results and performance analysis

We assess the capabilities of our POVM system for a number of generated vector beams, given in their general form by Eqn. 3.3.3. The following are the beams we consider,

[20] When dividing an image into smaller segments, a mean pixel value is calculated for each segment, representing the collection of pixels, forming what is known as a superpixel. The size of these superpixels can be anything; however, throughout our work, we employ square superpixels of dimensions $n \times n$. For example, if we segment a 1000×1000 image into a collection of 4×4 superpixels, we end up with a 250×250 image. This method can significantly boost processing speed, however, at the cost of resolution.

$$
\begin{aligned}
|\psi_1\rangle &= |\mathrm{HG}_{1,0}\rangle|H\rangle + |\mathrm{HG}_{0,1}\rangle|V\rangle \\
|\psi_2\rangle &= |\mathrm{HG}_{0,2}\rangle|H\rangle + |\mathrm{HG}_{2,0}\rangle|V\rangle \\
|\psi_3\rangle &= |\mathrm{LG}_1^0\rangle|H\rangle + |\mathrm{LG}_0^2\rangle|V\rangle \\
|\psi_4\rangle &= |\mathrm{HG}_{0,1}\rangle|H\rangle - |\mathrm{HG}_{1,0}\rangle|V\rangle \\
|\psi_5\rangle &= |\mathrm{LG}_1^0\rangle|H\rangle + |\mathrm{LG}_0^1\rangle|V\rangle,
\end{aligned}
\tag{3.7.1}
$$

where $|\mathrm{HG}_{n,m}\rangle$ are Hermite-Gaussian (HG) modes with their horizontal and vertical modes given by the indices n and m, respectively, while $|\mathrm{LG}_p^l\rangle$ describes a Laguerre-Gaussian (LG) mode with radial mode number p and the azimuthal mode number given by l (see Section 1.5.3 for more information). The spatial intensity profile of these vector beams can be found in Fig. 3.6 and Fig. 3.7 respectively.

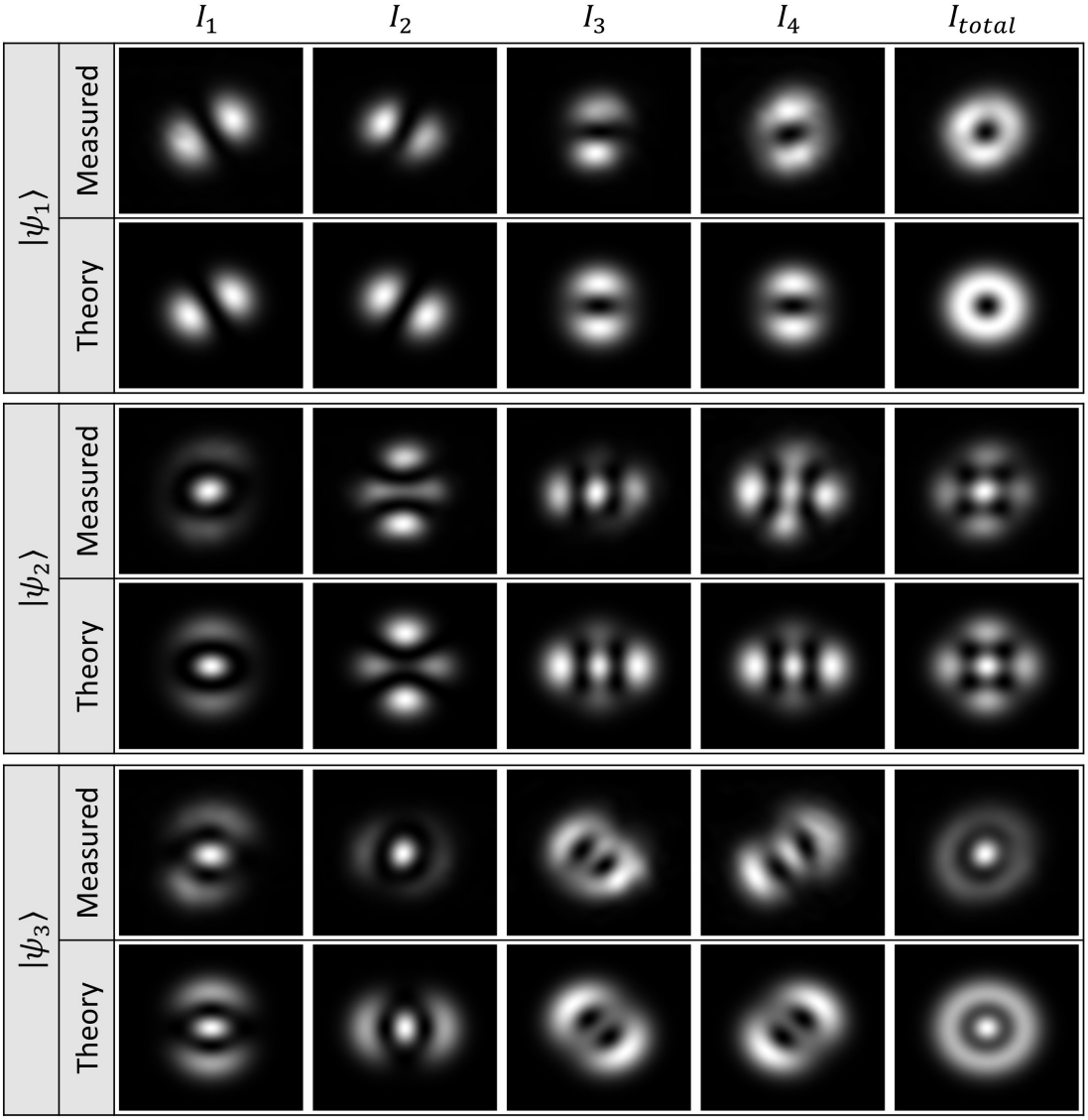

Figure 3.6: The total intensity and measurements of the POVM states of the three test beams $|\psi_1\rangle$, $|\psi_2\rangle$ and $|\psi_3\rangle$.

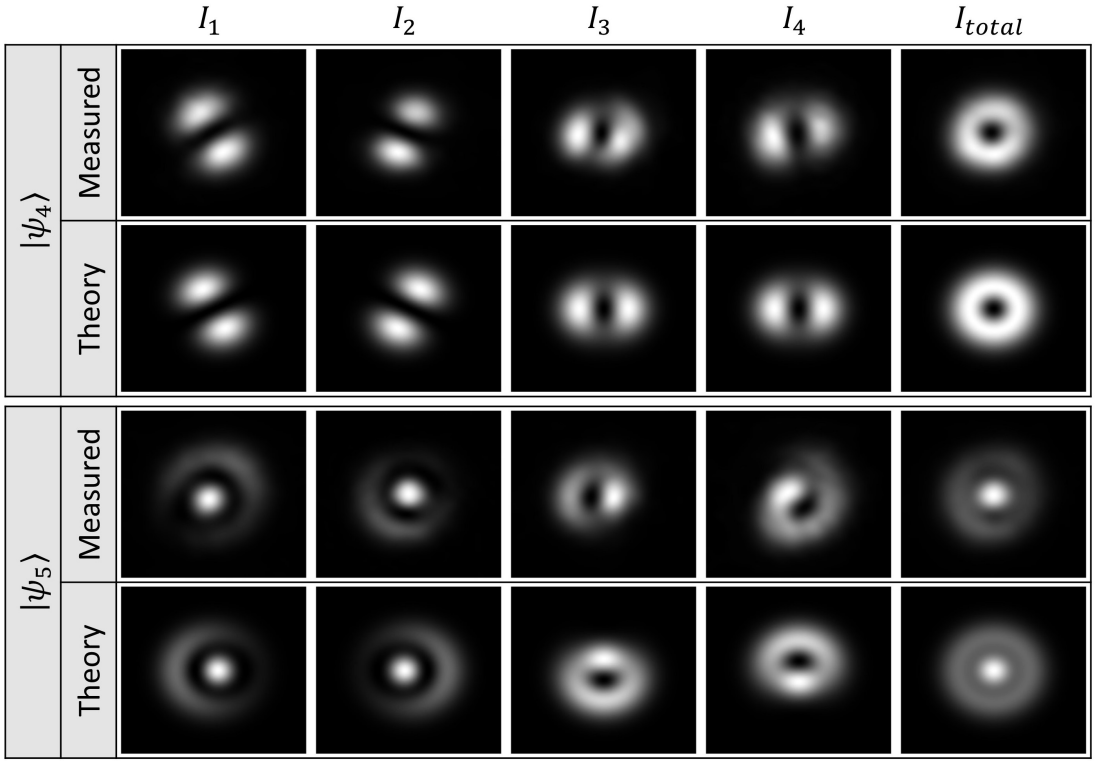

Figure 3.7: The total intensity and measurements of the POVM states of the two remaining test beams $|\psi_4\rangle$ and $|\psi_5\rangle$.

To better quantify the behaviour of our system, we employ a range of vector beams with different polarisation structures and spatial profiles. Initially, we chose two vector beams with radial and azimuthal polarisation structures (i.e. $|\psi_1\rangle$ and $|\psi_4\rangle$ respectively) to quantify the behaviour of our system, since these beams are typically involved in the interferometer calibration process[21].

These beams possess the most basic vector structure possible to generate and are well understood, making them ideal first beams to test our single-shot polarimeter with. The other beams possess a slightly more complex polarisation structure. For instance, the beam given by $|\psi_2\rangle$ is made of two overlapped orthogonal second-order HG modes, resulting in a unique cross-like pattern, while $|\psi_3\rangle$ and $|\psi_5\rangle$ are both Poincaré beams possessing all possible polarisations in their spatial profile. The complexity of their spatial and polarisation structures should provide useful insight into our system's behaviour. However, since higher-order vector beams possess a larger spatial profile, we were limited to lower-order test beams as a consequence of the small chip of our detector. For this reason, we test our polarimeter with vector modes up to the second order only. Given that the two beams $|\psi_1\rangle$ and $|\psi_4\rangle$ exhibit very similar characteristics (see Fig. 3.6 and Fig. 3.7), we opted to exclude $|\psi_4\rangle$ from any further investigation since it provides no additional insight into our system.

Recall from section 1.5.3 that the mode number of LG beams is given by $N = |l| + 2p$. Using this relation, we calculate the LG mode numbers for the horizontal and vertical components of our test beam $|\psi_5\rangle$ to equal 2 and 1, respectively. This discrepancy in mode numbers produces different Gouy phases (more information in Section 1.5.4) for the two beam components, resulting in a

[21] We have to ensure the light from the two interferometer arms is overlapping properly. When generating one of these beams and passing them through our interferometer, they split into their two $|H\rangle$ and $|V\rangle$ components, with a spatial profile resembling first-order HG modes. By ensuring the two HG modes remain superimposed throughout propagation for a distance of around $1.5\text{m} - 2\text{m}$ (roughly comparable to the interferometer path length). Only then do we consider our interferometer to be calibrated.

variable intensity profile throughout beam propagation, as shown in the comparison between the measured and theoretical intensities of $|\psi_5\rangle$ in Fig. 3.7. Such a quantity is difficult to accurately take into consideration when attempting to develop a solid understanding of our experimental system and quantify the accuracy of the POVM tomography reconstruction. For this reason, we choose to ignore this beam and any others with different mode numbers between the two polarisation components[22].

A vital step in assessing the performance of our POVM tomography technique is differentiating between any errors that occur in our setup as a result of the beam generation process and any as a consequence of the detection system. All of the intensity images obtained from our single-shot polarimeter, displayed in the first rows of Fig. 3.6 for the beams described by Eqn. 3.7.1, recorded in the four quadrants of the CMOS camera as demonstrated in the inset of Fig. 3.3 undergo a background subtraction to account for ambient noise, obtained by calculating an average light level over a small section of the camera far from the incident beam. Additionally, we attempt to identify the centres of the four beam components using moment analysis and remove any unwanted noise via a low-pass Fourier filter. We overlap the intensities of the four POVM components to generate the total intensity distribution (last column of Fig. 3.6), serving as a control measure to ensure proper overlap of the individual POVM intensity profiles. Generally, we find a good quantitative agreement between the experimental intensity measurements (top row) and the theoretically predicted intensity patterns displayed (bottom row) in Fig. 3.6.

By using the measured intensity information, we are able to reconstruct the spatially varying Stokes vectors by inverting Eqn. 3.5.9 and using the experimental instrument matrix from Eqn. 3.6.3 for any vector beam. Although homegeneously polarised beams exhibit near-perfect generation accuracy, unfortunately, this does not extend to complex polarisation structures. There may exist intrinsic uncertainties in the generation process of vector beams, causing slight deviations of the generated polarisation profile from the desired and expected polarisation pattern[23]. To quantify the accuracy of the measurement process, we compare POVM tomography with conventional six-measurement Stokes tomography (see Fig. 3.3). For the beams in Eqn. 3.7.1, we generate polarisation plots modulated by beam intensity to verify our POVM tomography, comparing them to theoretically simulated polarisation patterns and those from Stokes measurements. These patterns are displayed in Fig. 3.8 below.

[22] When attempting to understand a new experiment, it is best to keep things simple by removing as many variables as possible. In our case, the Gouy phase added an additional layer of complexity to the system, which would require the precise imaging of the beam generation plane to the imaging plane to account for the rotation of the various Gaussian modes caused by different propagation lengths between the two interferometer arms. This increased complexity would have to be considered for a commercial system; however, for a proof of principal device like our own, it was best to ignore for the time being.

[23] Although any homogeneous beam of arbitrary polarisation can be generated by three commercial polarisation optics (HWP, QWP and a polariser), our beam generation system comprises diffraction of a multiplexed hologram on a DMD with finite resolution, and spatial filtering of the desired order (see Section 2.5.1 for more information). Even in our group, which is internationally leading.

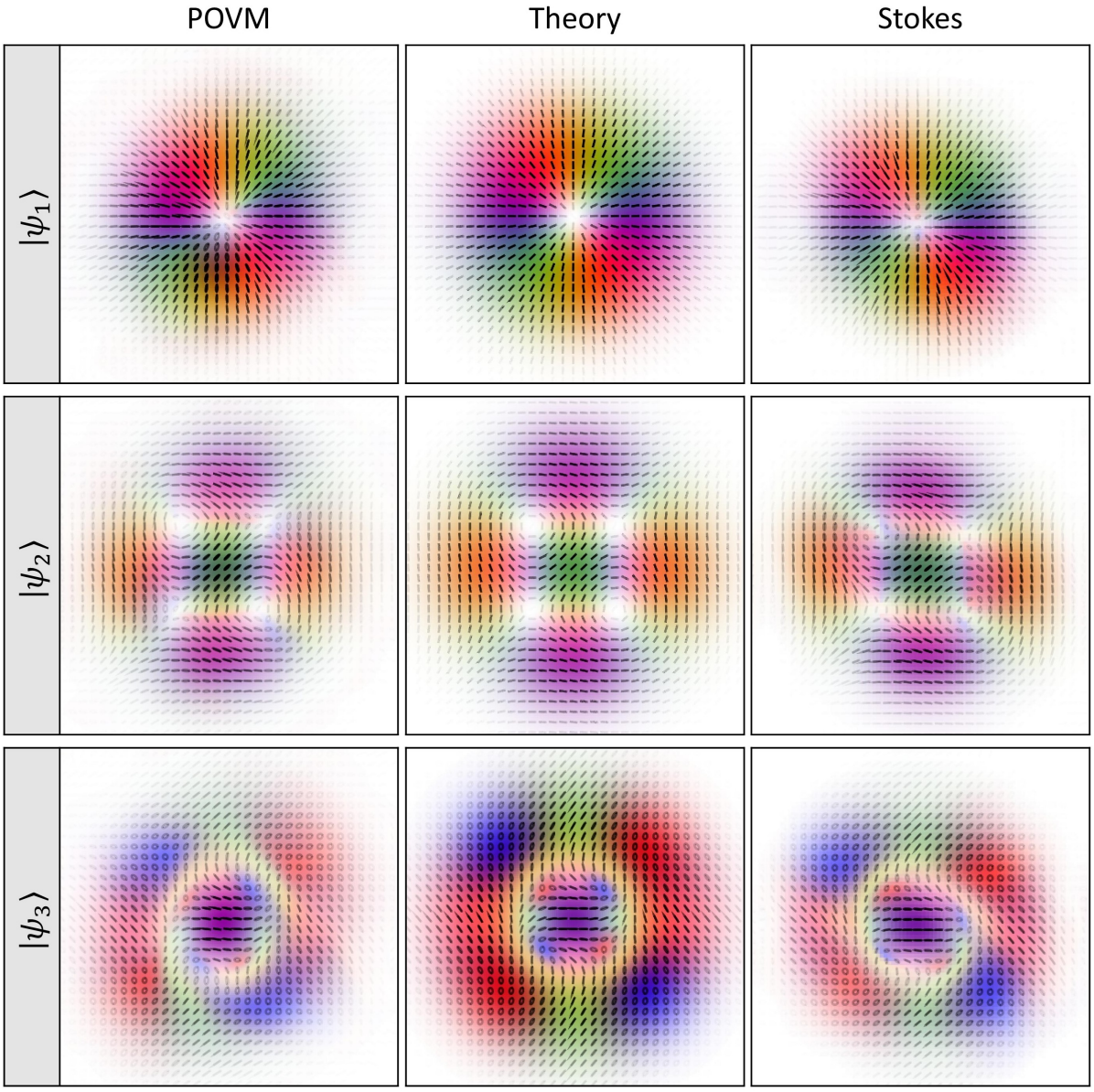

Figure 3.8: Polarisation state reconstruction of the test beams $|\psi_1\rangle$, $|\psi_2\rangle$, and $|\psi_3\rangle$ with POVM tomography (left), theoretical simulation (middle), and Stokes tomography (right). We use the same colour scheme indicated by the inset of Fig. 3.1 to characterise the polarisation profile and beam opacity for intensity distribution.

From the polarisation plots in Fig. 3.8, we can deduce the structure of the generated beams from Eqn. 3.7.1. We can see the first beam $|\psi_1\rangle$ has a radial polarisation structure, the second beam $|\psi_2\rangle$ is a non-radial symmetric beam with a four-fold symmetric pattern analogous to a clover, and the last beam $|\psi_3\rangle$ is a form of a Poincaré beam with all possible polarisations, carrying a net orbital angular momentum (OAM) of $1\hbar$ per photon, generated from different LG modes along the horizontal and vertical polarisation components.

Overall, we find an accurate reconstruction of the input states; however, there are some distortions affecting the fidelity as a consequence of the preparation process. We elaborate on the source of the observed distortion towards the end of this section. To quantify the accuracy of our reconstructed beams, we calculate a spatially resolved angular accuracy δ [144], providing a measure of the angular deviation of the polarisation states on the Poincaré sphere. The angular accuracy is given by,

$$\delta = \cos^{-1}\left(\frac{\mathbf{S}_{123}\cdot\mathbf{S}'_{123}}{|\mathbf{S}_{123}||\mathbf{S}'_{123}|}\right), \tag{3.7.2}$$

where $\mathbf{S}_{123} = (S_1^N, S_2^N, S_3^N)^T$ and $\mathbf{S}'_{123} = (S_1'^N, S_2'^N, S_3'^N)^T$ are the reduced Stokes vectors of the different beam reconstruction methods. Eqn. 3.7.2 provides a quantitative measure in terms of an angular value depicting the difference in the angle between the ellipse of the polarisation plots being compared, where a deviation angle of $\delta = 0°$ indicates perfect polarisation state reconstruction while an angle of $\delta = 180°$ indicates comparison of orthogonal states. We note that $\delta = \phi$ denotes a rotation in linear polarisation of $\phi/2$ as expected from the Poincaré sphere. We perform a pairwise comparison between POVM tomography, theoretical approximation, and Stokes tomography for our test beams from Eqn. 3.7.1 and present the results in Fig. 3.9, where we define an intensity-weighted angular accuracy, averaged over the entire beam structure, denoted by Δ.

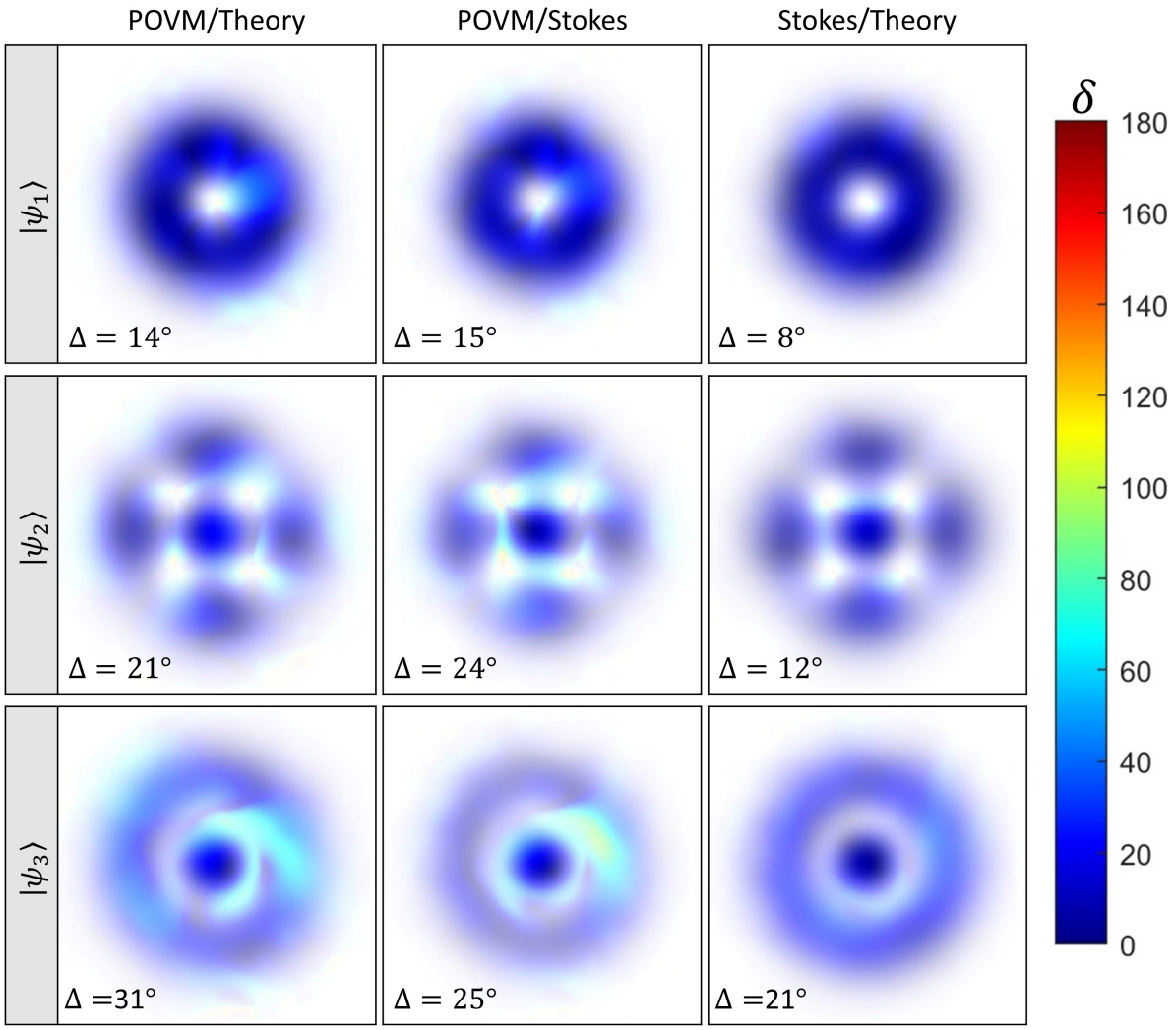

Figure 3.9: Quantitative evaluation of the angular accuracy δ, comparing the polarisation profiles of POVM tomography, Stokes tomography, and theory for the three test beams from Eqn. 3.7.1 in a pairwise fashion. Blue indicates strong agreement, while red indicates angular discrepancies in the ellipse orientations. Here Δ represents an intensity-weighted angular accuracy averaged over the entire beam profile.

From Fig. 3.9, we generally observe that large regions of angular deviation usually correspond

to regions of lower beam intensity, where noise is more prevalent and difficult to eliminate. We note that [121] offers a method to calculate the fidelity, first introduced by Uhlmann in 1976 [145] that measures the closeness between two quantum states μ and ν in terms of their density operators as $F(\mu,\nu) = [\mathrm{Tr}\left(\sqrt{\sqrt{\rho_\mu}\rho_\nu\sqrt{\rho_\mu}}\right)]^2$ [146]. However, due to the complex polarisation structure of our test beams, we use the angular accuracy as a more suitable method of detecting polarisation variations in our data to evaluate any uncertainties arising from the generation and detection processes.

Our analysis confirms that indeed, POVM tomography allows the reconstruction of input polarisation states from a minimal number of measurements, but with a slightly reduced accuracy when compared to Stokes tomography. The overcomplete nature of Stokes tomography provides additional information that serves to reduce the error in the reconstruction process and, when coupled with the complex experimental structure of the POVM setup, provides an overall indication for the discrepancy in accuracy between the two methods.

The discrepancies between Stokes tomography and the theoretically generated polarisation profiles arise from potential errors in both the beam generation and measurement processes, an example of which could be misalignment in the overlapped polarisation components emerging from the DMD. Additionally, the rotating waveplates used to perform Stokes measurements (see Section 1.4) could very well have been miscalibrated from prolonged use[24]. We expect any errors arising from the beam preparation process to affect our POVM measurements as well; however, we express that the main experimental challenge was the required compensation for the two Mach-Zehnder interferometer arms using the quartz plates QP_1 and QP_2, along the entire beam profile. As stated previously, the POVM setup is more complex, with much longer beam paths and far more optical elements in use, each with a tendency to affect the polarisation structure of our generated beams in undesired ways prior to the projection measurement. Finally, we generate our beams using holograms displayed on a DMD with homogeneously polarised test beams, confirming the polarisation structure with Stokes tomography before aligning our POVM system. Unfortunately, this method favours Stokes tomography in the alignment process, where we are able to adjust for any polarisation changes to the Stokes measurement system along the beam path but not the POVM polarimeter.

3.8 Conclusion

Our obtained results serve as a proof of principle that an experimental realisation of a system capable of arbitrary vector beam characterisation with a single-shot measurement is indeed possible. The slightly larger deviations in the polarisation pattern throughout propagation are mainly attributed to the lack of stability in the interferometer setup, which necessitates a need for recalibration between measurements, affecting the experimental accuracy of our POVM tomography. These stability issues with the interferometer were addressed in subsequent works when the Mach-Zehnder interferometer was replaced in favour of the more stable Sagnac configuration, which will be discussed in the following section. However, these variations in the polarisation profile were also observed for the simple Stokes tomography setup, becoming more noticeable for beams with a far more complicated polarisation structure (see Fig. 3.9). Interestingly, aberrations due to transverse phase variations acquired from propagation through optical elements and Gouy phase do not affect the overall topology of the beam, ensuring polarisation structure redistribution across the beam profile[25]. An investigation focused on vector quality [147] and optical skyrmion number [82] to

[24] As a consequence of gear backlash (see Section 1.4).

[25] By topology we mean topological charge, a conserved quantity related to the azimuthal phase index l as a consequence of helical phase fronts (more information in Section 1.5.3).

ensure invariance of the vector structure of the light as a consequence of the introduced aberrations and dephasing might be intriguing. Additionally, in future work, there is an interest in replacing the spatially resolved detection method with projection onto pre-determined spatial modes, enabling the experiment to run in the quantum regime with far greater efficiency utilising single photon detectors rather than a CMOS camera. Alternatively, we could explore potential integrated optics implementations of POVM state tomography using unique patterns imprinted onto silicon-based metasurfaces for polarimetry [148]. These systems could prove beneficial in reducing errors in input state beam reconstruction and potentially pave the road to the early stages of commercial realisation of a POVM tomography polarimeter.

3.9 Subsequent work

Previously, we proved our setup is capable of input beam reconstruction for complex polarisation structures, with some tolerated errors in the reconstruction accuracy as a consequence of introduced aberrations or potential misalignment throughout the optical system. During the experiment, we experienced difficulties maintaining the stability of the system, which required frequent calibrating of the POVM polarimeter due to the susceptible nature of the Mach-Zehnder interferometer to vibration noise. This caused noticeable misalignment in the beam profile after a moderate period of time, which was detected by our calibration technique. In this section, we briefly discuss our work published in [149], spearheaded by Amy McWilliam, that sees the reconstruction of the polarimeter setup replacing the Mach-Zehnder interferometer with a path-displaced Sagnac interferometer inspired by [143], offering a significant increase in common path noise reduction and thereby improving the stability of the experiment[26].

Many of the working concepts shown in Fig. 3.10 remain the same as in our previous work [71][27]. As the beam enters the Sagnac interferometer, it is once again split into its vertical and horizontal components by a PBS, propagating in the opposite directions. In this experiment, the phase arising from the path difference of the two beams is compensated with glass slides, where the same calibration method involving the elimination of orthogonal states discussed in Section 3.6.1 is employed. Additionally, both the clockwise and anti-clockwise paths contain a half waveplate (HWP_1 and HWP_2 from Fig. 3.10), responsible for introducing the beam splitting ratios a and b to the two polarisation components $\hat{H}$ and $\hat{V}$ given by Eqn. 3.5.2, essentially creating the partially polarising beam splitter (PPBS) before leaving the interferometer through the same PBS. The beam along the α path passes through a HWP_3 and a quartz plate used for polarisation-dependent calibration, while the beam along the β path is reflected into a QWP. All waveplate angles are identical to the original setup from Section 3.6. Finally, the beams along the two paths enter PBS_2, where the POVM elements are generated, before once again being incident on four different quadrants of a camera (see inset of Fig. 3.10) for a single-shot measurement of the spatially dependent polarisation profile.

[26] My contribution to this work extends to the design of the experimental setup and consultations based on my previous experience from our initial work.

[27] With the additional change of placing an optically active sample along the beam path.

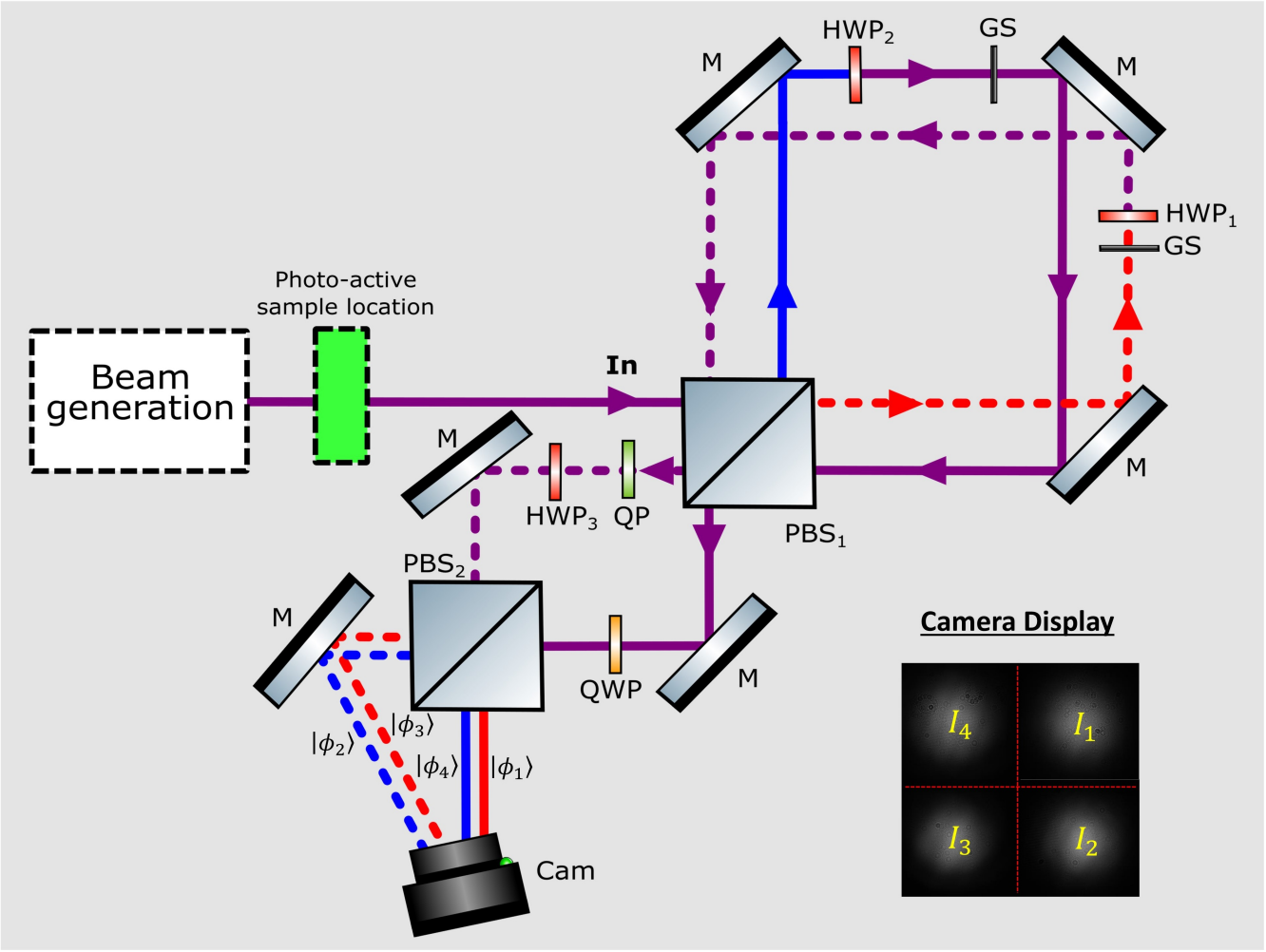

Figure 3.10: The improved Sagnac interferometer for the single-shot POVM tomography setup. The setup consists of polarising beam splitters (PBS), half waveplates (HWP), a quarter waveplate (QWP), glass slides (GS), a quartz plate (QP), and mirrors (M). The dashed and solid lines represent the α and β paths, respectively, while the inset displays the camera image with the four quadrants of the POVM measurements.

The analysis in [149] states the split path of the Sagnac interferometer creates a small difference in the optical path length that requires periodic calibration of the instrument matrix, where significant improvements to the interferometer stability are reported, measured over a period of 8 hours at 30-minute intervals in a calm laboratory setting. However, noticeable deviations in beam intensity were detected when the laboratory experienced increasing foot traffic. These deviations are attributed to the small shifts in the glass slides positions from the vibrational noise.

In the classical regime, one could determine the optical activity using a spatially dependent one-shot analysis of the photo-active material with our system, where identification of dichroism or birefringent behaviour requires Mueller matrix calculations of the light beam propagating through the active medium. Usually, this requires exposing the sample to the six input polarisation states $\mathbf{I}_i(\mathbf{r}_\perp)$ for $i \in \{H, V, D, A, R, L\}$, where Stokes tomography is performed across all six input beams, resulting in a total of 36 measurements. Alternatively, we could use POVM tomography to reduce the number of measurements down to 16, for a total of four sequential measurements due to the one-shot nature of the system. By exposing the sample to a Poincaré beam, we can test the response of the medium simultaneously across all polarisation profiles, generating a single-

shot optical activity detection system. This technique would be ideal for reconstructing optical activity information for photo-sensitive samples that exhibit rapid dynamic changes or those where prolonged exposure to light could be problematic. For this reason improvements to the stability of the interferometer is vital to eliminate inaccuracies in the reconstruction of the Muller matrices of the optically active medium. The experimental results discussed in [149] report successful Muller matrix reconstruction with a Poincaré beam for stationary, rotated, and tilted retardation plates using POVM measurements with excellent theoretical predictions and comparable accuracy to Stokes tomography, as documented in Section 4 of [149].

3.10 Summary

In this chapter, we provide a detailed description of our experimental work, realising a single-shot measurement system to characterise complex vector beams with generalised measurements. We introduce an extensive mathematical description of the nature of generalised measurements and the POVM sets in use. We discussed the experimental implementation of the MIC-POVM via an interferometric setup and compared the obtained results to pre-existing tomography methods. Finally, we gave a summary of later work involving a modified experimental configuration with greater system stability.

PART II

MATTER, SPECTROSCOPY AND MAGNETO-OPTICAL EFFECTS

Chapter 4

Atomic structure and the optical Bloch equations

4.1 Introduction

Thus far, we have solely focused on developing a foundational understanding of light phenomena relevant to our work. Starting from Maxwell's equations and moving to polarisation, discussing formalisms, generation methods, and measurement techniques before introducing transverse modes of propagation, and finally shedding light on our experimental work with a minimum informationally complete polarimeter. In this half of the thesis, our focus shifts to understanding the nature of atomic interactions with propagating light fields, with a particular emphasis on spectroscopic techniques involving spatially varying polarisation structures.

A large section of experimental research on matter-light interaction has used alkaline metals. These elements possess a single valence electron[1], which under certain assumptions can be treated like a simple nucleus-electron system analogous to the hydrogen atom, significantly reducing the complexity of their modelling. Rubidium is one such element with a manageable vaporisation temperature[2] that has been used in several matter-light interaction studies in recent years, with applications in atomic clocks [150–152], magnetometry [153–155], and quantum memories [156–158]. However, despite their experimentally friendly nature and rich atomic structure, the choice to use rubidium in modern-day experiments remains heavily motivated by historic reasons.

One of the main driving forces behind the early work on matter-light interaction was to create the fifth state of matter known as a Bose-Einstein condensate (BEC). As atoms are cooled into the nanokelvin regime, a single "superatom" is created where quantum mechanical behaviour begins to manifest in the macroscopic regime, making it easier to study and maybe even apply for real-world applications[3]. In 1995, Eric Cornell and Carl Wieman created the first BEC by laser cooling atoms, using diode lasers stripped from CD players that operated at a wavelength of around 780nm in the near infrared (NIR) region, close to the rubidium cooling transition. The choice to use rubidium had more to do with their leftover equipment from their previous work with cesium and less with rubidium being the ideal candidate for a BEC. Although the historical reasoning for rubidium cooling was based on convenience rather than scientific justification, it is worth noting that most department heads and senior researchers today were PhD students and early career researchers when the first BEC was formed, which would have influenced their ideas before being passed down

[1] Outermost electron.

[2] When compared to some of the other elements.

[3] Mathematically the whole atomic ensemble (i.e. "superatom") now possesses a single wavefunction.

to the next generation.

Furthermore, the diodes found in commercial CD players served as a low-cost laser source for underfunded groups to conduct interesting experiments investigating new concepts or expanding on existing ones. Unfortunately, the popularity of CDs waned over time in favour of DVDs, then DVD HD, followed by Bluray, and eventually being replaced entirely by online streaming services, raising the cost of laser diodes used for research purposes. Despite this, much of the equipment found in laboratories at the turn of the century is still in use today, ensuring rubidium remains a viable option for new experimental research in atom optics.

4.2 Rubidium energy structure

As the title of this section suggests, all of our atom experiments at the University of Glasgow use rubidium. In their natural state, there are two isotopes of Rubidium, namely Rubidium-85 (^{85}Rb) and Rubidium-87 (^{87}Rb), at an abundance of 72.19% and 27.83%, respectively [159]. We have considered both isotopes throughout different stages of our experimental work, where in the early stages of our system preparation, we took measurements with both isotopes by scanning our laser frequency (more information in Section 6.5), to evaluate our system accuracy when comparing our data to existing literature[4]. However, for reasons that will be covered in Section 6.6, we concentrated primarily on ^{85}Rb when carrying out our intended experiment. Nevertheless, we will discuss both isotope structures in this section, following the literature in [160, 161].

In a simplified model, the alkaline metals and any hydrogen-like atoms are treated as a single electron orbiting a nucleus, as illustrated in Fig. 4.1a. The rest of the electrons fill the internal structure of the atom completely, where it is assumed they do not interact with the valence electron (outermost electron) in any capacity[5]. For our work, it is sufficient to consider only two orbitals in the same shell, namely the $5S$ and the $5P$ orbitals, where S and P indicate an orbital angular momentum quantum number of $L = 0$ and $L = 1$, respectively. The magnitude of the orbital angular momentum vector $\mathbf{L}$ can be calculated from $|\mathbf{L}| = \sqrt{L(L+1)}\hbar$. It is worth mentioning that the magnitude of any momentum vector can be calculated with a similar expression, replacing L with the associated quantum number. Alongside L, there are four other fundamental quantum numbers that tell us the energy state of the electron[6], namely, n the principal quantum number (dictates energy level), m_L the magnetic moment number (determines the number of orbitals and their orientation in a L-subshell), and S the electron spin (angular momentum of the electron). In this scheme,

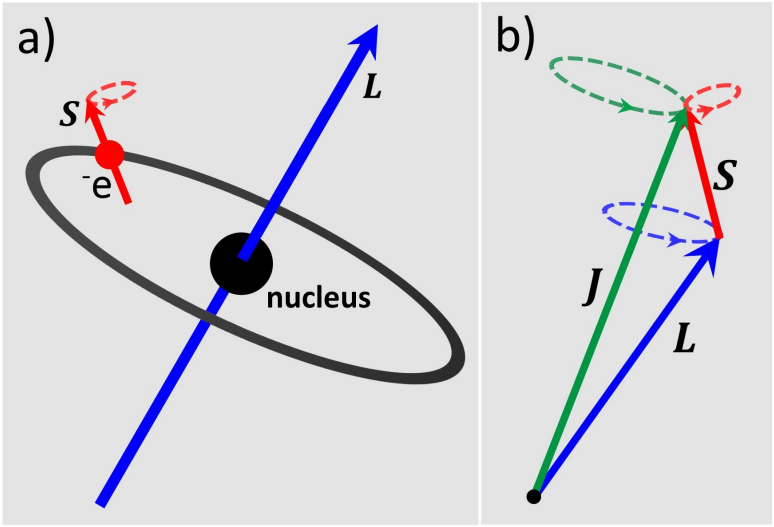

Figure 4.1: The electron spin-orbit interaction. a) An electron orbiting a nucleus with orbital angular momentum **L** (blue) and its spin precession axis **S** (red). b) The spin-orbit coupling with a total angular momentum **J** (green).

[4] Which was possible since there was no laser locking mechanism in place yet.

[5] In reality, the valence electron will feel an electrostatic contribution from the other electrons.

[6] Ignoring any momentum coupling.

the S orbital denotes the ground state and is separated by ~ 379.4THz (or ~ 788.1nm)[7] from the excited state orbital P.

Most fundamental particles possess an intrinsic spin[8], which varies for bosonic (integer spin) and fermionic (half integer spin) particles. In addition to the orbital angular momentum, the electron is an example of a spin-1/2 particle with a spin quantum number of $S = \pm 1/2$. Note that the electron spin motion resembles a precession around an axis, whose orientation is given by the sign of S. The total angular momentum in the system from both contributions is given by $\mathbf{J} = \mathbf{L} + \mathbf{S}$, generating an effect known as ***spin-orbit coupling***, as shown in Fig. 4.1b. The combined momentum number takes a value ranging between $|L - S| \leq J \leq L + S$, where the S orbital ($L = 0$) has $J = 1/2$ and the P orbital in the excited state ($L = 1$) can take J values of either $J = 1/2$ or $J = 3/2$. This creates an effect known as the ***fine structure splitting***. For alkaline metals, the transitions from the ground state $5S_{1/2}$ to the $5P_{1/2}$ or $5P_{3/2}$ excited states are known as the D1 and D2 transition lines, respectively.

Similar to the electron, the nucleus also possesses an intrinsic angular momentum spin[9], whose vector is given by $\mathbf{I}$ (as shown in Fig. 4.2a) and couples to the spin-orbit vector $\mathbf{J}$ to give a total angular momentum expressed by $\mathbf{F} = \mathbf{J} + \mathbf{I}$ as illustrated in Fig. 4.2b. This splits the fine structure into further sublevels labelled by F, an effect known as ***hyperfine splitting***, with values ranging from $|J - I| \leq F \leq J + I$. The two isotopes of rubidium possess different nuclear spins, namely, $I_{85} = 5/2$ and $I_{87} = 3/2$. The implications are that although both isotopes possess the same number of hyperfine levels, the hyperfine states of ^{85}Rb are larger by 1 (i.e. $F + 1$), compared to ^{87}Rb (e.g. for the D2 line excited states, ^{85}Rb has the hyperfine states $1 \leq F \leq 4$, while ^{87}Rb has the states $0 \leq F \leq 3$). The fine and hyperfine splitting are illustrated in the energy level diagram shown in Fig. 4.3, for both ^{85}Rb and ^{87}Rb. The notation for the fine structure is given by nL_J, and the frequency separation is around 7.1THz or 14.7nm. However, the hyperfine splitting (denoted F, F', and F'' for the ground, D1 line, and D2 line, respectively) is generally separated by a few gigahertz for the ground states and a few tens to a few hundred megahertz for the excited states, as seen in Fig. 4.3. In a very similar fashion to the orbital angular momentum L, the hyperfine structure possesses a set of $2F + 1$ magnetic sublevels, denoted by the quantum number m_F, and has the range $-F \leq m_F \leq F$. These sublevels are degenerate (i.e. they measure the same energy but possess different quantum numbers) in the absence of any external magnetic fields.

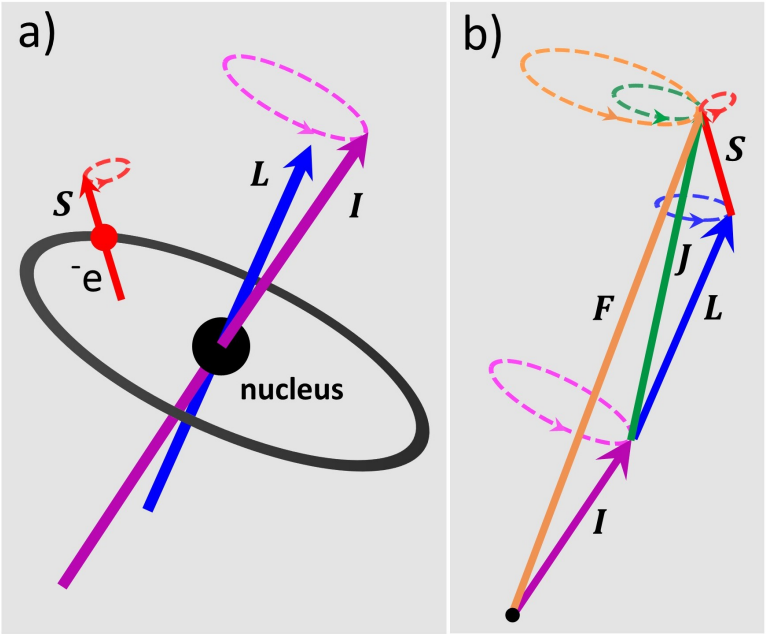

Figure 4.2: The hyperfine interaction between the nucleas and electron. a) A precessing electron $\mathbf{S}$ (red) orbiting the nucleus with orbital angular momentum $\mathbf{L}$ (blue), interacting with a precessing nucleus $\mathbf{I}$ (purple). b) The hyperfine interaction with total angular momentum $\mathbf{F}$ (orange).

[7] These values are calculated from numbers retrieved from [160, 161].
[8] With the exception of some bosons with zero spin (e.g. Higgs boson).
[9] This motion is also a precession.

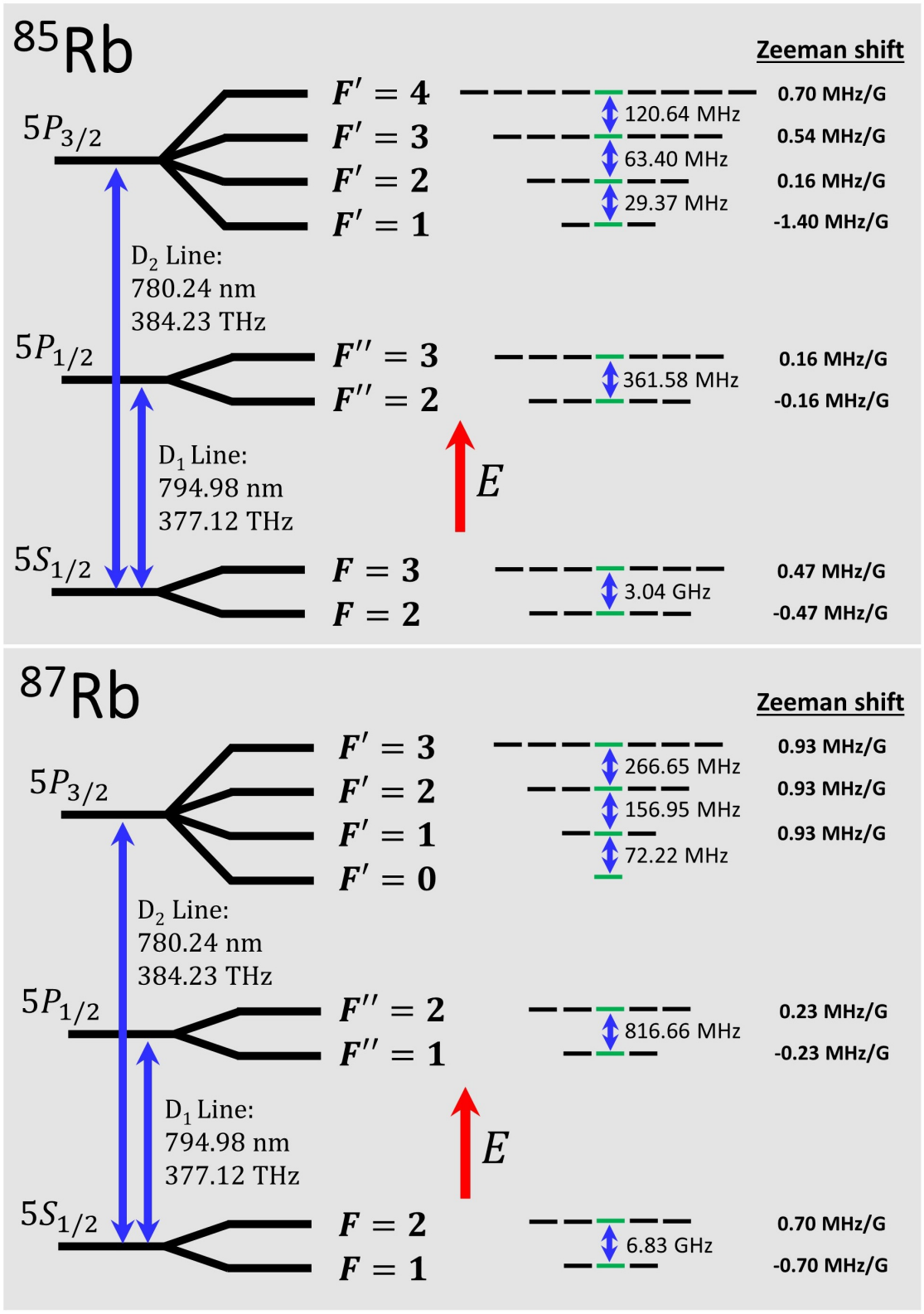

Figure 4.3: Energy levels of the ground state (F), lower excited (F''), and upper excited (F') states of the valence electron for ^{85}Rb and ^{87}Rb. Both the fine structure and hyperfine splitting are shown, with the red arrow indicating increasing energy. The magnetic sublevels are indicated on the right, where the green line is the zeroth magnetic sublevel. In our labs, we only make use of the D_2 lines; however, we included the D_1 line structure for completeness.

However, in the presence of a magnetic field, the m_F levels experience a frequency shift via the ***Zeeman effect***. For a weak magnetic field this shift is given by [162],

$$\Delta E_{|F,m_F\rangle} = \mu_B g_F m_F B_z, \tag{4.2.1}$$

where μ_B is the Bohr magneton[10] and B_z is the magnetic field in the z-direction. Here the z-axis corresponds to the quantisation axis of the angular momentum, and g_F is the Landé g-factor, expressed in its complete form by,

$$g_F = g_J \frac{F(F+1) - I(I+1) + J(J+1)}{2F(F+1)} + g_I \frac{F(F+1) + I(I+1) - J(J+1)}{2F(F+1)}, \tag{4.2.2}$$

where g_I is the nuclear spin g-factor and g_J is the fine structure Landé g-factor given by,

$$\begin{aligned} g_J &= g_L \frac{J(J+1) - S(S+1) + L(L+1)}{2J(J+1)} + g_S \frac{J(J+1) + S(S+1) - L(L+1)}{2J(J+1)} \\ &\simeq 1 + \frac{J(J+1) + S(S+1) - L(L+1)}{2J(J+1)}, \end{aligned} \tag{4.2.3}$$

here g_L and g_S are the orbital and spin g-factors of the electron, respectively. Since the largest contribution from g_I is around 0.15% of g_J, we can ignore the second term of Eqn. 4.2.2. Additionally, the final expression in Eqn. 4.2.3 comes from using the approximate g-factor values $g_L \approx 1$ and $g_S \approx 2$. If we write Eqn. 4.2.1 in frequency format and assume natural units we get,

$$\omega_L = 1.40 g_F m_F B_z. \tag{4.2.4}$$

This frequency is known as the ***Larmor frequency***, which describes the precession of the atom around an applied magnetic field[11]. This frequency is important when discussing magneto-optical effects and will be referred to throughout our work in Chapter 6. For the magnetic field in our experiment, the Zeeman splitting is on a much smaller scale compared to some of the frequencies discussed in this section. For example, the magnetic sublevels m_F of the upper ground state ($J = 1/2$, $F = 3$) in ^{85}Rb experience a shift of 0.47MHz/G, while the magnetic sublevels of the upper excited state $m_{F'}$ experience a shift of around 0.70MHz/G (see Fig. 4.3), where the shift between the furthest magnetic sublevels in the corresponding states (i.e. between $m_{\pm F}$ and $m_{\pm F'}$) for an external magnetic field of 1 G is around 2.80MHz and 5.60MHz, respectively. In addition to the magnitude of the Zeeman shift, the sign of the Landé g-factor also determines the shift direction of the magnetic sublevel. An example of this can be seen in Fig. 4.4, where the ground states of ^{85}Rb shift in the opposite direction under the effect of the external magnetic field.

[10] The Bohr magneton has a value of around $\sim 1.40h$ MHZ/G [160, 161], where h is the Planck constant. However, when discussing magnetic field shift, we assume natural units (i.e. h = 1).

[11] A common form of the Larmor frequency is $\omega_L = \gamma B$, where γ is a quantity known as the gyromagnetic ratio, given by $\gamma = -eg/2M$. Here e is the electron charge, g the Landé factor, and m the electron mass.

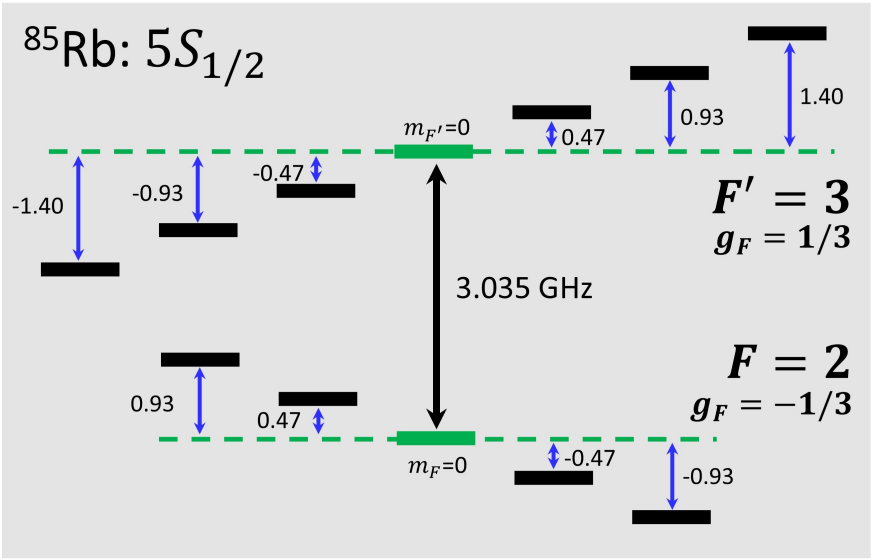

Figure 4.4: Zeeman splitting of ^{85}Rb ground state m_F levels. The different signs of the g-factor g_F indicate the splitting direction. The $m_F = 0$ state is in green, and the dashed line indicates the m_F sublevel positions in the absence of an external magnetic field. The m_F shift values are in MHz/G.

In an experimental setting, we are able to successfully observe the fine and hyperfine structure splitting with a simple spectroscopy setup (see Section 5.3 for more information); however, the Zeeman shifts of the magnetic sublevels in a low field regime are on the order of the natural linewidth of the transition Γ, making it difficult to resolve experimentally. However, light polarisation can be used to distinguish between the population in the different magnetic sublevels and plays an integral role in polarisation spectroscopy, which will be discussed in a later chapter. More information on the structure of ^{85}Rb and ^{87}Rb can be found in [160, 161].

4.3 Optical Bloch Equations: a two-level atom

In this section, we develop a mathematical model of a coherent light field interacting with an atomic medium, building an understanding of matter-light interaction following the literature in [163–166], leading to the derivation of the optical Bloch equations. Generally, we consider the simplest interaction model, which sees the atom being treated as a two-level system with a ground state $|g\rangle$ and an excited state $|e\rangle$, separated by an energy gap as shown in Fig. 4.5. The energy of a state $|\psi\rangle$ of any quantum mechanical system can be determined from the eigenvalue equation (often called the time-independent Schrödinger equation),

$$\hat{H}|\psi\rangle = E|\psi\rangle, \tag{4.3.1}$$

where $\hat{H}$ is the Hamiltonian operator and E is the system energy. We define the Hamiltonian operator as,

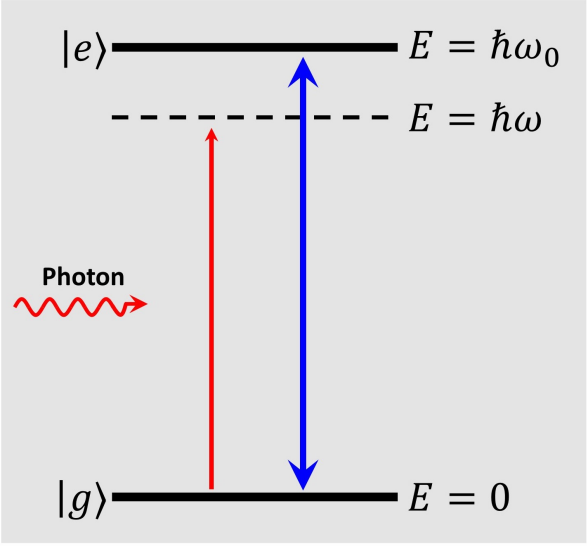

Figure 4.5: A two-level atomic system. The ground state energy is zero, the excited state energy is $\hbar\omega_0$, and the photon energy is $\hbar\omega$.

$$\hat{H} = \hat{T} + \hat{H}_0 + \hat{H}_I, \tag{4.3.2}$$

where $\hat{T}$ is the kinetic energy operator, $\hat{H}_0$ is the atomic Hamiltonian, and $\hat{H}_I$ is the interaction

Hamiltonian. For simplicity, we assume a stationary atom (i.e. $\hat{T} = 0$) and focus on the potentials instead. The atomic Hamiltonian $\hat{H}_0$ describes the base energy of the atom in the absence of external forces. This Hamiltonian takes into account the kinetic energy from the electron motion and the Coulomb potential from the electrostatic interaction between the nucleus and electron. For our system, the atomic energy of the two levels are given by,

$$\begin{aligned} \hat{H}_0|g\rangle &= 0 \\ \hat{H}_0|e\rangle &= \hbar\omega_0|\psi\rangle, \end{aligned} \tag{4.3.3}$$

where we have opted to set the ground state energy to zero and the excited state energy is given by the Planck relation as illustrated in Fig. 4.5. Here $\hbar$ is the reduced Planck constant and ω_0 is the required photon frequency to excite the atomic transition. However, the interaction hamiltonian is described by an electric dipole moment between the nucleus and the electron, taking the form,

$$\hat{H}_I = \hat{d} \cdot \mathbf{E}, \tag{4.3.4}$$

where $\hat{d}$ is the dipole operator and $\mathbf{E}$ the electric field of the incident photon. The dynamics of the system are described by the time-dependent Schrödinger equation,

$$i\hbar\frac{\partial|\Psi(\mathbf{r},t)\rangle}{\partial t} = \hat{H}|\mathbf{r},\Psi(t)\rangle, \tag{4.3.5}$$

where the atom can be described with the atomic wavefunction,

$$|\Psi(t)\rangle = c_g(t)|g\rangle + c_e(t)|e\rangle e^{-i\omega_o t}, \tag{4.3.6}$$

here $c_g(t)$ and $c_e(t)$ are the complex probability amplitudes of the ground and excited states, respectively, as a function of temporal variations. Substituting Eqn. 4.3.6 into Eqn. 4.3.5, we find,

$$i\hbar\frac{\mathrm{d}c_g(t)}{\mathrm{d}t}|g\rangle + i\hbar\frac{\mathrm{d}c_e(t)}{\mathrm{d}t}|e\rangle e^{-i\omega_o t} = (\hat{H}_0 + \hat{H}_I)(c_g(t)|g\rangle + c_e(t)|e\rangle e^{-i\omega_o t}). \tag{4.3.7}$$

Since Ψ only depends on t, the derivative is no longer partial. If we now multiply the equation above with $\langle g|$ and $|e\rangle$, respectively, we are left with two expressions,

$$\begin{aligned} i\hbar\frac{\mathrm{d}c_g(t)}{\mathrm{d}t} &= c_g(t)\langle g|(\hat{H}_0 + \hat{H}_I)|g\rangle + c_e(t)\langle g|(\hat{H}_0 + \hat{H}_I)|e\rangle e^{-i\omega_o t} \\ i\hbar\frac{\mathrm{d}c_e(t)}{\mathrm{d}t}e^{-i\omega_o t} &= c_g(t)\langle e|(\hat{H}_0 + \hat{H}_I)|g\rangle + c_e(t)\langle e|(\hat{H}_0 + \hat{H}_I)|e\rangle e^{-i\omega_o t}. \end{aligned} \tag{4.3.8}$$

Using Eqns. 4.3.3 and substituting Eqn. 4.3.4 into Eqns. 4.3.8 above, we are left with,

$$\begin{aligned} i\hbar\frac{\mathrm{d}c_g(t)}{\mathrm{d}t} &= c_e(t)\langle g|\hat{d}\cdot\mathbf{E}|e\rangle e^{-i\omega_o t} \\ i\hbar\frac{\mathrm{d}c_e(t)}{\mathrm{d}t} &= c_g(t)\langle e|\hat{d}\cdot\mathbf{E}|g\rangle e^{i\omega_o t}. \end{aligned} \tag{4.3.9}$$

Since the dipole operator $\hat{d}$ possesses an odd parity, both $\langle g|\hat{d}\cdot\mathbf{E}|g\rangle$ and $\langle e|\hat{d}\cdot\mathbf{E}|e\rangle$ vanish[12].

[12]This might be easier to spot in wavefunction format using the dipole matrix elements $\hat{d}_{ii}$. In this formalism, $\langle i|\hat{d}|i\rangle = \int dV|\Psi_i|^2\hat{d}$. Since the total integrand parity is odd, the volume integration over a finite space is zero.

Considering a monochromatic plane wave with an electric field similar to Eqn. 1.2.14 (i.e. $\mathbf{E} = E_0 \exp\big[i(\mathbf{k}\cdot\mathbf{r} - \omega t)\big]\hat{e}$) and photon energy $E = \hbar\omega$ (see Fig. 4.5), by substituting this field into Eqns. 4.3.9 we obtain the expressions[13],

$$\begin{aligned} i\hbar\frac{\mathrm{d}c_g(t)}{\mathrm{d}t} &= c_e(t)\hbar\Omega^*\left(\frac{e^{i(\omega-\omega_o)t} + e^{-i(\omega+\omega_o)t}}{2}\right) \\ i\hbar\frac{\mathrm{d}c_e(t)}{\mathrm{d}t} &= c_g(t)\hbar\Omega\left(\frac{e^{i(\omega+\omega_o)t} + e^{-i(\omega-\omega_o)t}}{2}\right), \end{aligned} \tag{4.3.10}$$

where the quantity Ω is given by,

$$\Omega = E_0\frac{\langle e|\hat{d}\cdot\hat{e}|g\rangle}{\hbar}. \tag{4.3.11}$$

In a two-level system, the process where the atom is excited by absorbing the energy from an incoming photon and decaying by re-emitting the photon describes a continuous interaction cycle, the rate of which is given by the ***Rabi frequency*** Ω. This frequency determines the coupling strength between the atom and the light field and depends on the beam intensity[14]. Note that the interaction strength for every intensity will vary depending on the driven atomic transition and light polarisation and must be calculated from the dipole matrix elements (see section 4.6 for more information).

For a low-intensity light field close to resonance, the oscillation terms given by $(\omega + \omega_0)$ are much faster than $(\omega - \omega_0)$, oscillating at roughly twice the frequency of the driving force. When averaged over timescales relevant to the atom (e.g. atomic decay) they vanish. This is known as the ***rotating wave approximation***. Applying this approximation to Eqns. 4.3.11 yields,

$$\begin{aligned} i\hbar\frac{\mathrm{d}c_g(t)}{\mathrm{d}t} &= c_e(t)\hbar\Omega^*\frac{e^{i\Delta t}}{2} \\ i\hbar\frac{\mathrm{d}c_e(t)}{\mathrm{d}t} &= c_g(t)\hbar\Omega\frac{e^{-i\Delta t}}{2}, \end{aligned} \tag{4.3.12}$$

where $\Delta = \omega - \omega_o$ is the difference between the frequency of the light field and atomic transition known as the ***detuning***. The interaction Hamiltonian can be read off from Eqns. 4.3.12; however, the complex amplitudes still contain time-dependent terms[15]. We remove these time dependencies by introducing the coordinate transformation in the frame of reference of the rotating light field, $c'_g = c_g(t)$ and $c'_e = c_e e^{i\Delta t}$ into Eqns. 4.3.12, to give,

$$\begin{aligned} i\hbar\frac{\mathrm{d}c'_g}{\mathrm{d}t} &= c'_e\frac{\hbar\Omega}{2} \\ i\hbar\frac{\mathrm{d}c'_e}{\mathrm{d}t} &= c'_g\frac{\hbar\Omega}{2} - c'_e\hbar\Delta, \end{aligned} \tag{4.3.13}$$

where we assume the complex amplitudes of the two states fluctuate identically (i.e. $\Omega = \Omega^*$). This signifies our interest in the local effects of the atom, discarding any global phase contributions. We

[13] We are only interested in the temporal evolution of the light field, which for a physical wave is given by $\mathfrak{Re}(\mathbf{E}) = \mathfrak{Re}(e^{-i\omega t}) = \cos(\omega t) = (e^{i\omega t} + e^{-i\omega t})/2$ (the second to last expression is from Euler's formula and the last expression is the cosine in exponential form).

[14] Recall that the intensity depends on the electric field by $I = |E|^2$.

[15] Remember, you can express a system of linear first-order coupled differential equations in matrix form.

can now read the total Hamiltonian of the system from Eqns. 4.3.13, expressed in matrix format,

$$\hat{H} = \frac{\hbar}{2}\begin{pmatrix} 0 & \Omega \\ \Omega & -2\Delta \end{pmatrix}. \tag{4.3.14}$$

In our current formalism of the two-level system we considered so far, the action of the light field causes the atom to oscillate between the ground and excited states, where the time evolution is given by the Schrödinger equation. In terms of energy, the monochromatic light field transfers the energy to the atom, where the atom re-emits the photon back into the light field when de-excited, ensuring energy conservation laws are obeyed. These two processes are known as ***absorption*** and ***stimulated emission***, respectively (as shown in Fig. 4.6a and Fig. 4.6b, respectively). However, in this interaction model an atom prepared in the excited state remains there unless acted upon by an external field. In reality, the excited state has a finite lifetime τ before decaying into the ground state and re-emitting a photon in a random direction via means of ***spontaneous emission*** (see Fig. 4.6c). Ultimately we consider the atom to be irreversibly coupled to an environment (which includes the light field)[16] where spontaneous emission simulates energy loss in the system, akin to oscillation damping from the Schrödinger picture. This process must be included in the formalism of the Hamiltonian to describe the atom-light interaction correctly.

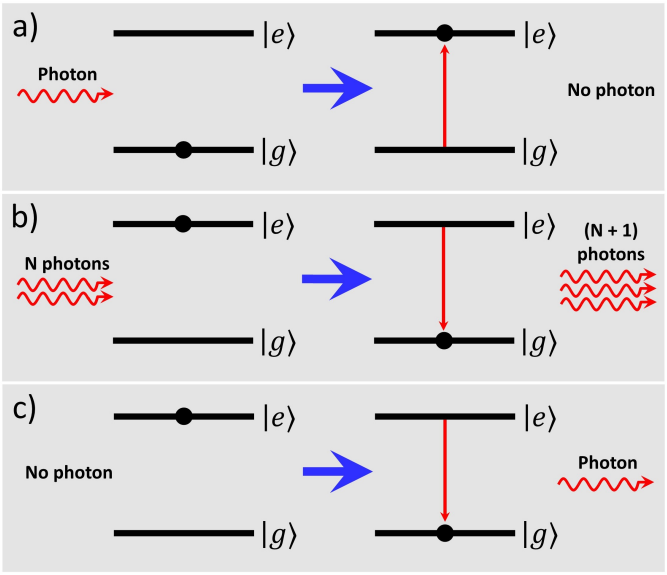

Figure 4.6: An atom interacting with an optical field (or absence of a field). a) atomic absorption; b) stimulated emission; and c) spontaneous emission.

Consider a beam interacting with an ensemble of atoms, where the state of each atom is given by the wavefunction $|\Psi\rangle = c_g|g\rangle + c_e|e\rangle$, and the state of all atom-light interactions is the sum of all atomic states $|\Psi_{int}\rangle = \sum_i (|\Psi\rangle)_i$. After performing the projection measurements on the atoms, the interaction state Ψ_{int} is a statistical mixture of the two pure states of the system, $|g\rangle$ and $|e\rangle$. Such a state is known as a mixed state and cannot be described by a single wavefunction, instead we use density matrices to represent them defined by $\hat{\rho} = |\psi\rangle\langle\psi|$ (see Section 3.4). Considering the atomic state in vector format, we represent the density operator in matrix format by,

$$\hat{\rho} = \begin{pmatrix} c_g \\ c_e \end{pmatrix}\begin{pmatrix} c_g^* & c_e^* \end{pmatrix} = \begin{pmatrix} |c_g|^2 & c_g c_e^* \\ c_g^* c_e & |c_e|^2 \end{pmatrix} = \begin{pmatrix} \rho_{gg} & \rho_{ge} \\ \rho_{eg} & \rho_{ee} \end{pmatrix}, \tag{4.3.15}$$

where the asterisk (*) denotes complex conjugate terms. Here the diagonal terms ρ_{gg} and ρ_{ee} represent population states, denoting the probability of finding the atom in the $|g\rangle$ or $|e\rangle$ state, respectively. The off-diagonal terms ρ_{ge} and ρ_{eg} are known as coherences, describing the phase relation between the two states. Since the atom-light interaction processes (i.e. absorption and

[16] Note that we do not care about the environment and only concern ourselves with the state of the atom.

spontaneous emission) are time-dependent, we obtain an expression of the time evolution of the density matrix using the von Neumann (or Liouville) equation given by,

$$-i\hbar\frac{\mathrm{d}\hat{\rho}}{\mathrm{d}t} = \left[\hat{\rho}, \hat{H}\right], \tag{4.3.16}$$

where $\hat{H}$ is the Hamiltonian and $\left[\hat{\rho}, \hat{H}\right] = \hat{\rho}\hat{H} - \hat{H}\hat{\rho}$ is the commutation relation. The derivation of the optical Bloch equations is nearly complete, but we are missing a term describing spontaneous decay. Unfortunately, a Hamiltonian cannot describe this process; however, we can incorporate dampening effects into the density matrix formalism. The expected rate of spontaneous emission can be expressed as the inverse of the excited state lifetime $1/\tau$, otherwise known as the decay rate Γ. After this decay, the atom is in the ground state, where the rate of depopulation in the excited state must equal the rate of repopulation in the ground state. We express the decay terms for the population states by,

$$\dot{\rho}_{ee} = -\dot{\rho}_{gg} = -\Gamma\rho_{ee}, \tag{4.3.17}$$

and the decay rate of the coherences by,

$$\begin{aligned} \dot{\rho}_{ge} &= -\frac{\Gamma}{2}\rho_{ge} \\ \dot{\rho}_{eg} &= -\frac{\Gamma}{2}\rho_{eg}, \end{aligned} \tag{4.3.18}$$

where the dot $(\cdot)$ denotes a time derivative. The final form of the von Neumann equation, including both the Hamiltonian of the matter-light interaction and the spontaneous decay and is given by,

$$-i\hbar\frac{\mathrm{d}\hat{\rho}}{\mathrm{d}t} = \left[\hat{\rho}, \hat{H}\right] - \Gamma\begin{pmatrix} -\rho_{ee} & \frac{1}{2}\rho_{ge} \\ \frac{1}{2}\rho_{eg} & \rho_{ee} \end{pmatrix}. \tag{4.3.19}$$

By substituting the Hamiltonian from Eqn. 4.3.14 into Eqn. 4.3.19 above and expanding, we obtain an expression for the optical Bloch equations,

$$\begin{aligned} \dot{\tilde{\rho}}_{gg} &= \frac{i\Omega}{2}(\tilde{\rho}_{ge} - \tilde{\rho}_{eg}) + \Gamma\tilde{\rho}_{ee} \\ \dot{\tilde{\rho}}_{ge} &= -\frac{i\Omega}{2}(\tilde{\rho}_{ee} - \tilde{\rho}_{gg}) - i\Delta\tilde{\rho}_{ge} - \frac{\Gamma}{2}\tilde{\rho}_{ge} \\ \dot{\tilde{\rho}}_{eg} &= \frac{i\Omega}{2}(\tilde{\rho}_{ee} - \tilde{\rho}_{gg}) + i\Delta\tilde{\rho}_{eg} - \frac{\Gamma}{2}\tilde{\rho}_{eg} \\ \dot{\tilde{\rho}}_{ee} &= -\frac{i\Omega}{2}(\tilde{\rho}_{ge} - \tilde{\rho}_{eg}) - \Gamma\tilde{\rho}_{ee}, \end{aligned} \tag{4.3.20}$$

where the tilde $(\sim)$ denotes being in the rotating frame of the light field similar to Eqns. 4.3.13. In addition to the Bloch equations, the populations of the density matrix also obey the completeness relation (i.e. $\rho_{gg} + \rho_{ee} = 1$), since the atom can only occupy these two states and the off-diagonal elements are complex conjugates of one another (i.e. $\tilde{\rho}_{ge} = \tilde{\rho}^*_{eg}$). There are analytic solutions to some special cases of the Bloch equations, but they are generally solved using numerical methods, especially when extended to multilevel atoms with more complex atomic structures.

Fortunately, for interaction with continuous wave (CW) lasers the dynamics of the absorption

process do not change over time, which makes the steady-state solution a suitable approximation to determine the scattering (or fluorescence) rate[17]. In this case we are interested in the population of the excited state $\tilde{\rho}_{ee}$ since only excited atoms can scatter, where we define the scattering rate as $\Gamma\tilde{\rho}_{ee}$. In an experimental setting where a light source probes the atomic medium, the scattering rate is proportional to the beam intensity up to a factor. By employing the steady state solution (i.e. $\dot{\tilde{\rho}}_{ee}^{ss} = 0$), we obtain an expression for the scattering rate,

$$R_{scatt} = \Gamma\tilde{\rho}_{ee}^{ss} = \frac{\Gamma}{2}\frac{(I/I_{sat})}{1 + (I/I_{sat}) + 4(\Delta/\Gamma)^2}, \tag{4.3.21}$$

where the saturation intensity I_{sat} is given by,

$$I_{sat} = \frac{c\varepsilon_0\Gamma^2\hbar^2}{4|\hat{d}\cdot\hat{e}|^2}, \tag{4.3.22}$$

and derived from $I/I_{sat} = 2(\Omega/\Gamma)^2$, where the intensity of the propagating wave is given by $I = (1/2)c\varepsilon_0 E_0^2$ [160, 161]. Here c is the speed of light and ε_0 is the permittivity of free space.

Although we have focused on the dynamics of a two-level atom in this section, a similar formalism can be applied to multilevel systems. Interestingly, in some experimental settings, an accurate theoretical model can be developed based entirely on the evolution of the populations, this idea will be explored further in Section 4.6.

4.4 Doppler broadening

The finite lifetime of the excited state leading to spontaneous decay of the atom into the ground state by releasing a photon results in the broadening of the atomic linewidth as a consequence of the Heisenberg uncertainty principle $\Delta E\Delta\tau \geq \hbar/2$. Instead of taking the idealised form of a Dirac delta function, the result more closely resembles a Lorentzian distribution[18]. Many different phenomena contribute to absorption line broadening, with the most commonly observed broadening effect being ***Doppler broadening***.

During the absorption process, a photon with frequency ω and wave vector $\mathbf{k}$ excites an atom with mass M from the ground state $|g\rangle$ into the excited state $|e\rangle$. This excited atom experiences a change in linear momentum from $\mathbf{P}$ to $\mathbf{P}'$ as a consequence of the photon interaction, as illustrated in Fig. 4.7 (left). The momentum change also applies to stimulated and spontaneous emission, where a photon is emitted instead as shown in Fig. 4.7 (right), where the atom decays from the excited state $|e\rangle$ back to the ground state $|g\rangle$. The external motion of the atom is related to the internal dynamics of the light-matter interaction for both the absorption and spontaneous emission processes (as illustrated in Fig. 4.6a and Fig. 4.6c, respectively) via the momentum and energy conservation laws. The momentum of the system is given by,

$$\mathbf{P}' = \mathbf{P} \pm \hbar\mathbf{k}, \tag{4.4.1}$$

where the $(\pm)$ expressions represent the absorption and the spontaneous emission, respectively. Similarly, the energy is expressed as,

[17] Some applications with shaped pulsed beams can change the dynamics of the absorption process and do not reach a steady state.

[18] This broadening effect is commonly known as natural broadening.

$$\hbar\omega = \hbar\omega_0 \pm \frac{(\mathbf{P}' \cdot \mathbf{P}')}{2M} \mp \frac{(\mathbf{P} \cdot \mathbf{P})}{2M}. \tag{4.4.2}$$

Here $\hbar\omega_0 = E_{|e\rangle} - E_{|g\rangle}$ and M is the mass of the atom. Note that the equation order for absorption and emission remains unchanged. Substituting Eqn. 4.4.1 into Eqn. 4.4.2 and expanding yields an expression for the photon energy,

$$\begin{aligned}\hbar\omega &= \hbar\omega_0 \pm \frac{1}{2M}\left[(\mathbf{P}\cdot\mathbf{P}) \pm 2\hbar\mathbf{P}\cdot\mathbf{k} + \hbar^2k^2\right] \mp \frac{(\mathbf{P}\cdot\mathbf{P})}{2M} \\ &= \hbar\omega_0 + \frac{\hbar}{M}\mathbf{P}\cdot\mathbf{k} \pm \frac{\hbar^2k^2}{2M} \\ &= \hbar\omega_0 + \hbar\mathbf{v}\cdot\mathbf{k} \pm \frac{\hbar^2k^2}{2M},\end{aligned} \tag{4.4.3}$$

where we have used $\mathbf{P} = M\mathbf{v}$ to arrive at the final expression. The second and third terms from the last expression of Eqn. 4.4.3 above are the Doppler shift and the recoil energy, respectively.

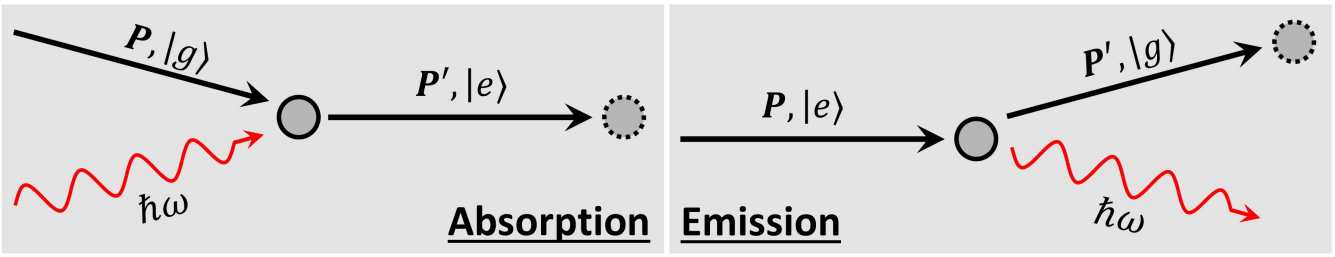

Figure 4.7: The internal and external dynamics of the atom-light interaction via conservation of linear momentum for absorption (left) and spontaneous emission (right).

The recoil energy becomes more significant when considering higher energy transitions. For the D_2 line of ^{85}Rb, it is approximately around 2.47μeV, which is several orders of magnitude less than the photon energy of the same transition of approximately 1.58eV. It is sufficient to state that the recoil energy contribution is negligible and is therefore disregarded, leaving us with a photon frequency given by,

$$\omega = \omega_0 \mp \omega_D, \tag{4.4.4}$$

where $\omega_D = -\mathbf{v}\cdot\mathbf{k}$ is the Doppler angular frequency. Note that the sign ($\mp$) is accounting for the red and blue Doppler shifts, respectively. The magnitude and nature of the frequency shift depends entirely on the atom's velocity and its direction of motion relative to the photon. For example, an atom counter propagating with the light field as shown in Fig. 4.8a, where the photon wavevector is given by $-\mathbf{k}$, has a Doppler frequency equal to $\omega_D = \mathbf{v}\cdot\mathbf{k}$. In this case, scattering is achieved by a laser frequency below the atomic resonance, as the Doppler effect will compensate for the frequency difference caused by the atom's motion. This is an example of ***red detuned light***. Similarly, for a co-propagating atom and photon, the Doppler frequency takes the form $\omega_D = -\mathbf{v}\cdot\mathbf{k}$, and scattering is achieved by a light frequency above the atomic resonance, where once again the Doppler shifts compensate for the frequency difference, as illustrated in Fig. 4.8b. This is an example of ***blue detuned light***. Note that although we describe how the atom observes the light field propagating in different directions relative to its own motion, the Doppler broadening is a consequence of the frequency of light emitted by the observed (i.e. atoms) from the perspective of a stationary observer (in this case the photodiode). For a vapour confined in a finite space with

a temperature T (in Kelvin), the atom velocities follow the Maxwell-Boltzmann distribution, where the Doppler broadening of the linewidth is given by [167],

$$\Delta\omega_D = \frac{2\omega_0}{c}\left(2\ln(2)\frac{k_B T}{M}\right)^2, \tag{4.4.5}$$

where ω_0 is the transition frequency, c is the speed of light, k_B is the Boltzmann constant, and M is the mass of the atom. For Rubidium at room temperature, this broadening is around 0.5GHz and is observed experimentally in Doppler free spectroscopy (see Section 5.3 for more information).

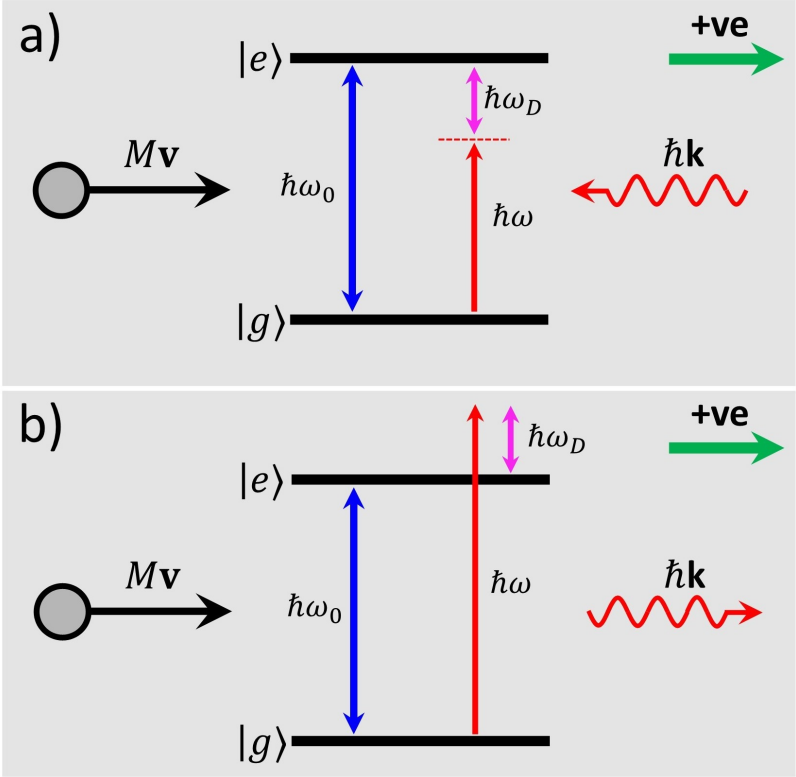

Figure 4.8: The Doppler effect occurring during atom-light interaction. An atom with mass M and velocity $\mathbf{v}$ counter or co-propagating with a photon with momentum $\hbar\mathbf{k}$ observes a difference in the photon frequency relative to its motion, where in a) the frequency is red shifted and in b) it is blue shifted. The green arrows indicate the $+z$-direction.

4.5 Optical pumping schemes

In the previous section we established a formalism for Doppler broadening from the conservation laws of linear momentum and energy during the interaction process between the atomic medium and the optical field. In a very similar fashion, angular momentum is also a conserved physical quantity, with rules governing the optical pumping of atomic media with beams of different polarisation structures. By definition, optical pumping refers to the redistribution of the atomic state population through interactions with the light field. Throughout our work, only dipole transitions are considered. For the allowed dipole transitions, there are three different light polarisations to consider, namely σ_-, π, and σ_+. The occurrence of these transitions very much depends on the quantisation axis of the angular momentum of the atom relative to the propagation direction of the light. In the case where the two are parallel to each other, the allowed transitions are $\sigma_\pm$, where σ_+ denotes left-circular ($\hat{L}$) and σ_- is right-circular ($\hat{R}$) polarised light (see Fig. 4.9a and Fig. 4.9b, respectively). However, if the quantisation axis and the light field are orthogonal to each other, then π transitions are allowed to occur (see Fig. 4.9c). Here π is linearly polarised light, transverse to the light propagation direction (and by definition parallel to the quantisation axis).

If the quantisation axis is at an arbitrary angle relative to the light field, then all three transitions can take place. Note that if a linearly polarised light beam is used when the quantisation axis of the atom is parallel to the light beam, then $\sigma_\pm$ transitions will still occur as π polarisation can be constructed from the orthogonal circular bases, that is $\pi = 1/\sqrt{2}(\sigma_+ + \sigma_-)$.

The question now is, how does one induce the desired transitions in an experimental setting? The answer is to use an external magnetic field $\mathbf{B}$ (which also causes Zeeman splitting)[19]. Since the atom's angular momentum precesses around the direction of the applied magnetic field, with a frequency given by the Larmor frequency ω_L from Eqn. 4.2.4, we can change the field orientation to drive the desired atomic transitions.

Interestingly, the atomic interaction with polarised light can induce special transitions among the magnetic sublevel, subject to the angular momentum selection rules. For the hyperfine states, these selection rules are given by $\Delta F = F' - F = 0, \pm 1$, and by $\Delta m_F = m_{F'} - m_F = q$, where $q = \pm 1$ for $\sigma_\pm$ polarised light and $q = 0$ for π-polarised light as illustrated in Fig. 4.9. These selection rules, coupled with the choice of the external magnetic field, provide a tool to manipulate the internal dynamics of the atom-light interaction in an experimental setup. For example, if we subject the atoms to an external magnetic field where only $\sigma_\pm$ transitions are permitted, we can force the majority of the atom population into the furthest away magnetic sublevels of the ground state (i.e. $m_F = \pm F$), where the only permitted transitions are $|F, m_F\rangle \longrightarrow |F' = F + 1, m_{F'} = m_F \pm q\rangle$ for the corresponding values of $\sigma_\pm$, pumping the atoms into a stretched state and forming what is known as a closed transition. In this scheme there are no other decay or excitation channels under the influence of the driving field polarisation, hence these two states have a 100% excitation and decay probability between one another (as shown by the transitions in the orange circle in Fig. 4.9a and Fig. 4.9b)[20]. This phenomenon is crucial in many important (and exciting) applications of atom-light interaction, including polarisation spectroscopy, which will be extensively discussed in Section 6.5. Note that since our interest lies in the D2 line of Rubidium (see Fig. 4.3), the selection rules for the orbital angular momentum and spin-orbit coupling are given by $\Delta L = \Delta J = 1$.

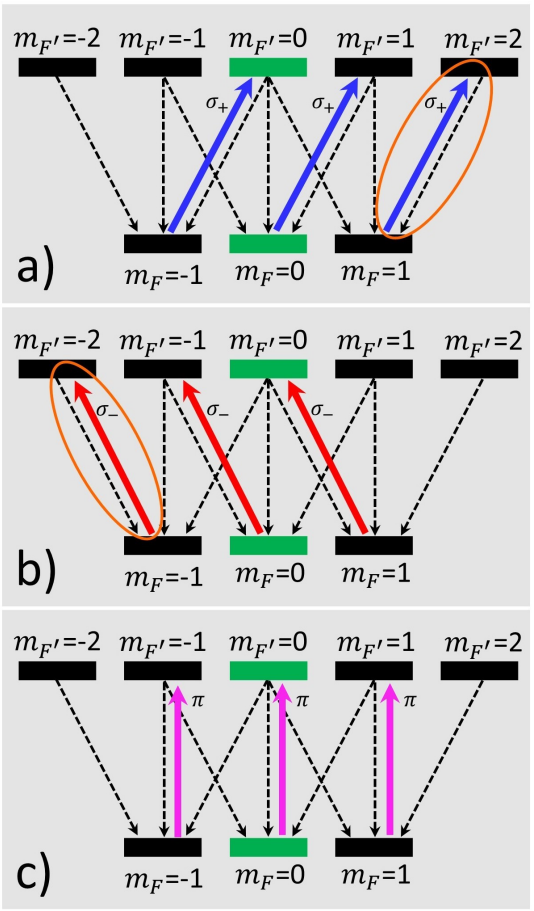

Figure 4.9: Optical pumping of magnetic sublevels with polarised light. a) σ_+ pumping. b) σ_- pumping. c) π pumping. Here the dashed lines indicate decay channels from the excited to the ground states, and the orange circles represent closed transitions.

The hyperfine selection rules limit the number of permitted transitions from a given state, where at most eight different transitions can be excited from a single hyperfine state, subject to the properties of the driving field. The same is also true for spontaneous decay; however, the random decay probability is determined by the dipole matrix elements of the Clebsch-Gordan coefficients.

[19] More precisely a B-field is often used to define a quantisation axis. This is not strictly necessary, as the dynamics of the system are independent of the mathematical choice.

[20] Here it is assumed the light field polarisation is purely $\sigma_\pm$; otherwise, repopulation to other states is possible.

4.6 Rate equations of multilevel systems

Theoretical and experimental work often complement one another, with the former offering predictions of phenomena in the physical world, which are verified by the latter. Unfortunately the real world is complex[21] and often clever techniques are used by experimentalists and theorists alike to help reduce the complexity of the problem under study. For example, here at the University of Glasgow's optics group, the cold atom experiment employs an additional depumping laser source [155], which de-excites the atoms down to the lower ground state of ^{87}Rb after they have been cooled by an optical molasses and trapped by an external magnetic field. The advantage is a simplification in the probed atomic structure, as the system under study possesses far fewer magnetic sublevels in both the ground and excited states. In the case of the cold atoms, the $|F = 1\rangle \rightarrow |F' = 0\rangle$ transition is investigated, resulting in what is known as a quasi-lambda-level structure, offering a significant reduction in the complexity of the theoretical model. However, such experimental changes can be difficult to implement. In this scenario, aside from having to procure an additional laser source, incorporating it into the experimental configuration presents additional engineering and alignment challenges for the experimentalist[22].

A similar approach can be considered when designing a theoretical model of a system. Recalling from Section 4.3, we derived an expression for the optical Bloch equations, which explain the interaction of the atomic media with the light field for a simplified case of two level atom. However, the rubidium D_2 line possess a rich hyperfine structure with a total number of magnetic sublevels equal to 24 and 36 for ^{87}Rb and ^{85}Rb, respectively. When considered in the matrix form of Eqn. 4.3.19, we are looking at a matrix array with 576 and 1296 elements for the two isotopes of rubidium, respectively, corresponding to an equivalent number of coupled differential equations for the population and coherences to be solved for the systems[23]. In the case of some experiments, we can simplify the model by ignoring the coherences.

If we assume the coherences evolve far too quickly that their steady-state solution can be considered, then when averaged over the lifetime of the linewidth Γ, their contributions vanish. This entails a reduction in the number of matrix elements from n^2 down to n, creating a system of coupled differential equations known as population ***rate equations***[24]. A prime example of an experiment that could be modelled this way is polarisation spectroscopy (Polspec), where the atomic medium is pumped with a circularly polarised light source (i.e. $\sigma_{\pm}$) and probed by a second beam, generating a differential signal used for laser locking purposes. Polspec will be covered in more detail in a later chapter of this thesis. Following the literature in [160, 161, 168–171], we define the system population rate equations for the lower ground states by,

$$\frac{\mathrm{d}P_{F,m_F}}{\mathrm{d}t} = \sum_{m_{F'}=m_F-1}^{m_{F'}=m_F+1} \sum_{F'=F-1}^{F'=F+1} R_{F,m_F\rightarrow F',m_{F'}} \Gamma P_{F',m_{F'}}, \tag{4.6.1}$$

the upper ground states,

[21] From both a physics and a social point of view.

[22] Although the cold atom setup is a monstrosity (see [70] for an image of the setup), the simplifications to the physics under study are well worth the experimental trouble, as those equations are equally monstrous.

[23] Although most of the coherences and population states will be zero, calculating matrices of such sizes is very computationally taxing.

[24] This could still be a computationally taxing calculation (depending on your computer hardware and how good a programmer you are), but is much more manageable now.

$$\frac{\mathrm{d}P_{F,m_F}}{\mathrm{d}t} = -\sum_{F'=F-1}^{F'=F+1} R_{F,m_F\to F',m_{F'}} \frac{\Gamma}{2}\frac{I}{I_{sat}}\frac{(P_{F,m_F}-P_{F',m_{F'}})}{1+4(\Delta/\Gamma)^2} + \sum_{m_{F'}=m_F-1}^{m_{F'}=m_F+1}\sum_{F'=F-1}^{F'=F+1} D_{F,m_F\to F',m_{F'}}\Gamma P_{F',m_{F'}}, \tag{4.6.2}$$

and the excited states,

$$\frac{\mathrm{d}P_{F',m_{F'}}}{\mathrm{d}t} = -\sum_{F_{upper}} R_{F,m_F\to F',m_{F'}} \frac{\Gamma}{2}\frac{I}{I_{sat}}\frac{(P_{F,m_F}-P_{F',m_{F'}})}{1+4(\Delta/\Gamma)^2} - \sum_{m_F=m_{F'}-1}^{m_F=m_{F'}+1}\sum_{F=F'-1}^{F=F'+1} D_{F,m_F\to F',m_{F'}}\Gamma P_{F',m_{F'}}, \tag{4.6.3}$$

where (F, m_F) and $(F', m_{F'})$ are the hyperfine levels in the ground and excited states, with P_{F,m_F} and $P_{F',m_{F'}}$ being their respective populations. Here Γ is the natural linewidth, I is the beam intensity, I_{sat} is the saturation intensity, Δ is the detuning, $R_{F,m_F\to F',m_{F'}}$ is the transition line strength ratio, and $D_{F,m_F\to F',m_{F'}}$ is the decay rate probability. The three terms in Eqn. 4.6.2 and Eqn. 4.6.3 correspond to stimulated emission, absorption, and spontaneous decay, respectively. This formalism only considers closed transitions where the driving light field is resonant with the upper ground state, explaining why the one term found in Eqn. 4.6.1 is the spontaneous decay, and why only F_{upper} is considered in Eqn. 4.6.3. However, the rate equations can be adjusted to best model the system under consideration. Since we are dealing with a multilevel system, the value of $R_{F,m_F\to F',m_{F'}}$ will have to be calculated for every different transition. We define the line strength ratio by,

$$R_{F,m_F\to F',m_{F'}} = \left(\frac{d_{F,m_F\to F',m_{F'}}}{d^{\star}_{F,m_F\to F',m_{F'}}}\right)^2, \tag{4.6.4}$$

where $d_{F,m_F\to F',m_{F'}}$ are the dipole matrix elements of the hyperfine transition and $d^{\star}_{F,m_F\to F',m_{F'}}$ is the strongest transition between the two hyperfine levels[25]. The dipole matrix elements are given by,

$$d_{F,m_F\to F',m_{F'}} = (-1)^{2F'+J+I+m_F}\sqrt{(2J+1)(2F'+1)(2F+1)} \times \begin{Bmatrix} J & J' & 1 \\ F' & F & I \end{Bmatrix} \begin{pmatrix} F & 1 & F' \\ m_F & q & -m_{F'} \end{pmatrix}, \tag{4.6.5}$$

where J and J' are the ground and excited state spin-orbit momentum, I is the nuclear spin, and q is the polarisation-induced transition constant defined in the previous section. Here the elements in the curly and curved brackets correspond to the Wigner $6J$ and $3J$ symbols, respectively. These symbols provide an alternative mathematical formalism of the Clebsch-Gordan coefficients

[25] Although this normalisation is not technically required, it does produce a transition strength value between 0 and 1.

for angular momentum coupling[26]. In a similar fashion, the decay rate is given by,

$$D_{F,m_F\to F',m_{F'}} = \frac{1}{A}(2F'+1)(2J+1)\begin{Bmatrix} J & J' & 1 \\ F' & F & I \end{Bmatrix}^2 . \tag{4.6.6}$$

Notice how the decay probability does not rely on the light field (hence why there is no "q" term in Eqn. 4.6.6)[27]; however, within the same hyperfine level F, the decay probability into any of the m_F states is equal and must sum to unity. At most, only three m_F transitions are permitted without violating the selection rules. We introduce the constant A to account for this modification to the spontaneous decay probability and summarise the values it can take, subject to the allowed number of transitions in Table 4.1 below.

Hyperfine transition	**Sublevel transition**	**Value of A**
$\Delta F = -1$	Any	3
$\Delta F = 0$	Any	2
$\Delta F = 1$, for $F' \geq 2$	$m_{F'} = \pm F'$	1
	$m_{F'} = \pm F' \mp 1$	2
	$-F'+2 \leq m_{F'} \leq F'-2$	3

Table 4.1: Modification constant A to the decay probability subject to the allowed hyperfine and magnetic sublevel transitions, where $\Delta F = F' - F$ and $\Delta m_F = m_{F'} - m_F$.

The first two conditions of Table 4.1 are straightforward: when decaying from a lower F' state to a higher F state, there are no restrictions on the possible m_F levels to occupy; however, when decaying from a similar hyperfine state $F' \to F = F'$, the only allowed sublevel transitions are $\Delta m_F = \pm 1$, as $\Delta m_F = 0$ violates the selection rules. Since the quantum numbers are directly linked to the angular momentum of the system, upon de-excitation, the atoms re-emit a photon into the light field, with a unit of angular momentum equal to $\pm\hbar$. Under conservation laws, the final decay state must have an angular momentum opposite to the photon; however, $|F, m_F\rangle \to |F' = F, m_{F'} = m_F\rangle$ transitions possess an unchanged angular momentum after photon re-emission, thereby violating conservation laws and hence are forbidden[28]. When considering a state decaying from a higher F' to a lower F value, one of three transitions is allowed for the magnetic sublevels. For the furthest apart sublevels, only a single transition is allowed as only one state exists that obeys $\Delta m_F = \pm 1$ (this decay process, coupled with the right pumping scheme, is how we generate the closed transitions discussed in the previous section), and for the second furthest states, only two transitions are allowed (again, only two states are present that obey $\Delta m_F = 0, \pm 1$), and finally for any $m_{F'}$ in between, any of the three magnetic sublevel transitions can occur[29]. Note that Table 4.1 does not include the case of a $\Delta F = 1$ system, where $F' = 1$, since there is only ever one decay channel and hence $A = 1$ is always expected.

Despite their intimidating appearance, the rate equations found in Eqn. 4.6.1, Eqn. 4.6.2, and Eqn. 4.6.3 are very much identical to the population equations found in Eqns. 4.3.20 (the first and

[26]These symbols have been studied in the context of abstract algebra pertaining to group theory and possess some interesting properties (i.e. the $3j$ symbol has cyclic permutations).

[27]As it should, this process is completely random.

[28]Note that these transitions are not forbidden for two photon absorption or emission.

[29]It might be easier to observe this for the case where $\Delta F = 1$ by looking at Fig. 4.9.

last equation), with the minor changes to the scattering rate and considering all possible allowed transitions[30]. Although these equations can be used to model the population of any hydrogen-like atom, we only concern ourselves with rubidium vapour. In Fig. 4.10 we demonstrate how the population of the hyperfine upper ground state changes over time for ^{87}Rb, pumped with σ_+ and σ_- light.

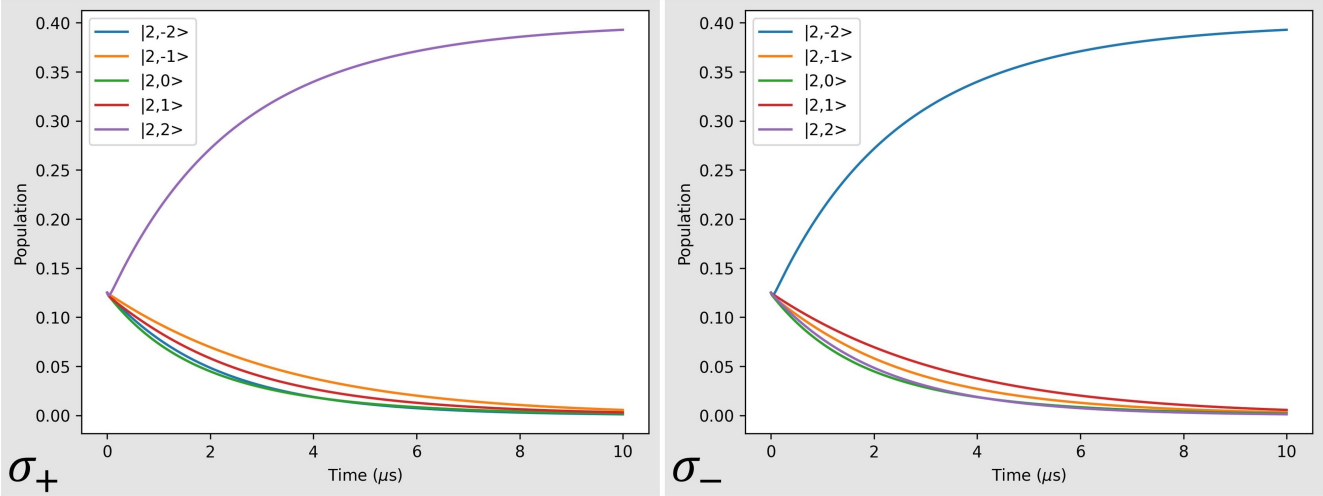

Figure 4.10: Time evolution of the upper ground state population of ^{87}Rb, pumped with σ_+ and σ_- polarised light. The beam is tuned to $|F = 2\rangle \rightarrow |F' = 3\rangle$ transition with an intensity of $I = 0.1I_{sat}$.

In this model, we assume an equal population distribution in the ground state sublevels prior to the atomic interaction with the light field. Since ^{87}Rb has eight magnetic sublevels between the $F = 1$ and $F = 2$ ground states, the probability of finding the atom at any particular sublevel at $t = 0$ is given by 1/8. Unfortunately, the atoms in the lower ground state will not interact with the optical field since they are far off-resonance and are considered lost in our system.

The change to the atomic population as a consequence of the pumping process is relatively straightforward; if we consider the case for σ_+ pumping, an atom in the m_F ground state will always be excited to the $m_{F'} = m_F + 1$ state under the influence of the light field. For example, an atom sitting in the $m_F = -1$ ground state will be pumped into the $m_{F'} = 0$ excited state, where the random nature of spontaneous decay could leave it in any of the $m_F = -1$, $m_F = 0$, or $m_F = 1$ sublevels, where the atom is once again pumped into any of the $m_{F'} = 0$, $m_{F'} = 1$, or $m_{F'} = 2$ excited states when interacting with the driving field. This process will continue until the atom reaches the $m_F = 2$ stretched state, leading to the $|F = 2, m_F = 2\rangle \rightarrow |F' = 3, m_{F'} = 3\rangle$ closed transition, where decaying into any another ground state is prohibited, leading to an increase in the population of the $|F = 2, m_F = 2\rangle$ state over time as shown in the left graph of Fig. 4.10. This process works exactly the same for σ_- pumping, where the majority of atoms will accumulate in the $|F = 2, m_F = -2\rangle$ stretched state, resulting in a population increase over time, as illustrated in the right graph of Fig. 4.10.

4.7 Summary

In this chapter, we introduced the interaction of matter with an optical field for a two-level system, leading to the derivation of the optical Bloch equations, and later extended and simplified the

[30]Which is why these equations have so many sums.

formalism to multilevel systems to obtain an expression for the population rate equations. We discussed the energy structure of the two isotopes of Rubidium and their behaviour under the influence of an external magnetic field. Lastly, we covered the concept of Doppler broadening and looked at the outcome of optical pumping schemes as a consequence of atomic interaction with polarised light.

Chapter 5

Laser light for atomic interaction

5.1 Introduction

From the previous section, we know that atoms possess a complex internal structure due to the numerous couplings of their orbital angular momenta. The momentum transfer caused by the interaction of the atoms with an external light field is known to change the kinetic behaviour of the atoms, leading to fascinating phenomena such as recoil cooling, which is required for many studies involving atomic trapping. However, the majority of work involving warm vapour is more concerned with probing the internal dynamics of the atoms, necessitating the use of a monochromatic and coherent light source with frequency stability on the order of the natural linewidth (around 6MHz for the D2 line of Rb [160, 161]), allowing for precise matching of the light wavelength to the atomic transition. One light source that meets all of the aforementioned characteristics is a diode laser. Diode lasers are not usually used by themselves and are instead housed inside cavities that offer a wide range of tunable output wavelengths, making them a convenient tool to probe a wide range of atomic transitions without the need for additional light sources.

There are many different types of diode laser cavities, with some of the most common being external cavity diode lasers (ECDL), vertical cavity surface-emitting lasers (VCSEL), and distributed Bragg reflectors (DBR), with operational frequencies spanning a wide range of the electromagnetic spectrum. For our applications with rubidium vapour, we use a near-infrared (NIR) laser diode (around 780nm output wavelength), housed inside an ECDL[1], with a tunable frequency range of around 9.4GHz, producing a linewidth spanning a few hundred kilohertz, with a maximum output power of about 120mW. This chapter describes the method by which ECDLs work and the requirements to prepare them for usage in experiments with atomic vapours.

5.2 External cavity diode lasers (ECDL)

The linewidth of a typical NIR diode laser spans a few hundred megahertz and possesses poor tunability. Additionally, they are particularly sensitive to temperature and current changes [172], lacking the required precision and stability for experimental use with atomic vapours. However, by building an external cavity around the laser diode (LD), we introduce a frequency selection mechanism controlled largely by the properties of the cavity. Over the years, many different cavity designs have been proposed, an example of which is the filter-stabilised ECDL, where the wavelength

[1] Although I have very briefly used a DBR laser in my investigation summarised in Section 6.5 (the reason is discussed in the section), the majority of my work with rubidium vapour was done with an ECDL.

selection is done using an interference filter [173, 174]. However, the most common and cheapest cavity design is the Littrow configuration [172, 175], using a reflective holographic grating. In this configuration, the LD is usually placed in a collimating mount housing a collimating lens (CL) with a short focal length, where the input beam (IB) is incident on an angled reflective grating (RG), which splits the beam into a spectrum of wavelengths. In the Littrow configuration, the ECDL output beam is the zeroth diffraction order (0^{th}) from the grating, while the first diffraction order (1^{st}) is back diffracted into the laser diode, forming an external cavity of length L and modifying the diode gain medium, thereby amplifying the selected wavelength. It is worth noting that back reflection of the first diffraction order is only possible when the angle of the beam incident on the grating equals the diffraction angle of the zeroth order[2]. An illustration of the Littrow configuration can be found in Fig. 5.1a below.

Although Littrow ECDLs are useful tools for atomic physics research, a major flaw in their design is that the output beam path is coupled to the grating angle, which controls the operational wavelength of the ECDL. This means the angle of the output beam path will change as the laser frequency is scanned, as illustrated by the blue beam in Fig. 5.1b. A modification to the Littrow configuration introduced by C. J. Hawthorn, K. P. Weber, and R. E. Scholten in [176] by introducing a mirror (M) parallel to the grating (at 45° relative to the beam path) as illustrated in Fig. 5.1c. The way it works is quite simple, since the 0^{th} diffraction order from the grating is diffracted by an angle equal to 2θ, where θ is the angle to the grating normal ($\hat{n}$) from Fig. 5.1c. If the grating is rotated by an angle α, the 0^{th} order beam diffracted from the grating is now rotated by an additional 2α. However, since the mirror is facing the opposite direction and is also rotated by α, the beam reflected off the mirror surface is rotated back by an angle of 2α, ensuring the output beam path remains unchanged[3].

Since the grating diffraction angle depends on the groove spacing[4], we can see from Fig. 5.1 that a larger cavity length results in a narrower laser linewidth as fewer wavelengths are fed back into the laser diode. However, another quantity to take into account is the cavity's free spectral range (FSP), mathematically expressed as the frequency range $\Delta\nu$, given by $\Delta\nu = c/2L$, where c is the speed of light and L is the cavity length. This quantity determines the mode hop-free tuning range of the cavity (i.e. the laser frequency scanning range). Usually, a larger mode hop-free range is desirable, which requires a shorter cavity; however, longer cavities are significantly easier to align as they are more sensitive to the grating angle. Ideally, a balance between the two is required to generate an ECDL with an optimal linewidth and frequency tuning range. However, there are additional parameters to consider when tuning an ECDL. Since the diode is electrically pumped, it is sensitive to variations in temperature and current, which affect the output spectrum. Therefore, ECDL optimisation requires careful consideration of all these parameters (cavity length, temperature, and current).

[2]Which is identical to the law of reflection (see Section 2.2 for more information).

[3]The mirror and grating are usually housed in the same mount. When the mount is rotated, both their incident angles are changed.

[4]Alongside the wavelength and desired diffraction order, however, both quantities are assumed to remain unchanged for Littrow ECDLs.

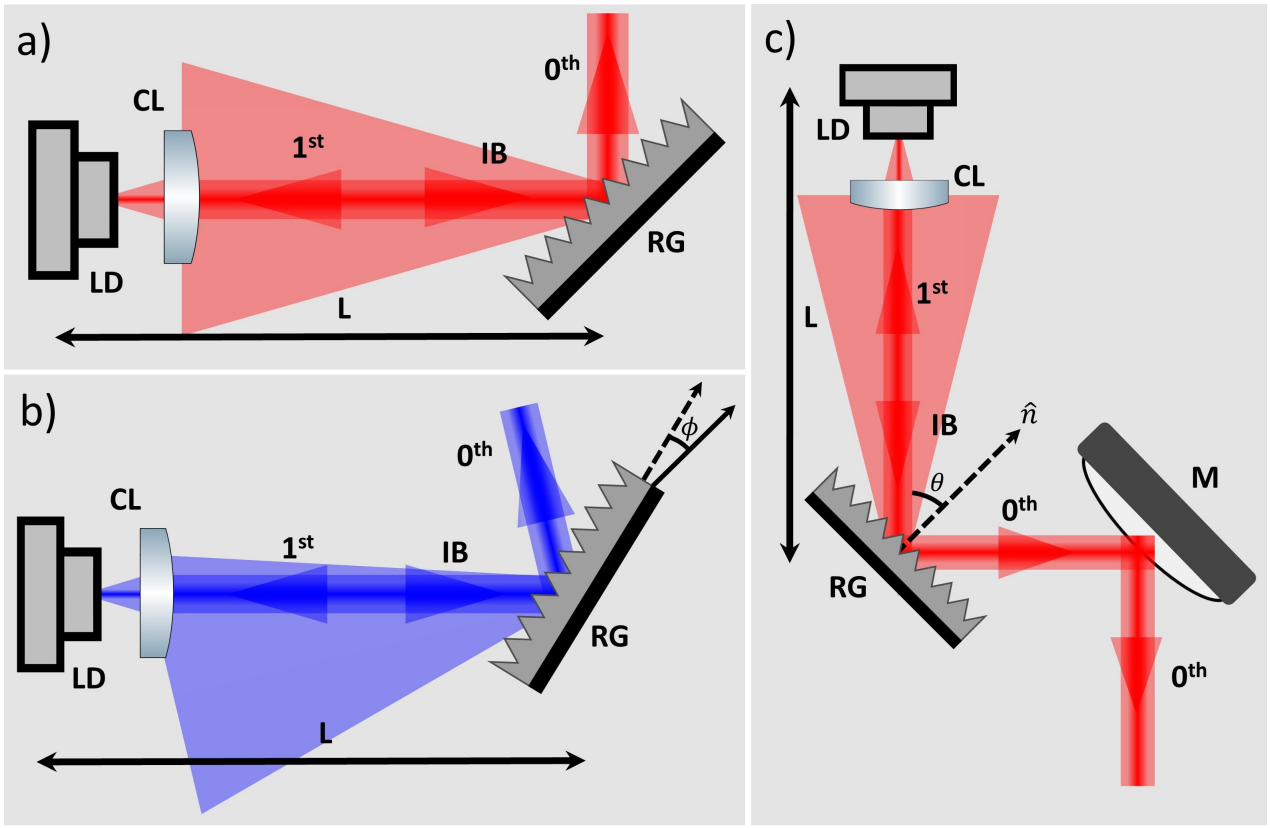

Figure 5.1: Littrow configuration external cavities of length L, formed by a laser diode (LD) input beam (IB) propagating through a collimating lens (CL) into a reflection grating (RG). Here, the first diffraction order (1^{st}) from the grating is back diffracted into the LD, modifying the output frequency, while the zeroth order (0^{th}) serves as the output light. a) A grating angled at 45° relative to the IB. b) A grating rotated by an angle ϕ, shifting the output beam path. c) A modified Littrow configuration introducing a mirror (M) to remove the path dependence on the grating angle.

Here in the atom's lab at the University of Glasgow, our experiments run on our homemade laser systems, utilising both the Littrow configurations and its modified version with the mirror. These lasers were manufactured by our colleagues in the mechanical workshop using aluminium parts, based on the designs of [172, 176]. In our warm vapour experiment, we employ a single modified Littrow ECDL (see Fig. 5.2), where the design consists of five parts, namely: a mounting platform, an aluminium chassis, the collimating tube, a grating and mirror mount, and a front plate. The laser diode is inserted into a collimating tube housing an adjustable threaded aspherical lens (a Thorlabs C110TME-B) with a 6.24mm focal length. The diode is held in place inside the tube with a brass back plate and three small screws. The collimating tube is then placed inside the ECDL chassis and secured in place by a grub screw, offering adequate contact between the diode and the cavity's main body for temperature stabilisation. A visible holographic blazed grating[5] with grove spacing of 1800/mm (Thorlabs GH13-18V) and a small square mirror are glued on a custom mount[6], which is attached to the front plate with two springs held in place by a set of two small metallic rods, as seen in Fig. 5.2a. The front plate is then attached to the chassis with two

[5]More information on how blazed gratings work can be found in [177].

[6]It is critical to ensure the grating (if blazed) is pointing in the right direction, as indicated by an arrow placed on the side of the grating. In the past, someone in our lab, who shall remain unnamed, glued all the ECDL gratings the wrong way round, forcing my supervisor Sonja and I to go around heating the grating mounts (using a heat gun at 300°C) to weaken the superglue hold and fix their orientation.

more springs, once again secured by a pair of metal rods[7]. The whole ECDL body sits on top of a 40mm × 40mm peltier module for temperature dissipation with a 10kΩ temperature sensor slotted in a small hole drilled into the chassis, right above the peltier unit for temperature feedback[8]. Finally, the assembled ECDL, with the peltier beneath, sits on a mounting platform with a M6 screw track to bolt the ECDL into the optical bench. A schematic of the ECDL internals can be found in Fig. 5.2b below.

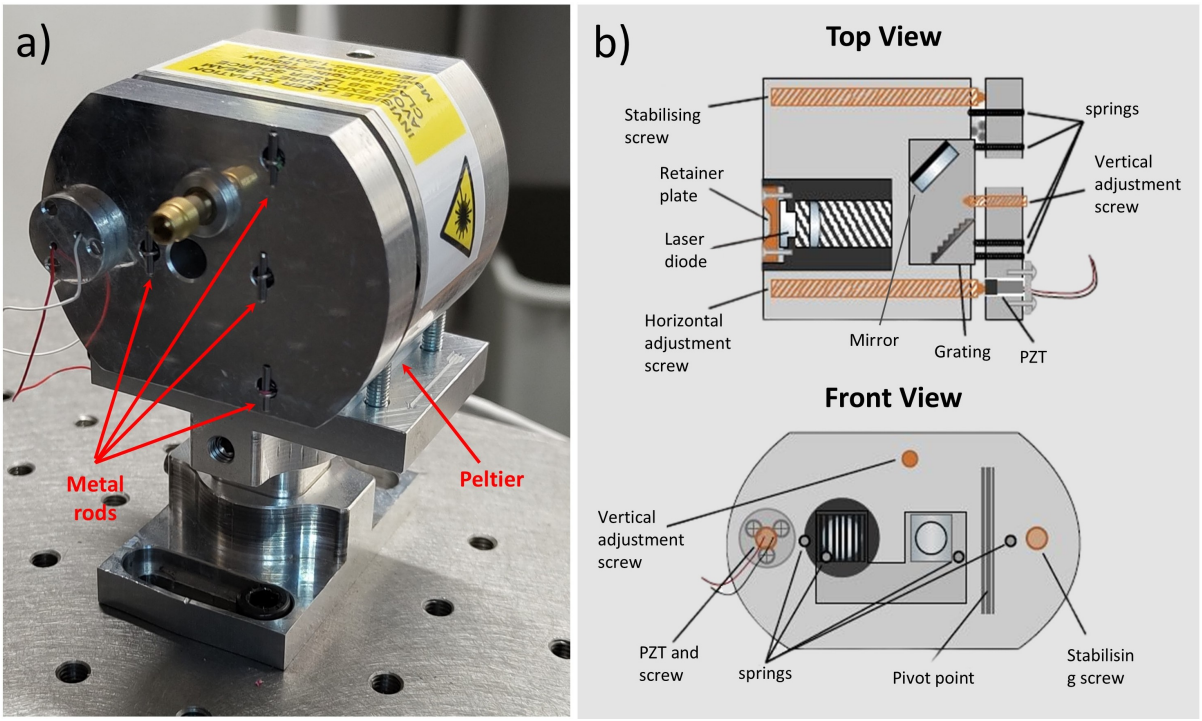

Figure 5.2: Schematics and image of our modified Littrow configuration ECDL used in the warm vapour experiment. a) Image of the ECDL, highlighting the position of the peltier and the metal rods holding the grating and mirror mount to the front plate and the front plate to the ECDL chassis. b) Front and top view schematics of the ECDL internal structure without the peltier and mounting platform. Schematics taken from [20].

Aligning an external cavity is a tedious process that can take up to a few hours even for the most skilled of practitioners, since there are a number of parameters to consider. However, before aligning the cavity to lase at the desired wavelength, we must first ensure the output beam from the diode, leaving the collimating tube, is indeed properly collimated. First, the collimating tube is removed from the ECDL chassis and clamped on a V-mount (Thorlabs VC3C/M). The beam shape throughout propagation is then observed for a distance comparable to the propagation distance of the light in the experiment in question. If the beam experiences significant changes to its profile (focusing or diverging) along the propagation distance, the collimating lens is incorrectly positioned and must be adjusted with a spanner wrench (like the Thorlabs SPW301). Note that since the diode output is a transverse mode of propagation (see Section 1.5), the beam size is still expected to change after traversing a sufficient distance; hence, we only concern ourselves with the beam

[7]In the past, these metallic rods were made from hardened metal; however, since they are easy to misplace, our friends at the mechanical workshop made a few more for us out of steel, which is strong enough to withstand the tension of the spring without deforming.

[8]Both the peltier and thermistor are covered in thermal paste to aid with temperature flow.

shape along a distance comparable to our experimental setting[9]. Once we are satisfied with the collimation, the tube is placed back into the aluminium mount and secured with the grub screw. The ECDL is now ready to be aligned for experimental use.

In principle, the alignment procedure itself is quite simple; however, its delicate nature is the reason for its increased complexity. The first step is to set the diode current to its lasing threshold; for our diodes, it constitutes a current of somewhere between $37\text{mA} - 41\text{mA}$, which generates an output beam with a power of $< 1\text{mW}$. It is vital to operate the diodes around their lasing threshold, since the diodes themselves are electrically pumped cavities, where the reflection from the front facet acts as feedback to the laser chip, forcing it to lase according to the properties of the internal cavity[10]. By running the diodes at threshold, we ensure their gain medium is amplified according to the properties of the external cavity when aligned and not their internal one (i.e. the diode itself)[11].

The next step is to adjust the horizontal wavelength selection screw until we observe a maximum output power on the power meter. Since these diodes are manufactured to run optimally around $780\text{nm} - 785\text{nm}$, this increase in power corresponds to the region of the cavity where our desired wavelength resides. Now comes the tricky bit, where we have to tune the vertical screw responsible for the feedback. What complicates this procedure is that changes in the output beam power are extremely sensitive to the vertical tilt angle of the grating. This process might have to be repeated a few times (i.e. adjusting the horizontal and vertical screws of the ECDL) until a spike in beam power is observed, measuring around $3\text{mW} - 5\text{mW}$, indicating an aligned cavity. Although the horizontal and vertical tilt axes of the grating are assumed to be independent, they can be coupled if the grating is not glued properly, which increases the difficulty of the alignment procedure[12].

To check the cavity is aligned properly, we introduce a spectrometer (Ocean Optics HR4000) to the beam path and ensure only a single linewidth is observed. When the horizontal screw on the ECDL is adjusted, the peak should move smoothly without any jumps. If secondary peaks begin to emerge or the laser spectral line experiences mode hops as the wavelength is scanned, the entire alignment process needs repeating, once again setting the diode current to its lasing threshold. Once we ensure the ECDL is aligned, the current can be adjusted to the desired value for experimental use.

5.3 Doppler free spectroscopy

Once the ECDL feedback has been aligned and tested, all that is left is to tune it to the desired atomic transitions of rubidium. Since our spectrometer lacks the sensitivity required to accurately determine the position of the atomic transitions, we tune our laser frequency using the atoms themselves. Experimentally, we use a low-pressure Rb reference cell at room temperature (the likes of Thorlabs GC25075-RB). As previously stated, the natural linewidth of the Rb transitions we are

[9]For our work, it is adequate to observe and correct for the changes in beam size by eye; however, for more sensitive applications, a beam profiler should be used instead.

[10]Note that the diode cavity formed by its back and front facet is technically still an external cavity. However, we label it as the internal cavity for differentiation. Additionally, this issue becomes much more problematic with high-powered diodes, where the contributions from the internal cavity can no longer be ignored.

[11]This problem becomes irrelevant if the diode has no front facet. However, removing the front facet risks destroying the semiconductor chip when exposed to the elements. An alternative solution is to use a laser diode with an angled front facet where there is no back reflection into the chip.

[12]In our labs, we have a decommissioned ECDL whose old grating had to be removed. However, the position where the grating sits on the mount has been excessively scratched when attempting to clean any residual superglue, leaving the newly inserted grating slightly crooked. Till this day I could never get that laser to work properly.

interested in (the D2 line) is around 6MHz, where the hyperfine splitting is on the order of a few tens to a few hundred megahertz, so our laser linewidth of a few hundred kilohertz is sufficient to resolve them all. Since our atoms are at room temperature, the atomic transitions are broadened by the Doppler effect, making it difficult to resolve our hyperfine transitions. A derivation of the Doppler effect from the conservation of momentum and energy can be found in Section 4.4.

A solution to this problem is to use the technique discussed in [178], called Doppler free saturated absorption spectroscopy (satspec)[13], which makes use of two counter-propagating laser beams, known as the pump and probe beams. Experimentally, we employ a pump with a power at least five times larger than the probe, which lets us work in what is known as the weak probe regime [179, 180]. The reasons for this will be discussed in Chapter 6. Generally, there are two experimental implementations of satspec, as seen in Fig. 5.3. In the more common setup, horizontally polarised light (red) propagates through a polarising beam splitter (PB) into the rubidium cell (Rb), pumping the atoms. The beam is then incident on a quarter waveplate (QWP) set at 45°, turning the beam circular (orange), before being reflected back by a planer mirror (M). This mirror changes the handedness of the beam (pink), where its circularity is undone by the QWP, resulting in a vertically polarised output (blue), which propagates back through the Rb cell probing the atoms before being reflected off the PBS and into a photodiode (PD), as illustrated in Fig. 5.3a. The second implementation of satspec is slightly different in construction. In this scheme, a diagonally polarised light source is split into its horizontal (red) and vertical (blue) components, where the vertical pump beam is reflected off two mirrors and into the Rb cell by a second PBS. Meanwhile, the horizontally polarised probe beam transmits through both the PBS and Rb cells before terminating at the PD, as demonstrated in Fig. 5.3b.

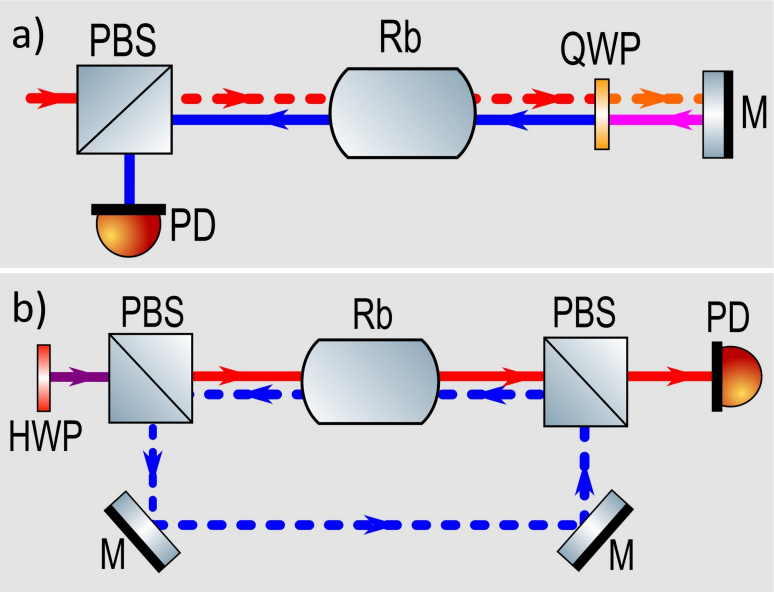

Figure 5.3: Experimental configuration of saturated absorption spectroscopy (satspec). a) The more common and simple satpsec setup, where the same beam pumps and probes the atoms. b) A slightly more complicated satspec setup, where the beams are overlapped in an interferometer-like style. Here red is a horizontal beam, blue is vertical, purple is diagonal, and circular is both orange and pink. Note that the beams are separated for clarity, where the dashed lines correspond to the pump beam, while the solid lines are the probe.

Although the satspec configuration mentioned in Fig. 5.3a is simple to construct, having the same beam act as both the pump and probe could lead to some inconveniences. The first is that it is difficult to control the ratio of the pump-probe powers, as the only available options being either neutral density (ND) filters or non-polarising beam splitters (NPBS). However, they both offer discreet changes to the light intensity, which could make it difficult to achieve the desired power ratios[14]. The second and more important concern being when the pump beam excites the

[13] In some literature, this technique is also called hyperfine pumping.

[14] One could calculate the value of the required ND filter and stack them (since they stack linearly) to achieve the desired result.

atoms, the frequencies corresponding to the atomic transitions in the light field have been interacted with. Therefore, when the reflected beam probes the Rb atoms there is a lower intensity of light corresponding to the transition frequencies, leading to a weaker transmission signal for the probe. However, both these issues are irrelevant for the satspec configuration seen in Fig. 5.3b. Although it requires more optical elements, it remains relatively simple to construct[15] and offers more control over the ratio of the pump-probe powers via the HWP before the PBS. Additionally, since the pump and probe are independent beams, the atomic frequencies are not depleted in the probe, providing a better satspec signal.

The role of the pump in satspec is to excite the atom and depopulate the ground state when the laser frequency is resonant with the atomic transition. This condition is met for any atom whose Doppler shift frequency (ω_D) compensates for the difference between the laser frequency (ω) and the frequency of the atomic transition (ω_0). Since the Doppler shift frequency from Eqn. 4.4.4 is given by $\omega_D = \pm(\omega - \omega_0)$, if the pump sees the atoms that are red shifted with a frequency of $\omega_1 = (\omega - \omega_0)$, then the probe sees the atoms blue shifted by a frequency of $\omega_2 = -(\omega - \omega_0)$, since both beams are counter propagating. If the same atom interacts with both the pump and probe (i.e. $\omega_1 = \omega_2$), then either $\omega = \omega_0$ or $\omega = 0$, and since $\omega \neq 0$, the Doppler shift for atoms interacting with both beams cancels out. Note that since the majority of the atoms have been excited by the strong pump, the probe beam observes fewer atoms in the ground state, which translates to a reduced absorption of the probe beam. If there are multiple atomic transition frequencies in the laser scan range, the pump and probe beams could be interacting with the same atoms at different transitions. For example, consider two atomic transitions, ω_{01} and ω_{02}. If an atom has the same Doppler shift frequency for both transitions but in opposite directions (i.e. red shifted to one and blue shifted to the other), we can express these frequencies as $\omega_{01} = \omega - \omega_D$ and $\omega_{02} = \omega + \omega_D$. From these two equations, we notice an atom whose Doppler shift is at half the difference between the two transitions (i.e. $2\omega_D = \omega_{02} - \omega_{01}$) is resonant with both, generating a peak halfway between the two actual transitions (i.e. at $\omega = (\omega_{02} + \omega_{01})/2$). These peaks are known as cross-over peaks and are usually stronger than their respective transition peaks. An example of an output signal from a satspec setup can be found in Fig. 5.4 below.

[15] Perhaps I am biassed by stating their construction is simple, since I spend endless hours perfecting the alignment of my spectroscopy setups to the smallest of details. However, such practices could severely backfire; in fact, I remember a time when my colleague Sphinx Svensson was complaining about a rogue signal messing with their satspec. When the cause was investigated, we found out they manage to perfectly align their optics, where a back reflection from an element more than a metre away was interfering with the satspec PD. The pursuit of perfection in an experimental setting is a time-wasting foolish endeavour, a lesson that if I had managed to learn, I might have achieved more during my time as a PhD student.

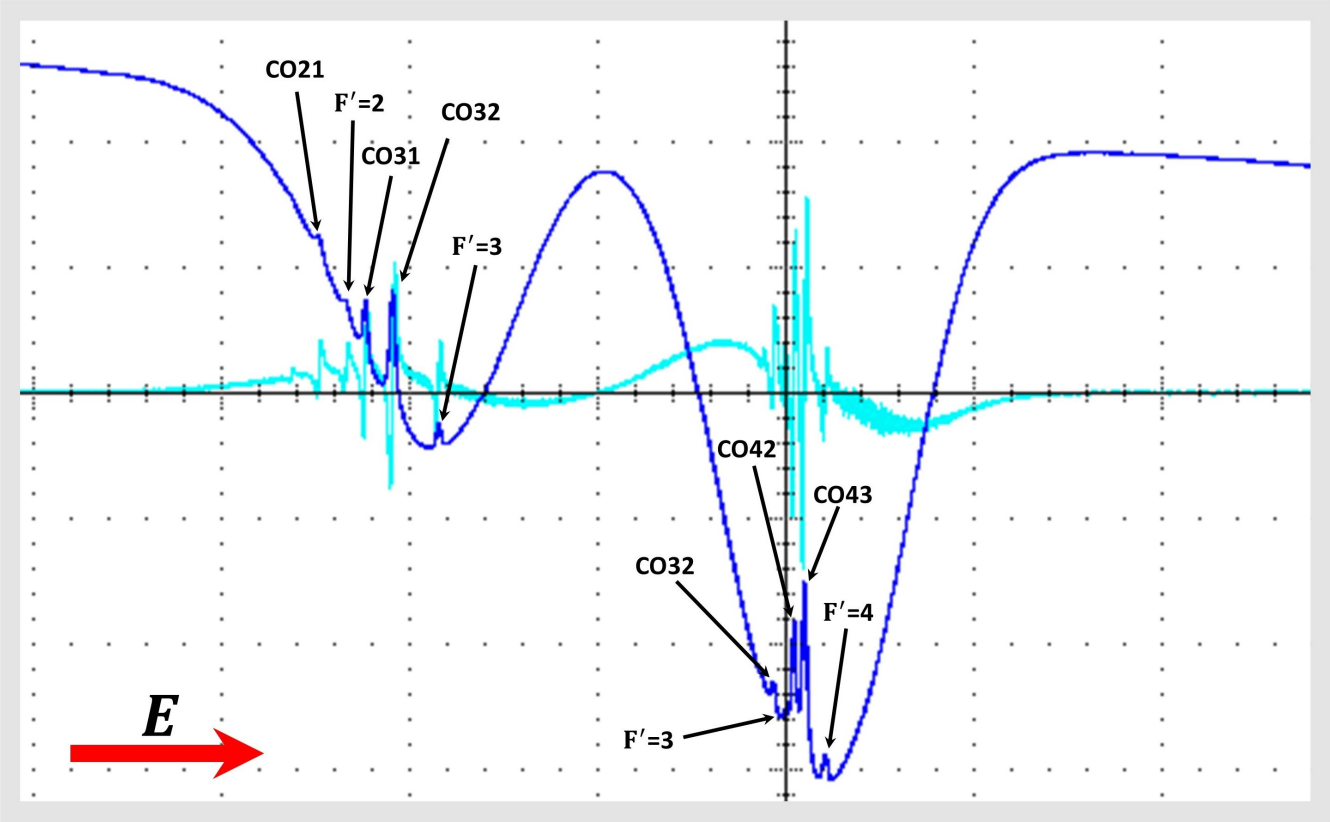

Figure 5.4: Satspec signal (dark blue) of the D2 upper ground level transitions for both ^{85}Rb (right) and ^{87}Rb (left). The wide dips correspond to the Doppler broadened profile of the upper ground-level transitions, while the individual Lorentzian shaped peaks are the hyperfine transitions and the cross-over (CO) peaks. All transitions are labelled with the exception of the last transition from both spectra (transitions are too weak). Note the red arrow corresponds to the direction of increasing energy (or frequency).

5.4 Laser frequency stabilisation

If left untouched, an ECDL experiences frequency drifts larger than the atomic linewidth on timescales of a few seconds, making it difficult to keep the laser frequency tuned to the atomic hyperfine transitions. There are several parameters that could be considered responsible for this drift, with the most obvious being air currents and vibrational noise. However, some simple precautions are in place to account for these effects, such as housing the ECDL inside a plastic box, eliminating the contributions from the air currents generated by the air conditioning unit. Additionally, the optical bench is equipped with stabilisation supports that mitigate the effect of vibrations experienced by the optics. However, drifts in the laser frequency are more likely associated with fluctuations in the current and temperature profiles of the ECDL. The continued usage of the ECDL heats up the diode laser, causing the peltier to dissipate the excess heat based on the readings from the thermistor. The problem is, the thermistor is not in direct contact with the diode chip, resulting in a delay between the heat generated by the diode and the changes in temperature measured by the thermistor before alerting the peltier to dissipate the heat. This delay affects the length of the diode's internal cavity, effectively changing the gain medium and causing frequency drifts over time. Since these drifts remain below the mode-hope-free tuning range of the ECDL, active feedback with the current or a piezoelectric transducer (PZT) should compensate for their

effect[16]. The easiest method to incorporate this experimentally is to generate an error signal that crosses zero at the peaks of the atomic transitions and cross-over peaks. A signal with these features can be produced from the derivative of the atomic spectrum, which is used as the reference for the MOGLab diode laser controller's dither locking. The cyan signal found in Fig. 5.4 is an example of such an error signal. These laser electronics are able to produce a 250kHz oscillator signal to dither the laser current or drive an external modulator (the PZT)[17]. A detailed guide on how to laser lock with the MOGLab boxes can be found in [181].

5.5 Laser control with acousto-optic modulators (AOM)

In our main experiment described in Chapter 6.6, there was a need for greater control over the frequency of the light field to quantify the observed magneto-optical effects and associate them to a specific frequency on the atomic spectrum. For this reason, an acousto-optic modulator (AOM) was introduced to the experimental setup. These devices consist of a crystal in contact with a piezoelectric transducer (PZT) that modifies its refractive index when subjected to mechanical stress. Usually they are driven by a radio frequency (RF), ranging from a few megahertz to a few gigahertz. When the PZT strikes the crystal, it generates a travelling acoustic wave with a changing refractive index, behaving like a Bragg grating. When an input light field with a frequency of ω_i propagates through the AOM crystal oscillating with a radio frequency given by ω_{RF}, the output beam will split into several diffracted modes, whose frequencies are given by,

$$\omega_m = \omega_i + m\omega_{RF}, \tag{5.5.1}$$

where m is an integer denoting the order number (i.e. $m \in \mathbb{Z}$, where $\mathbb{Z}$ denotes the set of all integers). The shift in frequency occurs via simple energy and momentum transfer between the phonons (sound particles) and the photons (light particles). Note that positive orders (i.e. $m \in \mathbb{Z}^+$) are diffracted away from the PZT, while negative orders (i.e. $m \in \mathbb{Z}^-$) are diffracted towards the PZT. The amount of light diffracted into the non-zero orders depends on the amplitude of the RF signal driving the PZT, which controls the strength of the acoustic wave and diffraction efficiency. These diffraction orders are a result of momentum transfer between the photons and phonons, with each order satisfying its specific Bragg condition[18]. Since multiple collisions of the light field with the sound wave is possible, the AOM will usually diffract the incoming beam into more than one diffraction order. The AOMs we use have efficiencies for the first diffraction order of

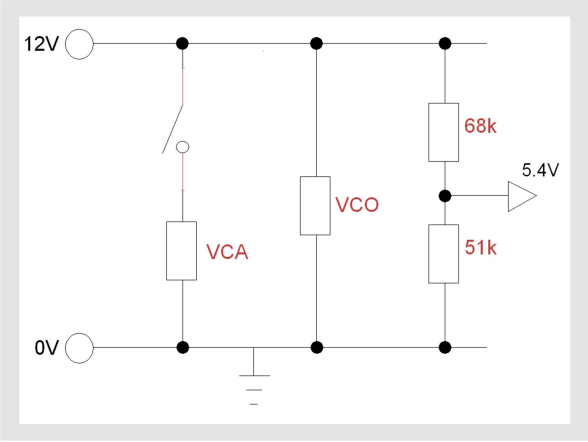

Figure 5.5: A simple circuit to control the AOM operation, consisting of a voltage control oscillator (VCO), a voltage control attenuator (VCA), resistors, and a switch.

[16] A PZT works by converting a voltage into mechanical work and vice versa. Compensating for frequency drifts requires applying a correcting voltage that adjusts the cavity length, bringing the laser back to the desired frequency.

[17] Unfortunately, for some reason, we never had much success locking the laser frequency by modulating the PZT and opted to dither the laser current instead.

[18] The Bragg condition is given by $m\lambda = 2\Lambda \sin(\theta)$, where m is the diffraction order, λ is the photon wavelength, Λ is the phonon wavelength, and θ is the diffraction angle [182].

around 68% to 80%[19].

Unfortunately, due to time constraints, we could not programme the AOM to work with a DAQ card, leaving us to manually control the AOM using a simple voltage control oscillator and voltage control attenuator circuit, as shown in Fig. 5.5. Varying the VCA changes the amplitude of the modulation signal, which will adjust the brightness of the diffraction orders, as illustrated in the left image of Fig. 5.6. When compared to a phase grating, the change is analogous to altering the height of the grooves, affecting the efficiency of the diffraction orders depending on the angle of the incoming light field[20]. On the other hand, variations to the VCO will change the modulation signal period, which is the same as changing the grating grooves (i.e. changing the number of lines per mm) and adjusting the separation distance between the diffraction modes, as illustrated in the right image of Fig. 5.6 below.

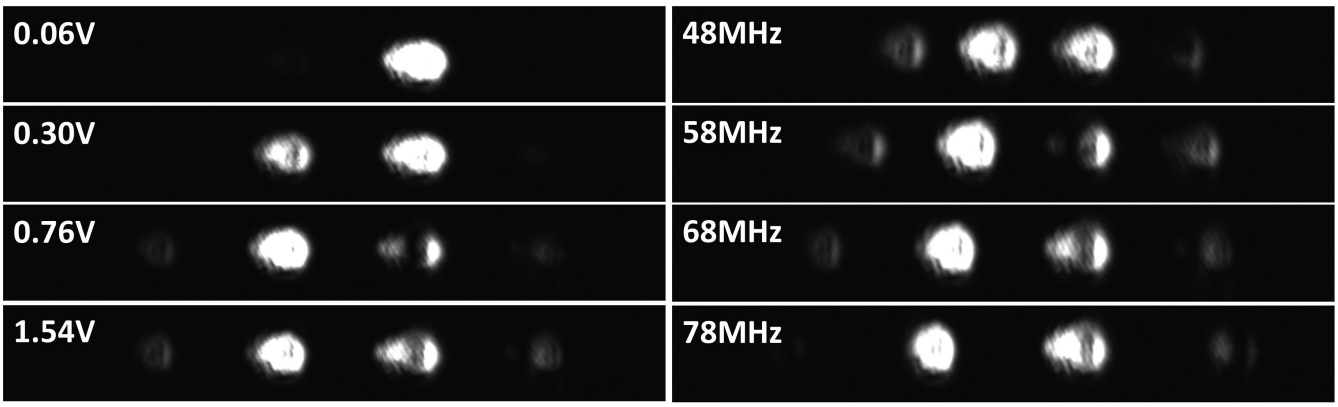

Figure 5.6: The effect of changes to the modulation signal on the diffraction orders. On the left images, the VCA is changed (signal amplitude), and on the right, the VCO is varied (signal period).

Since the beam angle changes when the RF is scanned, constant realignment of the optics will be required, which is not ideal in an experimental setting. A solution to this problem is to implement a double-pass AOM configuration [183], modifying the diffraction mode frequency by $\omega_m = \omega_i + 2m\omega_{RF}$. The setup is quite simple to understand[21], where a diagonally polarised beam is split into its horizontal and vertical components using a PBS, and the transmitted beam propagates through an iris opened just enough to let the beam through[22]. The beam is then focused into the AOM with a lens (L), which generates the diffraction orders. Another lens (L) is then positioned centrally, collimating the selected mode order, before it propagates through a second iris used for physical mode selection. Finally, the light passes through a quarter waveplate (QWP), turning the beam circular, which is reflected back by a mirror (M), inverting the beam's handedness. The light then propagates back through the QWP, undoing its circularity and generating a vertically polarised output. The beam is then transmitted through the AOM again, modifying its frequency once more before propagating towards the PBS, where it is reflected into the main experiment, as illustrated in Fig. 5.7 below. A detailed guide on setting up a double-pass AOM configuration can be found in [20, 70].

[19] Usually we are somewhere in the mid 70%.

[20] Normally the height of the groove is fixed; however, in the case of the AOM, the input beam is fixed and the grating height is changed to optimise the diffraction order efficiencies.

[21] However, setting it up takes some practice.

[22] This iris is very important for accurate alignment of the back reflected beam.

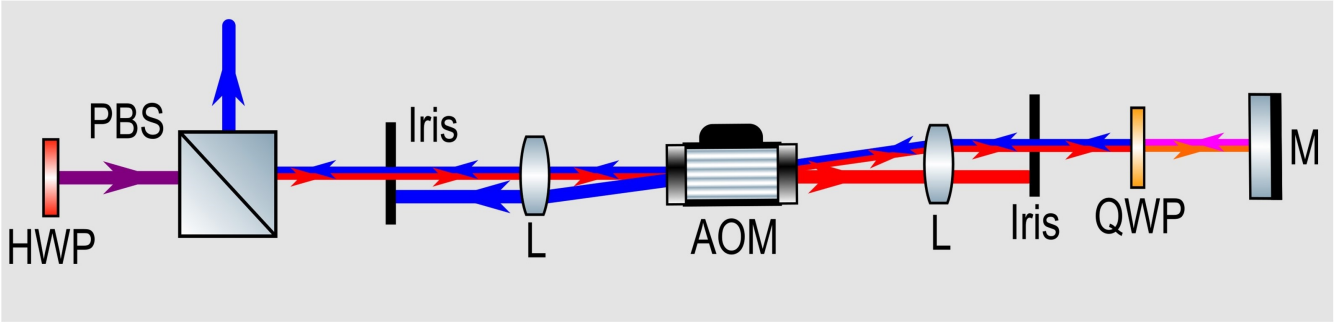

Figure 5.7: Experimental configuration of a double-pass AOM. Here the line colours indicated different polarisations, where red is horizontal, blue is vertical, purple is diagonal, while orange and pink are circularly polarised.

5.6 Power broadening: A brief investigation

In this section, we provide a summary of a brief investigation we conducted on the effects of power broadening on the peaks of the atomic transition for different ratios of pump-probe beam powers. Since our main work discussed in Chapter 6 involved the implementation of polarisation spectroscopy (polspec) as the starting point, a thorough investigation of the experimental configuration was necessary to quantify the behaviour of the system and develop our understanding of how this Doppler free spectroscopic technique works before adapting it for use with a spatially varying probe beam. Furthermore, this investigation will prove useful when optimising the saturated absorption spectroscopy (satspec) signal used to monitor the behaviour of the ECDL, which will eventually be used for stabilising the laser frequency to the desired atomic transition. The expression for the power broadening is incorporated into the absorption coefficient of the Lorentzian line shape. This line shape describes the linewidth of the atomic transition, which has a full width at half maximum (FWHM) given by [166],

$$\Delta\omega_{\text{FWHM}} = \Gamma\sqrt{\left(1 + \frac{I}{I_{sat}}\right)}, \tag{5.6.1}$$

where Γ is the natural linewidth, I is the beam intensity, and I_{sat} is the saturation intensity (around 1.669mW/cm^2). Since the beam power is proportional to the light intensity (i.e. $P \propto I$), changes to the beam power lead to broadening of the absorption lines as expected. We investigate these broadening effects for various power ratios of the pump-probe beams and present our findings in Fig. 5.8 and Fig. 5.9, for ^{85}Rb and ^{87}Rb, respectively. It is worth noting that we record both the absorption and saturation spectra for each data set and subtract one from the other to obtain the linewidth of the hyperfine transitions only.

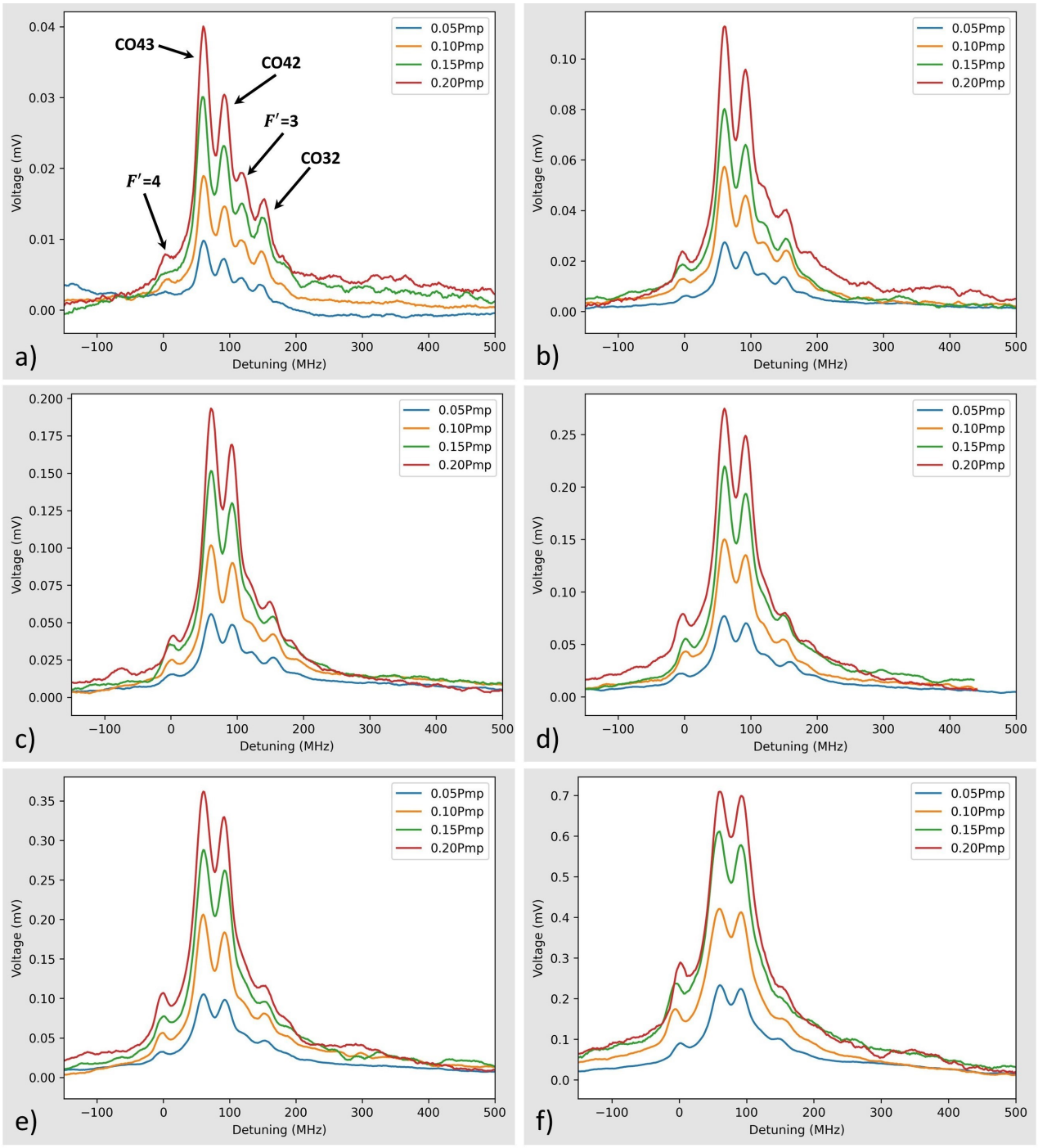

Figure 5.8: Power broadening data of ^{85}Rb, where four different probe beam powers are recorded (5%, 10%, 15%, and 20% of the pump) for a pump beam with a power of a) 0.2mW (with transitions labelling), b) 0.4mW, c) 0.6mW, d) 0.8mW, e) 1.0mW, and f) 2.0mW. Here zero detuning corresponds to the $|F = 3\rangle \rightarrow |F' = 4\rangle$ transition. Note the position of the $F' = 2$ excited state is difficult to accurately determine due to the weak nature of the transition.

We can see from Fig. 5.8 that the broadening effects become more apparent with the merging of the two cross-over peaks (CO43 and CO42), followed by the disappearance of the weaker transition $|F = 3\rangle \rightarrow |F' = 3\rangle$ and the third cross-over peak (CO32). However, the atomic resonance at zero detuning continues to grow as we continue to investigate larger pumping powers.

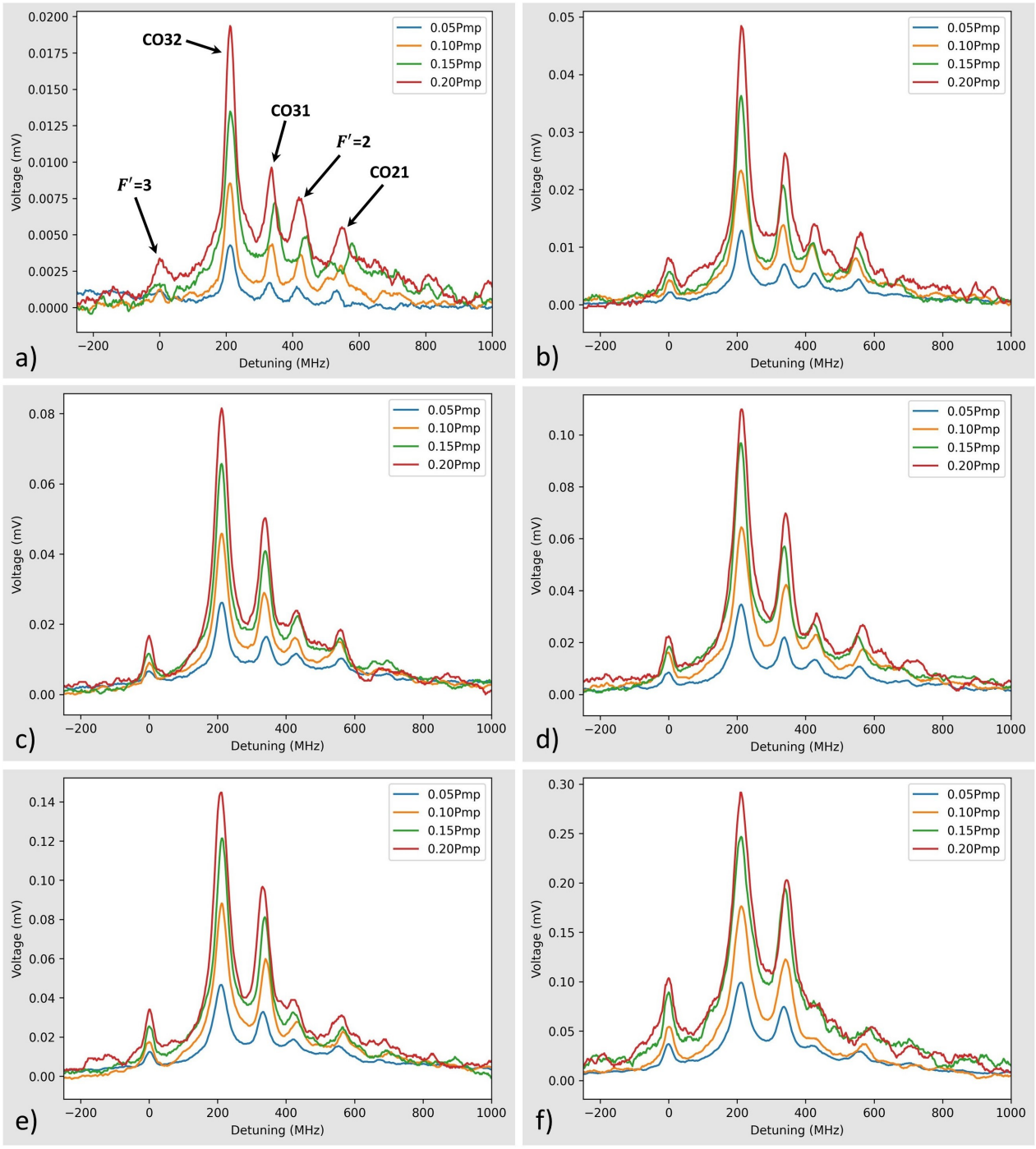

Figure 5.9: Power broadening data of ^{87}Rb, where four different probe beam powers are recorded (5%, 10%, 15%, and 20% of the pump) for a pump beam with a power of a) 0.2mW (with transitions labelling), b) 0.4mW, c) 0.6mW, d) 0.8mW, e) 1.0mW, and f) 2.0mW. Here zero detuning corresponds to the $|F = 2\rangle \rightarrow |F' = 3\rangle$ transition. Note the position of the $F' = 1$ excited state is difficult to accurately determine due to the weak nature of the transition.

Since the hyperfine spacing between the excited states in ^{87}Rb is more than twice as large as the spacing in ^{85}Rb, the effects of power broadening for similar pump-probe ratios on the $F' = 2$ excited state and the third cross-over peak (CO21) in ^{87}Rb are less prominent, as they can still be observed throughout all spectrums in Fig. 5.9, despite them being considered weak peaks. From our investigation we deduce that potential laser locking to these weak transitions might still be

possible, provided the right power settings are selected. It is worth mentioning that this data was recorded a while ago, and unfortunately, no information on the beam size was collected. Back then, we had a pinhole setup instead of a fibre, were still experimenting with optimal beam magnification for spectroscopy. In the end, we ended up running the satspec setup with a pump power of around 0.4mW to 0.5mW, and a probe power equivalent to 10% of the pump, which provided sufficient shielding from power broadening effects to access the desired atomic transitions while staying above the noise level of the photodiodes. However, in our polspec experiment, we used a 0.3mW pump with a 20% probe (i.e. 0.06mW), since the NPBS ends up throwing half of our light away, causing problems with our detection system.

5.7 Summary

In this chapter, we introduced external cavity diode lasers as the light source used for our experiments with atomic vapour. We briefly discussed Doppler free spectroscopy and how the geometry of the counter-propagating beams eliminates Doppler broadening of absorption lines and leads to the emergence of cross-over peaks. We then moved on to explore the properties of acousto-optic modulators and their application in laser frequency control before presenting our brief investigation into power broadening effects across various power ratios of the pump-probe beams and their impact on the absorption spectra of rubidium.

Chapter 6

Doppler free spectroscopy with vector vortex light

6.1 Introduction

In this final chapter, we shed light on our work incorporating our knowledge of vector beam generation and manipulation, with our understanding of atomic physics to realise an experimental configuration for a Doppler-free spectroscopic setup, combining an optically pumped atomic medium with a spatially varying polarisation signal, with an interest in laser frequency stabilisation. Although there are a few Doppler-free techniques in existence, with the most known being saturated absorption spectroscopy (satspec), the nature of our work is most comparable with polarisation spectroscopy (polspec).

Polarisation spectroscopy is a Doppler-free technique, providing a passive modulation-free signal for laser stabilisation purposes. It was first introduced by Wieman and Hänsch in 1976 [184], providing a useful tool for studying properties of atoms and materials with a plethora of applications, ranging from plasma physics [185–187], electro-optics [188], material physics [189] and even biomedical tissue analysis [190]. This technique works by pumping the atoms into the excited state, where they are probed by a diagonally polarised beam. This probe is then split into its horizontal and vertical polarisation components before being incident on two separate photodiodes, generating a Doppler-free differential signal made possible by the counter-propagating geometry of the pump and probe beams (see Section 5.3 for more information). Polspec provides an improved signal-to-noise ratio when compared to other Doppler free spectroscopic methods, prompting an interest in subsequent research over the years to better understand this technique [168, 169, 191–193]. However, before we can discuss our experimental configuration leading to our spatially variant system, we must first introduce the necessary theoretical background that will be used throughout this chapter, starting with the derivation of the absorption and dispersion coefficients from the electric susceptibility.

6.2 The electric susceptibility

Recall from chapter 1, we solved Maxwell's equations in vacuum to derive an expression for the propagating light wave, assuming an absence of external fields which significantly reduced the complexity of the equations in question. In the presence of an atomic medium, the wave experiences changes to its amplitude and phase as a consequence of the ***attenuation*** (or absorption) and ***dispersion*** (or refraction) effects, which can be calculated from the dipole moment interaction of

the atom and the light field. Since the theory remains a semi-classical one, we need to establish a link between the microscopic behaviour of the atomic ensemble and the macroscopic response of the polarisability (or polarisation density) to the incident light field. For a vapour with multiple atomic species, the polarisability is given by [194],

$$\mathbf{P} = \sum_j n_j^\rho \overline{\mathbf{d}_j}, \tag{6.2.1}$$

where n_j^ρ and $\overline{\mathbf{d}_j}$ are the number density and the average dipole moment across different volume segments of the j^{th} atomic species. Note that the number density is given by $n^\rho = N/V$ [195], where N is the number of atoms and V is the occupied volume[1]. Since macroscopically the atomic vapour is isotropic[2], the polarisability $\mathbf{P}$ is defined to be parallel to the electric field $\mathbf{E}$ and given by,

$$\mathbf{P} = \varepsilon_0 \chi \mathbf{E}, \tag{6.2.2}$$

here $\varepsilon_0\chi$ is a proportionality constant, where ε_0 is the permittivity of free space and χ is the dimensionless quantity known as the ***electric susceptibility***. Note that Eqn. 6.2.2 is only valid provided the electric field $\mathbf{E}$ is not too large; otherwise, nonlinear effects begin to emerge[3]. Assuming a low atomic density, we can neglect the local field corrections caused by the dipole-dipole interaction, which simplifies the average dipole moment across the volume segments of the gas to a dipole moment for the entire gas sample (i.e. $\overline{\mathbf{d}_j} \to \mathbf{d}_j$)[4]. So far, only a classical approach to polarisability has been considered; however, we now adopt a quantum description of the atomic polarisability defined in Eqn. 6.2.1, replacing the dipole moment $\mathbf{d}_j$ with the expectation value of the dipole operator $\langle \hat{d}_j \rangle$. Any experimental application that requires frequency stabilisation will see the laser locked to a specific transition, making use of only a single atomic species. Incorporating this into the formalism for quantum polarisability yields,

$$\mathbf{P} = n^\rho \langle \hat{d} \rangle. \tag{6.2.3}$$

Recalling Eqn. 3.4.5, we can express the expectation value of an operator in terms of the density matrix formalism as follows,

$$\langle \hat{d} \rangle = \mathrm{Tr}(\hat{\rho}\hat{d}) = \hat{d}_{eg}(\rho_{ge} + \rho_{eg}), \tag{6.2.4}$$

where $\hat{d}_{eg} = \langle e|\hat{d}|g\rangle$ is the off-diagonal element of the dipole matrix[5]. Note that here we assume both off-diagonal elements are equal and hence only consider one of them (i.e. $\hat{d}_{eg} = \hat{d}_{ge}$). After substituting Eqn. 6.2.4 into Eqn. 6.2.3 and equating it to Eqn. 6.2.2, we are left with the following,

$$n^\rho \hat{d}_{eg}(\rho_{ge} + \rho_{eg}) = \varepsilon_0 \chi \mathbf{E}. \tag{6.2.5}$$

[1] Note that the dipole approximation only holds when the light wavelength is much larger than the size of the atoms [166].

[2] Which means macroscopically the atomic vapour is uniform in all directions.

[3] This usually occurs when $\mathbf{E}$ is in the order of the atomic electric field strength [196].

[4] This assumption is reasonable given that we are working with atomic vapour at room temperature, where the pressure is low and the atoms are well separated. However, for applications that involve dense matter with tightly packed atoms, dipole-dipole interactions must be considered.

[5] Remember from the Trace identity we get $\mathrm{Tr}(\hat{\rho}\hat{d}) = \sum_{nij} \langle n|\rho_{ij}|i\rangle\langle j|\hat{d}|n\rangle = \sum_{ij} \rho_{ij}\langle j|\hat{d}|i\rangle$, where the diagonal elements disappear as a consequence of the odd parity of the dipole operator (see Section 4.3 for more information).

If we once again consider only the real part of the temporal evolution of the light field for a monochromatic plane wave (i.e. $\mathfrak{Re}(\mathbf{E}) = E_0\mathfrak{Re}(e^{-i\omega t}) = E_0\cos(\omega t)$) we get,

$$n^\rho \hat{d}_{eg}(\tilde{\rho}_{ge}e^{i\omega t} + \tilde{\rho}_{eg}e^{-i\omega t}) = \frac{1}{2}\varepsilon_0 E_0(\chi e^{-i\omega t} + \chi^* e^{i\omega t}), \tag{6.2.6}$$

where we have used Euler's formula to write $\cos(\omega t)$ in exponential form and expressed the elements of the density matrix using the rotating wave approximation $\rho_{ge} = \tilde{\rho}_{ge}e^{i\omega t}$ and $\rho_{eg} = \tilde{\rho}_{eg}e^{-i\omega t}$. Note that χ^* denotes the complex conjugate of χ, arising since the susceptibility is a function of frequency $\chi(\omega)$, obeying $\chi(-\omega) = \chi^*(\omega)$ [164]. By staring at Eqn. 6.2.6, we instantly recognise that,

$$\chi = \frac{2n^\rho \hat{d}_{eg}}{\varepsilon_0 E_0}\tilde{\rho}_{eg}. \tag{6.2.7}$$

All that remains is to find an expression for $\tilde{\rho}_{eg}$. Fortunately, the dynamics of the coherences do not change over time, and hence we can use the steady-state solution of the optical Bloch equations listed in Eqns. 4.3.20 to obtain an expression for the steady state coherence $\tilde{\rho}^{ss}_{eg}$, yielding,

$$\tilde{\rho}^{ss}_{eg} = \frac{\Omega}{2}\frac{i}{(i\Delta - \Gamma/2)}, \tag{6.2.8}$$

where Ω is the Rabi frequency, Δ is the detuning, Γ is the decay rate, and i is the imaginary number. A step-by-step derivation of Eqn. 6.2.8 can be found in Appendix B. By substituting Eqn. 6.2.8 back into Eqn. 6.2.7, we obtain an expression for the susceptibility in terms of the detuning given by,

$$\chi(\Delta) = \frac{n^\rho \hbar \Omega^2}{\varepsilon_0 E_0^2}\frac{i}{(i\Delta - \Gamma/2)}, \tag{6.2.9}$$

where we use the expression $\hat{d}_{eg} = \hbar\Omega/E_0$, obtained by substituting the quantities $I/I_{sat} = 2(\Omega/\Gamma)^2$ and $I = (1/2)c\varepsilon_0 E_0^2$ into Eqn. 4.3.22. We plot the susceptibility against the ratio of the detuning with the decay rate in Fig. 6.1 below.

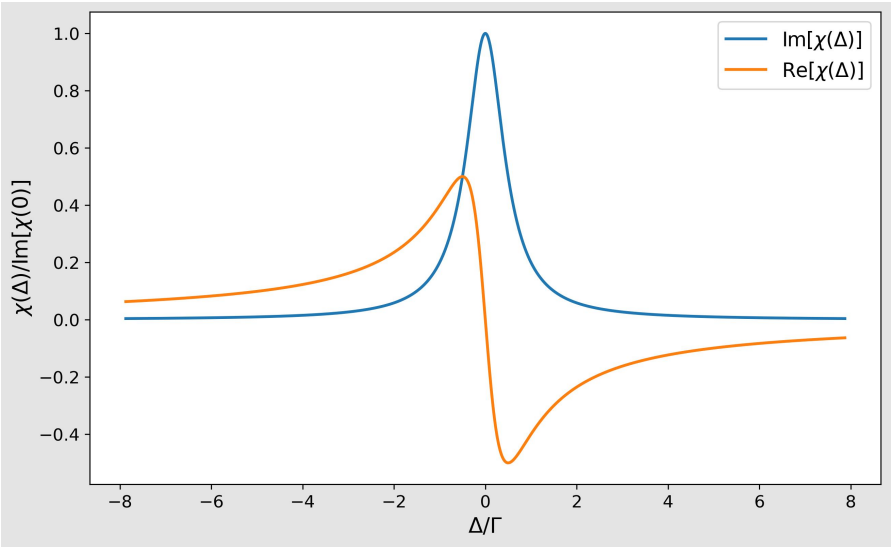

Figure 6.1: Graph of the real and imaginary parts of the steady state electric susceptibility $\chi(\Delta)$ normalised with respect to the imaginary component of the susceptibility at zero detuning $\mathrm{Im}[\chi(0)]$ for the D2 line of ^{87}Rb.

Since the interaction of the light field with the atomic medium affects both its amplitude and phase, a complex refractive index $\tilde{n}$ is required to characterise the changes to the beam profile. This refractive index is related to the electric susceptibility by [164],

$$\tilde{n} = \sqrt{1 + \chi(\Delta)}. \tag{6.2.10}$$

In fact, the two curves in Fig. 6.1 above should be very familiar to any individual studying atom optics; which are variations of the absorption $\mathrm{Im}[\chi(\Delta)]$ and dispersion $\mathrm{Re}[\chi(\Delta)]$ curves, respectively. For lower atomic densities, we can make the following approximation[6],

$$\tilde{n} = n + i\kappa \approx 1 + \frac{1}{2}\chi(\Delta), \tag{6.2.11}$$

where n and κ are the real and imaginary parts of the complex refractive index, corresponding to the dispersion and attenuation, respectively. Inserting Eqn. 6.2.9 into Eqn. 6.2.11 above yields,

$$n(\Delta) = 1 + \frac{n^{\rho}\hbar\Omega^2}{\varepsilon_0 E_0^2}\frac{\Delta/2}{(\Delta^2 + \Gamma^2/4)}, \tag{6.2.12}$$

$$\kappa(\Delta) = -\frac{n^{\rho}\hbar\Omega^2}{\varepsilon_0 E_0^2}\frac{\Gamma/4}{(\Delta^2 + \Gamma^2/4)}. \tag{6.2.13}$$

It is worth noting that the two expressions from Eqn. 6.2.12 and Eqn. 6.2.13 are related to each other through the Kramers-Kronig relations. This relation connects the real and imaginary components of a complex function via an integral and was independently established by Ralph Kronig in 1926 [197] and Hendrik Kramers in 1927 [198]. Note that the imaginary part of the complex refractive index κ is related to the absorption coefficient α via, $\alpha = 2k\kappa$, where $k = 2\pi/\lambda$ is the wavevector[7].

Since we are dealing with multilevel atoms, we can once again extend the formalism of the susceptibility to cover multilevel atomic systems by assuming that our beam is weak enough to prevent optical pumping during the time the atom spends in the light field [179, 180][8], which allows the multilevel atom to be treated as a combination of many different two-level systems, where the transition probability is given by the dipole matrix elements discussed in Section 4.6. By applying this change to the electric susceptibility in Eqn. 6.2.9, we are left with,

$$\chi_{|i\rangle\to|j\rangle}\left(\Delta_{|i\rangle\to|j\rangle}\right) = \frac{n^{\rho}\hbar\Omega^2_{|i\rangle\to|j\rangle}}{\varepsilon_0 E_0^2}\frac{i}{\left(i\Delta_{|i\rangle\to|j\rangle} - \Gamma/2\right)}. \tag{6.2.14}$$

The Rabi frequency is now given by $\Omega_{|i\rangle\to|j\rangle} = (E_0/\hbar)R_{|i\rangle\to|j\rangle}$, where$R_{|i\rangle\to|j\rangle}$ is the line strength ratio similar to the expression defined in Eqn. 4.6.4.

6.3 Atomic density

In the previous section we developed a mathematical description for the electric susceptibility from the optical Bloch equations, arriving at an expression for the dispersion and attenuation coefficients as a consequence of the light-matter interaction. Since both of these quantities have a dependence on the atomic density n^{ρ}, as demonstrated in Eqn. 6.2.12 and Eqn. 6.2.13, calculating a value for the number density could provide useful insight into the behaviour of our system and help generate

[6] For lower atomic densities, we have $\chi \ll 1$, and therefore, Taylor expansion leads to the expression in Eqn. 6.2.11.

[7] We emphasise that α is not a dimensionless quantity and has units of inverse length.

[8] This is referred to as the weak probe approximation, where the beam responsible for optical pumping possesses a higher intensity than the beam probing the atom. In our experiment, the power of the pump beam is at least five times the probe power.

a more accurate numerical model for comparison between experiment and theory. There are various ways to calculate the atomic density, where one potential method uses the spectral Faraday effect to calculate the atomic density of metallic vapours at different temperatures [199]. However, for the purpose of our work, a simple method requiring no specialised equipment based on Beer's law (or the Beer-Lambert law), following the literature in [200–202] is sufficient. Although we are only interested in rubidium, this method can be generalised to work for any ensemble of atoms or molecules. The first step is to determine the ratio of the light intensity absorbed by the atoms by investigating the difference between the beam intensity entering vs. leaving the atomic cell. For a general sample with M atomic species, the total absorption A is given by,

$$A = \sum_{m=1}^{M} A_m = \sum_{m=1}^{M} \log_{10}\left(\frac{I_m^i}{I_m^o}\right), \tag{6.3.1}$$

where A_m is the absorption of a single species, while I_m^o and I_m^i represent their output and input intensities. However, the absorption is also related to the molar absorption coefficient ε_m via,

$$A_m = \sum_{m=1}^{M} \varepsilon_m \int_0^l c_m(z)dz, \tag{6.3.2}$$

where the molar absorption coefficient (or absorptivity) ε_m, is defined as the fraction of the amount of incident radiation that is absorbed by the surface [203] and here $c_m(z)$ is the molar concentration along the optical path z. Experiments that require laser frequency stabilisation for a specific atomic transition only make use of a single isotope of the element, which helps simplify Eqn. 6.3.1 and Eqn. 6.3.2 into,

$$A = \log_{10}\left(\frac{I^i}{I^o}\right) = \varepsilon c l. \tag{6.3.3}$$

Since the Rb vapour is confined in a small cell of length l, we assume the molar concentration does not change along the optical path, reducing $\int_0^l c(z)dz$ into cl. By definition, the absorptivity and the molar concentration are given by,

$$\begin{aligned} \varepsilon &= \frac{N_A}{\ln 10}\sigma \\ c &= \frac{n^\rho}{N_A}, \end{aligned} \tag{6.3.4}$$

where N_A is the Avogadro constant, σ is the scattering (or attenuation) cross section, and n is the number density. The cross section is given by [160, 161],

$$\sigma = \frac{\sigma_0}{1 + I/I_{sat} + 4(\Delta/\Gamma)^2}, \tag{6.3.5}$$

where Δ is the detuning, Γ is the decay rate, I is the beam intensity, and I_{sat} is the saturation intensity. Here $\sigma_0 = \hbar\omega\Gamma/2I_{sat}$, where $\hbar$ is the reduced Planck constant and ω is the angular frequency. Substituting Eqns. 6.3.4 and Eqn. 6.3.5 into Eqn. 6.3.3 yields,

$$\ln(10)\log_{10}\left(\frac{I^i}{I^o}\right) = n^\rho l\left(\frac{\sigma_0}{1 + I/I_{sat} + 4(\Delta/\Gamma)^2}\right). \tag{6.3.6}$$

Using the logarithmic identity $\log_X Y \log_Y Z = \log_X Z$, and given that $\ln(10) = \log_e(10)$, we obtain the following expression for the number density,

$$n^\rho = \ln\left(\frac{I^i}{I^o}\right)\frac{1}{\sigma_0 l}\left(1 + I/I_{sat} + 4(\Delta/\Gamma)^2\right). \tag{6.3.7}$$

Since the number density is given by $n^\rho = N/V$ [195], where N is the number of atoms and V is the volume of the atom-light interaction region, we can rearrange Eqn. 6.3.7 to get an expression for the number of atoms interacting with the light field as follows,

$$N = \ln\left(\frac{I^i}{I^o}\right)\frac{A}{\sigma_0}\left(1 + I/I_{sat} + 4(\Delta/\Gamma)^2\right), \tag{6.3.8}$$

where A is the cross-sectional area of the beam. Experimentally, the intensity ratio I^i/I^o can be calculated with the help of a photodiode (PD).

The first step is to measure the PD voltage of a single-pass absorption spectrum far off-resonance; this corresponds to the input voltage V^i in the absence of atomic absorption (red dot in Fig. 6.2). The PD signal after the beam passes through the Rb cell is then recorded, corresponding to the output voltage V^o near resonance (green dot in Fig. 6.2). Note that the optical density of each isotope of rubidium must be calculated separately, and a resonance image must be taken for each one. If the incident beam on the PD corresponds to a signal larger than the ambient noise but below the PD saturation limit, and assuming the internal loss of the photodiode is negligible, we can equate the ratios of the intensity and voltage,

$$\frac{V^i}{V^o} = \frac{I^i}{I^o}. \tag{6.3.9}$$

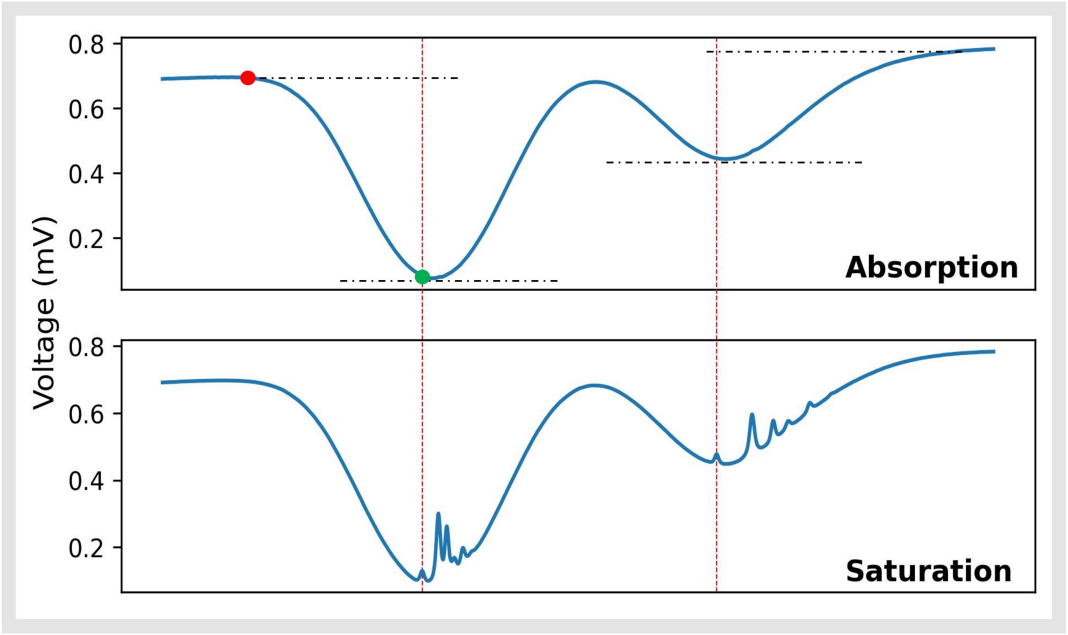

Figure 6.2: The absorption and saturation spectra of the D2 lines of ^{85}Rb and ^{87}Rb, used for optical density calculations. The saturation spectrum is used to pinpoint the location of the atomic transition on the absorption profile (red dashed lines) to obtain a more accurate PD measurement. The green and red dots denote the laser frequency at resonance and off-resonance, respectively.

Since increasing the beam intensity increases the number of incident photons, which increases the matter-light interaction, it is experimentally depicted as a deeper absorption curve profile on the oscilloscope. However, as $I \to I_{sat}$, the number of atoms interacting with the light field begins to decrease, resulting in a reduction in the expansion of the absorption curve profile. As we continue to increase the intensity further, $I > I_{sat}$, this expansion begins to further slow down and eventually will become difficult to observe. Since achieving more precise measurements relies on optimising the signal-to-noise ratio, it is imperative to adjust the beam intensity to avoid saturating both the atoms and the detector.

It is possible to determine the voltage ratio from the saturation profile of the atoms at a specific transition; however, one has to take into account the atoms interacting with two different beams, where a consequence of such a geometry is the emergence of the single hyperfine transition peaks (see Section 5.3 for more information) that slightly lift the trough of the Doppler broadened profile, potentially yielding a slightly lower atomic density value when calculated[9]. This method provides no advantages in the calculation; however, one can use the saturation spectrum as a guide to pinpoint the position of the transition where maximum absorption is expected and adjust the laser frequency to occupy this position, as illustrated by the dotted red lines in Fig. 6.2.

Alternatively, one can determine the intensity ratio directly from the incident beams using a CMOS or CCD camera instead. We prefer this method as it provides a number of key advantages. Although a reverse-biassed PD has a saturation threshold controlled by the supplied voltage, a camera gives the flexibility of changing the saturation limit by adjusting the exposure time without the need to alter the beam intensity[10]. Additionally, some image sensors provide control over their dynamic range, which helps maximise the signal contrast between the off-resonance and resonance images for a more accurate calculation.

The dynamic range is an intrinsic property of image sensors, defined as the ratio between the largest and smallest signal value perceived by the detector, often written in decibels or bits [204]. The camera converts incoming photons into a monochromatic digital signal expressed as a level in grey scale, ranging from pure black to pure white, where the available number of occupiable grey levels is subject to the property of the camera known as bit depth. For example, a 6-bit detector has access to 64 grayscale levels; an 8-bit camera has 256 levels; and a 10-bit detector can occupy any of the 1024 levels available. Ideally, one should utilise as much of the available dynamic range when using an image sensor in hopes of maximising the contrast. In the example of Fig. 6.3a, the light intensity and camera exposure time have been adjusted such that the brightest pixel (given by the blue lines) is just below the saturation limit of an 8-bit detector. However, these same quantities significantly exceed the limitations of a 6-bit detector but fall short of the capabilities of a 10-bit detector. Therefore, it is imperative to calibrate the system relative to the detector in use. In a similar fashion, Fig. 6.3b represents a system where either the beam intensity or exposure time falls below the capabilities of all detectors, where the brightest pixel (red lines) occupy a much lower greyscale level. In this case, the signal contrast has not been maximised and could result in larger uncertainties when calculating the intensity ratio with Eqn. 6.3.9.

[9] Here the weak probe regime is assumed, since operating the experiment with a strong probe will require measuring the probe's intensity as well.

[10] Increasing the exposure time makes the detector more susceptible to environmental noise. Ideally, it is highly recommended to capture a background image for post-process subtraction to eliminate this effect.

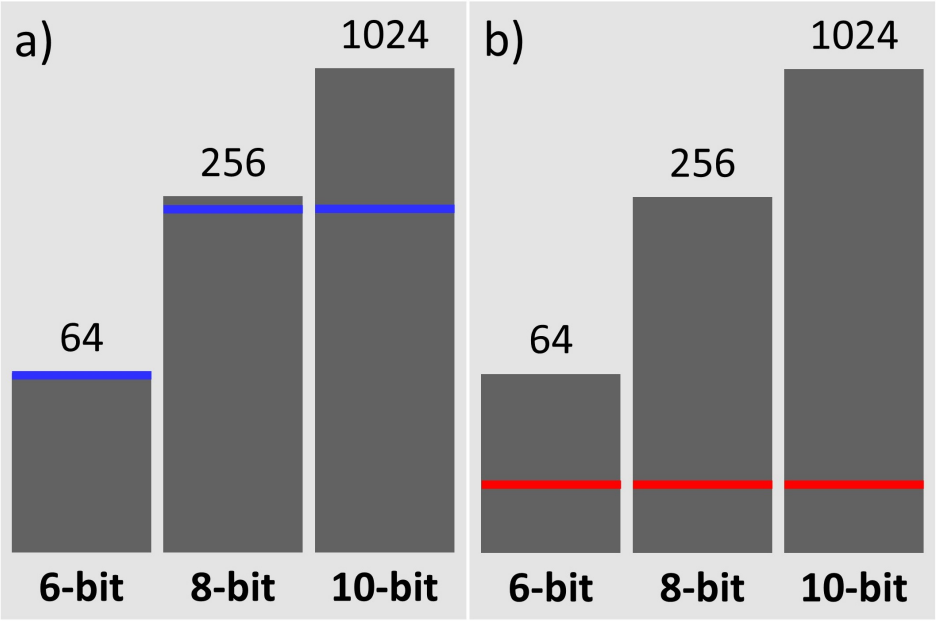

Figure 6.3: Dynamic range of detectors. a) The brightest pixel (blue) calibrated to maximise the dynamic range of an 8-bit detector would oversaturate and underutilise the 6-bit and 10-bit detectors, respectively. b) The brightest pixel (red) calibrated well below the maximum of all detectors, underutilising the dynamic range of all three and offering access to far fewer greyscale levels for image intensity comparison.

Experimentally, we use a CMOS detector (JAI GO-5000M-USB), where the camera exposure time is adjusted to ensure the off-resonance signal (no atomic absorption) is illuminated to the maximum possible without saturating the detector, thereby utilising as much of the available dynamic range of the camera as possible. Once an off-resonance measurement is taken, the laser frequency is then adjusted to resonance, where an image reflecting the atomic absorption is captured. This procedure can be repeated for any number of isotopes of the atomic medium. The next step is to determine the intensity of the beam. For Gaussian beams, we can calculate the intensity I of the light from the total power P using the following relation,

$$I = \frac{2P}{\pi w_0^2}, \tag{6.3.10}$$

where w_0 is the beam radius. In our case, the beam is fibre-coupled into a polarisation-maintaining single mode fibre (PM-SMF), where the waist is determined by the fixed focus output collimator (a Thorlabs F220FC-780 collimator), giving us a beam diameter of 2.1mm. However, we employ a telescope system magnifying the beam by a factor of two, leaving us with a beam diameter of 4.2mm and in turn, a beam radius of 2.1mm (the experimental setup will be extensively discussed in Section 6.6.1). All that remains is to measure the incident beam power to calculate the light intensity. Unsurprisingly, we observe small changes in beam power when shifting between on and off-resonance as a result of minor variations in diode current (and temperature). These modifications change the length of the external cavity of the diode laser and correspond to approximately a 3% difference in beam power, which is small enough to be ignored.

We investigated the atomic density of both rubidium isotopes at natural abundance (see Section 4.2) housed inside a 75mm long cell with an input beam power of around 0.2mW at room temperature ($\approx 20^{\circ}$C)[11]. We record a set of videos with 100 frames each for the beam, at resonance and off-resonance for the two isotopes of rubidium, and calculate a mean value of all frames to increase reliability. Additionally, a fourth video is recorded for the background (i.e. when the beam is blocked) to account for ambient noise subtraction in the analysis. A frame from the raw data as recorded by the detector can be found in Fig. 6.4 below. We calculate an intensity ratio

[11] We chose this power to be as close as possible to the pump beam power without saturating the CMOS detector.

I^i/I^o of 1.503 and 1.255 for ^{85}Rb and ^{87}Rb, respectively. Inserting these values into Eqn. 6.3.7 and Eqn. 6.3.8 with the appropriate parameters leaves us with,

$$\begin{aligned} n^{\rho}_{85} &= 5.383 \times 10^7 \text{cm}^{-3}, & N_{85} &= 5.594 \times 10^7, \\ n^{\rho}_{87} &= 2.999 \times 10^7 \text{cm}^{-3}, & N_{87} &= 3.116 \times 10^7, \end{aligned} \tag{6.3.11}$$

where n^{ρ}_{85} and n^{ρ}_{87} are the optical densities, while N_{85} and N_{87} correspond to the number of atoms interacting with the light field for both rubidium isotopes. Unfortunately, the experimental setup had no heating coils in place when I took the measurements; however, heating the cell would supply the atoms with more kinetic energy, expressed as a shift in the Maxwell-Boltzmann distribution of the atomic medium. This increase in the average kinetic energy of the atoms would increase the likelihood of collisions with the light field, which in turn would increase the values calculated in Eqn. 6.3.11 for the optical density and number of interacting atoms.

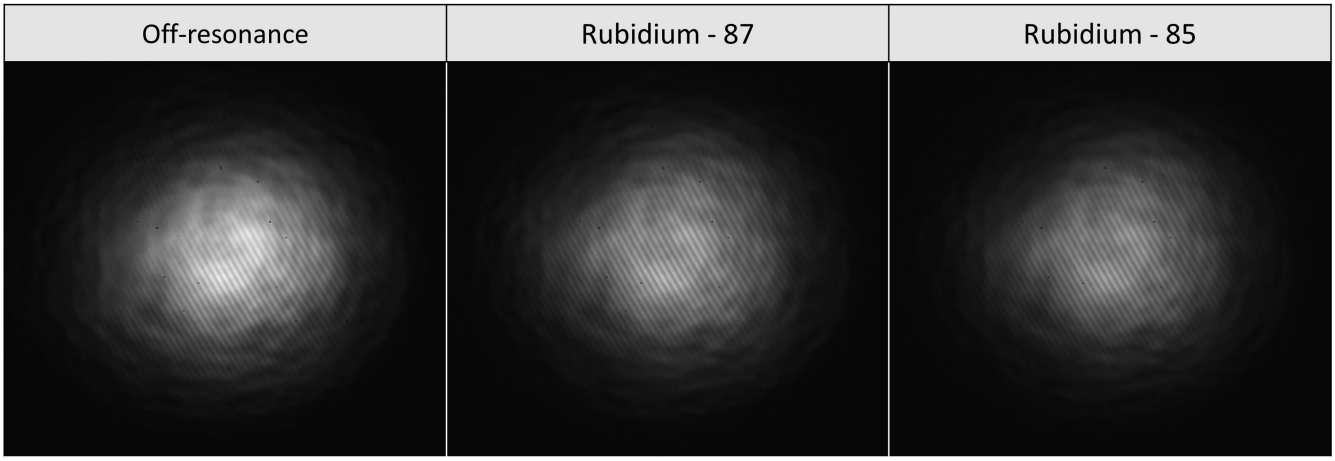

Figure 6.4: Beam intensity measurements used for optical density calculations. These images are frames from a set of videos recording the beam off-resonance and at resonance for both rubidium isotopes.

6.4 The Faraday effect

In chapter 4, we outlined the effect of an external magnetic field on the magnetic sublevels m_F of the hyperfine states, resulting in interesting magneto-optical effects that affect the atomic behaviour relative to the incident light field. In the absence of any magnetic fields, the m_F states are said to be degenerate, with no discernible imbalances in any of the pumping schemes, as seen in Fig. 6.5a. However, in the presence of an external magnetic field, Zeeman splitting occurs, shifting the magnetic sublevels by a frequency defined by Eqn. 4.2.1. This removes the degeneracy in the atomic structure, allowing only specific transitions to occur, determined by the orientation of the applied magnetic field relative to the propagation direction of the beam (see Section 4.5). Recall that in the case where the magnetic field is in the direction of beam propagation, only $\sigma_{\pm}$ transitions can occur (see Section 4.5 for more information). The shift in the magnetic sublevel frequency causes a deviation in the $\sigma_{\pm}$ transitions from resonance, the magnitude of which is determined by the strength of the external magnetic field. This deviation affects the excitation probability of the two transitions, as illustrated in Fig. 6.5b. The difference in the atomic response to $\sigma_{\pm}$ polarised

light translates to a change in the refractive index $n_\pm$ of the medium[12], where $n_+ \neq n_-$, giving rise to a phenomenon known as ***circular birefringence***[13], which eventually leads to the ***Faraday effect***.

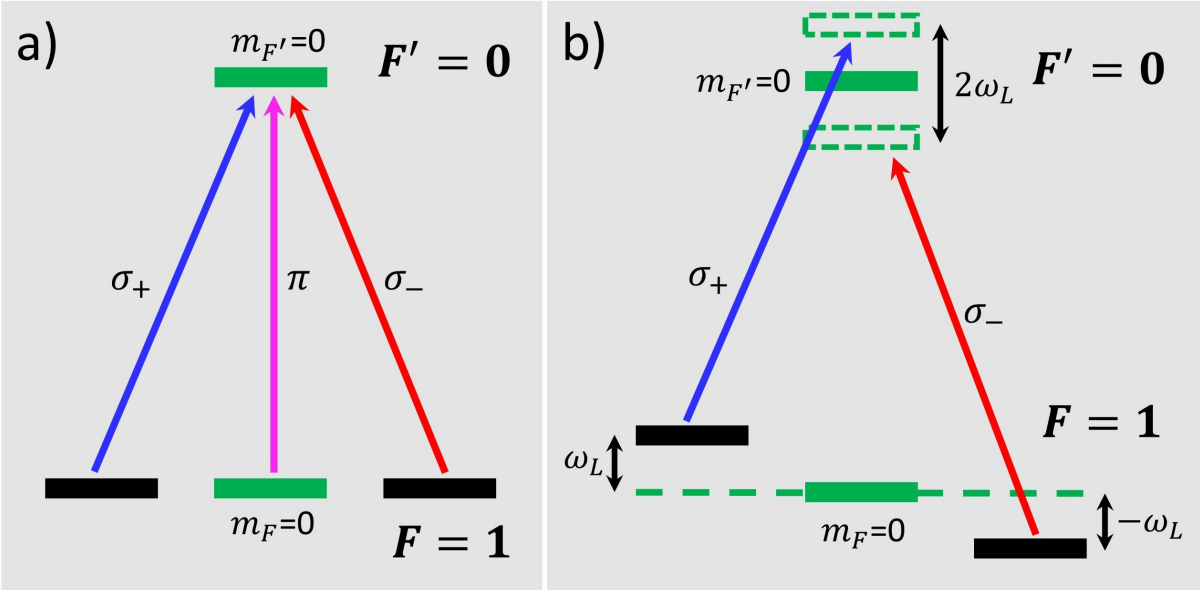

Figure 6.5: The energy levels in the absence and presence of circular birefringence for the D2 line transition of ^{87}Rb, $|F = 1\rangle \longrightarrow |F' = 0\rangle$. a) Degenerate energy levels in the absence of an external magnetic field. b) The introduced magnetic field only allows for $\sigma_\pm$ transitions, which are Zeeman shifted by the Larmor frequency $\pm\omega_L$, leading to circular birefringence in the atomic medium. Note that the difference in frequency shift between the two sublevels is equal to twice the Larmor frequency $2\omega_L$.

By definition, the Faraday effect (named after Michael Faraday, who discovered it in 1845) is the rotation of the plane of linear polarisation as it propagates through a medium with a magnetic field parallel to the propagation direction [205]. Since any linear input beam can be decomposed into the two orthogonal circular components $\sigma_\pm$ with equal amplitudes (and different phases), the definition of the Faraday effect holds, even for circular polarised light. The shift in the dispersion signal, given by the real part of the refractive index $n_\pm$, induces a rotation in the light field given by [206, 207],

$$\theta = (n_+ - n_-)lk, \tag{6.4.1}$$

where k is the wave vector $k = 2\pi/\lambda$, and l is the length of the medium. Interestingly, the Faraday effect is commonly employed in Faraday rotators. These rotators are typically used in some optical isolators, constructed from two polarisers with their transmission axes at 45° to one another, with a crystal sitting in between subjected to a strong magnetic field on the order of a few Tesla [208, 209]. This magnetic field induces a birefringence in the medium causing the polarisation structure of the light field to rotate by 45°, as illustrated in Fig. 6.6a. These isolators are usually the first optical elements placed immediately after the laser system, preventing any back-reflected light from ever reaching the laser, which reduces unwanted optical effects (e.g. frequency mode hops). Fig. 6.6b

[12]Note this is the real part of the complex refractive index describing the dispersion.
[13]Visit Section 2.4 for more information on birefringence.

shows an example where the back reflected light is rotated by an additional 45° after propagating through the crystal, turning the beam vertically polarised, which is absorbed by the polariser.

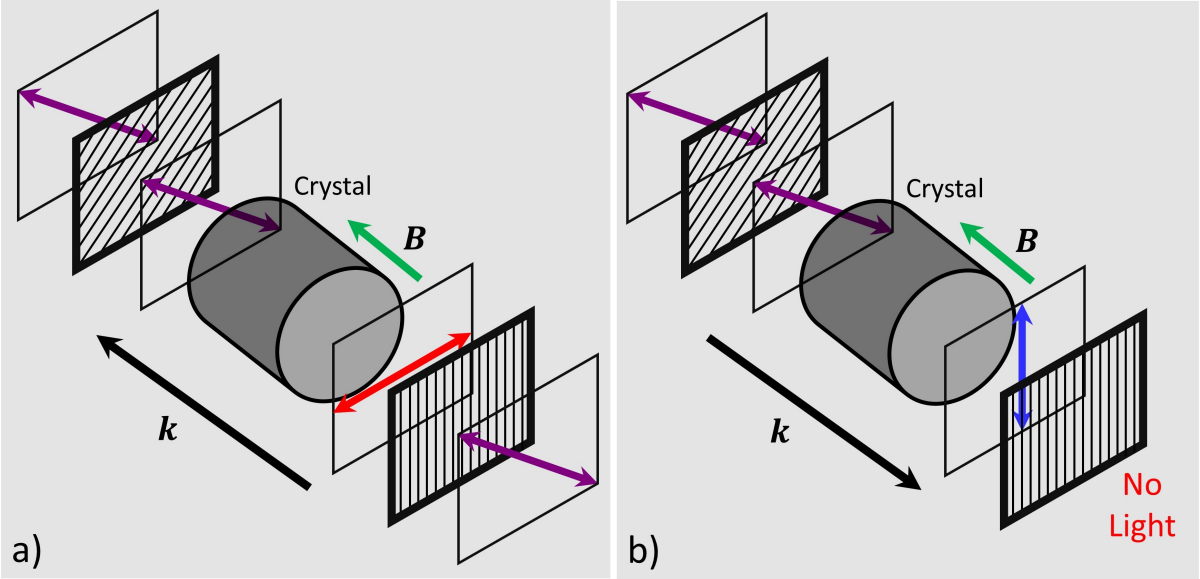

Figure 6.6: An optical isolator made from a crystal subjected to a strong magnetic field **B**, which rotates the polarisation of a propagating beam along **k** utilising the Faraday effect. a) A diagonal beam is left with only the horizontal component after passing through a polariser, which is rotated by 45° as it propagates through the crystal, leaving the system once again diagonally polarised. b) A diagonally reflected beam is turned vertical after passing through the crystal, which is absorbed by the second polariser (relative to the beam propagation direction), preventing the light from exiting the isolator[14].

In addition to circular birefringence, the external magnetic field also induces a circular dichroism (i.e. a preferential absorption of $\sigma_{\pm}$) in the medium (see Section 2.4 for more information on dichroism). If once again we assume only $\sigma_{\pm}$ transitions are permitted, a linearly polarised light propagating through a sample will evolve into an elliptically polarised beam after leaving the interaction medium, as a consequence of the difference in the attenuation coefficient of the two circular components (i.e. $\alpha_{+} \neq \alpha_{-}$). This effect becomes much more dominant close to resonance. It is worth noting that the Faraday effect only occurs in a longitudinal magnetic field. If the magnetic field is transverse to the beam propagation, then the Voigt effect would be observed, where the induced ellipticity and optical rotation are a result of the phase shift and differential absorption of the orthogonal linearly polarised components of the input light field [207]. The Faraday effect is still very much an active area of research, spanning an interest in a wide range of topics utilising atomic vapours [210–214]. In this work, we are only interested in the Faraday effect.

6.5 Polarisation spectroscopy (polspec)

As previously stated, setting up the polarisation spectroscopy experiment was a good starting point for our project, as usually building a well-understood system from previous literature can help lay

[14]Note that an optical isolator does not preserve the polarisation of the input beam. In this example, the output will always be diagonally polarised with the exception of vertically polarised light, which will be fully absorbed (remember from Section 2.4 that the polarisation parallel to the wire grid is absorbed).

the groundwork for one's own research. Inspired by the literature from [168, 169, 192] we adapt a polspec configuration to suit our needs, introducing some changes to the interferometer, which will be discussed in this section.

6.5.1 Theory and experimental realisation

We present our experimental setup in Fig. 6.7. The setup itself is quite simple, where a beam generated from an external cavity diode laser (ECDL) at 780nm, propagates through a Faraday isolator (FI), which is then diagonalised by a half waveplate (HWP) and separated into the horizontal and vertical polarisation components with a polarising beam splitter (PBS). The experiment consists of two parts: a saturated absorption spectroscopy (satspec) setup and the main polspec section, highlighted by the optics in the red and green borders in Fig. 6.7, respectively. The vertically polarised light is reflected from the PBS_1 towards a standard Doppler free satspec setup (see Section 5.3 for more information), used to monitor the laser stability. The vertical beam (blue) is then diagonalised, before being split by PBS_2 to generate a counter propagating pump-probe configuration, where the pump is reflected off both PBS_2 and PBS_3 before being incident on the rubidium cell (Rb), while the horizontal probe (red) is transmitted through both PBS_2 and PBS_3, eventually terminating at the photodiode (PD)[15]. Usually in satspec, a strong pump and a weaker probe are employed, in our setup the probe is normally around $10\% - 20\%$ the pump power. The pump-probe ratio in our experiment was carefully selected after an investigation on broadening effects experienced by the atoms as a consequence of beam power (more in Section 5.6).

On the other hand, the horizontally polarised light transmitted through PBS_1 bounces off a dual mirror setup, steering the beam into a telescope system (formed by the lenses L_1 and L_2) with a pinhole (Pin) placed at the focus of the two lenses, used to generate a spatially uniform intensity distribution and remove any deformities in the light profile, at the cost of beam power. We investigated various pinholes with diameters ranging from 10μm to 100μm to find the most suitable one for our needs. Since the beam profile generated from the ECDL was highly irregular, with an arbitrary geometric shape and a hole in the centre, a 20μm pinhole proved sufficient to clean the beam profile at a modest loss of power (around $30\% - 60\%$)[16]. The beam is then diagonalised and once again split into the horizontal and vertical components by PBS_4. The transmitted light propagating through the quarter waveplate (QWP), generating circularly polarised light, will act as our pump beam, exciting the atomic state population and creating a polarisation anisotropy in the atomic medium (see Section 2.4). This beam is then reflected off a 50:50 non-polarising beam splitter (NPBS) and a mirror (M), halving the light intensity[17], before passing through the rubidium cell at room temperature[18]. The cell is wrapped in μ-metal (but remains open from the sides), which is a soft ferromagnetic nickel-iron alloy with a very high magnetic permeability, shielding the cell from any external magnetic fields not in the direction of beam propagation[19]. In

[15] Since the PD chip is smaller than the beam diameter, the recorded signal is maximised by using a lens to focus the beam into the PD chip.

[16] Thankfully, polspec setup does not require high beam powers; in fact, the signal features were clearer when the intensity was kept well below saturation.

[17] Although the NPBS and mirror combination preserve the handedness of the beam circularity, identifying the polarisation structure of the pump was not a concern at this point in time.

[18] At room temperature, the pressure in the cell is low enough that de-excitation effects from atomic collisions can be ignored.

[19] The μ-metal needs heat treatment to increase its grain structure. By definition, grains are crystalline lattices consisting of a cluster of atoms separated by a boundary, where increasing the grain structure maximises the absorption of the magnetic field flux. This process is not to be confused with annealing, where the metal is heated and allowed to slowly cool to remove internal stresses. The difference between the two is briefly summarised in [215].

an attempt to eliminate the influence of the transverse magnetic fields, the μ-metal shielding was made longer than the rubidium cell, by around $1.5\text{cm} - 2\text{cm}$ on either side to ensure the component of the earth's magnetic field entering the cell is as parallel to the beam propagation direction as feasibly possible. Since the presence of a transverse magnetic field results in coupling of the ground state m_F sublevels (an example of such a coupling can be seen in Fig. 1 from [155]), this could lead to repopulation of our atomic states, destroying the anisotropy we created in the medium from the pumping process. In a similar fashion, the beam reflected off PBS_4 is diagonalised by a HWP before passing through the Rb cell probing our atomic medium. The beam then propagates into a mirror, transmitting through the NPBS and PBS_5 where the individual polarisation components ($\hat{H}$ and $\hat{V}$) are separated and focused into two different photodiodes.

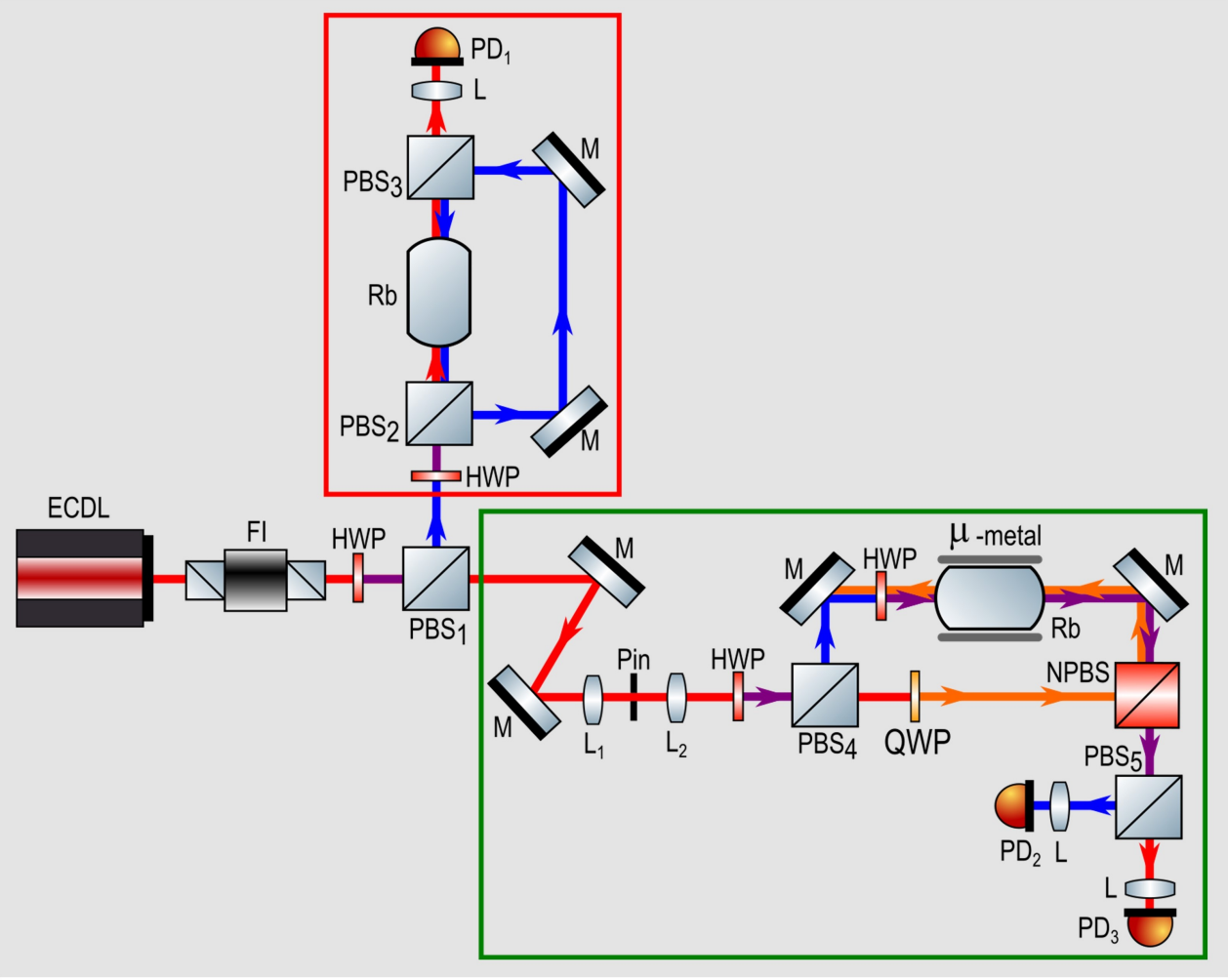

Figure 6.7: Experimental configuration of polarisation spectroscopy. The setup consists of a saturated absorption spectroscopy (satspec) part in the red border and the primary polarisation spectroscopy (polspec) section within the green border. The beam colours indicate different polarisation structures, where horizontal is red, vertical is blue, purple is a mixture of the two, and orange is circularly polarised. The experiment consists of an external cavity diode laser (ECDL), a Faraday isolator (FI), half waveplates (HWP), a quarter waveplate (QWP), polarising beam splitters (PBS), lenses (L), mirrors (M), a pinhole (Pin), rubidium vapour cells (Rb), a non-polarising beam splitter (NPBS), and photodiodes (PD).

Throughout our experiment, even at later stages when a vector vortex beam is introduced as

the probe, the atoms in our cell are only subjected to the earth's magnetic field[20]. Although we could have introduced coils for heating and magnetic field generation to the experiment in order to improve our signal, there was a strong desire to observe and quantify these magneto-optical using the most basic spectroscopy configuration possible, with minimal assistance from external elements.

Unlike satspec, the polarisation of the pump and probe differs in polspec, with the probe being linear and the pump circular. Because of this difference, introducing a normal or circular PBS will not achieve the overlapped counter-propagating beam configuration desired without significant changes to the light polarisation structure. There are two solutions to this problem. The first is to employ an experimental configuration where one of the beams enters the rubidium cell at a slight angle with respect to the other. The disadvantage is that many of the atoms excited by the pump will not be probed, resulting in a less sharp polspec signal. The other method (and the one we implemented) is to use an NPBS. This way, we can ensure the pump and probe beams are thoroughly overlapped, yielding a sharper differential signal. However, the added challenge with using a NPBS is the slight distortion to the polarisation profile experienced by the light field when propagating through them, which requires compensation (e.g. by rotating the waveplates slightly)[21].

To better understand the behaviour of the probe, we derive an expression of the signal generated from the two photodiode outputs and their differential counterpart. For a fully polarised probe beam, we can express the polarisation in Jones formalism by,

$$\mathbf{E} = \begin{pmatrix} E_x \\ E_y \end{pmatrix} = E_0 \begin{pmatrix} \cos(\theta) \\ \sin(\theta) \end{pmatrix}, \tag{6.5.1}$$

where E_0 is the initial wave amplitude and θ is the polarisation angle with respect to the horizontal. Since under the influence of the magnetic field, the occurring transitions are $\sigma_\pm$ transitions, it is convenient to write Eqn. 6.5.1 in the circular basis,

$$\begin{aligned} \mathbf{E} = \frac{1}{2}E_0 \begin{pmatrix} e^{i\theta} + e^{-i\theta} \\ -i(e^{i\theta} - e^{-i\theta}) \end{pmatrix} &= \frac{1}{2}E_0 \left[e^{i\theta} \begin{pmatrix} 1 \\ -i \end{pmatrix} + e^{-i\theta} \begin{pmatrix} 1 \\ i \end{pmatrix} \right] \\ &= \frac{\sqrt{2}}{2}E_0 \left(e^{i\theta}\sigma_- + e^{-i\theta}\sigma_+ \right), \end{aligned} \tag{6.5.2}$$

where $\sigma_\pm$ are the left and right circular polarisation components, respectively, defined in Eqns. 1.3.10. Note that the first matrix term in Eqn. 6.5.2 comes from using the exponential form of the sine and cosine functions. For a light field propagating through a cell of length L, the two circular components experience absorption and dispersion effects from the atomic vapour and the glass cell, where the birefringence in the glass cell is a consequence of the manufacturing

[20] More accurately, the atoms experience a component of the earth's magnetic field. There has been an attempt to measure it using a Gaussmeter (a Hirst Magnetics GM07), but since only a transverse probe was available at the time, the field along the z-axis inside the shielding could not be accurately determined. However, we recorded a measurement of $0.39\text{G} - 0.49\text{G}$ at the cell entrance without the shielding and a value of around $0.64\text{G} - 0.75\text{G}$ at the entrance of the shielded cell. Although this increase in the field line density is consistent with the expected behaviour of introducing the μ-metal around the cell, I would take these values with a pinch of salt.

[21] Although an angled pump-probe beam is the most common configuration found in literature, the choice to use a NPBS stems from attempting to obtain a maximal signal, given no heating coils are used.

process and pressure gradient, influencing the probe beam as follows [168],

$$\mathbf{E} = \frac{1}{\sqrt{2}} E_0 \left(e^{i\theta} \sigma_- e^{-ikn_+ L} e^{-\alpha_+ L/2} e^{-ik\tilde{n}_{g_+} l} + e^{-i\theta} \sigma_+ e^{-ikn_- L} e^{-\alpha_- L/2} e^{-ik\tilde{n}_{g_-} l} \right), \tag{6.5.3}$$

where $n_\pm$ is the refractive index, $\alpha_\pm$ is the absorption coefficient, and $\tilde{n}_{g_\pm}$ is the complex refractive index of the glass window for the polarisation state driving $\sigma_\pm$ transitions, respectively. Here l is the glass window thickness, $k = 2\pi/\lambda$ is the wavevector, and i is the imaginary number. We can decompose the complex refractive index of the glass window into its real and imaginary parts as $\tilde{n}_{g_\pm} = n_{g_\pm} - i\alpha_{g_\pm}/2k$ [216], describing the dispersion and absorption, respectively[22]. Substituting $\tilde{n}_{g_\pm}$ into Eqn. 6.5.3 above and rearranging, leaves us with,

$$\mathbf{E} = \frac{1}{\sqrt{2}} E_0 e^{-i\Lambda} (e^{i\theta} e^{-i\Pi} \sigma_- + e^{-i\theta} e^{i\Pi} \sigma_+), \tag{6.5.4}$$

where,

$$\begin{aligned} \Pi &= \frac{k}{2} \left(\Delta n L + \Delta n_g l \right) - \frac{i}{4} \left(\Delta\alpha L + \Delta\alpha_g l \right) \\ \Lambda &= k(nL + n_g l) - \frac{i}{2}(\alpha L + \alpha_g l), \end{aligned} \tag{6.5.5}$$

and,

$$\begin{aligned} n &= (n_+ + n_-)/2, & \Delta n &= (n_+ - n_-), \\ \alpha &= (\alpha_+ + \alpha_-)/2, & \Delta\alpha &= (\alpha_+ - \alpha_-), \\ n_g &= (n_{g_+} + n_{g_-})/2, & \Delta n_g &= (n_{g_+} - n_{g_-}), \\ \alpha_g &= (\alpha_{g_+} + \alpha_{g_-})/2, & \Delta\alpha_g &= (\alpha_{g_+} - \alpha_{g_-}). \end{aligned} \tag{6.5.6}$$

The full derivation of Eqn. 6.5.4 and Eqns. 6.5.5 beginning from Eqn. 6.5.3 can be found in Appenxid C. Since the photodiodes record the intensity of the light field in the horizontal and vertical polarisation states, as a consequence of PBS_5, we obtain an expression of the electric field in Eqn. 6.5.4 in the $\hat{H}$ and $\hat{V}$ basis by substituting in $\sigma_+ = (\hat{H} + i\hat{V})/\sqrt{2}$ and $\sigma_- = (\hat{H} - i\hat{V})/\sqrt{2}$, yielding,

$$\begin{aligned} \mathbf{E} &= E_0 e^{-i\Lambda} \left[e^{i\theta} (\hat{H} - i\hat{V}) e^{-i\Pi} + e^{-i\theta} (\hat{H} + i\hat{V}) e^{i\Pi} \right] \\ &= E_0 e^{\Lambda_I} e^{-i\Lambda_R} \Big\{ \left[e^{i(\theta - \Pi_R)} e^{\Pi_I} + e^{-i(\theta - \Pi_R)} e^{-\Pi_I} \right] \hat{H} \\ &\qquad - i \left[e^{i(\theta - \Pi_R)} e^{\Pi_I} - e^{-i(\theta - \Pi_R)} e^{-\Pi_I} \right] \hat{V} \Big\}, \end{aligned} \tag{6.5.7}$$

where Π_R and Π_I are the real and imaginary parts of Π, while Λ_R and Λ_I are the real and imaginary parts of Λ from Eqn. 6.5.5. By substituting Eqn. 6.5.7 into Eqn. 1.3.8, we obtain an expression for the intensity in the horizontal $I_{\hat{H}}$ and vertical $I_{\hat{V}}$ polarisation basis, given by,

[22] Note the quantity $\alpha_{g_\pm}/2k = \kappa_{g_\pm}$, where $\kappa_{g_\pm}$ is the imaginary part of the complex refractive index $\tilde{n}_{g_\pm}$.

$$I_{\hat{H}} = 2I_0 e^{2\Lambda_I}\left[\cos\big(2(\theta-\Pi_R)\big)+\cos(2\Pi_I)\right], \tag{6.5.8}$$

$$I_{\hat{V}} = 2I_0 e^{2\Lambda_I}\left[-\cos\big(2(\theta-\Pi_R)\big)+\cos(2\Pi_I)\right], \tag{6.5.9}$$

where the probe differential signal is expressed as,

$$I_{\text{probe}} = I_{\hat{H}} - I_{\hat{V}} = 4I_0 e^{-(\alpha L+\alpha_g l)}\cos\big(2(\theta-\Pi_R)\big). \tag{6.5.10}$$

As previously stated, the absorption and dispersion effects experienced by the light field from interacting with the rubidium atoms are related to one another via the Kramers-Kronig relation, and one can design an experiment to observe their respective effects. In the case of polspec, utilising a probe beam with a single polarisation structure, the birefringence in the cell is assumed to be small, which in turn results in a small rotation angle of the polarisation plane (Faraday rotation) as a consequence of the anisotropy in the atomic medium. This is a valid assumption since the Faraday rotation described by Eqn. 6.4.1 depends on the difference of the refractive index (i.e. $\Delta n = n_+ - n_-$) of the two $\sigma_\pm$ polarisations, who are in turn proportional to the shifted detuning (i.e. $n_\pm \propto \Delta_\pm$). This shift is proportional to twice the Larmor frequency (i.e. $\Delta_\pm \propto \pm 2\omega_L$), as described by Eqn. 4.2.4. However, in the presence of the earth's magnetic field, the detuning shift is very small, making Faraday rotation difficult to observe[23]. That is not to say the Faraday effect is completely absent in polspec; in fact, the introduced phase does contribute to the experimentally observed outcome for the spatial variation of this experiment, which will be discussed in the next section. For now, it is safe to say the observed differential signal from the photodiode is dominated by circular dichroism (i.e. preferential absorption of $\sigma_\pm$) caused by the anisotropy in the atomic medium as a consequence of the pumping process, given in terms of the absorption coefficient,

$$\Delta\alpha = \frac{\Delta\alpha_0}{1+4(\Delta_{\text{probe}}/\Gamma)}, \tag{6.5.11}$$

where $\Delta\alpha_0$ is the maximum absorption difference at the line centre, Δ_{probe} is the probe beam detuning and Γ is the decary rate. With the Kramers-Kronig relations, we can relate the refractive index to the absorption coefficient of Eqn. 6.5.11 as,

$$\Delta n = \frac{2\Delta_{\text{probe}}}{\Gamma k}\Delta\alpha, \tag{6.5.12}$$

where k is the wavevector. By applying the small angle approximation to a diagonal probe beam (i.e. $\theta = \pi/4$) and using Eqn. 6.5.12, we can express Eqn. 6.5.10 as,

$$I_{\text{probe}} = -4I_0 e^{-(\alpha L+\alpha_g l)}\left(\frac{2\Delta_{\text{probe}}}{\Gamma}\Delta\alpha L + \Delta n_g k l\right), \tag{6.5.13}$$

where we have used the trigonometric identity $\cos(x+y) = \cos(x)\cos(y) - \sin(x)\sin(y)$. This signal will have a similar shape to the dispersion curve in Fig. 6.1 and can be used to lock the laser frequency to the desired atomic transition. In previous literature, a polspec signal was recorded with very low beam intensities using a pump power of 10μW and a 1μW probe [168]. To observe the features on the polspec signal for other transitions, it is best to keep the beam intensity well below saturation; however, using such low powers presents a few challenges (e.g. a smaller signal-to-noise

[23]Since a photodiode converts the incoming light intensity into an electric signal, disregarding any phase information from the light field, the Faraday effect cannot be observed using just a photodiode anyway.

ratio) and is not feasible without specialised equipment (e.g. very sensitive photodiodes).

6.5.2 Results and analysis

This section presents our experimental findings from the polspec experiment. In Fig. 6.8 we summarise our results utilising beams with four different pumping powers of 0.4mW, 0.3mW, 0.2mW, and 0.1mW. The probe beam power is set at 10% with respect to each pump. Each signal has been digitally filtered to account for ambient and electronic noise, with zero detuning corresponding to ^{85}Rb D_2 line transition of $|F = 3\rangle \rightarrow |F' = 4\rangle$.

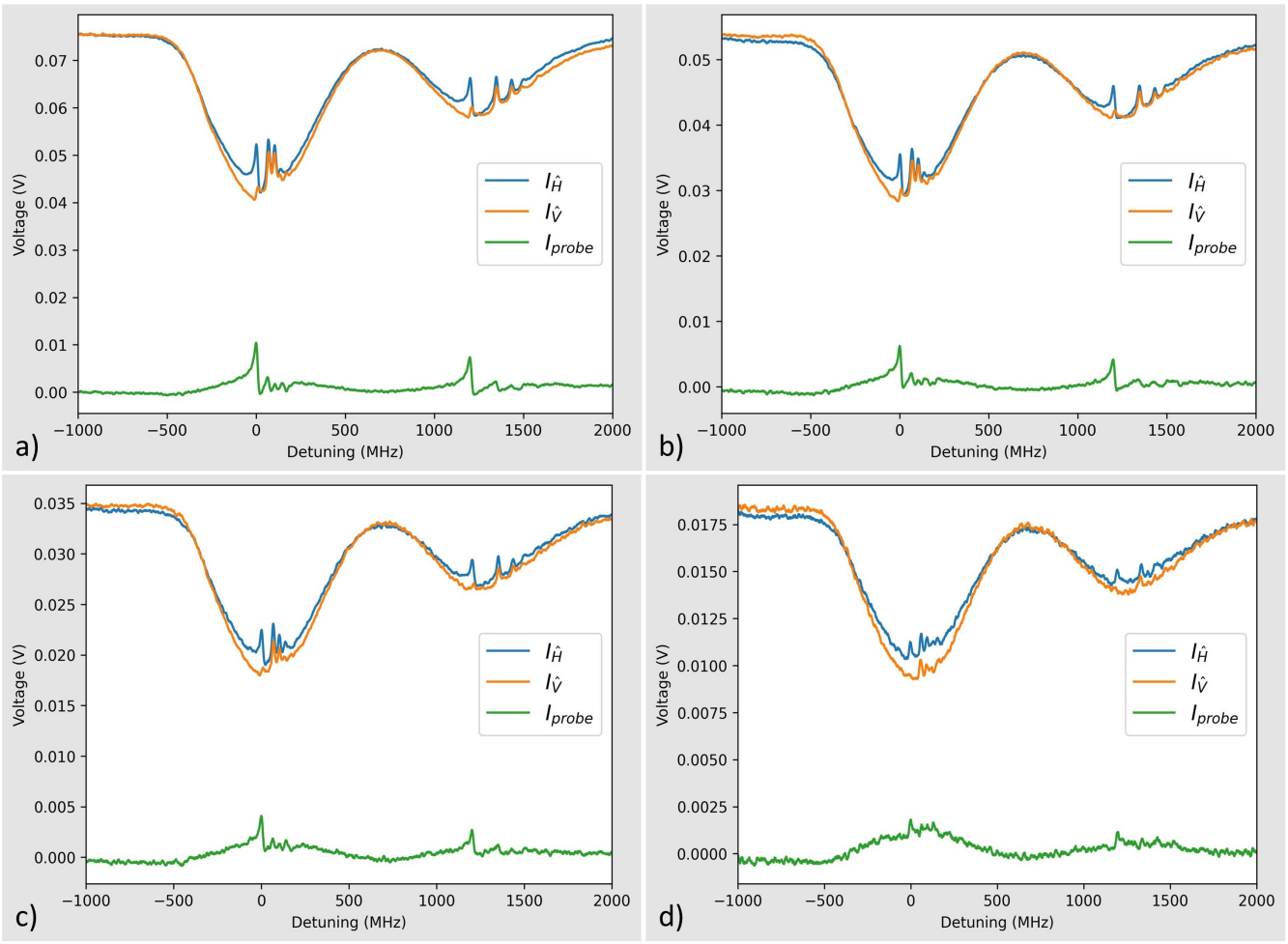

Figure 6.8: Polarisation spectroscopy signals for various pump-probe beam power. a) 0.4mW pump & 0.04mW probe; b) 0.3mW pump & 0.03mW probe; c) 0.2mW pump & 0.02mW probe; and d) 0.1mW pump & 0.01mW probe. The signal-to-noise ratio decreases, with decreasing beam power resulting in a more distorted spectrum. Here the intensity of the $\hat{H}$ beam corresponds to the blue signal, the orange spectrum is the $\hat{V}$ beam, and the differential signal $I_{\hat{H}} - I_{\hat{V}}$ is in green. Note that zero detuning is defined at the D_2 line transition ^{85}Rb : $|F = 3\rangle \rightarrow |F' = 4\rangle$.

In an attempt to further understand the experimental setup, we investigated methods to improve the output signal to determine the system limitations[24]. For this purpose, we built an

[24]Although it is intuitive to think the low power settings of the beams are the primary reason for the distorted signals seen in Fig. 6.8, this still needed to be investigated to identify the experimental limitations.

instrumentation amplifier (IA) with a variable gain, controlled by a potentiometer (pot). The amplifier schematic can be found in Fig. 6.9 and is split into three different parts. The electronics within the blue border form an input buffer and amplifier circuit; the components in the red border are responsible for the differential output signal; and what is inside the green border forms a DC voltage offset for the V2 signal.

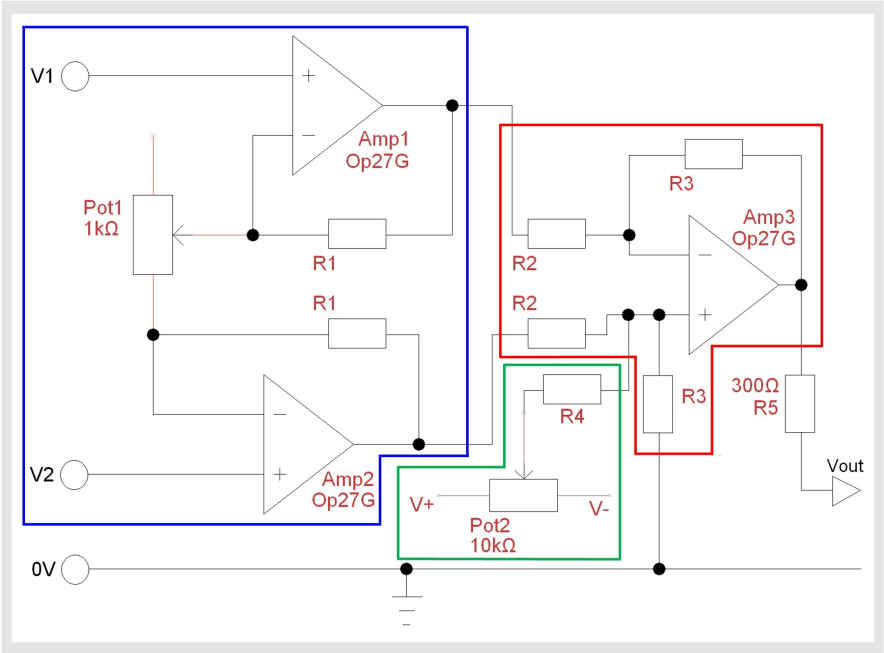

Figure 6.9: Schematic of an instrumentation amplifier with variable gain. The blue section is a buffer and amplification circuit; the red part generates the differential signal; and the green is an offset DC voltage. Here V1 and V2 are the signal inputs, while Vo1 and Vo2 are the signals after amplification, Vout is the differential signal output, 0V is the ground, Amps are operation amplifiers, pots are potentiometers, and resistors are labelled R. Note that R1-R4 have the same resistance of 910Ω.

The way this amplifier works is quite simple. The two signals from the photodiode enter via the V1 and V2 channels, where they are incident on two sets of operation amplifiers (Op-Amps), Amp1 and Amp2. These amplifiers are low-noise precision op-amps manufactured by analogue devices (Op27G), and together with the Pot1 potentiometer[25] and the R1 resistors serve to act as a buffer and amplifier circuit, the gain of which is controlled by the value of the potentiometer[26]. The amplified signals from the two buffer outputs (Vo1 and Vo2) now reaches the differential part of the circuit (in the red border), where one signal is subtracted from the other to generate the desired polspec signal (Vout), the gain of which is given by,

$$V\text{out} = \frac{R3}{R2}(1 + \frac{2R1}{R_{\text{Pot1}}})(V1 - V2). \tag{6.5.14}$$

By design, op-amps possess a very large internal gain and infinite input impedance (i.e. no current flows into the op-amp input pins), which is why resistors are needed to control the signal gain. Note that to eliminate common-mode rejection[27], all resistors (except R5) have the same resistance of 910Ω. In this case the ratio of R3 over R2 is equal to one, suggesting the gain to the differential signal is solely controlled by Pot1. Although the offset function of the amplifier (green border in Fig. 6.9) was not used, it introduces an offset voltage to the V2 signal, resulting in a

[25] Note that potentiometers are just variable resistors.

[26] The choice of resistors in this circuit was based on what pots I had available at the time. Ideally, it is best to choose resistors with resistances close to the value of the pot (if only signal amplification is desirable).

[27] Common-mode signals are unwanted noise that equally affects both input terminals of the IA, and an IA is designed to reject these signals and amplify only the difference between the inputs.

vertical shift in the differential signal[28]. Note that although not depicted in Fig. 6.9, each amplifier requires a differential voltage to operate, which can be achieved using a two-channel power supply[29]. Throughout our experiment, we used a differential voltage of ±12V. We successfully managed to use the instrumentation amplifier with the same photodiodes to obtain a more visible differential signal for low-intensity measurements, as shown in Fig. 6.10 below.

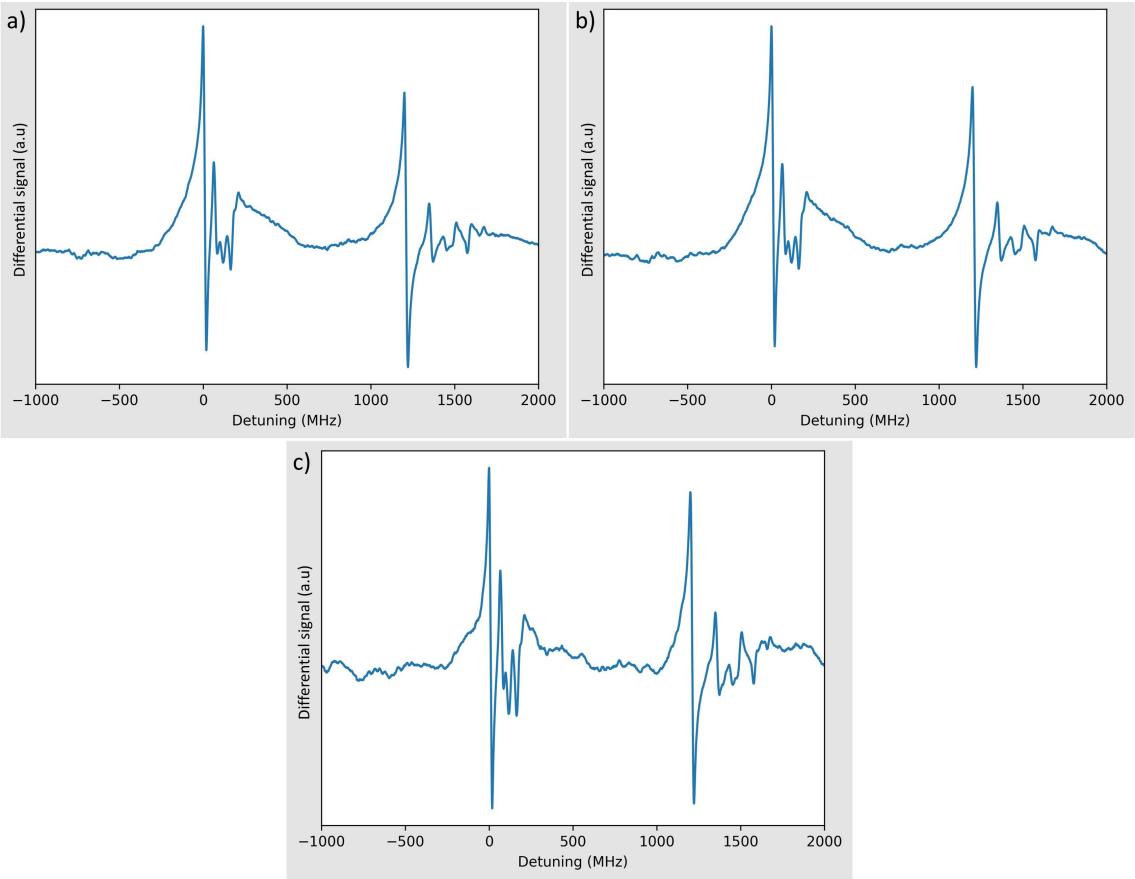

Figure 6.10: The polspec differential signals with an instrumentation amplifier. The signals are normalised with respect to the maximum at zero detuning. The powers of the pump and probe are a) a 0.4mW pump & 0.04mW probe; b) a 0.2mW pump & 0.02mW probe; and c) a 0.1mW pump & 0.01mW probe. Once again, zero detuning is at the D_2 line transition $^{85}\text{Rb} : |F = 3\rangle \rightarrow |F' = 4\rangle$.

The data from Fig. 6.10 proved the detection system was indeed a key limitation to generate a differential signal at low intensities. It would have been interesting to check the stability of the laser lock using these signals by connecting the IA to a servo[30]. Unfortunately, at the time I was using a Thorlabs laser diode controller (LDC210C) and temperature controller (TED200C) with an ISO-TECH synthetic frequency generator (GFG 2004), and had no access to a servo and hence no laser locking capabilities.

[28] I was later told this counts as data tampering since artificially shifting one of the input signals can cover up the imbalances in the light intensity incident on the two photodiodes. For this reason, I refrained from using it.

[29] A differential voltage can be achieved by connecting the positive terminal of one channel to the negative of the other and grounding them both. This essentially creates a 0V in the middle, where the remaining positive and negative terminals from the two channels supply a +V and -V voltage, respectively.

[30] Although rigorous testing of the IA would be required before any such connection is made, especially since the amplifier had to be remade. The first time around, I was chasing my tail trying to remove a rogue signal interfering with the spectrum (which later turned out to be a result of wrongly soldering two resistors).

Another interesting investigation we conducted was to observe the behaviour of the polspec signal when using probe beams of different polarisation structures, projected along different orthogonal polarisation bases. Unfortunately, at this point in time my experiment was down[31], however, our friends at the Fraunhofer Centre for Applied Photonics had an identical polspec setup in place and were kind enough to let me use it to complete my investigation. The two major differences were the laser system in their setup, used a distributed Bragg reflector (DBR) coupled into a single-mode fibre, instead of an external cavity diode laser (ECDL) and the polarimeter arms were reversed (i.e. the shielded cell sits between PBS_4 and the NPBS from Fig. 6.7), meaning the initial probe polarisation is horizontal. We present our findings in the figures below.

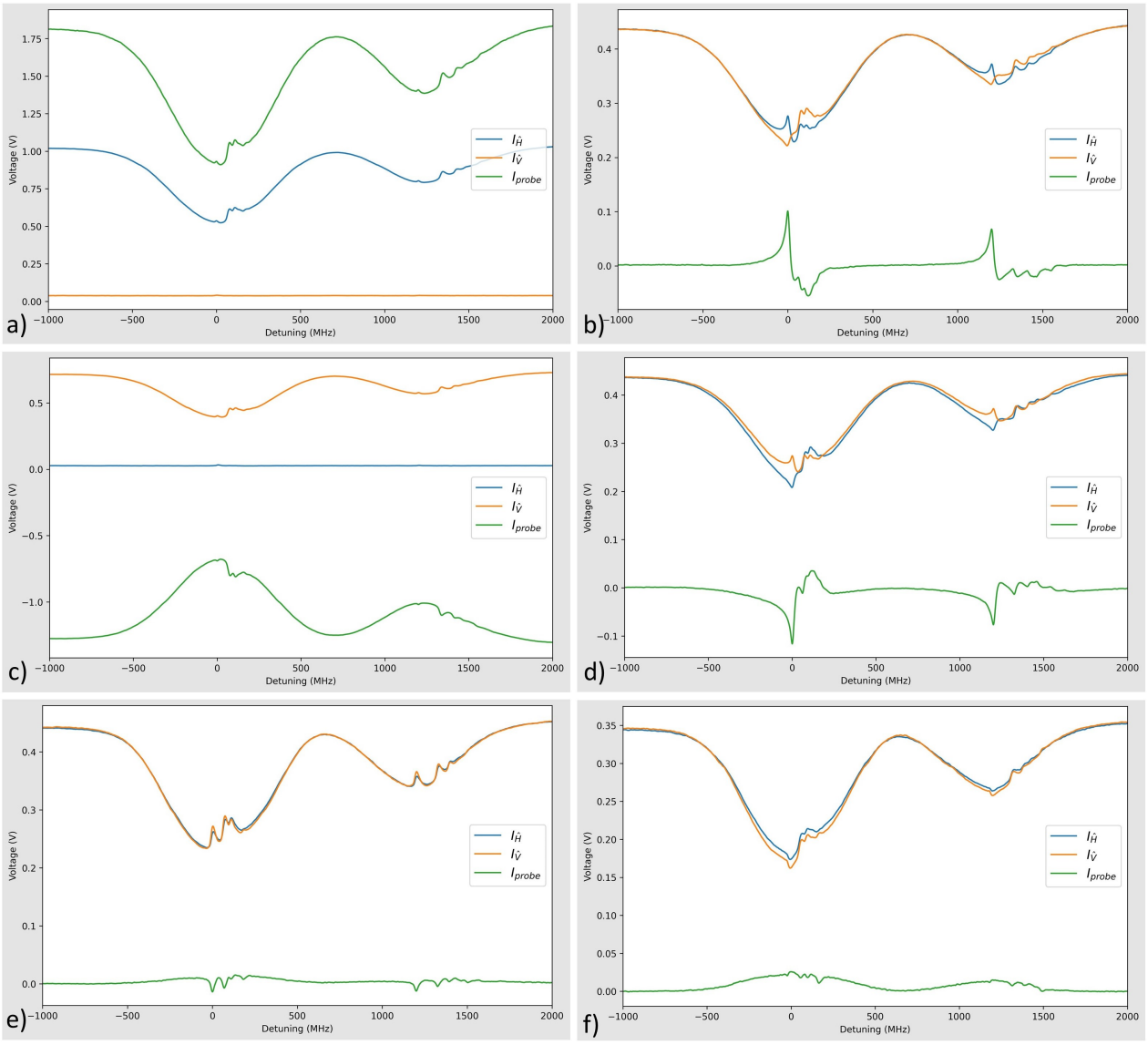

Figure 6.11: Polspec data with a HV measurement system for the six polarisation structures generated from a horizontal probe passing through waveplates at different angles. Here a) HWP at 0°, b) HWP at 22.5°, c) HWP at 45°, d) HWP at 67.5°, e) QWP at 45°, f) QWP at 135°.

Fig. 6.11 is generated from the normal horizontal and vertical (HV) measurement system by the PBS before the photodiodes (see Fig. 6.7). Here, the polarisation of the input probe beam is

[31] If I recall correctly, the ECDL stopped functioning and needed repairs, which meant the whole experiment had to be realigned.

varied across all six polarisation structures, and the polspec signal is recorded for each one. When observing the shape of the signals from Fig. 6.11, we see that a polspec signal was not generated for a probe beam with a horizontal (Fig. 6.11a) and vertical (Fig. 6.11c) polarisation structure. This phenomenon is to be expected since a component of the probe signal is now completely orthogonal to one of the detectors, and therefore we expect no light to be incident on it (i.e. $I_{\hat{H}}$ should be zero at PD_2 and $I_{\hat{V}}$ should be zero at PD_3)[32]. The outcome is that one of the two signal components is zero, and the recovered result resembles the profile of a satspec signal[33]. In a similar fashion, a HWP set at 45° is placed before the PBS splitting the beams into the photodiode to generate a signal projected along the diagonal and anti-diagonal (AD) bases, the result of which is illustrated in Fig. 6.12.

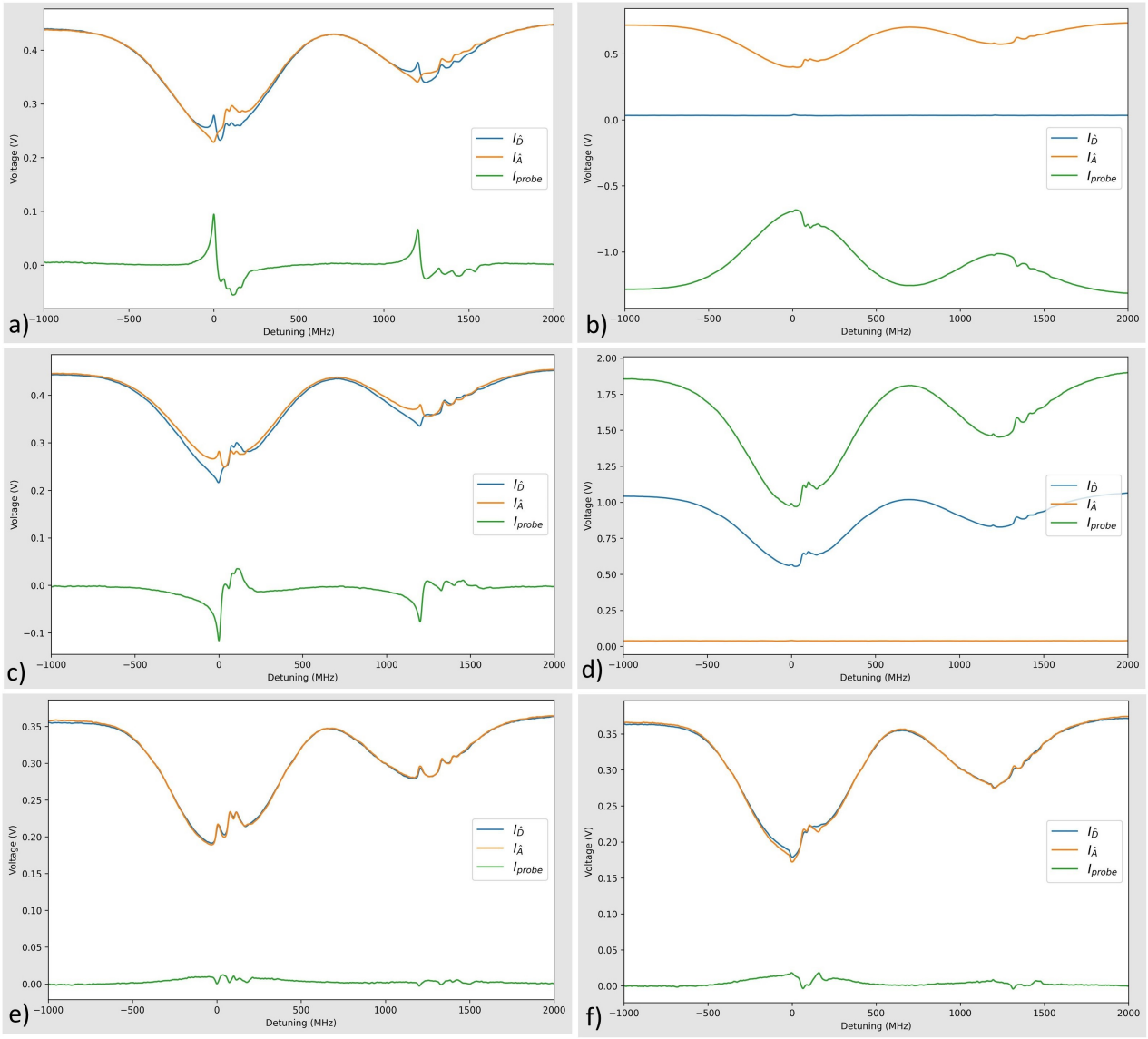

Figure 6.12: Polspec data with an AD measurement system for the six polarisation structures generated from a horizontal probe passing through waveplates at different angles. Here a) HWP at 0°, b) HWP at 22.5°, c) HWP at 45°, d) HWP at 67.5°, e) QWP at 45°, f) QWP at 135°.

[32] Although we expect this to be true, it actually depends on the extinction ratio of the optics in use. Since our PBS is not perfect, the signals are never exactly zero.

[33] Since the differential signal is always generated in the order given by Eqn. 6.5.10, one of the output signals will be inverted, as seen by Fig. 6.11c.

Once again we find the diagonal and anti-diagonal (Fig. 6.12b and Fig. 6.12d respectively) possess a signal component equal to zero, whereas the two other signals generated by the HWP have a normal spectral shape associated with a polspec signal. Finally, a QWP set at 45° is now used just before the PBS to generate the final data set, where the beam is projected along the right and left circular measurement bases (RL), which is displayed in Fig. 6.13.

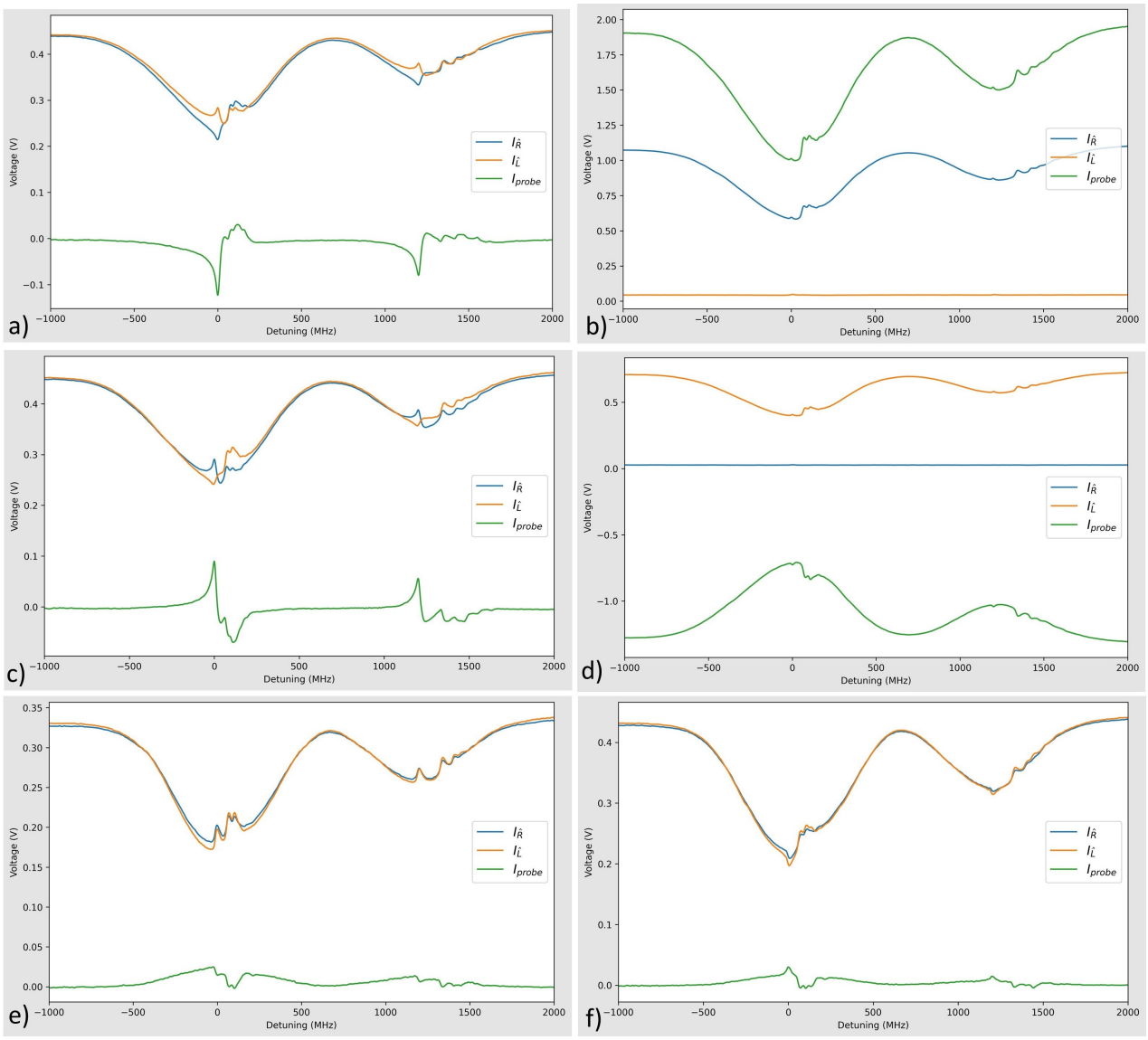

Figure 6.13: Polspec data with a RL measurement system for the six polarisation structures generated from a horizontal probe passing through waveplates at different angles. Here a) HWP at 0°, b) HWP at 22.5°, c) HWP at 45°, d) HWP at 67.5°, e) QWP at 45°, f) QWP at 135°.

The signals displayed in Fig. 6.13 are quite peculiar, and their behaviour differs from the previously illustrated results. Here, the probe beam with a circularly polarised structure does not return a signal with zero intensity across the two photodiodes, and from observation we can see that Fig. 6.13b and Fig. 6.13d are similar in shape to the signals in Fig. 6.12 but inverted (i.e. the HWP is set at −45°). One possible explanation is that the NPBS affects the ellipticity of the probe beam, turning the circular polarisation into linear and vice versa, such that the signal for the diago-

nals and circulars are swapped when the projection measurements are performed[34]. An interesting occurrence in the polspec signals (primarily those with a dispersive shape) is that one of the two signal components has a peak while the other a trough, which are mostly visible on the spectrum at the position corresponding to the transitions from the upper ground to the upper excited states and especially for the circular beams, as seen in Fig. 6.11 and Fig. 6.12. This phenomenon occurs as a consequence of the induced anisotropy in the medium from the pumping process, known as enhanced absorption (for the troughs) and diminished absorption (for the peaks). This provides definitive proof that circular dichroism and, by extension, circular birefringence exist in the atomic medium as measured by the absorption of the probe beams driving the $\sigma_{\pm}$ transitions. Note that we can also observe this effect in the cross-over peaks; for example, the height of the cross-over peaks in Fig 6.11e and Fig 6.11f are different, suggesting the probe beam in the former experiences less absorption when propagating through the Rb cell.

6.5.3 Final remarks

From all the data we have presented so far, it is obvious that the transitions given by $|F = I + 1/2\rangle \rightarrow |F' = I + 3/2\rangle$, where I is the nuclear spin, dominate the polarisation spectroscopy signal with a dispersive shape. These transitions leave the majority of the atoms in the stretched state, where the dipole selection rules prohibit the atoms from decaying to the lower ground state. For example, in ^{87}Rb ($I = 3/2$), the transition $|F = 2\rangle \rightarrow |F' = 3\rangle$ is closed, and hence the atoms can only decay back to the $|F = 2\rangle$ state. However, for the transitions $|F = 2\rangle \rightarrow |F' = 2\rangle$ and $|F = 2\rangle \rightarrow |F' = 1\rangle$, there is a decay channel to the lower ground state $|F = 1\rangle$, which is very far off-resonance from the probe beam (around 6.83GHz away) and does not contribute to the polarisation spectroscopy signal. For this reason, we expect the $|F = 2\rangle \rightarrow |F' = 3\rangle$ transition to be the largest for ^{87}Rb, and the $|F = 3\rangle \rightarrow |F' = 4\rangle$ transition to be the most dominant for ^{85}Rb, which is the case, as observed in both Fig. 6.8 and Fig. 6.10.

Note that the experiment required some calibration prior to data gathering, where a set of three waveplates were introduced (one HWP and two QWPs) placed before the last PBS in the setup, as shown in Fig. 6.14. Since the optics used throughout the experiment are far from perfect, the intensity ratio of the transmitted and reflected beams from the PBS could differ. The first step is to use a horizontal probe and adjust the compensation plates to minimise the vertical signal off-resonance. This should take into consideration the effects of the cell windows on the polarisation profile of the probe beam. We use the HWP to adjust the polarisation of the beam, while the QWP changes the ellipticity; however, the second QWP is required to undo the circularity introduced by the first QWP and return the beam to its initial polarisation state. For example, if we consider the case of a HV detection system with a diagonal probe beam, a single QWP will turn the beam circular thereby changing the polarisation structure of the input beam[35]. Therefore, the second QWP is used to revert the beam back into diagonal before being incident on the PDs. Additionally, the PBS does not seem to split circular light equally (favouring the reflected arm), and hence a neutral density (ND) filter is used to adjust the inequality in the intensity profile of the probe beam.

[34] Despite their name, a NPBS affecting the polarising structure of a beam in this manner is very common.

[35] As long as the QWP fast axis is not aligned with the polarisation direction of the probe, which is likely the case.

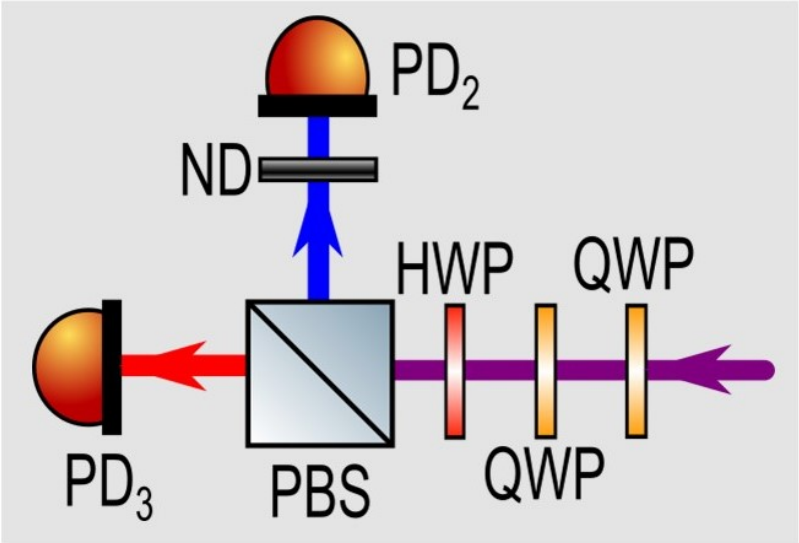

Figure 6.14: Polspec detection system with compensation plates. The HWP is used to adjust the polarisation of the probe beam, while the QWP changes the ellipticity. The second QWP is used to undo the circularity introduced by the first QWP.

In our attempt to understand the behaviour of this system, we had numerous discussions on the role played by the pump and the magnetic field in producing the polspec signals, and although I have discussed them in different sections throughout this chapter, highlighting their importance to the experiment, I would like to briefly summarise their roles before moving on to the spatial variation of this experimental setup. The introduction of the magnetic field in the direction of the beam propagation limits the allowed atomic transitions to $\sigma_{\pm}$ in the paraxial approximation, where the mathematically described axis of atomic precession is aligned with the direction of the magnetic field. In this configuration, we get a Zeeman splitting where the excited $m_{F'}$ and ground m_F magnetic sublevels each experience a frequency shift given by the Larmor frequency from Eqn. 4.2.4. A consequence of the Zeeman effect is that the driving transitions (i.e. $\sigma_{\pm}$) are also shifted, the magnitude of which is given by their respective Larmor frequencies $\omega_{L(\sigma_{\pm})}$, as demonstrated in Fig. 6.15, and observed in the components of the polspec signals presented in Section 6.5.2. The magnetic field alone is insufficient to produce the polspec signal because the frequency shift introduced to the $\sigma_{\pm}$ transitions applies to all m_F states, with a slight change to the transition probability. In this configuration, all possible magnetic sublevel transitions obeying the selection rules can occur[36] and the atomic medium is isotropic, lacking the capacity for preferential absorption and dispersion that are required for the production of a polspec signal. However, the pumping process using a circular probe takes care of this, introducing an anisotropy in the medium, leading to circular dichroism (preferential absorption of the $\sigma_{\pm}$ components) and birefringence (added phase shift to the $\sigma_{\pm}$ components). In terms of the atomic energy scheme, the atoms are now concentrated in the furthest away m_F level, as illustrated in Fig. 6.15 below, and the passing probe beam now experiences a preferential absorption of the two polarisation components, leading to the phenomena of enhanced and diminished absorption used to generate the polspec signals presented in this section[37]. Note that although it is assumed the majority of the atoms will occupy the last magnetic sublevel (i.e. $m_F = 3$), some of the atoms will end up in other ground states from external effects like collisions with the cell wall. Additionally, some of the atoms that joined the system recently might occupy these ground states, since the population of the ground state in

[36] In terms of the spectrum, these m_F transition peaks are small Lorentzian peaks occupying the area below the larger Lorentzian peak representing the $|F\rangle \rightarrow |F'\rangle$ transition. These peaks can be resolved using higher magnetic fields or lasers with a small enough linewidth.

[37] In terms of the spectrum, and using the example in Fig. 6.15, the Lorentzian peak corresponding to the $|F = 3\rangle \rightarrow |F' = 4\rangle$ transition of ^{85}Rb now has only two smaller Lorenzian peaks within its profile corresponding to the $|F = 3, m_F = 3\rangle \rightarrow |F' = 4, m_{F'} = 2\rangle$ and the $|F = 3, m_F = 3\rangle \rightarrow |F' = 4, m_{F'} = 4\rangle$ transitions.

the absence of a driving field is assumed to be uniform[38].

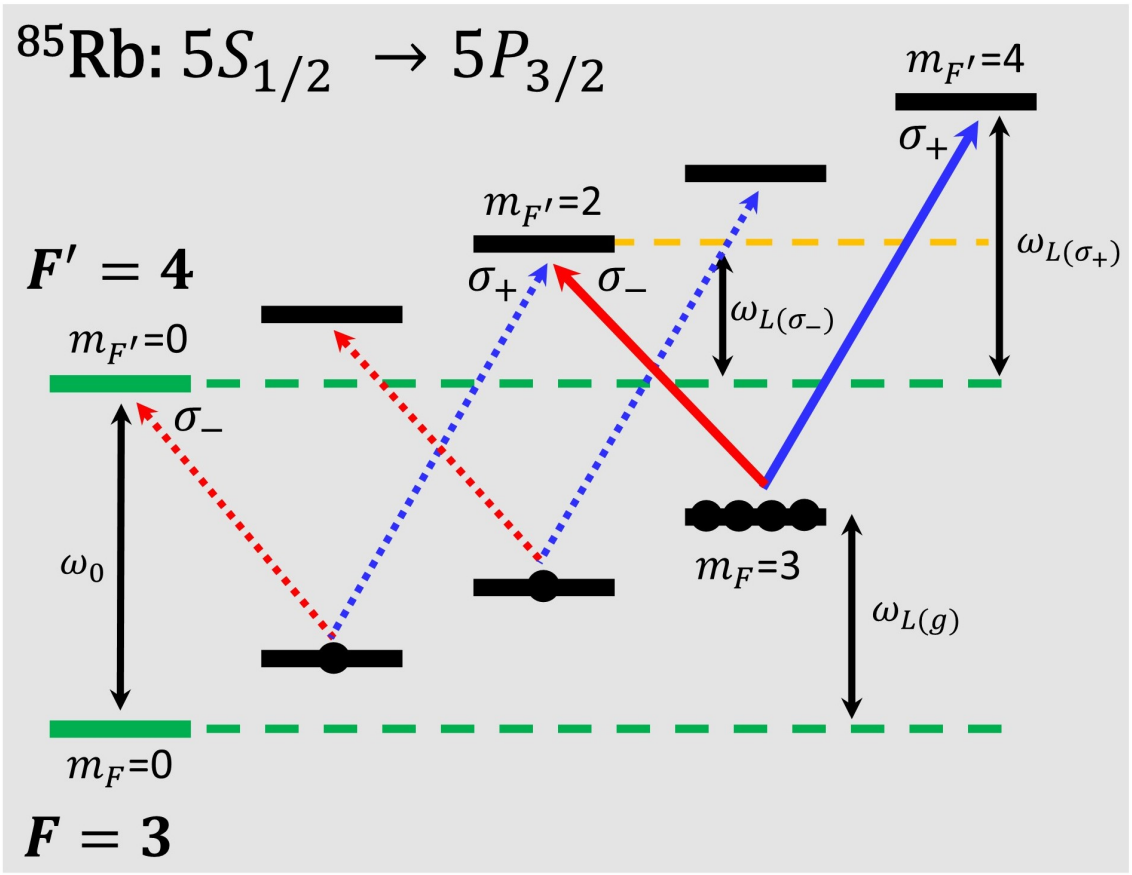

Figure 6.15: The magnetic field and pumping scheme required for a polspec signal in the $|F = 3\rangle \rightarrow |F' = 4\rangle$ transitions of ^{85}Rb. An external magnetic field parallel to the beam propagation direction permits only $\sigma_\pm$ transitions from occurring, which also shifts the ground state sublevel and the $\sigma_\pm$ transition by their Larmor frequencies $\omega_{L(g)}$ and $\omega_{L(\sigma_\pm)}$, respectively. Meanwhile, the pump generates an anisotropy in the atomic medium, where the majority of the atoms occupy the furthest ground state ($m_F = 3$), introducing a preferential absorption of the two $\sigma_\pm$ components in the probe beam. These two effects together result in generating two absorption signals separated by their Larmor frequencies, whose difference $(\omega_{L(\sigma_+)} - \omega_{L(\sigma_-)})$ produces the polspec signal. Note that we only consider half the magnetic sublevels in this figure; however, the concept remains the same for the negative magnetic sublevels.

6.6 Spatial polarisation spectroscopy (spatpolspec)

The final objective of the second half of my PhD was to set up a system capable of detecting a spatially varying polarisation signal using a vector vortex probe beam in an optically pumped medium under the influence of an external magnetic field. The intention is to establish a pattern between the spatial structure of the output beam and the frequency of the light source using polarisation spectroscopy (polspec) as a stepping stone for laser locking purposes with a spatially varying frequency modulated signal. In this section, we explore our work realising an experimental

[38] Although we magnify our beams as much as possible, it is difficult to fully occupy the entire diameter of the cell without replacing many of our optical elements with 2-inch optics.

configuration of spatial polarisation spectroscopy (spatpolspec), discussing changes to the initial polspec setup and the theoretical model, providing preliminary results utilising an acousto-optic modulator (AOM) for laser frequency modulation, and investigating the changes to the spatially resolved polarisation signal around atomic resonance. We test the signal using two different hybrid beams generated from a vector vortex plate and a quarter waveplate (QWP), drawing a comparison between our system's outcome and a simple theoretical model of light absorption and dispersion. We conclude by reviewing key limitations to the experimental configuration, discussing potential improvements to the setup, and explore possible methods of implementation for laser frequency stabilisations.

6.6.1 Experimental realisation

Many of the concepts introduced in the previous section remain the same; however, the altered setup for spatpolspec can be seen in Fig. 6.16 below.

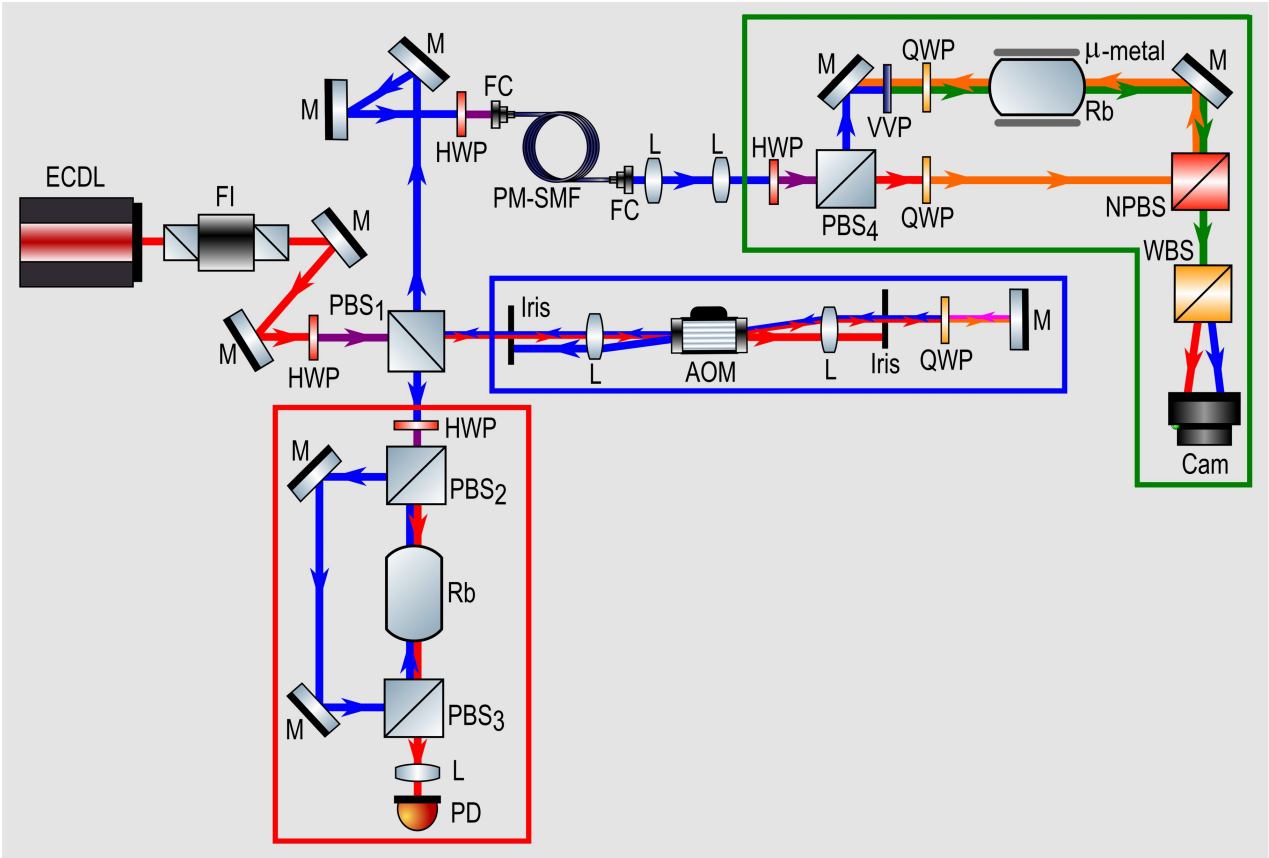

Figure 6.16: The experimental configuration for Spatial polarisation spectroscopy. The setup is split into three parts: a saturated absorption setup (red border), an AOM frequency modulation configuration (blue border), and the main spatpolspec section (green border). Once again, the beam colours indicate different polarisation structures, where horizontal is red, vertical is blue, purple is a diagonal, orange and pink are circulars, and green is a vector beam. The experiment is made up of an external cavity diode laser (ECDL), a Faraday isolator (FI), a polarisation-maintaining single mode fibre (PM-SMF) attached to fibre collimators (FC), half waveplates (HWP), quarter waveplates (QWP), a vector vortex plate (VVP), polarising beam splitters (PBS), lenses (L), mirrors (M), rubidium vapour cells (Rb), Irises, an acousto-optic modulator (AOM), a non-polarising beam splitter (NPBS), a Wollaston beam splitter (WBS), a photodiode (PD), and a camera (Cam).

The transition from the polspec setup depicated in Fig. 6.7 to the final spatpolspec setup shown in Fig. 6.16 was not instantaneous, and instead changes to the experimental configuration were introduced out of necessity to quantify the behaviour of our system. In the early stages of the spatpolspec experiment, the HWP used to diagonalise the probe beam was removed in favour of a vector vortex plate (or q-plate) and a quarter waveplate in the order seen in Fig. 6.16, whereas the two photodiodes shown in Fig. 6.7 were replaced by a CMOS camera (JAI GO-5000M-USB) to observe the changes to the spatial signal as the laser frequency is varied. The first step was to turn off the laser scanning and manually change the laser frequency[39], as we scanned the laser frequency across certain regions of the rubidium spectrum, we observed changes in the beam shape as lobes began to form in some parts of the beam profile, which were rotated when the laser frequency changed. There was no doubt something interesting was occurring, and to investigate this effect, further changes to the experimental setup were required. Next we introduced an AOM (a Gooch & Housego 3080-125) in a double-pass configuration to control the laser frequency and prevent changes to the beam path[40], as seen in the setup within the blue border in Fig. 6.16. Note that for an AOM to work, the input beam has to be frequency stabilised. Since at the time I had no servo in place, I decided to replace all the electronics running the ECDL with a MOGLabs diode laser controller instead, to lock the laser to the desired atomic transition[41].

Although in a double-pass configuration the beam position should not change, and despite my best efforts, it is very difficult to perfectly align the lenses in the AOM setup. As a consequence, the beam path experiences slight shifts in position as the AOM frequency is scanned. These shifts are negligible in free space but significant enough to interfere with a lens focusing a beam into a 20μm pinhole, obstructing the light and preventing the output beam from propagating through. For this reason, the pinhole was replaced in favour of a polarisation-maintaining single mode fibre (PM-SMF) in the panda configuration to clean the beam profile from the ECDL[42]. This fibre was attached to two fibre collimators (FC) on each end, acting similar to the two lenses that focus and collimate the beam into and out of the pinhole, as demonstrated in Fig. 6.7.

A PM-SMF is made polarisation-maintaining via two flexible stress rods that span the entire length of the fibre, introducing mechanical stress and creating a birefringence in the fibre core. The input light is focused by the FC into the core, which is located between the two stress rods, surrounded by the cladding, and housed inside a thick rubber jacket to prevent light leakage and ensure the fibre components are well protected from any external elements (see Fig. 6.17). Since the focal length of the FC lens is relatively small[43], the positional shift of the beam path caused by changes to the AOM frequency is significantly reduced, ensuring there is an output beam for the entire AOM scan range. However, the trade-off is that the intensity of the light from the fibre

[39]Since our lasers have an oscillating piezoelectric transducer (PZT) to change the cavity length and scan the frequency, the amount in which it expands or contracts is controlled by the amplitude of the provided signal. To manually scan the laser, we simply set the amplitude to zero and adjust the PZT by changing the offset frequency on the signal generator. Note that if the amplitude is set to zero, the supplied frequency no longer has an effect on the PZT.

[40]More information on AOMs can be found in Section 5.5; however, in a double-pass configuration, the laser frequency is adjusted by twice the frequency of the selected AOM mode and the beam path is expected to remain unchanged througout propagation.

[41]These controllers are very useful and easy to use, containing a laser driver, temperature controller, signal generator, and servo all built into the circuitry, offering plenty of options for customisation. Unfortunately, this makes them very expensive.

[42]The fibre was manufactured by Evanescent Optics Inc., constructed from a standard PM780-HP type fibre with a core diameter of 4.5μm [217].

[43]We used two Thorlabs FC/APC fibre collimation packages at 780nm (F220APC-780) with a focal length of 11.07mm, generating an output beam with a diameter of 2.1mm.

changes as the AOM frequency is scanned, caused by a slight misalignment of the focusing of the input beam to the fibre core, as illustrated by the comparison of two input beams in Fig. 6.17a. Similar to wave retarders, these fibres also possess a fast and slow axis (see Fig. 6.17b). However, they do not preserve all polarisation structures and only maintain the polarisation of a linear input beam aligned parallel to one of the two axes, meaning at most only two beams with orthogonal linear polarisation structures can be coupled into the same PM-SMF[44]. Experimentally, since fibres are normally screwed into a static lens or mirror mount, a HWP (sometimes with a PBS) is introduced before the input FC to adjust the polarisation structure of the input beam to match the alignment of the fibre axes (as seen from Fig. 6.16)[45].

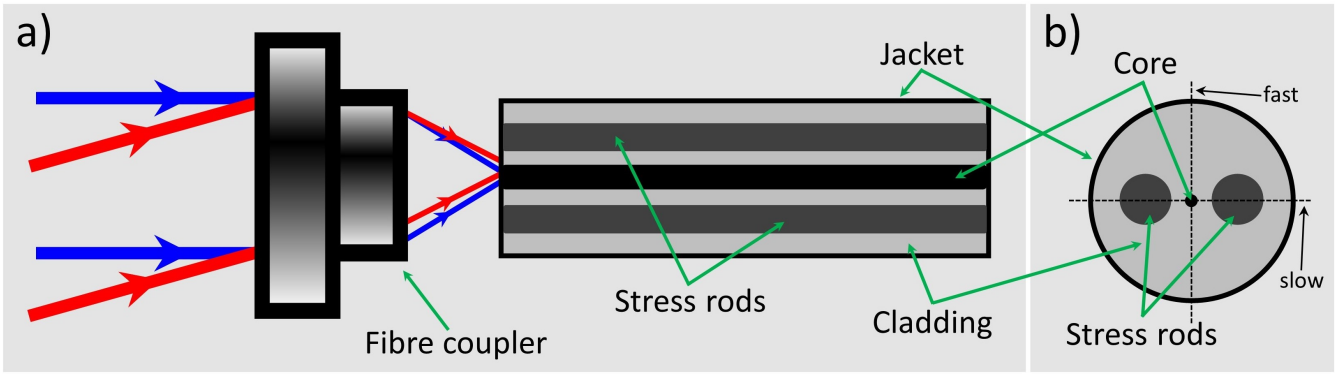

Figure 6.17: A panda configuration polarisation maintaining single mode fibre (PM-SMF), consisting of the core, two stress rods, cladding, and jacket. a) Top view of the fibre and fibre collimator (FC). The parallel beam (blue) is aligned to ensure perfect fibre coupling, resulting in maximum output intensity; however, the angled beam (red) is not fully coupled into the core and will experience significant intensity losses. b) Front view of the fibre. The dotted lines highlight the orientation of the fast and slow axes of the fibre. Note that the size of the fibre core has been enlarged for clarity.

Although fibre coupling an input beam can be a tedious process, there are several advantages to using a fibre in an experimental setup. Single mode fibres are efficient at cleaning the shape of even the most bizarre of input beams, generating an output light field with a transverse mode profile resembling a Gaussian beam (see Section 1.5 on Gaussian modes). In the case of our single-mode fibre, the output is the fundamental transverse mode labelled TEM00. Additionally, they can separate the alignment of different sections of an experiment. For example, if the beam prior to entering the fibre shown in Fig. 6.16 experiences significant changes to the alignment, then the alignment of the spatpolspec setup (green border in Fig. 6.16) will remain unchanged, provided the position and orientation of the output FC have not been adjusted. However, despite their usefulness, there are some disadvantages associated with using fibres. Since coupling a beam into a fibre is never 100% efficient, some of the light is lost in the process, resulting in an output beam with reduced power. Another common issue is that dust particles can be burnt on the core as a result of prolonged exposure to focused laser light, severely affecting the shape and power of the output

[44]Note that it is possible to create a fibre that maintains circular polarisation. The easiest way is to rotate a PM-SMF, creating a circular birefringence in the fibre core, which introducing different phase velocities to the two circular components. An example of such a fibre is the Thorlabs Spun PM Optical Fibre (SHB1500).

[45]One can ensure the correct beam polarisation is entering the fibre by connecting the fibre output to a polarisation analyser, like the one by Schäfter+Kirchhoff (SK010PA), and rotating the HWP to minimise fluctuations in the output beam polarisation profile while manually stressing the fibre. If a polarisation analyser is unavailable, a power meter with a polariser can be used instead.

beam[46]. Additionally, since the output from a fibre is very divergent, it is difficult to replace an output collimator with a lens for beam magnification[47]. Therefore, a telescope system to magnify the beam by a factor of two was introduced in the setup, increasing the beam diameter from 2.1mm to 4.2mm, in an attempt to cover as much of the Rb vapour cell as possible in the spatposlpec experiment. The final adjustment we made to the setup was replacing the PBS before the camera with a Wollaston beam splitter (WBS) to capture the projections of both orthogonal polarisation states in a single-shot image. Although the position of the satspec was changed (red border from Fig. 6.16), it remains the same in structure as the previous polspec setup seen in Fig. 6.7.

From Fig. 6.16 we observe that in our experiment, a vertical probe beam propagates through a q-plate, followed by a QWP with its fast axis orientated at 45° with respect to the horizontal, generating our vortex beams. Using Eqn. 1.3.21 and Eqn. 2.5.1, we calculate an expression for the Jones matrix of our vortex beam as follows,

$$\begin{aligned}\mathbf{E}_{\text{probe}} &= \mathbf{J}_{QWP(45°)}\mathbf{J}_{qp}\hat{V} = e^{\frac{i\pi}{4}}\begin{pmatrix}1 & i\\ i & 1\end{pmatrix}\begin{pmatrix}\cos(2\theta) & \sin(2\theta)\\ \sin(2\theta) & -\cos(2\theta)\end{pmatrix}\begin{pmatrix}0\\ 1\end{pmatrix}\\ &= \frac{1}{2\sqrt{2}}\left[(\mathrm{LG}_0^{|l|}e^{2i\delta} + \mathrm{LG}_0^{-|l|}e^{-2i\delta})\sigma_+ - (\mathrm{LG}_0^{|l|}e^{2i\delta} - \mathrm{LG}_0^{-|l|}e^{-2i\delta})\sigma_-\right],\end{aligned} \tag{6.6.1}$$

where $\mathrm{LG}_0^{|l|}$ and $\mathrm{LG}_0^{-|l|}$ are the Laguerre-Gaussian modes discussed in Section 1.5.3 with an azimuthal index l and a radial index $p = 0$. Here $\theta = q\phi + \delta$, where q is the q-plate order, ϕ is the azimuthal angle, and δ is the orientation of the q-plate fast axis[48]. Following the same calculation expressed in Appendix C, we can rewrite Eqn. 6.6.1, similar to Eqn. 6.5.4 as,

$$\begin{aligned}\mathbf{E}_{\text{probe}} = \frac{1}{2\sqrt{2}}E_0e^{-i\Lambda}\Big[&(\mathrm{LG}_0^{|l|}e^{2i\delta}+\mathrm{LG}_0^{-|l|}e^{-2i\delta})e^{i\Pi}\sigma_+\\ &- (\mathrm{LG}_0^{|l|}e^{2i\delta} - \mathrm{LG}_0^{-|l|}e^{-2i\delta})e^{-i\Pi}\sigma_-\Big],\end{aligned} \tag{6.6.2}$$

where Λ and Π are the same quantities from Eqn. 6.5.5. Experimentally, we employ a left circular (or σ_+) pump beam and two different spatially variant hybrid probe beams, generated with a set of two vortex retarders, namely $q = 1/2$ and $q = 1$ plates. The first probe beam is a hybrid beam[49] generated with a vertically polarised light propagating through a $q = 1/2$ vortex plate, followed by a QWP at 45°. The second beam is also a hybrid, following the same generation method as the first, with the distinction that a $q = 1$ q-plate is used instead.

The AOM has an operation frequency of 80MHz and is connected to a simple voltage-controlled attenuator (VCA) and voltage-controlled oscillator (VCO) circuit, controlling the amplitude and frequency of the PZT modulation signal used to oscillate the AOM crystal[50]. The VCO itself has a limited scan range of 50MHz to 100MHz (or 100MHz to 200MHz in a double-pass configuration); therefore, it was vital to carefully consider which transition of which isotope of rubidium to lock our

[46]The fibre would require polishing using sandpaper of different grits (ranging from 30μm to 0.1μm). This process takes around 30 minutes with a fibre polishing machine; however, it can take much longer if done by hand.

[47]At the time, only these specific collimators were available for use. Note there are collimators with adjustable lenses (like the 60FC-SF collimators from Schäfter+Kirchhoff), which can significantly help with fibre coupling efficiency.

[48]For more information, visit Section 2.5.2.

[49]Hybrid beams are those that possess both linear and circular polarisation structures across the beam profile.

[50]Note that the amplitude and frequency of the modulation signal were manually controlled by a set of two potentiometers (pots).

laser to. Based on our previous work with the initial polspec experiment described in Section 6.5, we decided to investigate one of the closed transitions of rubidium for the same reasons discussed in Section 6.5.3. Initially, we locked our laser to the ^{87}Rb: $|F = 2\rangle \rightarrow |F' = \text{CO32}\rangle$ spectral feature[51], positioned around 133.325MHz [161] away from the $|F = 2\rangle \rightarrow |F' = 3\rangle$ closed transition, and falls within the frequency range of our AOM VCO. However, since ^{87}Rb has a lower natural abundance than ^{85}Rb, there are fewer atoms for the light field to interact with, making it difficult to observe any distinct changes to the probe profile as the AOM frequency is varied[52], unlike the clear rotation seen before in the probe beam when the laser frequency was arbitrarily scanning across a large section of the atomic spectrum. For this reason, we decided to switch to the closed transition of ^{85}Rb instead. Unlike the cross-over peak in ^{87}Rb we could lock to, which generated a strong and clear error signal, the smaller frequency separations in the excited hyperfine states of ^{85}Rb meant we had to lock our laser to the D2 line $|F = 3\rangle \rightarrow |F' = \text{CO32}\rangle$ transition of ^{85}Rb for the AOM in use. This peak sits around 152.341MHz [160] away from the $|F = 3\rangle \rightarrow |F' = 4\rangle$ closed transition and unfortunately produces a relatively weak signal, sensitive to the smallest of ambient noise. However, by adjusting the settings of the MOGLabs box and using a suitable power ratio for the satspec pump-probe beams, we managed to successfully produce a satisfactory error signal to lock our laser to for the entire duration of our data collection runs[53].

6.6.2 Results and analysis

In this section, we present our experimental findings and compare the results to a theoretical model based on a simplified form of Eqn. 6.6.2. As previously stated, we lock our laser to the CO23 cross-over peak of ^{85}Rb and use a double-pass AOM to change the laser frequency by a range spanning from 134MHz to 170MHz, as depicted by the red outline on the atomic spectrum in Fig. 6.18. It is believed that this frequency range is sufficient to capture the entire behaviour of the probe beam rotation. Normally, we define zero detuning at resonance (i.e. the $|F = 3\rangle \rightarrow |F' = 4\rangle$ transitions); unfortunately, since the AOM is manually controlled, the frequency is accurate to the nearest MHz[54]. The limitation in the flexibility of the AOM scan meant we were in fact slightly shifted by 340.5kHz from resonance[55]. Note that if 152MHz is considered to be at zero detuning (i.e. $\Delta = 0$), then our scan ranges from $\Delta = \pm 9$MHz.

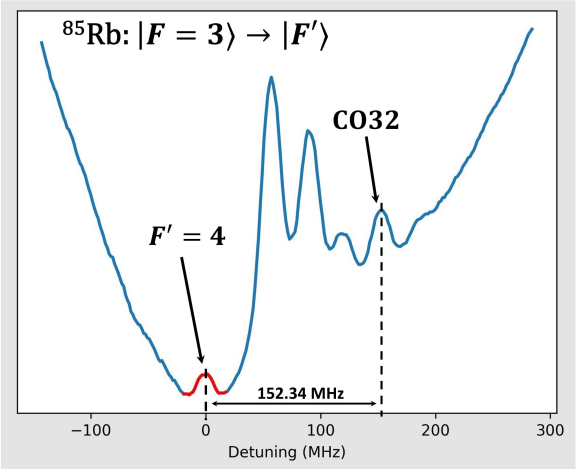

Figure 6.18: The AOM scan region is outlined in red across the $F' = 4$ D2 line transition of ^{85}Rb. We lock our laser to the CO32 cross-over peak, positioned 152.34MHz away from the desired transition.

[51] CO32 is the cross-over peak sitting between the $|F' = 2\rangle$ and $|F' = 3\rangle$ transitions. More information can be found in Section 5.3.

[52] Remember the absorption and dispersion coefficients introduced in Section 6.2 depend on the atomic density n^{ρ}.

[53] Occasional laser re-locking might be required when accidentally bumping into the optical bench.

[54] The AOM circuit was connected to a picoscope, where the beam images are recorded for the AOM frequency ranging from 67MHz to 85MHz, which corresponds to the laser frequency range stated above of 134MHz to 170MHz when considering the AOM double pass.

[55] Which means we label the zero detuning relative to the AOM double pass frequency of 152MHz, whereas the $|F = 3\rangle \rightarrow |F' = 4\rangle$ transition is actually 152.341MHz away from the CO32 peak of ^{85}Rb. Note that this is taken into consideration in our theoretical model.

Once the correct waveplates are placed in the probe beam path, we capture an image of the beam profile far off-resonance, which will account for changes experienced by the probe beam as a consequence of external parameters (e.g. birefringent from optics, ambient light, etc.). We then lock the laser to the CO32 transition, scan the AOM frequency across our detuning range, and record an image of the probe beam interaction with the rubidium vapour for every frequency increment. Since the Wollaston beam splitter (WBS) placed before the camera projects the probe beam along the horizontal and vertical polarisation states, the entire measurement process is repeated twice more for the two diagonal and two circular states, using the appropriate waveplates placed before the WBS[56]. The intensity profiles of the experimental (off-resonance) and theoretical beams taken off-resonance for both the $q = 1/2$ and $q = 1$ hybrid probes can be found in Fig. 6.19 and Fig. 6.20 respectively.

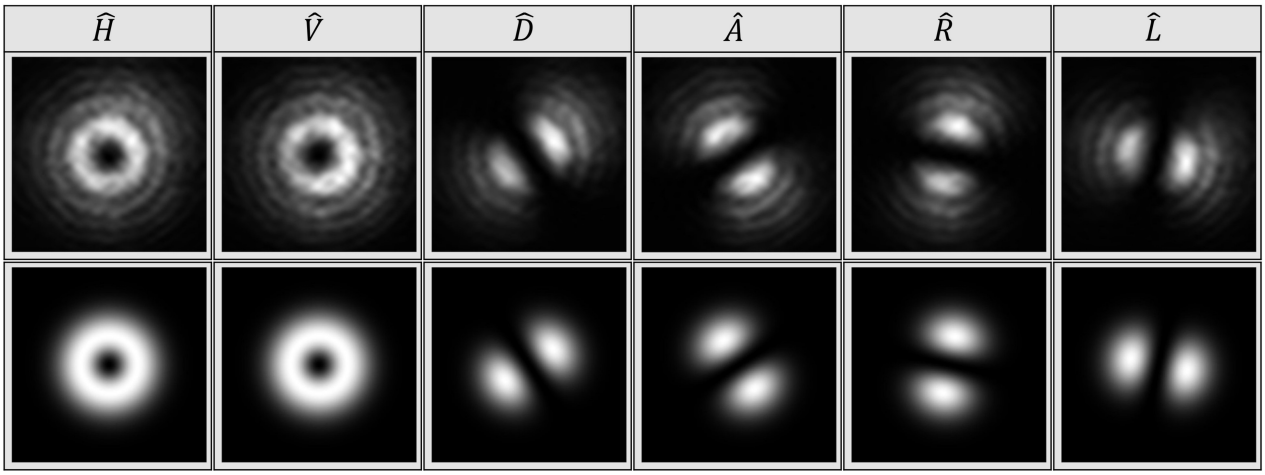

Figure 6.19: Intensity profile of the $q = 1/2$ hybrid probe beam projected onto the six Stokes bases. The top row contains our experimental beams (off-resonance), while the bottom row are the simulated beams.

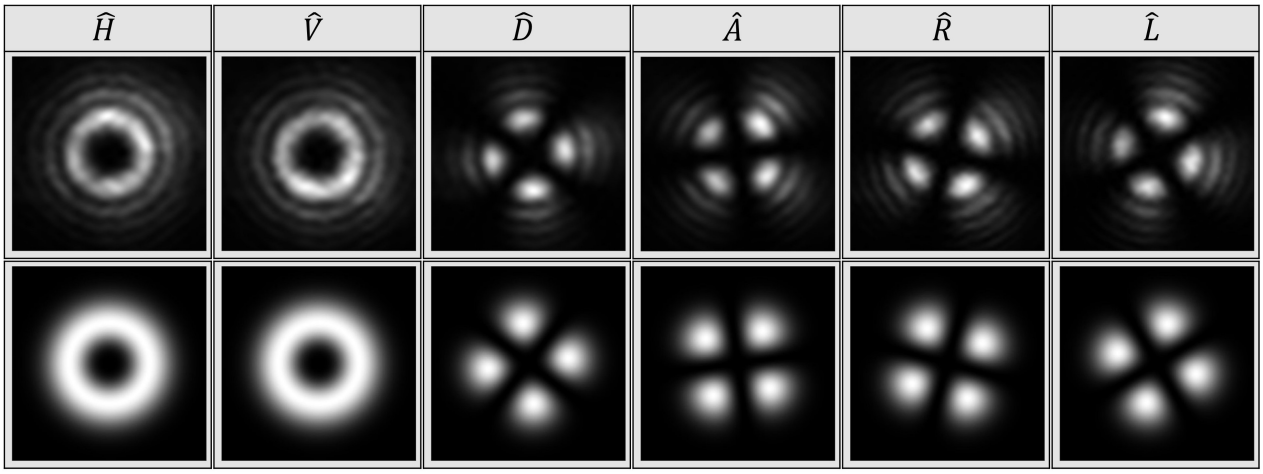

Figure 6.20: Intensity profile of the $q = 1$ hybrid probe beam projected onto the six Stokes bases. The top row contains our experimental beams (off-resonance), while the bottom row are the simulated beams.

[56]Note that every single one of our images has been background subtracted and passed through a low-pass Fourier filter to remove unwanted noise; however, the ring-like structures surrounding our beams are interference patterns modifying the probe intensity profile, generated by the vortex plates, and cannot be removed by low-pass filtering.

The off-resonance images help determine the characteristics of the hybrid beams used in the experiment, since unfortunately, the fast axis orientation of the vortex plates was not recorded when the data was collected. However, we can estimate a value for these angles by matching the intensity profile of the theoretical plots to our experimental data, as shown in Fig. 6.19 and Fig. 6.20. By doing so, we estimate the fast axis angle δ of the $q = 1/2$ plate to have been around $-6°$, while the fast axis angle of the $q = 1$ plate is estimated to have been around $-15°$. Note that one can derive an expression for the electric field of both hybrid probes as they interact with the atomic medium by substituting the azimuthal index $l = 1$ for the $q = 1/2$ waveplate and $l = 2$ for the $q = 1$ waveplate, along with their δ values stated above into Eqn. 6.6.2.

To best visualise the effect of the atoms on the light field, the probe images (example in Fig. 6.21a) collected by shifting the AOM frequency are normalised by the off-resonance beam, which generates a beam with a unique lobe structure[57]. In the case of our $q = 1$ beam, there are four lobes in the shape of an "X" (Fig. 6.21b); however, it is worth mentioning that the number of observed lobes is always twice the azimuthal index $2l$. Since all our hybrid beams are vortex beams with a singularity at the centre, we apply a digital mask to the images in the shape of a hollow disc with different inner and outer radii (red circles from Fig. 6.21b) relative to the beam's central coordinate (red dot in Fig. 6.21b)[58], where the portion of the beam outside the mask is excluded from further analysis. Finally, the beam within the mask is unwrapped into a polar plot, where the polar angle at 0 degrees is defined along the x-axis (see inset of Fig. 6.21b), and positive angles are measured counter-clockwise for a full 2π rotation. The unwrapped image of the probe beam can be found in Fig. 6.21c below.

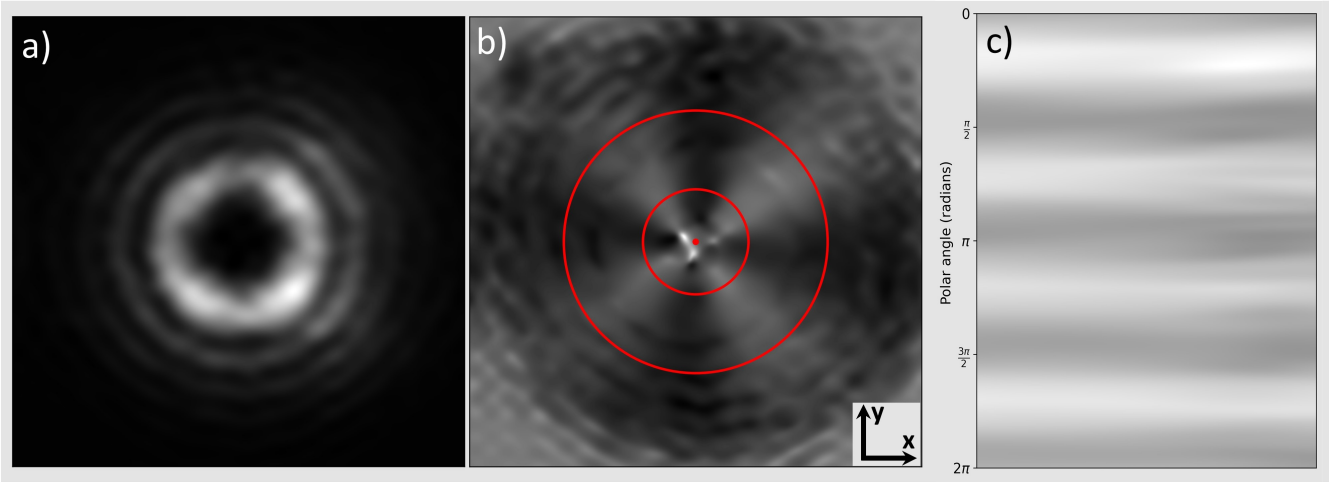

Figure 6.21: Analysis of a spatpolspec probe beam. a) An experimental $q = 1$ probe beam. b) A $q = 1$ probe beam normalised with the off-resonance image, producing a four-fold "X" pattern. The red dot is an estimation of the beam centre using moment analysis, while the two red circles highlight the region of the beam to be unwrapped. The polar coordinate is defined with 0 radians along the x-axis increasing counter-clockwise. c) The unwrapped image of the beam in the desired region, where the polar angle is along the vertical axis.

We continue to normalise all the probe beam images by the off-resonance image before unwrapping and overlapping them to construct a continuous polar profile plot of the beam behaviour

[57]Note that to prevent division by zero, which can occur in regions of the off-resonance beam where light is absent, all pixels with values under 1 are set to 1 in the analysis.

[58]The coordinates of the beam centre are found using moment analysis. This technique uses thresholding to estimate the central coordinates of the beam by approximating the beam shape from the image pixel values (i.e. intensity).

across the entire AOM frequency scanning range. We then compare our experimental data to a theoretically generated probe beam in the same frequency range. We demonstrate such a plot for our $q = 1$ hybrid probe beam, projected over the horizontal and vertical polarisation states in the top and bottom rows of Fig. 6.22, respectively. Just from observation, we can deduce that the rotation direction of the $\hat{H}$ projected beam in Fig. 6.22a1 and Fig. 6.22a2 is counter-clockwise, while the beam projected along $\hat{V}$ in Fig. 6.22b1 and Fig. 6.22b2 rotates clockwise, with increasing AOM frequency.

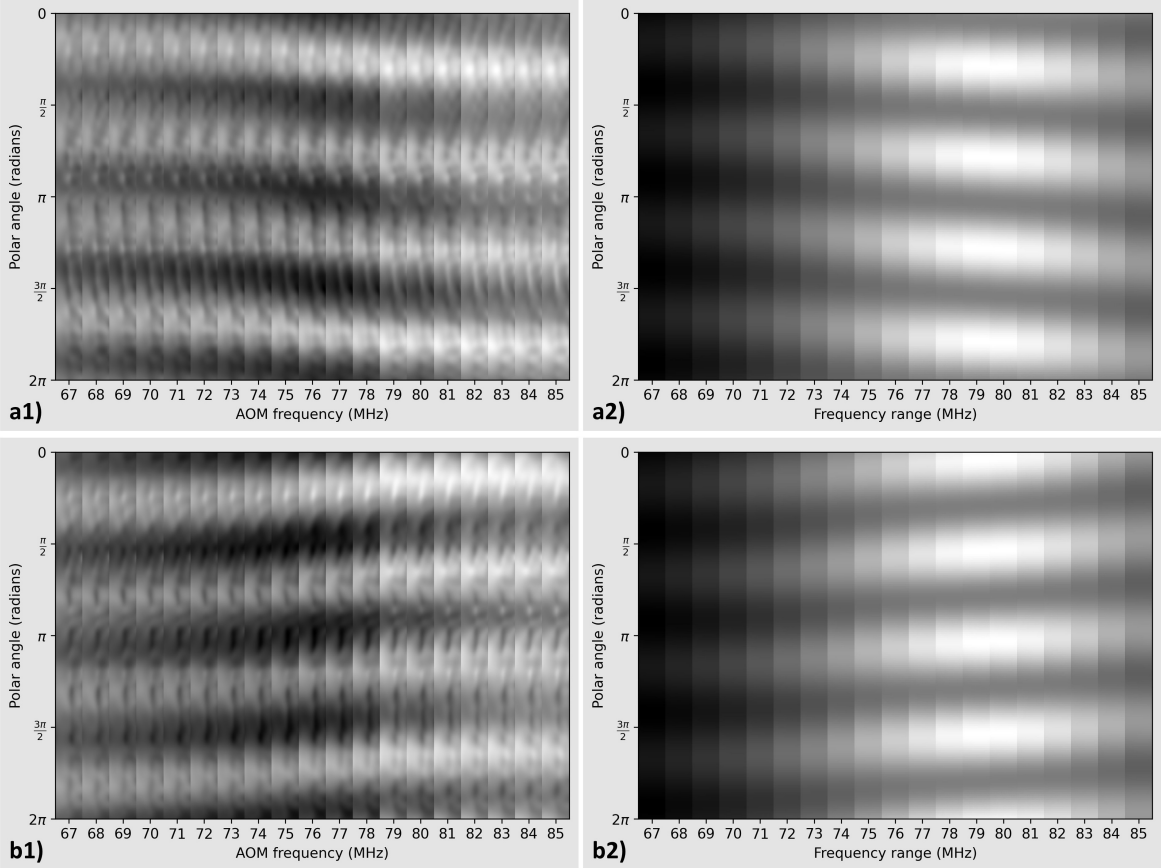

Figure 6.22: Experimental (left) and theoretical (right) polar plots of our $q = 1$ hybrid probe beam projected along a) the $\hat{H}$ state, and b) the $\hat{V}$ state, across our desired range of AOM frequencies.

To translate this rotation into an angle, we calculate the sum of all pixel values for every polar angle normalising by the highest pixel value and plot the intensity distribution against the polar angle to generate a curve with sinusoidal features that mimic the beam rotation pattern. Note that we only consider the curves for the first and last polar plots (i.e. the AOM frequency at 67MHz and 85MHz), since the beams rotate in one direction, and hence the rotation angle can be calculated from the difference between the two curves. An example of these plots can be found in Fig. 6.23 and Fig. 6.24 for the beam projected along the horizontal and vertical polarisation states, respectively. Since the intensity profile of the experimental beam is not uniform, which is reflected as inconsistencies in the sinusoidal profile of the curve, we fit the data to a sine curve, which helps us with determining the position of the curve peaks. By taking the difference between the two sets of peaks that correspond to the AOM frequency at 67MHz and 85MHz, we calculate an average rotation angle of all four peaks[59] of our experimental (exp) and simulated (sim) beams for the data

[59]We do this for improved accuracy. However, the number of peaks will vary, i.e. a $q = 1$ will have four peaks from its four-fold pattern, while a $q = 1/2$ beam will only have two.

set presented in Fig. 6.22. The results are summarised in Table 6.1 below.

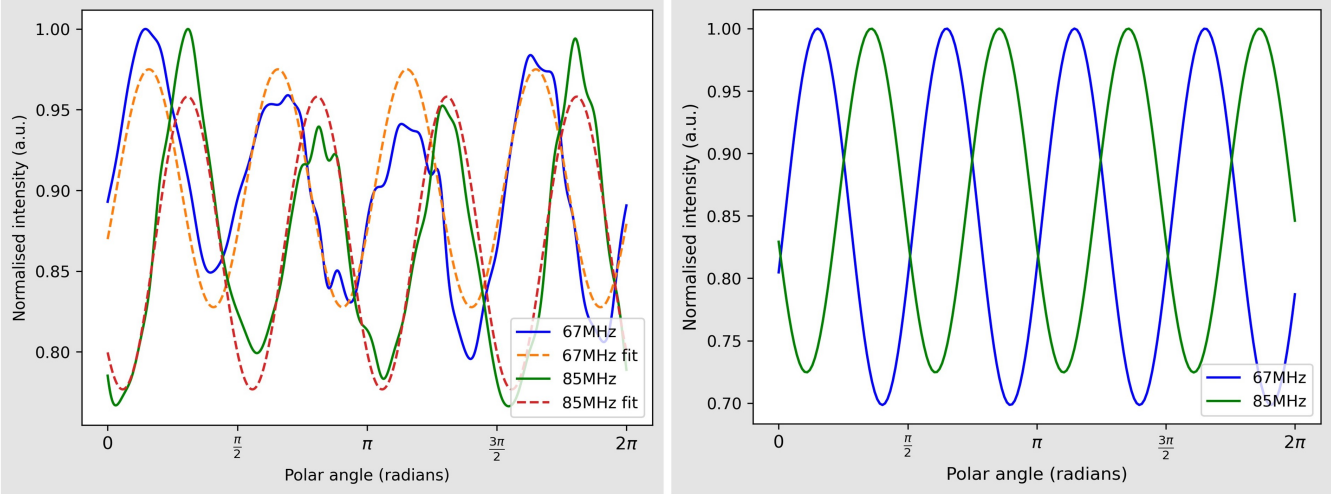

Figure 6.23: Experimental (left) and theoretical (right) plots of the normalised intensity against the polar angle for our $q = 1$ beam, projected along $\hat{H}$, for the AOM frequency at 67MHz (blue) and 85MHz (green). The solid lines represent the raw data, while the dashed lines are fitted curves.

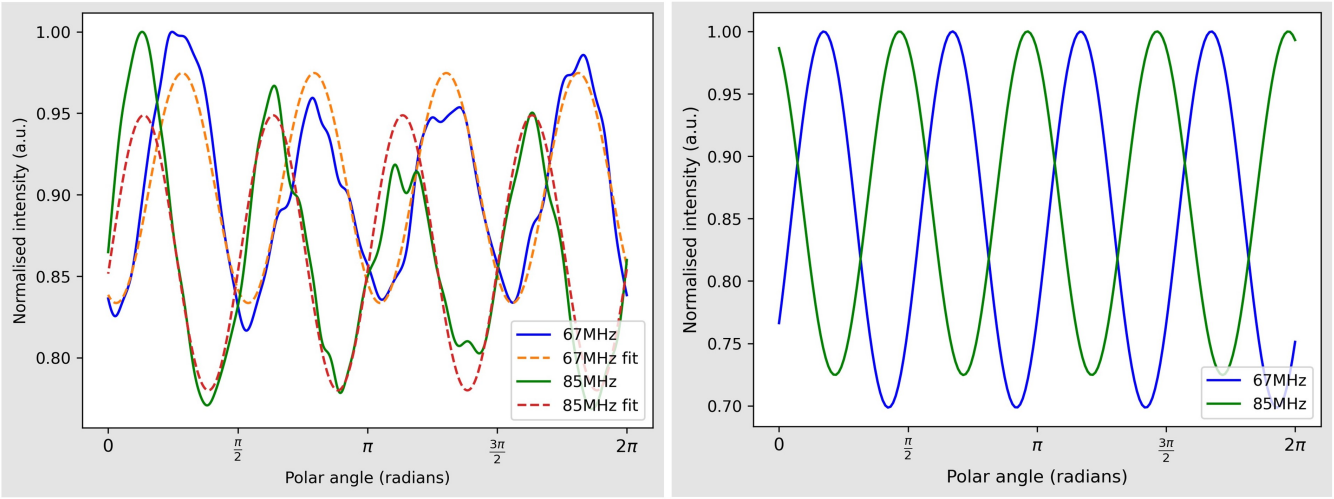

Figure 6.24: Experimental (left) and theoretical (right) plots of the normalised intensity against the polar angle for our $q = 1$ beam, projected along $\hat{V}$, for the AOM frequency at 67MHz (blue) and 85MHz (green). The solid lines represent the raw data, while the dashed lines are fitted curves.

Projection	Rotation angle (exp)	Rotation angle (sim)	Rotation difference (sim - exp)
$\hat{H}$	$27.55° \pm 0.58°$	$37.54° \pm 0.78°$	$9.98° \pm 0.97°$
$\hat{V}$	$29.61° \pm 2.08°$	$37.09° \pm 1.28°$	$7.47° \pm 2.44°$

Table 6.1: Rotation angles of the experimental (exp) and theoretical (sim) $q = 1$ beam pattern, projected along $\hat{H}$ and $\hat{V}$, along with the difference in rotation between the two.

In a similar fashion, we generate the polar plots and intensity curves for the $q = 1$ probe beam projected along the diagonal ($\hat{D}$) and anti-diagonal ($\hat{A}$), along with the right ($\hat{R}$) and left ($\hat{L}$) circular states. These plots can be found in Fig. 6.25 and Fig. 6.26, respectively.

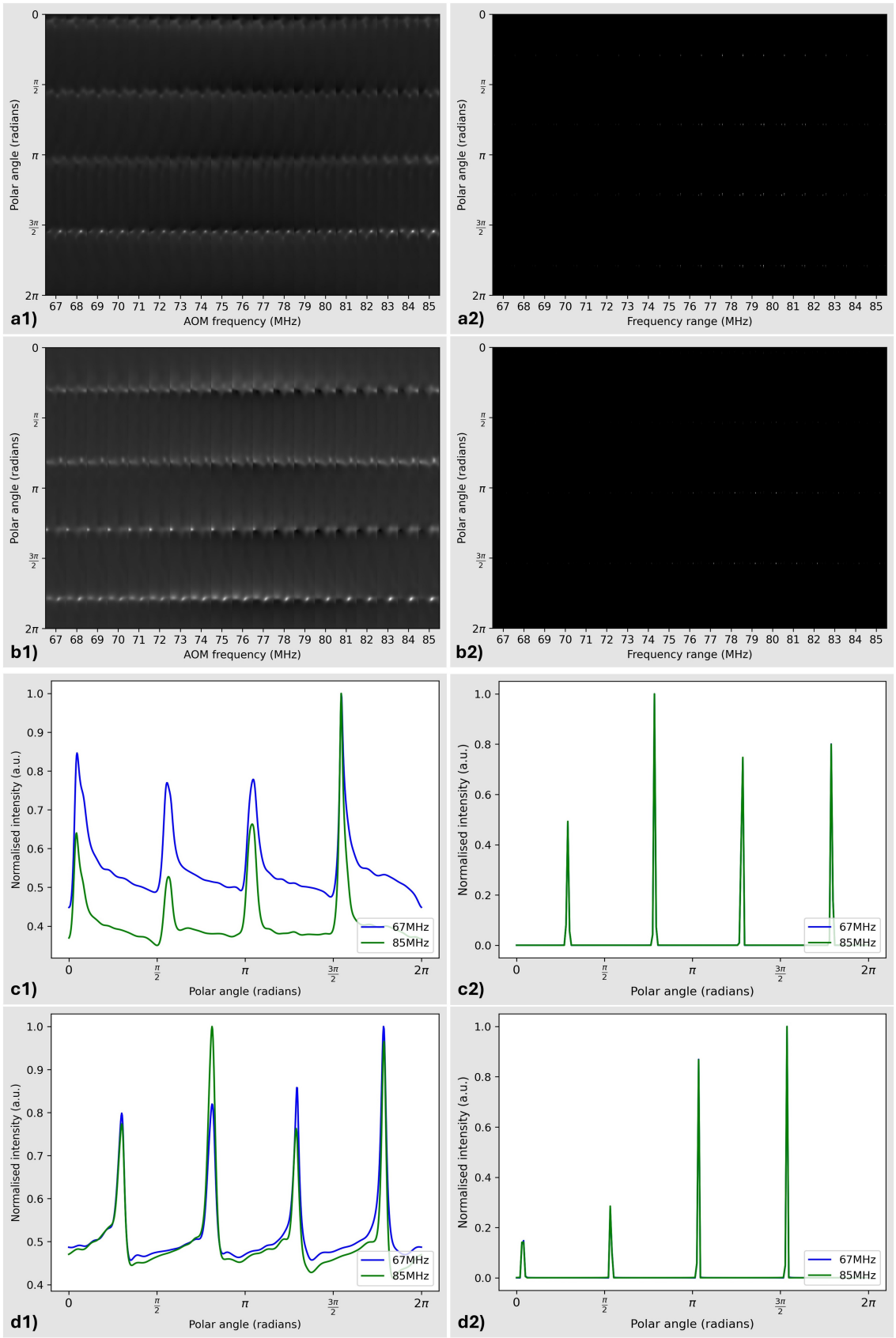

Figure 6.25: Experimental (left) and theoretical (right) polar plots (a and b) and plots of intensity against polar angle (c and d) of our $q = 1$ hybrid probe beam projected along the $\hat{A}$ (a and c) and $\hat{D}$ (b and d) bases.

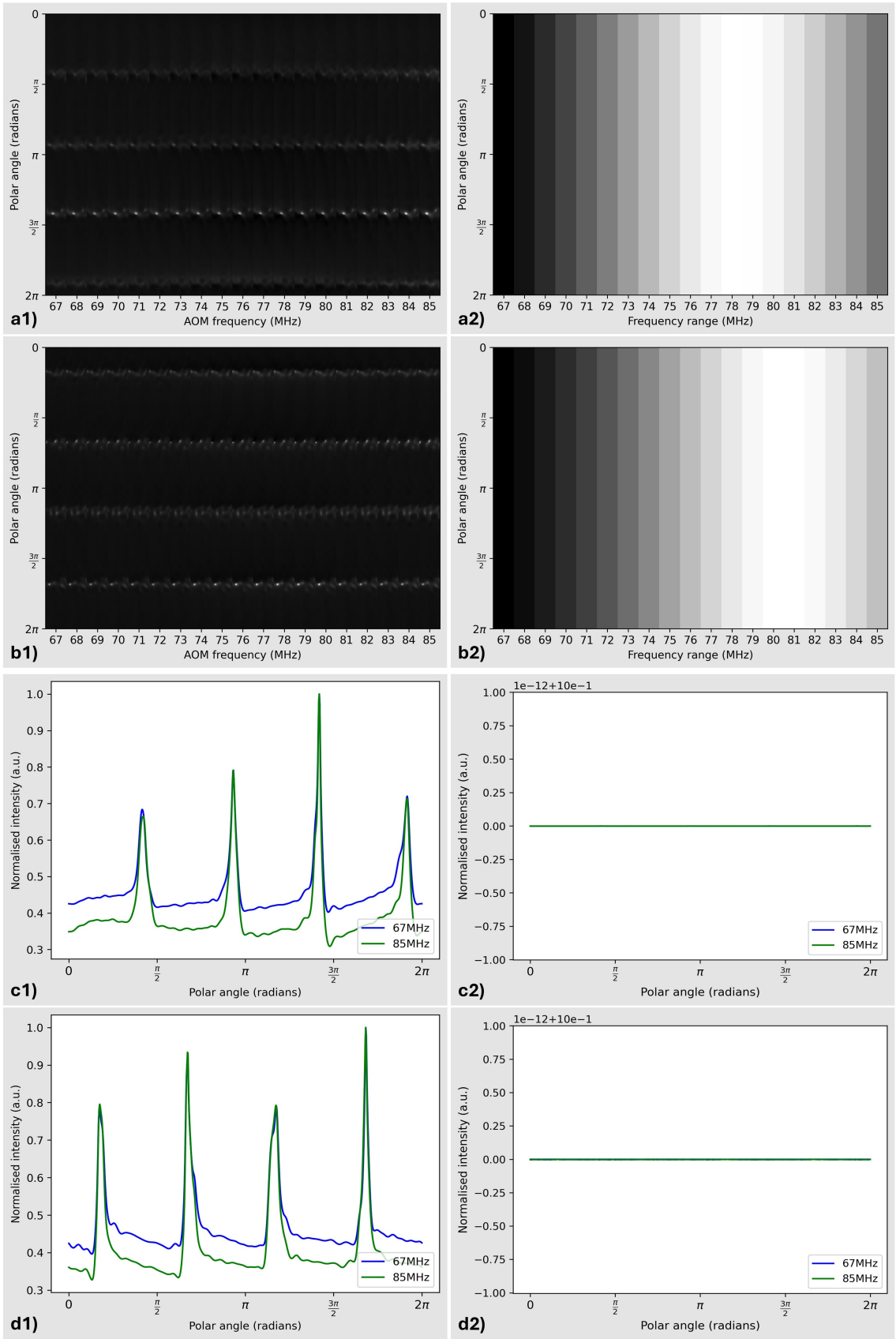

Figure 6.26: Experimental (left) and theoretical (right) polar plots (a and b) and plots of intensity against polar angle (c and d) of our $q = 1$ hybrid probe beam projected along the $\hat{R}$ (a and c) and $\hat{L}$ (b and d) bases.

Once again, the calculated rotation angles for the data from Fig. 6.26 and Fig. 6.25 are summarised in the table below.

Projection	Rotation angle (exp)	Rotation angle (sim)	Rotation difference (sim - exp)
$\hat{A}$	$0.77^\circ \pm 0.58^\circ$	0°	$-0.77^\circ \pm 0.58^\circ$
$\hat{D}$	$0.26^\circ \pm 0.26^\circ$	0°	$-0.26^\circ \pm 0.26^\circ$
$\hat{R}$	$0.39^\circ \pm 0.43^\circ$	0°	$-0.39^\circ \pm 0.43^\circ$
$\hat{L}$	$0.13^\circ \pm 0.22^\circ$	0°	$-0.13^\circ \pm 0.22^\circ$

Table 6.2: Rotation angles of the beam pattern for the experiment (exp) and theory (sim) and their rotation difference for a $q = 1$ hybrid probe projected along $\hat{A}$, $\hat{D}$, $\hat{R}$, and $\hat{L}$. Since the simulated rotation angles are all zero, we recover the experimental rotation angles when calculating the difference between the two.

By observing the beam behaviour projected along the $\hat{H}$ and $\hat{V}$ polarisation states, we deduce the rotation pattern follows the same direction when compared to our theoretical model. However, there are slight discrepancies between the values of the rotation angle, as seen from Table 6.1. As previously stated, our simulation modelling the light interaction with the atomic medium is very simple and lacks many features and parameters found in an experimental setting (e.g. Doppler broadening, temperature variations, transverse magnetic field contributions, birefringent effect of optics, etc.)[60], limiting our ability to accurately model our spatpolspec system.

Shifting our focus to the plots in Fig. 6.26 where our beam is projected along the circular bases, we observe no distinct features or patterns in the simulated beam profile, apart from a gradual variation in the light intensity across our frequency range. Given that our $q = 1$ hybrid beam possesses both circular components, a projection onto the circular bases (i.e. $\hat{R}$ and $\hat{L}$) will produce dark regions in the beam profile, corresponding to an orthogonal projection. Recall that the magnetic field in our system is assumed to be longitudinal (i.e. in the direction of beam propagation, where only $\sigma_\pm$ transitions are allowed); this projection essentially throws away half of the information encoded in the light field from the interaction with the atomic vapour. Since the rotation of the beam pattern is a magneto-optical effect generated from the preferential absorption of the $\sigma_\pm$ components and the phase difference between the two (i.e the Faraday effect, see Section 6.4), it is no surprise that eliminating one of the $\sigma_\pm$ components gets rid of the rotation completely. Additionally, the regions in the polar plots from Fig. 6.26a2 and Fig. 6.26b2, where the brightness is maximum, occur at the frequency of the respective $\sigma_\pm$ transition, shifted by the external magnetic field[61]. Given that our beams are normalised by the off-resonance image, we assume the smallest discrepancy between the two occurs at the resonance of the two $\sigma_\pm$ transitions, hence why the intensity is highest around that region. From the plots in Fig. 6.26c2 and Fig. 6.26d2, we deduce that the off-resonant beam and the beams across our frequency range are identical in structure, and hence no distinct patterns are found from any of these plots. Unlike in theory, experimentally

[60] Although Eqn. 6.6.2 contains the birefringent effect of the glass cell, due to time constraints it was not included into the simulation (although clear glass generally absorbs between $2\% - 4\%$ of the light field [218], which for the two Rb cell windows would be around $4\% - 8\%$), which is relatively small and therefore can be ignored.

[61] We model our system assuming a magnetic field of 0.5G, which gives a Larmor frequency shift of approximately 4.4MHz for σ_- and 8.8MHz for σ_+. Since zero detuning is assumed to be at 76MHz, a shift of 4.4MHz and 8.8MHz MHz corresponds to 78.2MHz and 80.8MHz on our AOM frequency range, which sits within the bright region of the polar plots in Fig. 6.26.

generated beams are not perfect, and variations in the intensity and polarisation profiles are to be expected. Although the beam possesses a subtle structure (shaped like a thin "X", similar to the pattern in Fig. 6.21), the polar plots suggest the beam experiences a very small rotation peaking near resonance ($\approx$ 76MHz), but rotates back as it clears the $F' = 4$ transition, in a motion akin to a slight wiggle. However, the beam does rotate slightly by a very small angle, as stated in Table 6.2.

Since our beams also possess diagonal components, when we project our light onto the $\hat{D}$ and $\hat{A}$ bases, we expect to see dark regions in the beam profile corresponding to orthogonal projection, where we once again lose the light intensity before reaching the detector. Although it is very difficult to see, some regions in the polar plot of the probe beam from Fig. 6.25a2 and Fig. 6.25b2 are still illuminated, suggesting the off-resonance and resonance beams are not fully identical and some magneto-optical effect is in play. However, similarly to the case in Fig. 6.26, the effect is far too small to induce a rotation in the beam profile, as seen from the angles summarised in Table 6.2. On the other hand, our experimental beam behaves identically to the beams in Fig. 6.26, displaying a very small rotation angle as seen from Table 6.2.

In a similar fashion, we calculate the rotation angle of the $q = 1/2$ probe beam for all six Stokes projections and summarise the values in Table 6.3 below. Note that the polar plots and intensity figures for the $q = 1/2$ probe can be found in Appendix D.

Projection	Rotation angle (exp)	Rotation angle (sim)	Rotation difference (sim - exp)
$\hat{H}$	$57.17° \pm 2.06°$	$74.17 \pm 1.81°$	$17.00° \pm 2.74°$
$\hat{V}$	$57.68° \pm 0.52°$	$74.17°$	$16.49° \pm 0.52°$
$\hat{A}$	0	$0°$	0
$\hat{D}$	$0.52°$	$0°$	$-0.52°$
$\hat{R}$	$2.06°$	$0°$	$-2.06°$
$\hat{L}$	$0.77° \pm 0.26°$	$0°$	$-0.77° \pm 0.26°$

Table 6.3: Rotation angles of the beam pattern for the experimental (exp) and theoretical (sim) $q = 1/2$ hybrid probe and the difference between them, projected across all polarisation bases.

6.6.3 A brief description of our theoretical model

So far, I have extensively compared our data to a theoretical model that we developed to shed light on the behaviour of our experimental setup. However, I am yet to provide any details about this model[62], and I will take the opportunity to briefly do so here.

The model can be split into three different sections: the first is the beam generation element, the second is the interaction with the atoms, and the third is the analysis of the emerging beam. The beam generation method is quite simple; we define the appropriate parameters associated with an LG beam (e.g. Rayleigh range, beam waist, radius of curvature, etc.) and insert them into the LG mode equation, given by Eqn. 1.5.18, to generate our desired modes. We then superimpose the LG modes to generate the amplitude terms of the probe electric field seen in Eqn. 6.6.2 (the terms in circular brackets), choosing appropriate values for the q-plate fast axis orientation δ. By now, we are done preparing the initial beam and shift our focus to the atoms.

[62]For all you know, it's all a hoax. But all jokes aside, it really does exist (source: Trust me!).

First, we defined some of the textbook parameters (e.g. natural linewidth Γ, saturation intensity I_{sat}, etc.) and some parameters derived from our experimental setup (e.g. atomic density n^{ρ}, cell length l, etc.). We then define our electric susceptibility function from Eqn. 6.2.9, considering the refractive index and absorption coefficient from the susceptibility and taking into account the Larmor frequency, which we calculate for the two $\sigma_{\pm}$ components from Eqn. 4.2.4. These interaction coefficients are inserted into Eqn. 6.6.2; however, for simplicity, we ignore the complex refractive index contributions from the glass cell windows. This should give us the light field after the interaction with the atoms, and all that remains to flush out the effect of the atoms is to subtract this output beam from the input beam we generated at the start. The final step is to introduce a polarisation structure into the beam for projection measurements[63].

The last part of the model handles the analysis. The beams are first normalised with their off-resonance counter part before being unwrapped and cropped accordingly. This process is repeated for every single detuning value (in our case, we simulate a detuning from 67MHz to 85MHz to mimic the AOM frequency), to generate the polar plots like the ones seen in Fig. 6.22. Finally, we sum the intensity values of the first and last polar plots to generate the intensity figures like the ones seen in Fig. 6.23 and Fig. 6.24. I have included the code in Appendix E; however, I would like to emphasise that some parts of the code might need to be highlighted in or out in order to include or exclude various functionalities. Additionally, the output from certain functions might need to be manually checked to ensure accuracy[64].

6.6.4 Conclusion

The results discussed in this section serve as proof that the experimental realisation of a Doppler-free spectroscopic system using vector vortex light is indeed possible, achieved by associating the spatial mode of the probe beam with a rotation angle corresponding to a specific frequency on the atomic spectrum. The slight differences in the rotation angles between our experimental results and those generated from the numeric simulation could be attributed to a number of reasons. Although the numerical model does support the behaviour of our data, the simulation lacks many of the quantities and parameters found in an experimental setting that should be considered when developing a model of an experimental setup[65]. Although we ensure the counter-propagating pump-probe beams experience as much overlap as possible, in the hope of probing excited atoms, there is no guarantee that the interaction of the light field spans the entire length of the rubidium cell and instead could be concentrated at the entrance around the glass windows, where the light fields are yet to experience a substantial reduction in their respective intensities throughout propagation. Depending on the outcome of such an investigation, the theoretical model could be adapted to include an effective cell length for a more accurate representation of the interaction region.

Additionally, our experiment proves these magneto-optical effects can still be successfully observed and quantified at room temperature, solely utilising the magnetic field of the earth. However, it would have been interesting to investigate these parameters to generate the most optimal spatial

[63] We introduce the polarisation structure at the end for simplicity; however, we code the simulation to follow the behaviour expected from light interacting with an atomic medium where the magnetic field is in the direction of propagation (i.e. only $\sigma_{\pm}$ transitions are permitted) and hence do not need the polarisation structure until we are ready to perform the projection measurements.

[64] If the reader expects a polished and optimised piece of code, I regret to disappoint. By no means am I a software developer, but I do have three close friends who are, and they would definitely have a heart attack if they saw this thing.

[65] Our numeric model was in fact developed towards the very end of my PhD period (Huge thanks to Adam Selyem for getting the ball rolling), and unfortunately not much time was invested in refining it.

signal using a more controlled temperature and magnetic field environment while scanning across the entire range of the D2 line transitions of both rubidium isotopes[66].

Although the introduction of the AOM to the experiment provided me with a wealth of knowledge and eventually became a critical component to running the experiment, I still consider it to be my biggest experimental blunder during my time as a PhD student. Not only is it extremely challenging to perfectly align the AOM to avoid the shift in beam path in the double-pass configuration, they operate at specific frequencies, requiring careful consideration when selecting the atomic transition to lock the laser to. In the case of our 80MHz AOM, probing the stretched state of ^{85}Rb forced us to lock the laser to the $F' = $ CO32 cross-over peak, which is a relatively weak peak, introducing an added challenge when attempting to frequency stabilise our ECDL. Additionally, the change in the beam path interfered with our fibre coupling, affecting the total intensity of the output beam, once again introducing an additional challenge to the analysis process. Finally, due to time constraints, it was not possible to set up digital control over the AOM using a data acquisition (DAQ) card, so a simple voltage control oscillator and attenuator circuit controlled by two potentiometers was used, making it difficult to accurately select the desired modulation frequency of the AOM. A more efficient solution to correlate the probe beam to the atomic spectrum is to trigger the camera with the oscilloscope and adjust the camera frame rate and laser scanning frequency to associate every probe beam image with a point on the rubidium spectrum. Alternatively, one could introduce a very slow scanning frequency (< 0.5Hz) and capture a video of the probe beam, associating the sum of the pixel values of each frame to a specific region on the atomic spectrum[67]. One disadvantage to this method being the off-resonance images can quickly saturate when using a sensitive camera, while the beam at resonance is far too dim to observe (very common when heating the rubidium vapour), which sounds like an analysis nightmare.

Despite not achieving the goal of designing and constructing a laser locking system using a spatially dependent locking signal, our experimental findings serve as the first milestone in realising such a system. The general problem with polarisation spectroscopy is the susceptibility to changes in the beam polarisation as a consequence of changes to the birefringence of the glass cell, especially in the presence of temperature variations, despite polspec signals offering an improved signal-to-noise ratio. However, it is assumed that using a larger spatial signal offers a more robust solution to the additional distortions experienced by conventional polspec signals, simply by selecting a region of the beam least affected by such disturbances. The real challenge lies in implementing a stable detection scheme fast enough to receive the probe beam, generate the error signal, and feed it to a servo to stabilise the laser frequency (for reference, the PZT in our ECDL oscillates at a frequency of around 250kHz to maintain the laser lock). However, schemes that provide passive modulation-free laser locking utilising variations in the spatial structure of the beam profile have been explored before [219]. This squash locking technique could provide useful insight into realising a fast and efficient laser locking system utilising diferences in the spatial patterns of the probe beam.

6.7 Summary

In this chapter, we provide a detailed account of our experimental work, realising a Doppler-free spectroscopic setup using vector vortex light. We start by introducing the electric susceptibility

[66] In fact, this task now falls to my successor, Richard Maduro, who has already made significant improvements to what used to be my experimental setup. Well done, Richard!

[67] My supervisor, Sonja Franke-Arnold, might have suggested something along those lines a while back. I have no idea why I chose to follow the AOM route; however, after my experiences with one of them, an apology is definitely warranted. Sorry Sonja!

in relation to the density matrix elements of the optical Bloch equations, moving on to discuss a method for optical density calculation based on Beer's law. We then briefly discuss the Faraday effect, before introducing the theory and experimental configuration of our polarisation spectroscopy (polspec) setup and discussing our findings. Finally, we provide a detailed account of the changes to the polspec configuration to generate our spatial polarisation spectroscopy (spatpolspec) setup and compare our obtained results to a simple numeric model of matter-light interaction.

Conclusion

Before we conclude with a few words, we would like to provide a full summary of the work presented in this thesis. In the first part, the primary focus was on the properties of light, introducing the electromagnetic nature of light, then derived an expression of the plane wave solutions from Maxwell's theory before spending a great deal of time establishing a solid understanding of light polarisation, its generation, manipulation, and representation both mathematically (Jones and Stokes) and graphically (polarisation ellipse and Poincaré sphere). We then explored the implementation of polarisation state reconstruction via Stokes tomography, before introducing Gaussian modes, investigating their behaviour throughout propagation. The next chapter introduced some properties of light manipulation, beginning with the basic phenomena of reflection, focusing, and imaging. We then discuss the concepts of birefringence and dichroism, which are both very important properties of optical elements with a recurring theme throughout this thesis. This chapter concludes with a detailed description for generation methods of complex light fields using digital micromirror devices and vector vortex plates to produce beams with varying polarisation structures for experimental use. The first part concludes with a detailed explanation of our experimental work, which uses the elements of an unbiased positive operator valued measure set to realise an experimental configuration for a single-shot polarimeter for polarisation state reconstruction with a reduced number of required measurements. We provide a detailed account of the underlying theory and the experimental setup before comparing our measurements from the POVM system with measurements from a conventional Stokes tomography and theoretically produced data. This study eventually concludes with a description of the subsequent work that followed, introducing changes to the interferometric setup for improved stability.

In the second part, we shift our focus to the study of light-matter interaction, introducing the basic structure of rubidium atoms and the interaction of a light field with a two-level atom generating a series of coupled differential equations known as the Optical Bloch equations. We then provide an introduction to pumping schemes, discussing how the polarisation of the light field causes different atomic transitions and how an atomic medium subjected to an external magnetic field will only experience certain transitions as a consequence of the magnetic field orientation. The chapter concludes with a discussion of population rate equations, where we investigate the changes in the populations of the upper ground state of ^{87}Rb as a consequence of the pumping process with circularly polarised light. We then spend a moderate amount of time explaining in detail the method for generating coherent and monochromatic resonance light with ECDLs, exploring spectroscopic techniques for generation of Doppler free spectra for laser stabilisation purposes. The chapter concludes with a brief description of acousto-optic modulators and the way they work before delving into a brief study conducted a while back about the effects of power broadening on the spectral lines of the hyperfine transitions. This investigation played a key role in our choice of experimental beam powers. In the last chapter of part two, we combined the knowledge we have accumulated so far to realise an experimental configuration for Doppler free spectroscopy with vector vortex light. By using the density matrix elements from the optical Bloch equations, we

derive an expression for the electric susceptibility, which we use to define the complex refractive index of our system in order to model the effects of absorption and dispersion of the light field from interaction with the atomic medium. We then introduce a simple method to determine the atomic density of our rubidium vapour based on the Beer-Lambert law, before moving on to discuss how the Faraday effect emerges as a consequence of circular birefringence. In the second to last section, we provide a detailed description of the theory and experimental implementation of polarisation spectroscopy, a Doppler-free spectroscopic technique that served as the foundation for our primary project. In this section, we share our findings and conclude with final remarks that provide a summary of the roles played by the external magnetic field and the pumping process in producing the experimentally observed signal. In the final section of this chapter, we extensively discuss our work, adapting the experimental configuration from polarisation spectroscopy and introducing a probe beam with a spatially varying polarisation structure, along with an acousto-optic modulator as a means of shifting the laser frequency to scan around the desired atomic transition. We then share our experimental findings, discussing the interesting effects we observe and comparing the results to a simple simulation. Finally, we provide a brief description of our theoretical model and the equations required to generate the numerical data before concluding with an overview of our work with spatial polarisation spectroscopy.

I would like to iterate that I might be one of the few individuals at the University of Glasgow's optics group in the past decade that was entrusted with the responsibility of an active role in projects of both a pure optical nature and those with an element of matter-light interaction. Regardless of the differences between these projects, structured light remains at the core of each one of our experiments. Although, the technique introduced in Chapter 3 of a polarimeter projecting the light field on a suitable set of generalised measurements has been realised in previous literature, our investigation has proved that reconstruction of vector beams using this technique in a single-shot measurement system is indeed possible. Despite the good agreement between our data and those generated from both a theoretical model and Stokes tomography, the instability of the interferometer made this experiment more challenging than initially anticipated. However, the next iteration of the project addressed the stability issues by replacing the Mach-Zehnder interferometer with the Sagnac configuration, providing a more robust experimental setup for potential reconstruction of the optical activity information of dynamically changing materials. On the other hand, variations in the Gouy phase from overlapped beams with non-matching spatial mode numbers remain a key limitation of our experimental technique, as well as a potentially new and exciting avenue of study to explore in any future work with POVM polarimetry utilising complex light fields.

Shifting to our experiment with matter-light interaction, I would like to emphasise that the results of our work described in Chapter 6, building on the well-known technique of polarisation spectroscopy, which demonstrates that a Doppler-free spectroscopic configuration using vector vortex light is indeed possible, were promising and in agreement with a simple theoretical model we devised. These results clearly associate the behaviour of the probing beam, in the form of a unique rotation, with specific frequencies on the atomic spectrum as a consequence of magneto-optical effects. Despite this first successful milestone and the effort it took to reach it, we have merely scratched the surface of our investigation into a potential new technique for modulation-free laser frequency stabilisation utilising a spatially varying error signal. Although the experimental configuration was adapted accordingly, the introduction of the acousto-optic modulator (AOM) to the setup as a means for laser frequency control limited our scanning range to a specific region of the atomic spectrum. In addition, the slight angular deviations experienced by the beam double-passed through the AOM were reflected as changes in the light intensity emerging from the single-mode fibre. A practical solution to this problem is to remove the AOM and introduce a very slow laser

frequency scan while recording the behaviour of the spatial probe, where summing all pixel values of the spatial signal, accounting for ambient noise, will recover the absorption features of the atomic spectrum. This method provides a new avenue of study to explore the magneto-optical effects arising in other regions of the atomic spectrum as a result of optical pumping and the interaction of the medium with external magnetic fields. However, I must confess that it deeply saddens me to realise that my involvement in this work has officially come to an end, especially since I was the one who built this experiment from nothing. However, as the first-generation experimentalist at the University of Glasgow to work on spatial polarisation spectroscopy, I have high hopes for the future of this experiment.

Alas, our dear readers, we have come to the end. However, before we say our farewells and go our separate ways, I would like to conclude with a few of my final thoughts. As I reflect on my time at the University of Glasgow, I find it amusing that the countless hours spent aligning optics, soldering electronics, gathering data, or writing code for analysis purposes are labours where an experimental PhD student will spend the bulk of their time on; however, they are merely silent contributors to producing this thesis. I would like to emphasise that experimental work is often unpredictable by nature. Things can break where you least expect, or you could end up wasting an entire day looking for a single electronic or optical component and still find nothing, only to be forced to salvage from old discarded items collecting dust in a cupboard. However, I can say with utmost confidence that the feeling of joy you experience when your experiment works and your data behaves in the intended manner is indescribable. Finally, I would like to state that my introduction to the world of experimental optics was riddled with various difficulties. After just three months of being a PhD student, the unforeseen pandemic of 2020 resulted in months of extensive restrictions to the labs at both the university and our industrial partners, which severely affected my experimental growth. At times, I cannot help but wonder how different my time as a PhD student would have been if the pandemic had not occurred, and how different this thesis might have been. Despite it all, I would not trade the wealth of knowledge and experiences I have accumulated in the past four years for anything. I hope, dear readers, that by now you have found what you were looking for and that I was successful in my quest to provide a clear depiction of the nature of experimental optics.

Bibliography

[1] Alexander Franzen. *ComponentLibrary*. URL: https://www.gwoptics.org/ComponentLibrary/ (visited on July 3, 2024) (Cited on page ii).

[2] Eugene Hecht. *Optics*. 4th ed. Philadelphia, PA: Pearson Education, Aug. 2001 (Cited on pages 1, 5, 14–15, 17, 36, 40).

[3] M. Suhail Zubairy. "A Very Brief History of Light". In: *Optics in Our Time*. Springer International Publishing, 2016, pp. 3–24. ISBN: 9783319319032. DOI: 10.1007/978-3-319-31903-2_1. URL: http://dx.doi.org/10.1007/978-3-319-31903-2_1 (Cited on page 1).

[4] James Clerk Maxwell. *A Treatise on Electricity and Magnetism*. Cambridge University Press, June 2010. ISBN: 9780511709333. DOI: 10.1017/cbo9780511709333. URL: http://dx.doi.org/10.1017/CBO9780511709333 (Cited on page 1).

[5] A. Einstein. "On the Quantum Theory of Radiation". In: *Concepts of Quantum Optics*. Ed. by P.L. Knight and L. Allen. Pergamon, 1983, pp. 93–104. ISBN: 978-0-08-029160-4. DOI: https://doi.org/10.1016/B978-0-08-029160-4.50016-6. URL: https://www.sciencedirect.com/science/article/pii/B9780080291604500166 (Cited on page 1).

[6] T. H. Maiman. "Stimulated Optical Radiation in Ruby". In: *Nature* 187.4736 (Aug. 1960), pp. 493–494. ISSN: 1476-4687. DOI: 10.1038/187493a0. URL: http://dx.doi.org/10.1038/187493a0 (Cited on page 1).

[7] P. F. Moulton. "Spectroscopic and laser characteristics of Ti:Al2O3". In: *J. Opt. Soc. Am. B* 3.1 (Jan. 1986), pp. 125–133. DOI: 10.1364/JOSAB.3.000125. URL: https://opg.optica.org/josab/abstract.cfm?URI=josab-3-1-125 (Cited on page 1).

[8] Vasanthi Sivaprakasam and Dennis K. Killinger. "Tunable ultraviolet laser-induced fluorescence detection of trace plastics and dissolved organic compounds in water". In: *Appl. Opt.* 42.33 (Nov. 2003), pp. 6739–6746. DOI: 10.1364/AO.42.006739. URL: https://opg.optica.org/ao/abstract.cfm?URI=ao-42-33-6739 (Cited on page 1).

[9] Graham M. Gibson et al. "Real-time imaging of methane gas leaks using a single-pixel camera". In: *Opt. Express* 25.4 (Feb. 2017), pp. 2998–3005. DOI: 10.1364/OE.25.002998. URL: https://opg.optica.org/oe/abstract.cfm?URI=oe-25-4-2998 (Cited on page 1).

[10] Kyle J. Nutt et al. "Developing a portable gas imaging camera using highly tunable active-illumination and computer vision". In: *Opt. Express* 28.13 (June 2020), pp. 18566–18576. DOI: 10.1364/OE.389634. URL: https://opg.optica.org/oe/abstract.cfm?URI=oe-28-13-18566 (Cited on page 1).

[11] Carl E. Wieman and Leo Hollberg. "Using diode lasers for atomic physics". In: *Review of Scientific Instruments* 62.1 (Jan. 1991), pp. 1–20. ISSN: 1089-7623. DOI: 10.1063/1.1142305. URL: http://dx.doi.org/10.1063/1.1142305 (Cited on page 1).

[12] Daniel A. Steck. *Classical and Modern Optics*. Revised edition. July 2021. URL: http://steck.us/teaching (Cited on page 5).

[13] R Dorn, S Quabis, and G Leuchs. "Sharper focus for a radially polarized light beam". en. In: *Phys. Rev. Lett.* 91.23 (Dec. 2003), p. 233901 (Cited on page 11).

[14] F Maucher et al. "Creating complex optical longitudinal polarization structures". In: *Phys. Rev. Lett.* 120.16 (Apr. 2018) (Cited on page 11).

[15] K Youngworth and T Brown. "Focusing of high numerical aperture cylindrical-vector beams". en. In: *Opt. Express* 7.2 (July 2000), pp. 77–87 (Cited on page 11).

[16] Grant R Fowles. *Introduction to modern optics*. en. Dover Books on Physics. Mineola, NY: Dover Publications, June 1989. ISBN: 9780486659572 (Cited on page 12).

[17] Edward Collett. *Field Guide to Polarization*. SPIE, Sept. 2005. ISBN: 9780819478207. DOI: 10.1117/3.626141. URL: http://dx.doi.org/10.1117/3.626141 (Cited on pages 12, 14–15, 17).

[18] Anthony Gerrard and J M Burch. *Introduction to matrix methods in optics*. Pure & Applied Optics S. Chichester, England: John Wiley & Sons, Jan. 1975 (Cited on pages 14, 17).

[19] Ryan Daniel Hawley. "Applications and practical considerations of polarisation structuring by a Fresnel cone". PhD thesis. College of Science and Engineering, School of Physics and Astronomy, 2022. DOI: 10.5525/GLA.THESIS.82650. URL: http://theses.gla.ac.uk/id/eprint/82650 (Cited on pages 18, 22).

[20] Adam Selyem. "Three-dimensional light sculptures and their interaction with atomic media: an experimentalist's guide". PhD thesis. College of Science and Engineering, School of Physics and Astronomy, 2019. DOI: 10.5525/GLA.THESIS.74416. URL: http://theses.gla.ac.uk/id/eprint/74416 (Cited on pages 22–23, 43, 47, 95, 101).

[21] Robert Balmer and William Keat. *Exploring engineering*. 5th ed. San Diego, CA: Academic Press, July 2020 (Cited on page 23).

[22] Robert Kim Guenther. *Modern Optics*. Brisbane, QLD, Australia: John Wiley and Sons (WIE), Feb. 1990 (Cited on pages 24, 26).

[23] Orazio Svelto. *Principles of Lasers*. Springer US, 2010. ISBN: 9781441913029. DOI: 10.1007/978-1-4419-1302-9. URL: http://dx.doi.org/10.1007/978-1-4419-1302-9 (Cited on pages 25, 27).

[24] Joseph W Goodman. *Introduction to Fourier Optics*. 2nd ed. McGraw-Hill series in electrical and computer engineering. Electromagnetics. London, England: McGraw-Hill Publishing, Mar. 1996 (Cited on page 25).

[25] Pierre Hillion. "A Note on the Derivation of Paraxial Equation in Nonhomogeneous Media". In: *SIAM Journal on Applied Mathematics* 52.2 (1992), pp. 337–346. ISSN: 00361399. URL: http://www.jstor.org/stable/2102413 (visited on Mar. 28, 2024) (Cited on page 25).

[26] Francesco Pampaloni and Joerg Enderlein. *Gaussian, Hermite-Gaussian, and Laguerre-Gaussian beams: A primer*. 2004. arXiv: physics/0410021 [physics.optics]. URL: https://arxiv.org/abs/physics/0410021 (Cited on page 26).

[27] Giuseppe Vallone. "On the properties of circular beams: normalization, Laguerre–Gauss expansion, and free-space divergence". In: *Optics Letters* 40.8 (Apr. 2015), p. 1717. ISSN: 1539-4794. DOI: 10.1364/ol.40.001717. URL: http://dx.doi.org/10.1364/OL.40.001717 (Cited on page 28).

[28] L. Allen et al. "Orbital angular momentum of light and the transformation of Laguerre-Gaussian laser modes". In: *Phys. Rev. A* 45 (11 June 1992), pp. 8185–8189. DOI: 10.1103/PhysRevA.45.8185. URL: https://link.aps.org/doi/10.1103/PhysRevA.45.8185 (Cited on page 30).

[29] L. Allen, M.J. Padgett, and M. Babiker. "IV The Orbital Angular Momentum of Light". In: *Progress in Optics*. Elsevier, 1999, pp. 291–372. DOI: 10.1016/s0079-6638(08)70391-3. URL: http://dx.doi.org/10.1016/S0079-6638(08)70391-3 (Cited on page 30).

[30] Alison M. Yao and Miles J. Padgett. "Orbital angular momentum: origins, behavior and applications". In: *Advances in Optics and Photonics* 3.2 (May 2011), p. 161. ISSN: 1943-8206. DOI: 10.1364/aop.3.000161. URL: http://dx.doi.org/10.1364/AOP.3.000161 (Cited on page 30).

[31] Jonathan Leach et al. "Interferometric Methods to Measure Orbital and Spin, or the Total Angular Momentum of a Single Photon". In: *Physical Review Letters* 92.1 (Jan. 2004). ISSN: 1079-7114. DOI: 10.1103/physrevlett.92.013601. URL: http://dx.doi.org/10.1103/PhysRevLett.92.013601 (Cited on page 30).

[32] Frédéric Bouchard et al. "Measuring azimuthal and radial modes of photons". In: *Optics Express* 26.24 (Nov. 2018), p. 31925. ISSN: 1094-4087. DOI: 10.1364/oe.26.031925. URL: http://dx.doi.org/10.1364/OE.26.031925 (Cited on page 30).

[33] Mirko Siano et al. "Experimental high sensitive local identification of azimuthal index of Laguerre–Gauss beams". In: *Optics Communications* 557 (2024), p. 130349. ISSN: 0030-4018. DOI: https://doi.org/10.1016/j.optcom.2024.130349. URL: https://www.sciencedirect.com/science/article/pii/S0030401824000865 (Cited on page 30).

[34] Miguel A. Bandres and Julio C. Gutiérrez-Vega. "Ince–Gaussian modes of the paraxial wave equation and stable resonators". In: *Journal of the Optical Society of America A* 21.5 (May 2004), p. 873. ISSN: 1520-8532. DOI: 10.1364/josaa.21.000873. URL: http://dx.doi.org/10.1364/JOSAA.21.000873 (Cited on page 30).

[35] Jinwen Wang et al. "Exploring the ellipticity dependency on vector helical Ince-Gaussian beams and their focusing properties". In: *Optics Express* 30.14 (June 2022), p. 24497. ISSN: 1094-4087. DOI: 10.1364/oe.462105. URL: http://dx.doi.org/10.1364/OE.462105 (Cited on page 30).

[36] Simin Feng and Herbert G. Winful. "Physical origin of the Gouy phase shift". In: *Optics Letters* 26.8 (Apr. 2001), p. 485. ISSN: 1539-4794. DOI: 10.1364/ol.26.000485. URL: http://dx.doi.org/10.1364/OL.26.000485 (Cited on page 31).

[37] A. G. Fox and Tingye Li. "Resonant modes in a maser interferometer". In: *The Bell System Technical Journal* 40.2 (1961), pp. 453–488. DOI: 10.1002/j.1538-7305.1961.tb01625.x (Cited on page 34).

[38] A. Fox and Tingye Li. "Computation of optical resonator modes by the method of resonance excitation". In: *IEEE Journal of Quantum Electronics* 4.7 (1968), pp. 460–465. DOI: 10.1109/JQE.1968.1075368 (Cited on page 34).

[39] A. L. Fymat. "Jones's Matrix Representation of Optical Instruments I: Beam Splitters". In: *Applied Optics* 10.11 (Nov. 1971), p. 2499. ISSN: 1539-4522. DOI: 10.1364/ao.10.002499. URL: http://dx.doi.org/10.1364/AO.10.002499 (Cited on page 35).

[40] A. L. Fymat. "Jones's Matrix Representation of Optical Instruments 2: Fourier Interferometers (Spectrometers and Spectropolarimeters)". In: *Applied Optics* 10.12 (Dec. 1971), p. 2711. ISSN: 1539-4522. DOI: 10.1364/ao.10.002711. URL: http://dx.doi.org/10.1364/AO.10.002711 (Cited on page 35).

[41] C. Beck et al. "A polarization model for the German Vacuum Tower Telescope from in situ and laboratory measurements". In: *Astronomy & Astrophysics* 443.3 (Nov. 2005), pp. 1047–1053. ISSN: 1432-0746. DOI: 10.1051/0004-6361:20052935. URL: http://dx.doi.org/10.1051/0004-6361:20052935 (Cited on page 37).

[42] Sidney A. Self. "Focusing of spherical Gaussian beams". In: *Applied Optics* 22.5 (Mar. 1983), p. 658. ISSN: 1539-4522. DOI: 10.1364/ao.22.000658. URL: http://dx.doi.org/10.1364/AO.22.000658 (Cited on page 39).

[43] Y. Mushiake, K. Matsumura, and N. Nakajima. "Generation of radially polarized optical beam mode by laser oscillation". In: *Proceedings of the IEEE* 60.9 (1972), pp. 1107–1109. DOI: 10.1109/PROC.1972.8865 (Cited on page 41).

[44] Jinwen Wang, Francesco Castellucci, and Sonja Franke-Arnold. "Vectorial light–matter interaction: Exploring spatially structured complex light fields". In: *AVS Quantum Science* 2.3 (Sept. 2020). ISSN: 2639-0213. DOI: 10.1116/5.0016007. URL: http://dx.doi.org/10.1116/5.0016007 (Cited on page 41).

[45] Carmelo Rosales-Guzmán, Bienvenu Ndagano, and Andrew Forbes. "A review of complex vector light fields and their applications". In: *Journal of Optics* 20.12 (Nov. 2018), p. 123001. ISSN: 2040-8986. DOI: 10.1088/2040-8986/aaeb7d. URL: http://dx.doi.org/10.1088/2040-8986/aaeb7d (Cited on page 41).

[46] Jian Chen, Chenhao Wan, and Qiwen Zhan. "Vectorial optical fields: recent advances and future prospects". In: *Science Bulletin* 63.1 (Jan. 2018), pp. 54–74. ISSN: 2095-9273. DOI: 10.1016/j.scib.2017.12.014. URL: http://dx.doi.org/10.1016/j.scib.2017.12.014 (Cited on page 41).

[47] Andrew Forbes and Isaac Nape. "Quantum mechanics with patterns of light: Progress in high dimensional and multidimensional entanglement with structured light". In: *AVS Quantum Science* 1.1 (Oct. 2019). ISSN: 2639-0213. DOI: 10.1116/1.5112027. URL: http://dx.doi.org/10.1116/1.5112027 (Cited on page 41).

[48] L Marrucci, C Manzo, and D Paparo. "Optical spin-to-orbital angular momentum conversion in inhomogeneous anisotropic media". en. In: *Phys. Rev. Lett.* 96.16 (Apr. 2006), p. 163905 (Cited on pages 41, 45).

[49] L. Marrucci, C. Manzo, and D. Paparo. "Pancharatnam-Berry phase optical elements for wave front shaping in the visible domain: Switchable helical mode generation". In: *Applied Physics Letters* 88.22 (May 2006). ISSN: 1077-3118. DOI: 10.1063/1.2207993. URL: http://dx.doi.org/10.1063/1.2207993 (Cited on page 41).

[50] Andrea Rubano et al. "Q-plate technology: a progress review [Invited]". en. In: *J. Opt. Soc. Am. B* 36.5 (May 2019), p. D70 (Cited on page 41).

[51] Robert C Devlin et al. "Arbitrary spin-to–orbital angular momentum conversion of light". en. In: *Science* 358.6365 (Nov. 2017), pp. 896–901 (Cited on page 41).

[52] Fuyong Yue et al. "Vector vortex beam generation with a single plasmonic metasurface". en. In: *ACS Photonics* 3.9 (Sept. 2016), pp. 1558–1563 (Cited on page 41).

[53] Yuttana Intaravanne and Xianzhong Chen. "Recent advances in optical metasurfaces for polarization detection and engineered polarization profiles". en. In: *Nanophotonics* 9.5 (May 2020), pp. 1003–1014 (Cited on page 41).

[54] N Radwell et al. "Achromatic vector vortex beams from a glass cone". en. In: *Nat. Commun.* 7.1 (Feb. 2016), p. 10564 (Cited on page 41).

[55] Ryan D Hawley et al. "Tight focal spots using azimuthally polarised light from a Fresnel cone". In: *Biomedical Spectroscopy, Microscopy, and Imaging*. Ed. by Jürgen Popp and Csilla Gergely. Online Only, France: SPIE, Apr. 2020 (Cited on pages 41, 47).

[56] Yuichi Kozawa and Shunichi Sato. "Generation of a radially polarized laser beam by use of a conical Brewster prism". en. In: *Opt. Lett.* 30.22 (Nov. 2005), pp. 3063–3065 (Cited on page 41).

[57] J A Davis et al. "Two-dimensional polarization encoding with a phase-only liquid-crystal spatial light modulator". en. In: *Appl. Opt.* 39.10 (Apr. 2000), pp. 1549–1554 (Cited on page 42).

[58] Carmelo Rosales-Guzmán, Nkosiphile Bhebhe, and Andrew Forbes. "Simultaneous generation of multiple vector beams on a single SLM". en. In: *Opt. Express* 25.21 (Oct. 2017), p. 25697 (Cited on page 42).

[59] Zhen-Yu Rong et al. "Generation of arbitrary vector beams with cascaded liquid crystal spatial light modulators". en. In: *Opt. Express* 22.2 (Jan. 2014), pp. 1636–1644 (Cited on page 42).

[60] Kevin J Mitchell et al. "Polarisation structuring of broadband light". en. In: *Opt. Express* 25.21 (Oct. 2017), p. 25079 (Cited on page 42).

[61] Adam Selyem et al. "Basis-independent tomography and nonseparability witnesses of pure complex vectorial light fields by Stokes projections". In: *Phys. Rev. A* 100 (6 Dec. 2019), p. 063842. DOI: 10.1103/PhysRevA.100.063842. URL: https://link.aps.org/doi/10.1103/PhysRevA.100.063842 (Cited on pages 42–43, 48–49, 57).

[62] Yu-Xuan Ren, Rong-de Lu, and Lei Gong. "Tailoring light with a digital micromirror device". en. In: *Ann. Phys.* 527.7-8 (Aug. 2015), pp. 447–470 (Cited on page 42).

[63] Kevin J Mitchell et al. "High-speed spatial control of the intensity, phase and polarisation of vector beams using a digital micro-mirror device". In: *Opt. Express* 24.25 (Dec. 2016), p. 29269 (Cited on page 42).

[64] Stirling Scholes et al. "Structured light with digital micromirror devices: a guide to best practice". In: *Opt. Eng.* 59.04 (Nov. 2019), p. 1 (Cited on page 42).

[65] Lei Gong et al. "Generation of cylindrically polarized vector vortex beams with digital micromirror device". en. In: *J. Appl. Phys.* 116.18 (Nov. 2014), p. 183105 (Cited on page 42).

[66] Carmelo Rosales-Guzmán et al. "Polarisation-insensitive generation of complex vector modes from a digital micromirror device". In: *Scientific Reports* 10.1 (2020), pp. 1–9 (Cited on pages 42, 49).

[67] Sam Delaney et al. "Arithmetic with q-plates". In: *Applied Optics* 56.3 (Jan. 2017), p. 596. ISSN: 1539-4522. DOI: 10.1364/ao.56.000596. URL: http://dx.doi.org/10.1364/AO.56.000596 (Cited on page 45).

[68] Thorlabs. *Zero-Order Vortex Half-Wave Retarders*. URL: https://www.thorlabs.com/newgrouppage9.cfm?objectgroup_id=9098 (visited on May 8, 2024) (Cited on page 46).

[69] Thomas W. Clark. "Sculpting shadows. On the spatial structuring of fields & atoms: a tale of light and darkness". PhD thesis. College of Science and Engineering, School of Physics and Astronomy, 2016. URL: https://theses.gla.ac.uk/id/eprint/8029 (Cited on page 47).

[70] Francesco Castellucci. "Novel applications of structured light in the field of atom optics. Imagining optical magnetometry with images". PhD thesis. College of Science and Engineering, School of Physics and Astronomy, 2022. DOI: 10.5525/GLA.THESIS.82732. URL: http://theses.gla.ac.uk/id/eprint/82732 (Cited on pages 47, 87, 101).

[71] M. A. Al Khafaji et al. "Single-shot characterization of vector beams by generalized measurements". In: *Optics Express* 30.13 (June 2022), p. 22396. ISSN: 1094-4087. DOI: 10.1364/oe.458352. URL: http://dx.doi.org/10.1364/OE.458352 (Cited on pages 48–49, 55, 69).

[72] Filippo Cardano et al. "Polarization pattern of vector vortex beams generated by q-plates with different topological charges". In: *Appl. Opt.* 51.10 (Apr. 2012), pp. C1–C6. DOI: 10.1364/AO.51.0000C1. URL: https://opg.optica.org/ao/abstract.cfm?URI=ao-51-10-C1 (Cited on page 48).

[73] Mark R. Dennis, Kevin O'Holleran, and Miles J. Padgett. "Singular Optics: Optical Vortices and Polarization Singularities". English. In: *PROGRESS IN OPTICS, VOL 53*. Amsterdam:Elsevier, 2009, pp. 293–363. DOI: 10.1016/S0079-6638(08)00205-9 (Cited on page 48).

[74] Qiwen Zhan. "Cylindrical vector beams: from mathematical concepts to applications". In: *Adv. Opt. Photon.* 1.1 (Jan. 2009), pp. 1–57. DOI: 10.1364/AOP.1.000001. URL: https://opg.optica.org/aop/abstract.cfm?URI=aop-1-1-1 (Cited on page 48).

[75] Junmin Liu et al. "Generation of arbitrary cylindrical vector vortex beams with cross-polarized modulation". In: *Results in Physics* 19 (2020), p. 103455. ISSN: 2211-3797. DOI: https://doi.org/10.1016/j.rinp.2020.103455. URL: https://www.sciencedirect.com/science/article/pii/S2211379720319161 (Cited on page 48).

[76] Domitille Schanne et al. "Spontaneous Emission of Vector Vortex Beams". In: *Physical Review Applied* 14.6 (Dec. 2020). ISSN: 2331-7019. DOI: 10.1103/physrevapplied.14.064077. URL: http://dx.doi.org/10.1103/PhysRevApplied.14.064077 (Cited on page 48).

[77] Delin Li et al. "Generation of arbitrary perfect Poincaré beams". In: *Journal of Applied Physics* 125.7 (Feb. 2019). ISSN: 1089-7550. DOI: 10.1063/1.5079850. URL: http://dx.doi.org/10.1063/1.5079850 (Cited on page 48).

[78] Amber M. Beckley, Thomas G. Brown, and Miguel A. Alonso. "Full Poincaré beams". In: *Optics Express* 18.10 (May 2010), p. 10777. ISSN: 1094-4087. DOI: 10.1364/oe.18.010777. URL: http://dx.doi.org/10.1364/OE.18.010777 (Cited on page 48).

[79] Amber M. Beckley, Thomas G. Brown, and Miguel A. Alonso. "Full Poincaré beams II: partial polarization". In: *Optics Express* 20.9 (Apr. 2012), p. 9357. ISSN: 1094-4087. DOI: 10.1364/oe.20.009357. URL: http://dx.doi.org/10.1364/OE.20.009357 (Cited on page 48).

[80] Mingze Liu et al. "Broadband generation of perfect Poincaré beams via dielectric spin-multiplexed metasurface". In: *Nature Communications* 12.1 (Apr. 2021). ISSN: 2041-1723. DOI: 10.1038/s41467-021-22462-z. URL: http://dx.doi.org/10.1038/s41467-021-22462-z (Cited on page 48).

[81] Dorilian Lopez-Mago. "On the overall polarisation properties of Poincaré beams". In: *Journal of Optics* 21.11 (Oct. 2019), p. 115605. ISSN: 2040-8986. DOI: 10.1088/2040-8986/ab4c25. URL: http://dx.doi.org/10.1088/2040-8986/ab4c25 (Cited on page 48).

[82] Sijia Gao et al. "Paraxial skyrmionic beams". In: *Physical Review A* 102.5 (Nov. 2020). ISSN: 2469-9934. DOI: 10.1103/physreva.102.053513. URL: http://dx.doi.org/10.1103/PhysRevA.102.053513 (Cited on pages 48, 68).

[83] A. McWilliam et al. *Topological approach of characterizing optical Skyrmions and Skyrmion lattices*. 2023. arXiv: 2209.06734 [physics.optics] (Cited on page 48).

[84] Wenbo Lin et al. "Microcavity-based generation of full Poincaré beams with arbitrary skyrmion numbers". In: *Phys. Rev. Res.* 3 (2 Apr. 2021), p. 023055. DOI: 10.1103/PhysRevResearch.3.023055. URL: https://link.aps.org/doi/10.1103/PhysRevResearch.3.023055 (Cited on page 48).

[85] W. F. Balthazar et al. "Tripartite nonseparability in classical optics". In: *Optics Letters* 41.24 (Dec. 2016), p. 5797. ISSN: 1539-4794. DOI: 10.1364/ol.41.005797. URL: http://dx.doi.org/10.1364/OL.41.005797 (Cited on page 48).

[86] Robert Fickler et al. "Quantum entanglement of complex photon polarization patterns in vector beams". In: *Phys. Rev. A* 89 (6 June 2014), p. 060301. DOI: 10.1103/PhysRevA.89.060301. URL: https://link.aps.org/doi/10.1103/PhysRevA.89.060301 (Cited on page 48).

[87] Bienvenu Ndagano et al. "Beam quality measure for vector beams". In: *Opt. Lett.* 41.15 (Aug. 2016), pp. 3407–3410. DOI: 10.1364/OL.41.003407. URL: https://opg.optica.org/ol/abstract.cfm?URI=ol-41-15-3407 (Cited on pages 48–49).

[88] Jinwen Wang et al. "Measuring the Optical Concurrence of Vector Beams with an Atomic-State Interferometer". In: *Phys. Rev. Lett.* 132 (19 May 2024), p. 193803. DOI: 10.1103/PhysRevLett.132.193803. URL: https://link.aps.org/doi/10.1103/PhysRevLett.132.193803 (Cited on page 48).

[89] Giovanni Milione et al. "Using the nonseparability of vector beams to encode information for optical communication". In: *Optics Letters* 40.21 (Oct. 2015), p. 4887. ISSN: 1539-4794. DOI: 10.1364/ol.40.004887. URL: http://dx.doi.org/10.1364/OL.40.004887 (Cited on page 48).

[90] Yifan Zhao and Jian Wang. "High-base vector beam encoding/decoding for visible-light communications". In: *Optics Letters* 40.21 (Oct. 2015), p. 4843. ISSN: 1539-4794. DOI: 10.1364/ol.40.004843. URL: http://dx.doi.org/10.1364/OL.40.004843 (Cited on page 48).

[91] Vincenzo D'Ambrosio et al. "Complete experimental toolbox for alignment-free quantum communication". In: *Nature Communications* 3.1 (July 2012). ISSN: 2041-1723. DOI: 10.1038/ncomms1951. URL: http://dx.doi.org/10.1038/ncomms1951 (Cited on page 48).

[92] Valentina Parigi et al. "Storage and retrieval of vector beams of light in a multiple-degree-of-freedom quantum memory". In: *Nature Communications* 6.1 (July 2015). ISSN: 2041-1723. DOI: 10.1038/ncomms8706. URL: http://dx.doi.org/10.1038/ncomms8706 (Cited on page 48).

[93] Alicia Sit et al. "High-dimensional intracity quantum cryptography with structured photons". In: *Optica* 4.9 (Aug. 2017), p. 1006. ISSN: 2334-2536. DOI: 10.1364/optica.4.001006. URL: http://dx.doi.org/10.1364/OPTICA.4.001006 (Cited on page 48).

[94] Stefan Berg-Johansen et al. "Classically entangled optical beams for high-speed kinematic sensing". In: *Optica* 2.10 (Sept. 2015), p. 864. ISSN: 2334-2536. DOI: 10.1364/optica.2.000864. URL: http://dx.doi.org/10.1364/OPTICA.2.000864 (Cited on page 48).

[95] Vincenzo D'Ambrosio et al. "Entangled vector vortex beams". In: *Phys. Rev. A* 94 (3 Sept. 2016), p. 030304. DOI: 10.1103/PhysRevA.94.030304. URL: https://link.aps.org/doi/10.1103/PhysRevA.94.030304 (Cited on page 48).

[96] Pengyun Li, Bo Wang, and Xiangdong Zhang. "High-dimensional encoding based on classical nonseparability". In: *Optics Express* 24.13 (June 2016), p. 15143. ISSN: 1094-4087. DOI: 10.1364/oe.24.015143. URL: http://dx.doi.org/10.1364/OE.24.015143 (Cited on page 48).

[97] Junliang Jia et al. "Mode sorter designed for (de)multiplexing vector vortex modes". In: *Applied Optics* 58.26 (Sept. 2019), p. 7094. ISSN: 2155-3165. DOI: 10.1364/ao.58.007094. URL: http://dx.doi.org/10.1364/AO.58.007094 (Cited on page 48).

[98] Lea Kopf et al. "Spectral vector beams for high-speed spectroscopic measurements". In: *Optica* 8.6 (June 2021), p. 930. ISSN: 2334-2536. DOI: 10.1364/optica.424960. URL: http://dx.doi.org/10.1364/OPTICA.424960 (Cited on page 48).

[99] Falk Töppel et al. "Classical entanglement in polarization metrology". In: *New Journal of Physics* 16.7 (July 2014), p. 073019. ISSN: 1367-2630. DOI: 10.1088/1367-2630/16/7/073019. URL: http://dx.doi.org/10.1088/1367-2630/16/7/073019 (Cited on page 48).

[100] E.J. Hearn. "Chapter 6 - Experimental Stress Analysis". In: *Mechanics of Materials 2 (Third Edition)*. Ed. by E.J. Hearn. Third Edition. Oxford: Butterworth-Heinemann, 1997, pp. 166–192. ISBN: 978-0-7506-3266-9. DOI: https://doi.org/10.1016/B978-075063266-9/50007-X. URL: https://www.sciencedirect.com/science/article/pii/B978075063266950007X (Cited on page 48).

[101] Karen E. Daniels, Jonathan E. Kollmer, and James G. Puckett. "Photoelastic force measurements in granular materials". In: *Review of Scientific Instruments* 88.5 (May 2017). ISSN: 1089-7623. DOI: 10.1063/1.4983049. URL: http://dx.doi.org/10.1063/1.4983049 (Cited on page 48).

[102] William B. Sparks et al. "Detection of circular polarization in light scattered from photosynthetic microbes". In: *Proceedings of the National Academy of Sciences* 106.19 (May 2009), pp. 7816–7821. ISSN: 1091-6490. DOI: 10.1073/pnas.0810215106. URL: http://dx.doi.org/10.1073/pnas.0810215106 (Cited on page 48).

[103] Joseph P. Angelo, Thomas A. Germer, and Maritoni Litorja. "Structured illumination Mueller matrix imaging". In: *Biomedical Optics Express* 10.6 (May 2019), p. 2861. ISSN: 2156-7085. DOI: 10.1364/boe.10.002861. URL: http://dx.doi.org/10.1364/BOE.10.002861 (Cited on page 48).

[104] R. M. A. Azzam. "Polarization, thin-film optics, ellipsometry, and polarimetry: Retrospective". In: *Journal of Vacuum Science & Technology B, Nanotechnology and Microelectronics: Materials, Processing, Measurement, and Phenomena* 37.6 (Oct. 2019). ISSN: 2166-2754. DOI: 10.1116/1.5122802. URL: http://dx.doi.org/10.1116/1.5122802 (Cited on page 48).

[105] R M A Azzam and N M Bashara. *Ellipsometry and polarized light*. North Holland, 1977 (Cited on page 48).

[106] Mathias Schubert. "Infrared ellipsometry on semiconductor layer structures phonons, plasmons, and polaritons". In: *Springer Tracts in Modern Physics* 209 (2005), pp. 1–190. ISSN: 0081-3869 (Cited on page 48).

[107] Maria Losurdo and Kurt Hingerl, eds. *Ellipsometry at the Nanoscale*. Springer, 2013. DOI: 10.1007/978-3-642-33956-1. URL: https://doi.org/10.1007/978-3-642-33956-1 (Cited on page 48).

[108] Karsten Hinrichs and Klaus-J. Eichhorn. "Ellipsometry of Functional Organic Surfaces and Films". In: *Ellipsometry of Functional Organic Surfaces and Films* (2014) (Cited on page 48).

[109] Ivan Ohlídal et al. "Ellipsometric characterization of inhomogeneous thin films with complicated thickness non-uniformity: application to inhomogeneous polymer-like thin films". In: *Opt. Express* 28.24 (Nov. 2020), pp. 36796–36811. DOI: 10.1364/OE.412043. URL: http://www.osapublishing.org/oe/abstract.cfm?URI=oe-28-24-36796 (Cited on page 48).

[110] L. Rudnicki et al. "Fundamental quantum limits in ellipsometry". In: *Opt. Lett.* 45.16 (Aug. 2020), pp. 4607–4610. DOI: 10.1364/OL.392955. URL: http://www.osapublishing.org/ol/abstract.cfm?URI=ol-45-16-4607 (Cited on page 48).

[111] Kimani C. Toussaint et al. "Quantum ellipsometry using correlated-photon beams". In: *Phys. Rev. A* 70 (2 Aug. 2004), p. 023801. DOI: 10.1103/PhysRevA.70.023801. URL: https://link.aps.org/doi/10.1103/PhysRevA.70.023801 (Cited on page 48).

[112] Carlton M. Caves, Christopher A. Fuchs, and Rüdiger Schack. "Unknown quantum states: The quantum de Finetti representation". In: *Journal of Mathematical Physics* 43.9 (Sept. 2002), pp. 4537–4559. ISSN: 1089-7658. DOI: 10.1063/1.1494475. URL: http://dx.doi.org/10.1063/1.1494475 (Cited on page 49).

[113] J. B. Altepeter, E. R. Jeffrey, and P. G. Kwiat. "Photonic State Tomography". English (US). In: ed. by P.R. Berman and C.C. Lin. Vol. 52. Advances In Atomic, Molecular, and Optical Physics. Academic Press, 2005, pp. 105–159. ISBN: 9780120038527. DOI: 10.1016/S1049-250X(05)52003-2 (Cited on pages 49, 56).

[114] Daniel F. V. James et al. "Measurement of qubits". In: *Phys. Rev. A* 64 (5 Oct. 2001), p. 052312. DOI: 10.1103/PhysRevA.64.052312. URL: https://link.aps.org/doi/10.1103/PhysRevA.64.052312 (Cited on page 49).

[115] K Banaszek, M Cramer, and D Gross. "Focus on quantum tomography". In: *New Journal of Physics* 15.12 (Dec. 2013), p. 125020. DOI: 10.1088/1367-2630/15/12/125020. URL: https://doi.org/10.1088/1367-2630/15/12/125020 (Cited on page 49).

[116] Ermes Toninelli et al. "Concepts in quantum state tomography and classical implementation with intense light: a tutorial". In: *Adv. Opt. Photon.* 11.1 (Mar. 2019), pp. 67–134. DOI: 10.1364/AOP.11.000067. URL: https://opg.optica.org/aop/abstract.cfm?URI=aop-11-1-67 (Cited on pages 49, 57).

[117] Matthew R. Foreman, Alberto Favaro, and Andrea Aiello. "Optimal Frames for Polarization State Reconstruction". In: *Phys. Rev. Lett.* 115 (26 Dec. 2015), p. 263901. DOI: 10.1103/PhysRevLett.115.263901. URL: https://link.aps.org/doi/10.1103/PhysRevLett.115.263901 (Cited on page 49).

[118] Stephen Barnett. *Quantum Information*. Oxford University Press, Inc., 2009. ISBN: 0198527632 (Cited on pages 49, 51, 54–55, 167).

[119] Roger B. M. Clarke et al. "Experimental realization of optimal detection strategies for overcomplete states". In: *Physical Review A* 64.1 (May 2001). ISSN: 1094-1622. DOI: 10.1103/physreva.64.012303. URL: http://dx.doi.org/10.1103/PhysRevA.64.012303 (Cited on pages 49, 51, 54–55).

[120] Michael A. Nielsen and Isaac L. Chuang. *Quantum Computation and Quantum Information: 10th Anniversary Edition*. Cambridge University Press, 2010 (Cited on pages 49, 51, 55).

[121] Alexander Ling et al. "Experimental polarization state tomography using optimal polarimeters". In: *Physical Review A* 74.2 (Aug. 2006). ISSN: 1094-1622. DOI: 10.1103/physreva.74.022309. URL: http://dx.doi.org/10.1103/PhysRevA.74.022309 (Cited on pages 49, 54–58, 60, 68).

[122] Jaroslav Řehá ček, Berthold-Georg Englert, and Dagomir Kaszlikowski. "Minimal qubit tomography". In: *Phys. Rev. A* 70 (5 Nov. 2004), p. 052321. DOI: 10.1103/PhysRevA.70.052321. URL: https://link.aps.org/doi/10.1103/PhysRevA.70.052321 (Cited on page 49).

[123] W. M. Pimenta et al. "Minimal state tomography of spatial qubits using a spatial light modulator". In: *Opt. Express* 18.24 (Nov. 2010), pp. 24423–24433. DOI: 10.1364/OE.18.024423. URL: http://www.osapublishing.org/oe/abstract.cfm?URI=oe-18-24-24423 (Cited on page 49).

[124] W. M. Pimenta et al. "Minimum tomography of two entangled qutrits using local measurements of one-qutrit symmetric informationally complete positive operator-valued measure". In: *Phys. Rev. A* 88 (1 July 2013), p. 012112. DOI: 10.1103/PhysRevA.88.012112. URL: https://link.aps.org/doi/10.1103/PhysRevA.88.012112 (Cited on page 49).

[125] Adetunmise C. Dada et al. "Optimal simultaneous measurements of incompatible observables of a single photon". In: *OPTICA* 6.3 (Feb. 2019), p. 257. DOI: 10.1364/optica.6.000257. URL: https://doi.org/10.1364/optica.6.000257 (Cited on page 49).

[126] Joseph M. Renes et al. "Symmetric informationally complete quantum measurements". In: *Journal of Mathematical Physics* 45.6 (June 2004), pp. 2171–2180. ISSN: 1089-7658. DOI: 10.1063/1.1737053. URL: http://dx.doi.org/10.1063/1.1737053 (Cited on pages 49, 54).

[127] N. Bent et al. "Experimental Realization of Quantum Tomography of Photonic Qudits via Symmetric Informationally Complete Positive Operator-Valued Measures". In: *Phys. Rev. X* 5 (4 Oct. 2015), p. 041006. DOI: 10.1103/PhysRevX.5.041006. URL: https://link.aps.org/doi/10.1103/PhysRevX.5.041006 (Cited on page 49).

[128] C. Paiva-Sánchez et al. "Quantum tomography via equidistant states". In: *Phys. Rev. A* 82 (3 Sept. 2010), p. 032115. DOI: 10.1103/PhysRevA.82.032115. URL: https://link.aps.org/doi/10.1103/PhysRevA.82.032115 (Cited on page 49).

[129] Alexander Ling et al. "An optimal photon counting polarimeter". In: *Journal of Modern Optics* 53.10 (July 2006), pp. 1523–1528. ISSN: 1362-3044. DOI: 10.1080/09500340600674242. URL: http://dx.doi.org/10.1080/09500340600674242 (Cited on pages 49, 55).

[130] Mohammad Mirhosseini et al. "Rapid generation of light beams carrying orbital angular momentum". In: *Opt. Express* 21.25 (Dec. 2013), pp. 30196–30203. DOI: 10.1364/OE.21.030196. URL: http://www.osapublishing.org/oe/abstract.cfm?URI=oe-21-25-30196 (Cited on page 49).

[131] Kevin J. Mitchell et al. "High-speed spatial control of the intensity, phase and polarisation of vector beams using a digital micro-mirror device". In: *Opt. Express* 24.25 (Dec. 2016), pp. 29269–29282. DOI: 10.1364/OE.24.029269. URL: http://www.osapublishing.org/oe/abstract.cfm?URI=oe-24-25-29269 (Cited on page 49).

[132] Alessio D'Errico et al. "Topological features of vector vortex beams perturbed with uniformly polarized light". In: *Scientific Reports* 7 (1 2017), p. 40195. DOI: 10.1038/srep40195. URL: https://doi.org/10.1038/srep40195 (Cited on page 49).

[133] J. G. Ureta, B. Khajavi, and E. J. Galvez. "Decoding Vortex Beams with Shear Interferometry". In: *Latin America Optics and Photonics Conference*. OSA, 2018. DOI: 10.1364/laop.2018.w3a.2. URL: https://doi.org/10.1364/laop.2018.w3a.2 (Cited on page 49).

[134] Stephen M. Barnett and Sarah Croke. "Quantum state discrimination". In: *Advances in Optics and Photonics* 1.2 (Feb. 2009), p. 238. ISSN: 1943-8206. DOI: 10.1364/aop.1.000238. URL: http://dx.doi.org/10.1364/AOP.1.000238 (Cited on page 51).

[135] Kuldeep Singh. *Linear algebra*. London, England: Oxford University Press, Oct. 2013 (Cited on page 51).

[136] Asher Peres. *Quantum Theory: Concepts and Methods*. 1995th ed. Fundamental Theories of Physics. Dordrecht, Netherlands: Springer, Oct. 1993 (Cited on page 54).

[137] E. Prugovečki. "Information-theoretical aspects of quantum measurement". In: *International Journal of Theoretical Physics* 16.5 (May 1977), pp. 321–331. ISSN: 1572-9575. DOI: 10.1007/bf01807146. URL: http://dx.doi.org/10.1007/BF01807146 (Cited on page 54).

[138] Franklin E. Schroeck. *Quantum Mechanics on Phase Space*. Springer Netherlands, 1996. ISBN: 9789401728300. DOI: 10.1007/978-94-017-2830-0. URL: http://dx.doi.org/10.1007/978-94-017-2830-0 (Cited on page 54).

[139] Paul Busch. "Informationally complete sets of physical quantities". In: *International Journal of Theoretical Physics* 30.9 (Sept. 1991), pp. 1217–1227. ISSN: 1572-9575. DOI: 10.1007/bf00671008. URL: http://dx.doi.org/10.1007/BF00671008 (Cited on page 54).

[140] G M D'Ariano, P Perinotti, and M F Sacchi. "Informationally complete measurements and group representation". In: *Journal of Optics B: Quantum and Semiclassical Optics* 6.6 (May 2004), S487. DOI: 10.1088/1464-4266/6/6/005. URL: https://dx.doi.org/10.1088/1464-4266/6/6/005 (Cited on page 54).

[141] R. M. A. Azzam, I. M. Elminyawi, and A. M. El-Saba. "General analysis and optimization of the four-detector photopolarimeter". In: *J. Opt. Soc. Am. A* 5.5 (May 1988), pp. 681–689. DOI: 10.1364/JOSAA.5.000681. URL: https://opg.optica.org/josaa/abstract.cfm?URI=josaa-5-5-681 (Cited on page 56).

[142] Daniel M. Greenberger, Michael A. Horne, and Anton Zeilinger. *Going Beyond Bell's Theorem*. 2007. arXiv: 0712.0921 [quant-ph] (Cited on page 58).

[143] Jefferson Flórez et al. "A variable partially polarizing beam splitter". In: *Review of Scientific Instruments* 89.2 (Feb. 2018). ISSN: 1089-7623. DOI: 10.1063/1.5004805. URL: http://dx.doi.org/10.1063/1.5004805 (Cited on pages 58, 69).

[144] R. D. Hawley et al. "Passive broadband full Stokes polarimeter using a Fresnel cone". In: *Scientific Reports* 9.1 (Feb. 2019). ISSN: 2045-2322. DOI: 10.1038/s41598-019-39118-0. URL: http://dx.doi.org/10.1038/s41598-019-39118-0 (Cited on page 66).

[145] A. Uhlmann. "The "transition probability" in the state space of a *-algebra". In: *Reports on Mathematical Physics* 9.2 (1976), pp. 273–279. ISSN: 0034-4877. DOI: https://doi.org/10.1016/0034-4877(76)90060-4. URL: https://www.sciencedirect.com/science/article/pii/0034487776900604 (Cited on page 68).

[146] Richard Jozsa. "Fidelity for Mixed Quantum States". In: *Journal of Modern Optics* 41.12 (Dec. 1994), pp. 2315–2323. ISSN: 1362-3044. DOI: 10.1080/09500349414552171. URL: http://dx.doi.org/10.1080/09500349414552171 (Cited on page 68).

[147] Isaac Nape et al. "Revealing the invariance of vectorial structured light in perturbing media". In: *arXiv* (2021). DOI: arXiv:2108.13890v2. URL: https://arxiv.org/pdf/2108.13890v2.pdf (Cited on page 68).

[148] Yash D. Shah et al. "An All-Dielectric Metasurface Polarimeter". In: *ACS Photonics* 9.10 (Sept. 2022), pp. 3245–3252. ISSN: 2330-4022. DOI: 10.1021/acsphotonics.2c00395. URL: http://dx.doi.org/10.1021/acsphotonics.2c00395 (Cited on page 69).

[149] Amy McWilliam et al. "Dynamic Mueller matrix polarimetry using generalized measurements". In: *Opt. Express* 32.12 (June 2024), pp. 21909–21924. DOI: 10.1364/OE.521069. URL: https://opg.optica.org/oe/abstract.cfm?URI=oe-32-12-21909 (Cited on pages 69–71).

[150] PL Bender. "Atomic frequency standards and clocks". In: *Quantum Electronics*. Columbia University Press, 1960, pp. 111–112 (Cited on page 73).

[151] Kyle W Martin et al. "Compact optical atomic clock based on a two-photon transition in rubidium". In: *Physical Review Applied* 9.1 (2018), p. 014019 (Cited on page 73).

[152] Aldo Godone et al. "The pulsed rubidium clock". In: *IEEE transactions on ultrasonics, ferroelectrics, and frequency control* 53.3 (2006), pp. 525–529 (Cited on page 73).

[153] AJ Fairweather and MJ Usher. "A vector rubidium magnetometer". In: *Journal of Physics E: Scientific Instruments* 5.10 (1972), p. 986 (Cited on page 73).

[154] PDD Schwindt, Leo Hollberg, and John Kitching. "Self-oscillating rubidium magnetometer using nonlinear magneto-optical rotation". In: *Review of Scientific Instruments* 76.12 (2005) (Cited on page 73).

[155] Francesco Castellucci et al. "Atomic Compass: Detecting 3D Magnetic Field Alignment with Vector Vortex Light". In: *Phys. Rev. Lett.* 127 (23 Nov. 2021), p. 233202. DOI: 10.1103/PhysRevLett.127.233202. URL: https://link.aps.org/doi/10.1103/PhysRevLett.127.233202 (Cited on pages 73, 87, 118).

[156] S-Y Lan et al. "A multiplexed quantum memory". In: *Optics express* 17.16 (2009), pp. 13639–13645 (Cited on page 73).

[157] R Zhao et al. "Long-lived quantum memory". In: *Nature Physics* 5.2 (2009), pp. 100–104 (Cited on page 73).

[158] Mahdi Hosseini et al. "High efficiency coherent optical memory with warm rubidium vapour". In: *Nature communications* 2.1 (2011), p. 174 (Cited on page 73).

[159] William M Haynes, ed. *CRC handbook of chemistry and physics, 95th edition*. 95th ed. Oakville, MO: Apple Academic Press, June 2014 (Cited on page 74).

[160] Daniel A. Steck. *Rubidium 85 D Line Data*. Revised edition. Sept. 2023. URL: http://steck.us/alkalidata (Cited on pages 74–75, 77–78, 83, 87, 92, 110, 135).

[161] Daniel A. Steck. *Rubidium 87 D Line Data*. Revised edition. Sept. 2023. URL: http://steck.us/alkalidata (Cited on pages 74–75, 77–78, 83, 87, 92, 110, 135).

[162] Alan Corney. *Atomic and Laser Spectroscopy*. en. Oxford science publications. London, England: Oxford University Press, Jan. 1980 (Cited on page 77).

[163] M. P. A. Jones. *Atom-Light Interactions*. URL: http://info.phys.unm.edu/~ideutsch/Classes/Phys566F13/Notes%20from%20others/Atom-Light%20Interactions.pdf (visited on Apr. 11, 2024) (Cited on page 78).

[164] Rodney Loudon. *The quantum theory of light*. en. 3rd ed. London, England: Oxford University Press, Sept. 2000 (Cited on pages 78, 108).

[165] Daniel A. Steck. *Quantum and Atom Optics*. Revised edition. Feb. 2024. URL: http://steck.us/teaching (Cited on pages 78, 170).

[166] C J Foot. *Atomic Physics*. Oxford Master Series in Physics. London, England: Oxford University Press, Nov. 2004 (Cited on pages 78, 102, 107).

[167] H Haken and Hans C Wolf. *The physics of atoms and quanta*. en. 7th ed. Advanced Texts in Physics. Berlin, Germany: Springer, Sept. 2005 (Cited on page 85).

[168] C P Pearman et al. "Polarization spectroscopy of a closed atomic transition: applications to laser frequency locking". In: *Journal of Physics B: Atomic, Molecular and Optical Physics* 35.24 (Dec. 2002), pp. 5141–5151. ISSN: 0953-4075. DOI: 10.1088/0953-4075/35/24/315. URL: http://dx.doi.org/10.1088/0953-4075/35/24/315 (Cited on pages 87, 106, 117, 120–121).

[169] M. L. Harris et al. "Polarization spectroscopy in rubidium and cesium". In: *Physical Review A* 73.6 (June 2006). ISSN: 1094-1622. DOI: 10.1103/physreva.73.062509. URL: http://dx.doi.org/10.1103/PhysRevA.73.062509 (Cited on pages 87, 106, 117).

[170] Geol Moon and Heung-Ryoul Noh. "Theoretical Calculation of the Saturated Absorption Spectrum for a Multilevel Atom". In: *Journal of the Korean Physical Society* 50.4 (Apr. 2007), p. 1037. ISSN: 0374-4884. DOI: 10.3938/jkps.50.1037. URL: http://dx.doi.org/10.3938/jkps.50.1037 (Cited on page 87).

[171] Huy Diep Do, Geol Moon, and Heung-Ryoul Noh. "Polarization spectroscopy of rubidium atoms: Theory and experiment". In: *Physical Review A* 77.3 (Mar. 2008). ISSN: 1094-1622. DOI: 10.1103/physreva.77.032513. URL: http://dx.doi.org/10.1103/PhysRevA.77.032513 (Cited on page 87).

[172] A. S. Arnold, J. S. Wilson, and M. G. Boshier. "A simple extended-cavity diode laser". In: *Review of Scientific Instruments* 69.3 (Mar. 1998), pp. 1236–1239. ISSN: 1089-7623. DOI: 10.1063/1.1148756. URL: http://dx.doi.org/10.1063/1.1148756 (Cited on pages 92–94).

[173] X. Baillard et al. "Interference-filter-stabilized external-cavity diode lasers". In: *Optics Communications* 266.2 (Oct. 2006), pp. 609–613. ISSN: 0030-4018. DOI: 10.1016/j.optcom.2006.05.011. URL: http://dx.doi.org/10.1016/j.optcom.2006.05.011 (Cited on page 93).

[174] M. Gilowski et al. "Narrow bandwidth interference filter-stabilized diode laser systems for the manipulation of neutral atoms". In: *Optics Communications* 280.2 (Dec. 2007), pp. 443–447. ISSN: 0030-4018. DOI: 10.1016/j.optcom.2007.08.043. URL: http://dx.doi.org/10.1016/j.optcom.2007.08.043 (Cited on page 93).

[175] K. B. MacAdam, A. Steinbach, and C. Wieman. "A narrow-band tunable diode laser system with grating feedback, and a saturated absorption spectrometer for Cs and Rb". In: *American Journal of Physics* 60.12 (Dec. 1992), pp. 1098–1111. ISSN: 1943-2909. DOI: 10.1119/1.16955. URL: http://dx.doi.org/10.1119/1.16955 (Cited on page 93).

[176] C. J. Hawthorn, K. P. Weber, and R. E. Scholten. "Littrow configuration tunable external cavity diode laser with fixed direction output beam". In: *Review of Scientific Instruments* 72.12 (Dec. 2001), pp. 4477–4479. ISSN: 1089-7623. DOI: 10.1063/1.1419217. URL: http://dx.doi.org/10.1063/1.1419217 (Cited on pages 93–94).

[177] Thorlabs. *Diffraction Gratings Tutorial: Blazed (Ruled) Gratings*. URL: https://www.thorlabs.com/newgrouppage9.cfm?objectgroup_id=25 (visited on July 2, 2024) (Cited on page 94).

[178] Daryl W. Preston. "Doppler-free saturated absorption: Laser spectroscopy". In: *American Journal of Physics* 64 (1996), pp. 1432–1436. URL: https://api.semanticscholar.org/CorpusID:15254298 (Cited on page 97).

[179] David A. Smith and Ifan G. Hughes. "The role of hyperfine pumping in multilevel systems exhibiting saturated absorption". In: *American Journal of Physics* 72.5 (Apr. 2004), pp. 631–637. ISSN: 1943-2909. DOI: 10.1119/1.1652039. URL: http://dx.doi.org/10.1119/1.1652039 (Cited on pages 97, 109).

[180] Ben E. Sherlock and Ifan G. Hughes. "How weak is a weak probe in laser spectroscopy?" In: *American Journal of Physics* 77.2 (Feb. 2009), pp. 111–115. ISSN: 1943-2909. DOI: 10.1119/1.3013197. URL: http://dx.doi.org/10.1119/1.3013197 (Cited on pages 97, 109).

[181] MOGLabs. *External Cavity Diode Laser Controller*. URL: https://www.moglabs.com/products/laser-electronics/diode-laser-controller/MOGLabs_DLC_manual.pdf (visited on July 3, 2024) (Cited on page 100).

[182] Daniel J McCarron. *A guide to acousto-optic modulators*. 2007. URL: http://themccarrongroup.com/wp-content/uploads/2020/03/AOM-Guide.pdf (Cited on page 100).

[183] E. A. Donley et al. "Double-pass acousto-optic modulator system". In: *Review of Scientific Instruments* 76.6 (June 2005). ISSN: 1089-7623. DOI: 10.1063/1.1930095. URL: http://dx.doi.org/10.1063/1.1930095 (Cited on page 101).

[184] C. Wieman and T. W. Hänsch. "Doppler-Free Laser Polarization Spectroscopy". In: *Phys. Rev. Lett.* 36 (20 May 1976), pp. 1170–1173. DOI: 10.1103/PhysRevLett.36.1170. URL: https://link.aps.org/doi/10.1103/PhysRevLett.36.1170 (Cited on page 106).

[185] Takashi Fujimoto and Sergei A Kazantsev. "Plasma polarization spectroscopy". In: *Plasma Physics and Controlled Fusion* 39.9 (Sept. 1997), pp. 1267–1294. ISSN: 1361-6587. DOI: 10.1088/0741-3335/39/9/002. URL: http://dx.doi.org/10.1088/0741-3335/39/9/002 (Cited on page 106).

[186] K. Danzmann, K. Grützmacher, and B. Wende. "Doppler-Free Two-Photon Polarization-Spectroscopic Measurement of the Stark-Broadened Profile of the Hydrogen L_α Line in a Dense Plasma". In: *Phys. Rev. Lett.* 57 (17 Oct. 1986), pp. 2151–2153. DOI: 10.1103/PhysRevLett.57.2151. URL: https://link.aps.org/doi/10.1103/PhysRevLett.57.2151 (Cited on page 106).

[187] G. Rosenzweig et al. “Local measurements of the spatial magnetic field distribution in a z-pinch plasma during and near stagnation using polarization spectroscopy”. In: *Physics of Plasmas* 27.2 (Feb. 2020), p. 022705. ISSN: 1070-664X. DOI: 10.1063/1.5126934. eprint: https://pubs.aip.org/aip/pop/article-pdf/doi/10.1063/1.5126934/15773671/022705_1_online.pdf. URL: https://doi.org/10.1063/1.5126934 (Cited on page 106).

[188] Ashok K. Mohapatra et al. “A giant electro-optic effect using polarizable dark states”. In: *Nature Physics* 4.11 (Sept. 2008), pp. 890–894. ISSN: 1745-2481. DOI: 10.1038/nphys1091. URL: http://dx.doi.org/10.1038/nphys1091 (Cited on page 106).

[189] Alexia Gobrecht et al. “Combining linear polarization spectroscopy and the Representative Layer Theory to measure the Beer–Lambert law absorbance of highly scattering materials”. In: *Analytica Chimica Acta* 853 (Jan. 2015), pp. 486–494. ISSN: 0003-2670. DOI: 10.1016/j.aca.2014.10.014. URL: http://dx.doi.org/10.1016/j.aca.2014.10.014 (Cited on page 106).

[190] Johannes F. de Boer, Christoph K. Hitzenberger, and Yoshiaki Yasuno. “Polarization sensitive optical coherence tomography – a review [Invited]”. In: *Biomedical Optics Express* 8.3 (Feb. 2017), p. 1838. ISSN: 2156-7085. DOI: 10.1364/boe.8.001838. URL: http://dx.doi.org/10.1364/BOE.8.001838 (Cited on page 106).

[191] R. E. Teets et al. “Laser Polarization Spectroscopy”. In: *Advances in Laser Spectroscopy I*. Ed. by Ahmed H. Zewail. Vol. 0113. International Society for Optics and Photonics. SPIE, 1977, pp. 80–87. DOI: 10.1117/12.955605. URL: https://doi.org/10.1117/12.955605 (Cited on page 106).

[192] Christopher Carr, Charles S. Adams, and Kevin J. Weatherill. “Polarization spectroscopy of an excited state transition”. In: *Optics Letters* 37.1 (Jan. 2012), p. 118. ISSN: 1539-4794. DOI: 10.1364/ol.37.000118. URL: http://dx.doi.org/10.1364/OL.37.000118 (Cited on pages 106, 117).

[193] K. Pahwa, L. Mudarikwa, and J. Goldwin. “Polarization spectroscopy and magnetically-induced dichroism of the potassium D_2 lines”. In: *Optics Express* 20.16 (July 2012), p. 17456. ISSN: 1094-4087. DOI: 10.1364/oe.20.017456. URL: http://dx.doi.org/10.1364/OE.20.017456 (Cited on page 106).

[194] John David Jackson. *Classical electrodynamics*. en. John Wiley & Sons Ltd, 1962 (Cited on page 107).

[195] A. D. McNaught and Wilkinson A. “The IUPAC Compendium of Chemical Terminology”. In: International Union of Pure and Applied Chemistry (IUPAC), Feb. 2014. DOI: 10.1351/goldbook.n04260. URL: http://dx.doi.org/10.1351/goldbook.N04260 (Cited on pages 107, 111).

[196] Robert W. Boyd. *Nonlinear Optics, Fourth Edition*. 4th. USA: Academic Press, Inc., 2020. ISBN: 9780128110027 (Cited on page 107).

[197] R. de L. Kronig. “On the Theory of Dispersion of X-Rays”. In: *Journal of the Optical Society of America* 12.6 (June 1926), p. 547. ISSN: 0030-3941. DOI: 10.1364/josa.12.000547. URL: http://dx.doi.org/10.1364/JOSA.12.000547 (Cited on page 109).

[198] H.A. Kramers. “La diffusion de la lumière par les atomes”. In: *Atti del Congresso Internationale dei Fisici (Proceedings of the International Congress of Physicists)* 2 (1926), pp. 545–557 (Cited on page 109).

[199] M. M. Tehranchi, S. M. Hamidi, and B. Abaie. "Determination of the atomic number density of Rb vapor by using spectral Faraday rotation measurements". In: *Journal of the Korean Physical Society* 62.5 (Mar. 2013), pp. 731–733. ISSN: 1976-8524. DOI: 10.3938/jkps.62.731. URL: http://dx.doi.org/10.3938/jkps.62.731 (Cited on page 110).

[200] A. D. McNaught and Wilkinson A. "The IUPAC Compendium of Chemical Terminology". In: International Union of Pure and Applied Chemistry (IUPAC), Feb. 2014. DOI: 10.1351/goldbook.b00626. URL: http://dx.doi.org/10.1351/goldbook.B00626 (Cited on page 110).

[201] "3 - MECHANISMS OF UV STABILIZATION". In: *Handbook of UV Degradation and Stabilization (Second Edition)*. Ed. by George Wypych. Second Edition. ChemTec Publishing, 2015, pp. 37–65. ISBN: 978-1-895198-86-7. DOI: https://doi.org/10.1016/B978-1-895198-86-7.50005-X. URL: https://www.sciencedirect.com/science/article/pii/B978189519886750005X (Cited on page 110).

[202] Jim Clark. *THE BEER-LAMBERT LAW*. 2007. URL: https://www.chemguide.co.uk/analysis/uvvisible/beerlambert.html (visited on Apr. 30, 2004) (Cited on page 110).

[203] David A. Rubenstein, Wei Yin, and Mary D. Frame. "Chapter 4 - Introduction to heat transfer". In: *Biofluid Mechanics (Third Edition)*. Ed. by David A. Rubenstein, Wei Yin, and Mary D. Frame. Third Edition. Biomedical Engineering. Academic Press, 2022, pp. 135–156. ISBN: 978-0-12-818034-1. DOI: https://doi.org/10.1016/B978-0-12-818034-1.00004-9. URL: https://www.sciencedirect.com/science/article/pii/B9780128180341000049 (Cited on page 110).

[204] Teledyne Photometrics. *Bit Depth, Full Well, and Dynamic Range*. URL: https://www.photometrics.com/learn/camera-basics/bit-depth (visited on Apr. 30, 2024) (Cited on page 112).

[205] N. Miura. "2.08 - Magneto-Spectroscopy of Semiconductors". In: *Comprehensive Semiconductor Science and Technology*. Ed. by Pallab Bhattacharya, Roberto Fornari, and Hiroshi Kamimura. Amsterdam: Elsevier, 2011, pp. 256–342. ISBN: 978-0-444-53153-7. DOI: https://doi.org/10.1016/B978-0-44-453153-7.00085-7. URL: https://www.sciencedirect.com/science/article/pii/B9780444531537000857 (Cited on page 115).

[206] Stefan L Kemp, Ifan G Hughes, and Simon L Cornish. "An analytical model of off-resonant Faraday rotation in hot alkali metal vapours". In: *Journal of Physics B: Atomic, Molecular and Optical Physics* 44.23 (Nov. 2011), p. 235004. ISSN: 1361-6455. DOI: 10.1088/0953-4075/44/23/235004. URL: http://dx.doi.org/10.1088/0953-4075/44/23/235004 (Cited on page 115).

[207] D. Budker et al. "Resonant nonlinear magneto-optical effects in atoms". In: *Reviews of Modern Physics* 74.4 (Nov. 2002), pp. 1153–1201. ISSN: 1539-0756. DOI: 10.1103/revmodphys.74.1153. URL: http://dx.doi.org/10.1103/RevModPhys.74.1153 (Cited on pages 115–116).

[208] Gérard Trénec et al. "Permanent magnets for Faraday rotators inspired by the design of the magic sphere". In: *Applied Optics* 50.24 (Aug. 2011), p. 4788. ISSN: 1539-4522. DOI: 10.1364/ao.50.004788. URL: http://dx.doi.org/10.1364/AO.50.004788 (Cited on page 115).

[209] Ivan Mukhin et al. "2.1 Tesla permanent-magnet Faraday isolator for subkilowatt average power lasers". In: *Optics Communications* 282.10 (May 2009), pp. 1969–1972. ISSN: 0030-4018. DOI: 10.1016/j.optcom.2009.02.008. URL: http://dx.doi.org/10.1016/j.optcom.2009.02.008 (Cited on page 115).

[210] Paul Siddons. "Faraday Rotation of Pulsed and Continuous-wave Light in Atomic Vapour". PhD thesis. Department of Physics, Faculty of Science, 2011. URL: https://etheses.dur.ac.uk/11212/ (Cited on page 116).

[211] Mark A Zentile et al. "The hyperfine Paschen–Back Faraday effect". In: *Journal of Physics B: Atomic, Molecular and Optical Physics* 47.7 (Mar. 2014), p. 075005. ISSN: 1361-6455. DOI: 10.1088/0953-4075/47/7/075005. URL: http://dx.doi.org/10.1088/0953-4075/47/7/075005 (Cited on page 116).

[212] K.H Drake, W Lange, and J Mlynek. "Nonlinear faraday and voigt effect in a $J = 1$ to $J' = 0$ transition in atomic samarium vapor". In: *Optics Communications* 66.5–6 (May 1988), pp. 315–320. ISSN: 0030-4018. DOI: 10.1016/0030-4018(88)90422-1. URL: http://dx.doi.org/10.1016/0030-4018(88)90422-1 (Cited on page 116).

[213] Rafael Drampyan, Andrew D. Greentree, and A.V. Durrant. "Two field nonlinear Faraday rotation in rubidium vapor in a Doppler-free geometry". In: *Optics Communications* 276.2 (2007), pp. 251–260. ISSN: 0030-4018. DOI: https://doi.org/10.1016/j.optcom.2007.04.027. URL: https://www.sciencedirect.com/science/article/pii/S0030401807004294 (Cited on page 116).

[214] Anthony Zentile Mark. "Applications of the Faraday Effect in Hot Atomic Vapours". PhD thesis. Department of Physics, Faculty of Science, 2015. URL: https://etheses.dur.ac.uk/11212/ (Cited on page 116).

[215] MμShield. *Heat Treating vs Annealing*. URL: https://www.mushield.com/heat-treating/magnetic-shielding-heat-treating-vs-annealing/ (visited on June 5, 2024) (Cited on page 117).

[216] Wolfgang Demtröder. "Laser spectroscopy: Fourth edition". In: *Laser Spectroscopy: Fourth Edition* 1 (Jan. 2008). DOI: 10.1007/978-3-540-73418-5 (Cited on page 120).

[217] Thorlabs. *Polarization-Maintaining Fiber: PANDA Style (PM780-HP)*. URL: https://www.thorlabs.com/drawings/dedd176b3ca2de07-1FDF74D3-DC69-9049-FB8A4C000C733507/PM780-HP-SpecSheet.pdf (visited on June 30, 2024) (Cited on page 132).

[218] Swift Glass. *Understanding Glass Properties: The Absorption Spectrum*. URL: https://www.swiftglass.com/blog/understanding-absorption-spectrum/#:~:text=Composition,absorbs%20between%205%2D10%25. (visited on June 29, 2024) (Cited on page 142).

[219] Fritz Diorico, Artem Zhutov, and Onur Hosten. "Laser-cavity locking utilizing beam ellipticity: accessing the 10^{-7} instability scale relative to cavity linewidth". In: *Optica* 11.1 (Jan. 2024), p. 26. ISSN: 2334-2536. DOI: 10.1364/optica.507451. URL: http://dx.doi.org/10.1364/OPTICA.507451 (Cited on page 145).

Appendix A

Naimark extension of the POVM elements

We provide more details on the realisation of the Naimark extension of the POVM states to implement the four-outcome POVM measurement system described in the text. The unitary transformation applied to the input state, as written in the extended basis, reads,

$$U = \sum_{\substack{i,j=1,2;\\ \mu,\nu=\alpha,\beta}} U_{\mu i j \nu} |k_\mu\rangle |e_i\rangle\langle e_j| \langle k_\nu|, \tag{A.1}$$

where $\langle e_1|$ and $\langle e_2|$ denote orthogonal polarisation states and $\langle k_\alpha|$ and $\langle k_\beta|$ different propagation paths. Here $U_{\mu i j \nu} = \langle k_\mu|\langle e_i|U|e_j\rangle|k_\nu\rangle$ are the elements of the matrix U,

$$U = \frac{\sqrt{2}}{2} \begin{pmatrix} -ia & ib & a & -b \\ -ia & -ib & -a & -b \\ -ib & -a & -ib & a \\ -b & -ia & b & -ia \end{pmatrix}, \tag{A.2}$$

written in the basis of the extended Hilbert space $\{|e_1\rangle|k_\alpha\rangle, |e_2\rangle|k_\alpha\rangle, |e_1\rangle|k_\beta\rangle, |e_2\rangle|k_\beta\rangle\}$ in this order. With a polarising beam splitter and a CMOS camera, the final projection measurement P can be realised for spatial resolution detection. For an input state defined in the extended state space,

$$|\psi\rangle \otimes |k_\alpha\rangle = \Big(|u_H\rangle|H\rangle + e^{i\phi}|u_V\rangle|V\rangle\Big) \otimes |k_\alpha\rangle, \tag{A.3}$$

the probability that a photon is detected in one of the interferometer arms, identified by the path ν and polarisation i, is therefore given by [118],

$$\langle\psi|\hat{\pi}_{i\nu}|\psi\rangle = |\langle k_\nu|\langle e_i|U|\psi\rangle|k_\alpha\rangle|^2, \tag{A.4}$$

where $\hat{\pi}_{i\nu} = \langle k_\alpha|U^\dagger|e_i\rangle|k_\nu\rangle\langle k_\nu|\langle e_i|U|k_\alpha\rangle$ are the POVM elements, which using Eqn. (A.1) may be expressed as,

$$\hat{\pi}_{i\nu} = \sum_{j',j=1,2} U^*_{\nu i j' \alpha} U_{\nu i j \alpha} |\hat{e}_{j'}\rangle\langle\hat{e}_j|. \tag{A.5}$$

It is then readily verified that choosing U as given in Eqn. (A.2) and using the notation transformation $\hat{\pi}_1 = \hat{\pi}_{1\alpha}$, $\hat{\pi}_2 = \hat{\pi}_{2\alpha}$, $\hat{\pi}_3 = \hat{\pi}_{1\beta}$ and $\hat{\pi}_4 = \hat{\pi}_{2\beta}$, we obtain $\hat{\pi}_i = \frac{1}{2}|\phi_i\rangle\langle\phi_i|$ for $i \in \{1, 2, 3, 4\}$, with the projection measurements given by their respective expectation values $P_i = \langle\psi|\hat{\pi}_i|\psi\rangle$.

Appendix B

The coherence density matrix element ρ_{eg} in the steady state solution

Recall from Section 4.3 that the optical Bloch equations in the rotating wave approximation are given by,

$$\dot{\tilde{\rho}}_{gg} = \frac{i\Omega}{2}(\tilde{\rho}_{ge} - \tilde{\rho}_{eg}) + \Gamma\tilde{\rho}_{ee}, \tag{B.1}$$

$$\dot{\tilde{\rho}}_{ge} = -\frac{i\Omega}{2}(\tilde{\rho}_{ee} - \tilde{\rho}_{gg}) - i\Delta\tilde{\rho}_{ge} - \frac{\Gamma}{2}\tilde{\rho}_{ge}, \tag{B.2}$$

$$\dot{\tilde{\rho}}_{eg} = \frac{i\Omega}{2}(\tilde{\rho}_{ee} - \tilde{\rho}_{gg}) + i\Delta\tilde{\rho}_{eg} - \frac{\Gamma}{2}\tilde{\rho}_{eg}, \tag{B.3}$$

$$\dot{\tilde{\rho}}_{ee} = -\frac{i\Omega}{2}(\tilde{\rho}_{ge} - \tilde{\rho}_{eg}) - \Gamma\tilde{\rho}_{ee}, \tag{B.4}$$

where the populations obey $\tilde{\rho}_{gg} + \tilde{\rho}_{ee} = 1$. For the steady state solution, $\dot{\tilde{\rho}}^{ss}_{gg} = \dot{\tilde{\rho}}^{ss}_{ge} = \dot{\tilde{\rho}}^{ss}_{eg} = \dot{\tilde{\rho}}^{ss}_{ee} = 0$, we have,

$$0 = -\frac{i\Omega}{2}(\tilde{\rho}^{ss}_{ee} - \tilde{\rho}^{ss}_{gg}) - i\Delta\tilde{\rho}^{ss}_{ge} - \frac{\Gamma}{2}\tilde{\rho}^{ss}_{ge}, \tag{B.5}$$

$$0 = \frac{i\Omega}{2}(\tilde{\rho}^{ss}_{ee} - \tilde{\rho}^{ss}_{gg}) + i\Delta\tilde{\rho}^{ss}_{eg} - \frac{\Gamma}{2}\tilde{\rho}^{ss}_{eg}, \tag{B.6}$$

$$0 = -\frac{i\Omega}{2}(\tilde{\rho}^{ss}_{ge} - \tilde{\rho}^{ss}_{eg}) - \Gamma\tilde{\rho}^{ss}_{ee}, \tag{B.7}$$

where we have ignored Eqn. B.1. If we add Eqn. B.5 and Eqn. B.6, we are left with,

$$\tilde{\rho}^{ss}_{ge} = \frac{i\Delta - \Gamma/2}{i\Delta + \Gamma/2}\tilde{\rho}^{ss}_{eg}. \tag{B.8}$$

Inserting Eqn. B.8 into Eqn. B.7, we get,

$$\tilde{\rho}^{ss}_{ee} = \frac{i\Omega}{i\Delta + \Gamma/2}\tilde{\rho}^{ss}_{eg}. \tag{B.9}$$

Now, by substituting Eqn. B.9 and $\tilde{\rho}^{ss}_{gg} = 1 - \tilde{\rho}^{ss}_{ee}$ back into Eqn. B.6, we find,

$$
\begin{aligned}
0 &= \frac{i\Omega}{2}(2\tilde{\rho}_{ee}^{ss} - 1) + (i\Delta - \Gamma/2)\tilde{\rho}_{eg}^{ss} \\
0 &= \frac{i\Omega}{2}\left(2\left[\frac{i\Omega}{i\Delta + \Gamma/2}\tilde{\rho}_{eg}^{ss}\right] - 1\right) + (i\Delta - \Gamma/2)\tilde{\rho}_{eg}^{ss} \\
\frac{i\Omega}{2} &= \left[\frac{-\Omega^2}{i\Delta + \Gamma/2}\tilde{\rho}_{eg}^{ss}\right] + (i\Delta - \Gamma/2)\tilde{\rho}_{eg}^{ss} \\
\frac{i\Omega}{2}(i\Delta + \Gamma/2) &= [-\Omega^2 + (i\Delta - \Gamma/2)(i\Delta + \Gamma/2)]\tilde{\rho}_{eg}^{ss} \\
\therefore\ \tilde{\rho}_{eg}^{ss} &= \frac{i\Omega}{2}\frac{(i\Delta + \Gamma/2)}{[-\Omega^2 + (i\Delta - \Gamma/2)(i\Delta + \Gamma/2)]}.
\end{aligned}
\tag{B.10}
$$

Since the Rabi frequency is proportional to the electric field amplitude $\Omega \propto E_0$, for strong driving fields, the Rabi frequency is much larger than the detuning (i.e. $\Omega \gg \Delta$); however, for weak driving fields, we have $\Omega \ll \Delta$ [165]. If we assume our light fields are weak (they generally are), then $\Omega^2 \to 0$ and Eqn. B.10 reduces to the following,

$$
\tilde{\rho}_{eg}^{ss} = \frac{\Omega}{2}\frac{i}{(i\Delta - \Gamma/2)}, \tag{B.11}
$$

which is the final expression of $\tilde{\rho}_{eg}^{ss}$ found in Eqn. 6.2.8.

Appendix C

Complex electric field of the probe beam in polarisation spectroscopy

Starting with Eqn. 6.5.3,

$$\mathbf{E} = \frac{\sqrt{2}}{2} E_0 \left(e^{i\theta}\sigma_- e^{-ikn_+L} e^{-\alpha_+ L/2} e^{-ik\tilde{n}_{g_+} l} + e^{-i\theta}\sigma_+ e^{-ikn_-L} e^{-\alpha_- L/2} e^{-ik\tilde{n}_{g_-} l} \right). \tag{C.1}$$

Substituting $\tilde{n}_{g_\pm} = n_{g_\pm} - i\alpha_{g_\pm}/2k$ into the equation above yields,

$$\begin{aligned}\mathbf{E} = \frac{\sqrt{2}}{2} E_0 (e^{i\theta}\sigma_- e^{-ikn_+L} e^{-\alpha_+ L/2} e^{-ikn_{g_+} l} e^{-\alpha_{g_+} l/2} \\ + e^{-i\theta}\sigma_+ e^{-ikn_-L} e^{-\alpha_- L/2} e^{-ikn_{g_-} l} e^{-\alpha_{g_-} l/2}).\end{aligned} \tag{C.2}$$

If we factor out everything within the bracket with the exception of $e^{i\theta}\sigma_-$ and $e^{-i\theta}\sigma_+$, we are left with,

$$\begin{aligned}\mathbf{E} = \frac{1}{\sqrt{2}} E_0 e^{-ikn_+L} e^{-\alpha_+ L/2} e^{-ikn_{g_+} l} e^{-\alpha_{g_+} l/2} e^{-ikn_-L} e^{-\alpha_- L/2} e^{-ikn_{g_-} l} e^{-\alpha_{g_-} l/2} \\ (e^{i\theta}\sigma_- e^{ikn_-L} e^{\alpha_- L/2} e^{ikn_{g_-} l} e^{\alpha_{g_-} l/2} + e^{-i\theta}\sigma_+ e^{ikn_+L} e^{\alpha_+ L/2} e^{ikn_{g_+} l} e^{\alpha_{g_+} l/2}).\end{aligned} \tag{C.3}$$

Focusing on the term outside the brackets, if we gather the terms together, we are left with,

$$\begin{aligned}\implies & \frac{1}{\sqrt{2}} E_0 e^{-ikn_+L} e^{-\alpha_+ L/2} e^{-ikn_{g_+} l} e^{-\alpha_{g_+} l/2} e^{-ikn_-L} e^{-\alpha_- L/2} e^{-ikn_{g_-} l} e^{-\alpha_{g_-} l/2} \\ &= \frac{1}{\sqrt{2}} E_0 e^{-2ik(n_+ + n_-)L/2} e^{-2ik(n_{g_+} + n_{g_+})l/2} e^{-2(\alpha_+ + \alpha_-)L/4} e^{-2(\alpha_{g_+} + \alpha_{g_-})l/4} \\ &= \frac{1}{\sqrt{2}} E_0 e^{-2i[k(nL + n_g l) - i(\alpha L + \alpha_g l)/2]}.\end{aligned} \tag{C.4}$$

If we define an exponential e^{2x}, we can separate it into $e^{2x} = e^x e^x$ (which holds by the property of exponential functions, i.e. $e^x e^x = e^{x+x} = e^{2x}$). Applying this to the exponent in Eqn. C.4 above and multiplying the left term inside the bracket of Eqn. C.3 with $e^{-i[k(nL+n_g l) - i(\alpha L + \alpha_g l)/2]}$ gives,

$$
\begin{aligned}
\implies & e^{-i[k(nL+n_g l)-i(\alpha L+\alpha_g l)/2]}\left(e^{i\theta}\sigma_- e^{ikn_- L}e^{\alpha_- L/2}e^{ikn_{g_-}l}e^{\alpha_{g_-}l/2}\right) \\
&= e^{i\theta}\sigma_- e^{-i[k(\{n-n_-\}L+\{n_g-n_{g_-}\}l)-\frac{i}{2}(\{\alpha-\alpha_-\}L+\{\alpha_g-\alpha_{g_-}\}l)]} \\
&= e^{i\theta}\sigma_- e^{-i\left[\frac{k}{2}\left(\Delta nL+\Delta n_g l\right)-\frac{i}{4}\left(\Delta\alpha L+\Delta\alpha_g l\right)\right]},
\end{aligned}
\tag{C.5}
$$

where the definitions of the variables in Eqn. 6.5.6 hold[1]. Similarly, if we multiply the right side of the term inside the bracket of Eqn. C.3 by $e^{-i[k(nL+n_g l)-i(\alpha L+\alpha_g l)/2]}$, we are left with,

$$
\begin{aligned}
\implies & = e^{-i\theta}\sigma_+ e^{-i[k(\{n-n_+\}L+\{n_g-n_{g_+}\}l)-\frac{i}{2}(\{\alpha-\alpha_+\}L+\{\alpha_g-\alpha_{g_+}\}l)]} \\
&= e^{-i\theta}\sigma_+ e^{i\left[\frac{k}{2}\left(\Delta nL+\Delta n_g l\right)-\frac{i}{4}\left(\Delta\alpha L+\Delta\alpha_g l\right)\right]}.
\end{aligned}
\tag{C.6}
$$

Combining all three calculations from Eqn. C.4, Eqn. C.5, and Eqn. C.6, we are left with the final form of Eqn. C.3 given by,

$$
\mathbf{E} = \frac{1}{\sqrt{2}}E_0 e^{-i\Lambda}(e^{i\theta}\sigma_- e^{-i\Pi} + e^{-i\theta}\sigma_+ e^{i\Pi}),
\tag{C.7}
$$

where,

$$
\begin{aligned}
\Pi &= \frac{k}{2}\left(\Delta nL + \Delta n_g l\right) - \frac{i}{4}\left(\Delta\alpha L + \Delta\alpha_g l\right) \\
\Lambda &= k(nL + n_g l) - \frac{i}{2}(\alpha L + \alpha_g l),
\end{aligned}
\tag{C.8}
$$

obtaining the results from Eqn. 6.5.4 and Eqn. 6.5.5, respectively.

[1] Preforming this calculation means we are left with $e^{-i[k(nL+n_g l)-i(\alpha L+\alpha_g l)/2]}$ outside the bracket in Eqn. C.4.

Appendix D

Polar plots and intensity figures for the q=1/2 hybrid probe beam

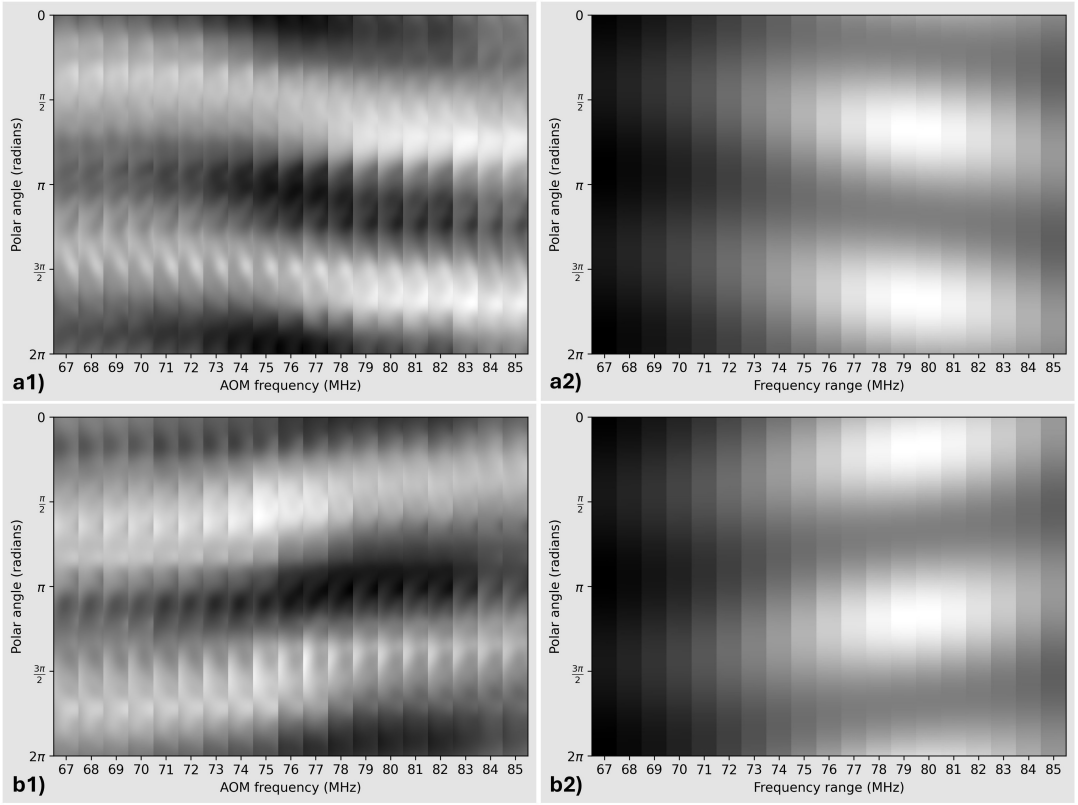

Figure D.1: Experimental (left) and theoretical (right) polar plot of the $q = 1/2$ hybrid probe beam projected along a) the $\hat{H}$ state, and b) the $\hat{V}$ state, across the AOM scan.

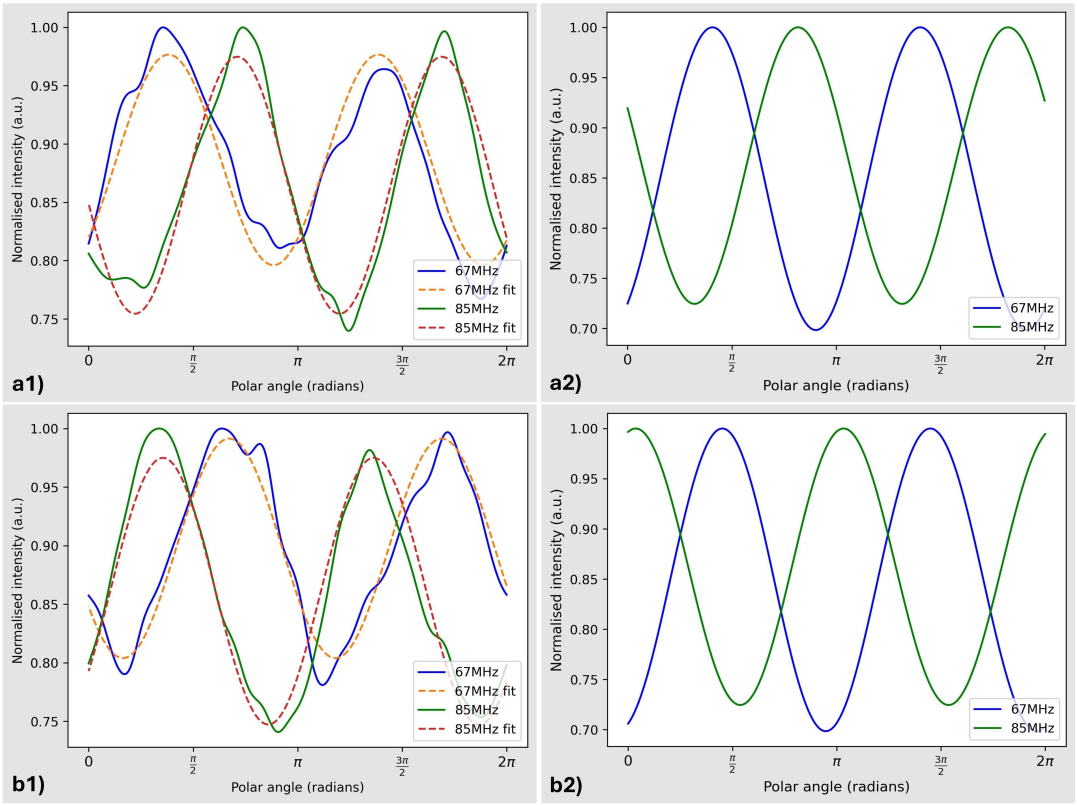

Figure D.2: Experimental (left) and theoretical (right) intensity against polar angle for the $q = 1/2$ hybrid probe beam projected along a) the $\hat{H}$ state, and b) the $\hat{V}$ state, across the AOM scan.

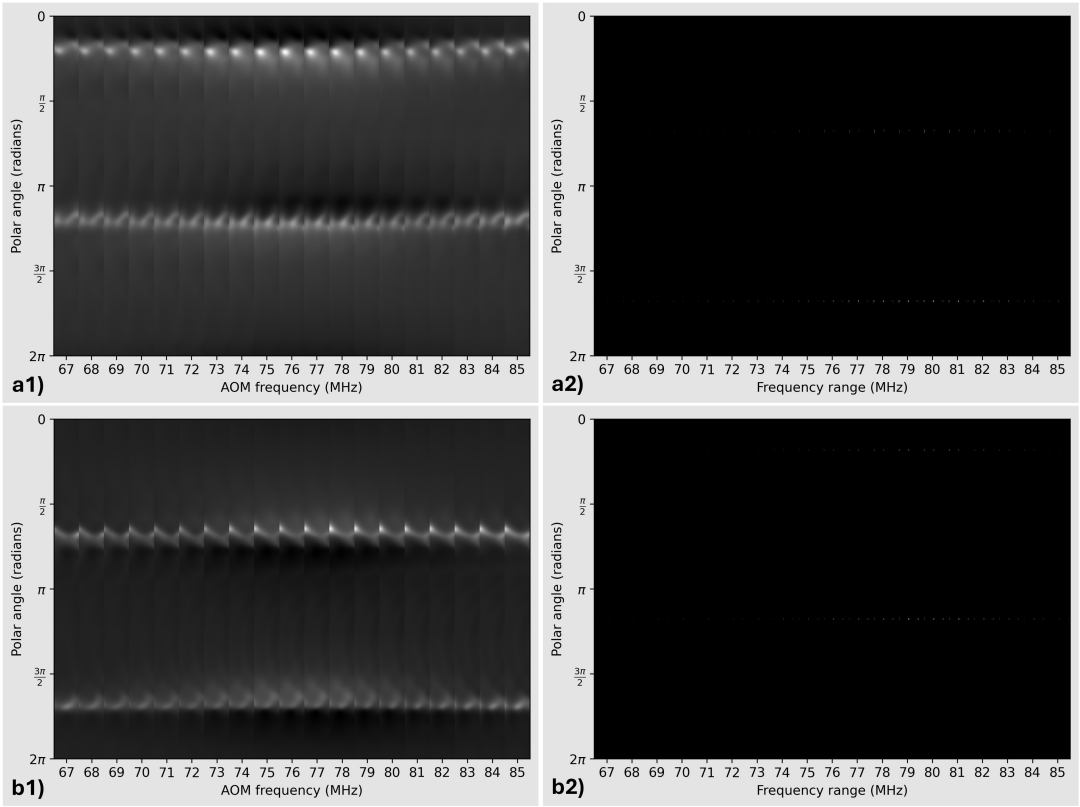

Figure D.3: Experimental (left) and theoretical (right) polar plot of the $q = 1/2$ hybrid probe beam projected along a) the $\hat{A}$ state, and b) the $\hat{D}$ state, across the AOM scan.

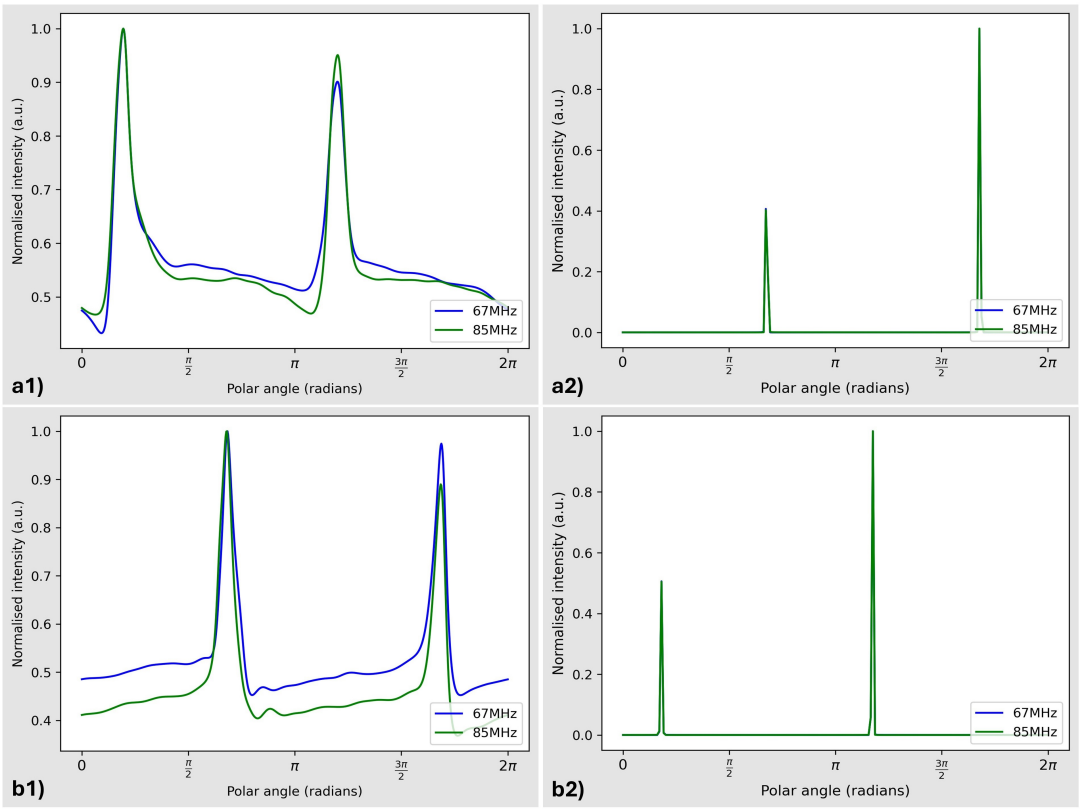

Figure D.4: Experimental (left) and theoretical (right) intensity against polar angle for the $q = 1/2$ hybrid probe beam projected along a) the $\hat{A}$ state, and b) the $\hat{D}$ state, across the AOM scan.

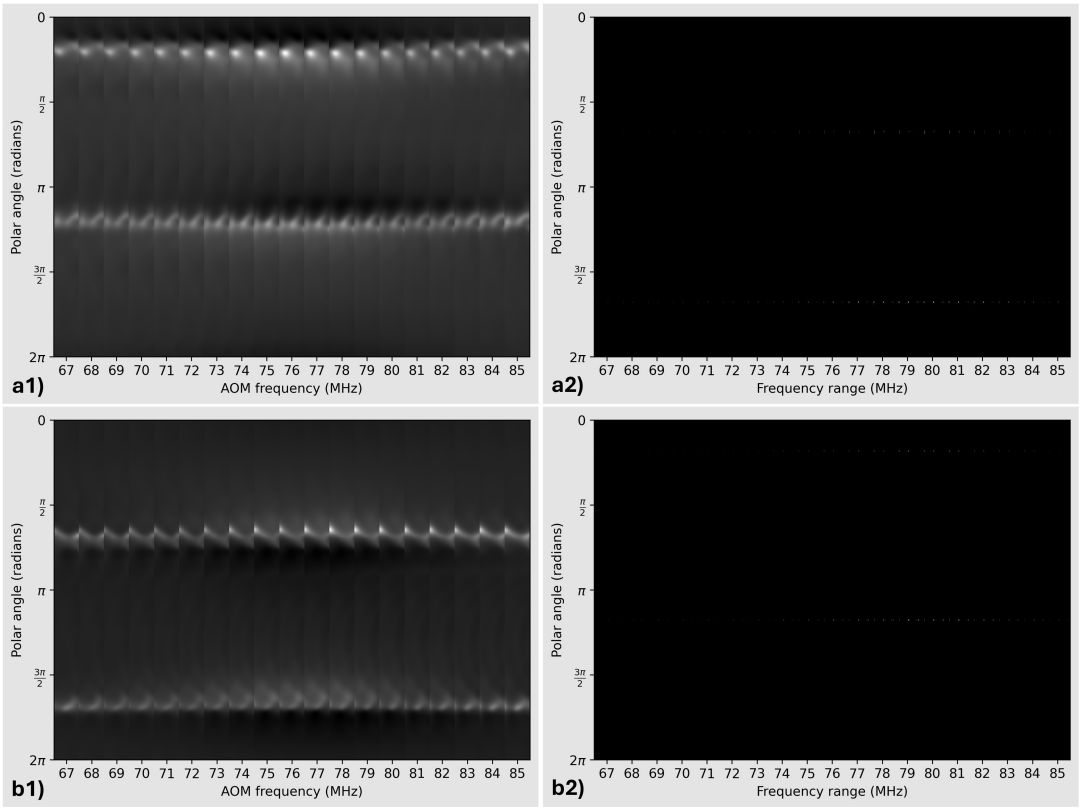

Figure D.5: Experimental (left) and theoretical (right) polar plot of the $q = 1/2$ hybrid probe beam projected along a) the $\hat{R}$ state, and b) the $\hat{L}$ state, across the AOM scan.

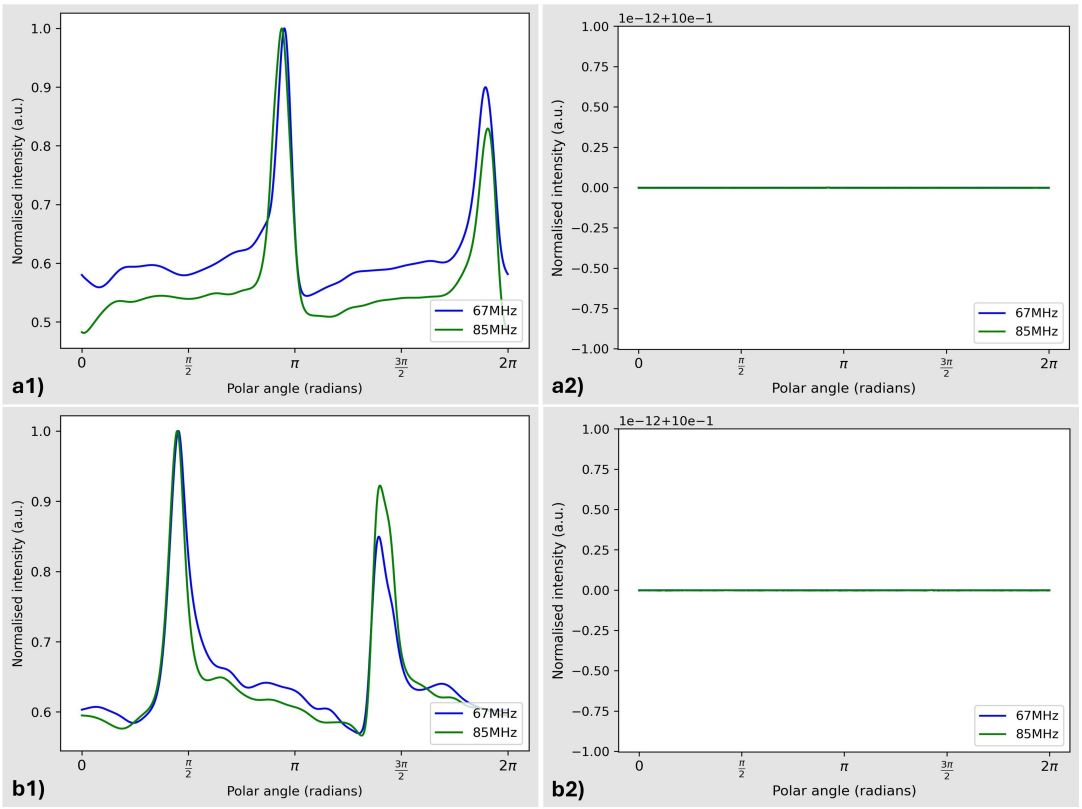

Figure D.6: Experimental (left) and theoretical (right) intensity against polar angle for the $q = 1/2$ hybrid probe beam projected along a) the $\hat{R}$ state, and b) the $\hat{L}$ state, across the AOM scan.

Appendix E

Python coded to simulate spatial polarisation spectroscopy

Below is the annotated Python code used to generate our theoretical spatpolspec data (warning, it is lengthy). I would like to emphasise that the code was constantly altered throughout use, which means the code below might slightly differ from the one I used to generate the data. However, all functionalities should remain the same.

```
import numpy as np  # for arrays
import cv2
from functools import lru_cache
import matplotlib.pyplot as plt  # for plots
import sympy as sp  # symbolic calculations
# Laguerre Polynomial for simulations
from sympy import assoc_laguerre as laguerrePoly
from scipy import constants as const
from scipy.signal import find_peaks


# This function projects the beam onto the respective polarisation basis
def projection(proj, beam):
    result = np.empty(proj.shape, dtype=object)
    row, col = proj.shape


    for i in range(row):
```

```
        for j in range(col):
            result[i][j] = np.absolute(np.vdot(proj[i][j], beam[i][j]))**2
    return result

# Converts a cartesian meshgrid to polar
def cart2pol(x, y):
    r = np.sqrt(x**2 + y**2)
    phi = np.arctan2(y, x)
    return r, phi

# Rayleigh range, also z_0
@lru_cache(maxsize=None)
def rayleigh(beam_waist, wave_length):
    return np.pi*beam_waist**2/wave_length

# Evolution of beamwaist with distance z, also w(z)
@lru_cache(maxsize=None)
def waist(z, beam_waist, z_0):
    return beam_waist*(1+(z/z_0)**2)**(1/2)

# Evolution of radius of curvature with distance z, also R(z)
@lru_cache(maxsize=None)
def radius(z, z_0):
    try:
        return z*(1+(z_0/z)**2)
    except ZeroDivisionError:
        return np.Inf
```

```
# This function generates the Laguerre-Gaussian beam electric field (U_lp)
def laguerre(l, p, r_val, phi_val, z, beam_waist, wavelength):
    r, phi = sp.symbols('r phi')
    k = 2 * np.pi / wavelength
    z_0 = rayleigh(beam_waist, wavelength)
    w_z = waist(z, beam_waist, z_0)
    psi_z = (sp.Abs(l) + 2*p + 1) * np.arctan(z / z_0)

    lg_beam = (beam_waist/w_z) * ((r*sp.sqrt(2))/w_z)**sp.Abs(l) * \
              sp.exp(-(r/w_z)**2) * \
              laguerrePoly(p, sp.Abs(l), (2*r**2)/w_z**2) * \
              sp.exp(-1j*(l*phi-psi_z+k*r**2/(2*radius(z, z_0))))
    func = sp.lambdify([r, phi], lg_beam)
    return func(r_val, phi_val)

# Create a matrix where each element
# is a jones vector describing the polarisation direction
def jones_matrix(array, rows, cols):
    array = np.array(array)
    array = (1 / np.linalg.norm(array)) * array
    matrix = np.empty((rows, cols), dtype=object)
    it = np.nditer(matrix, flags=['multi_index', 'refs_ok'],
                   op_flags=['readwrite'])

    for element in it:
        matrix[it.multi_index] = array
```

```
    return matrix


##############################################################################
wave_length = 780e-9    # m
w0 = 2.1    # mm (beam waist)
##############################################################################
# Define grid physical dimensions
x_length = 5  # Physical length in the x direction (desired unit mm)
y_length = 5  # Physical length in the y direction (desired unit mm)
grid_points = 200   # number of points in the grid

# Create coordinate arrays
x_grid = np.linspace(-x_length, x_length, grid_points)
y_grid = np.linspace(-y_length, y_length, grid_points)
grid_size = int(grid_points/2)

# Creates a meshgrid of x and y values from the range specified below
xx, yy, = np.meshgrid(x_grid, y_grid)
# converts cartesian coordinates to polar
rr, pphi = cart2pol(xx, yy)

# creating an array of Jones vectors for all Stokes bases
horizontal_matrix = jones_matrix([1, 0], 2*grid_size, 2*grid_size)
vertical_matrix = jones_matrix([0, 1], 2*grid_size, 2*grid_size)
diagonal_matrix = jones_matrix([1/np.sqrt(2), 1/np.sqrt(2)],
                               2*grid_size, 2*grid_size)
```

```
antidiagonal_matrix = jones_matrix([1/np.sqrt(2), -1/np.sqrt(2)],
                                   2*grid_size, 2*grid_size)
right_matrix = jones_matrix([1/np.sqrt(2), -1j/np.sqrt(2)],
                            2*grid_size, 2*grid_size)
left_matrix = jones_matrix([1/np.sqrt(2), 1j/np.sqrt(2)],
                           2*grid_size, 2*grid_size)


# The q-plate fast-axis orientation
phase_half = -(6 * np.pi)/180    # q=1/2 phase
phase_one = -(15 * np.pi)/180    # q=1 phase


# Assigning the beam mode to the sigma plus/minus E field
# BEAM SELECTION: COMMENT/UNCOMMENT THE ELECTRIC FIELDS
# CORRESPONDING TO THE DESIRED BEAM
# ------------------------------------------------------------------------
# # Generates the q=1/2 beam
# LG10 = laguerre(1, 0, rr, pphi, 0, w0, wave_length)
# LGn10 = laguerre(-1, 0, rr, pphi, 0, w0, wave_length)
# E_plus_field = np.flip((LG10 * np.exp(2 * 1j * phase_half) +
#                         LGn10 * np.exp(-2 * 1j * phase_half)), axis=1)
# E_minus_field = np.flip(-(LG10 * np.exp(2 * 1j * phase_half) -
#                           LGn10 * np.exp(-2 * 1j * phase_half)), axis=1)
# ------------------------------------------------------------------------
# Generates the q=1 beam
LG20 = laguerre(2, 0, rr, pphi, 0, w0, wave_length)
LGn20 = laguerre(-2, 0, rr, pphi, 0, w0, wave_length)
E_plus_field = np.flip((LG20 * np.exp(2 * 1j * phase_one) +
```

```
                        LGn20 * np.exp(-2 * 1j * phase_one)), axis=1)
E_minus_field = np.flip(-(LG20 * np.exp(2 * 1j * phase_one) -
                          LGn20 * np.exp(-2 * 1j * phase_one)), axis=1)
# ------------------------------------------------------------------------

#############################################
# Atomic functions
#############################################

n_rho = 5.383e07 * 1e6  # m^-3 (atomic density from experiment)
Gamma = 2 * np.pi * 6.065e6  # Hz (natural line width)
# Hz (D2 line 85Rb: From F=3 ground state)
# [upper state hyperfine splitting ignored (too small)]
omega0 = 2 * np.pi * (384.230e12 - 1.265e9)
# W/m^2 (saturation intensity)
Isat = (const.hbar * Gamma * omega0**3) / (12 * np.pi * const.c**2)
cell_length = 75e-3      # m

# This function calculates shift from the B-field calculation for
# 85Rb: Fg = 3 --> Fe = 4 (B-field in Gauss)
def B_field_detuning(Bz):
    # Zeeman splitting of ground state
    # vaues: 1.4 from Bohr magneton, 3 from mf, 1/3 from g_F
    zeeman_split_ground = 1.4 * 3 * 1/3 * Bz

    # Zeeman splitting of the two sigma components
    zeeman_split_excited_plus = 1.4e6 * 4 * 1/2 * Bz
```

```
    zeeman_split_excited_minus = 1.4e6 * 2 * 1/2 * Bz

    # angular frequency of the two sigma components
    omega_plus = omega0 - 2*np.pi*(zeeman_split_ground +
                                   zeeman_split_excited_plus)
    omega_minus = omega0 - 2*np.pi*(zeeman_split_ground +
                                    zeeman_split_excited_minus)
    # detuning of the two sigma components
    detuning_plus = omega_plus - omega0
    detuning_minus = omega_minus - omega0
    return detuning_plus, detuning_minus

# susceptibility function to calculate the absorption and dispersion
def susceptibility(delta, larmor):
    return ((n_rho*const.hbar*const.c)/4)*(Gamma**2/Isat) * \
        (1j/((1j*(delta+larmor))-Gamma/2))

# Atomic interaction function with the light field
def atomic_interaction(detuning, E_sigma_plus, E_sigma_minus,
                       alpha_scaling, n_scaling, off_res=1):
    # assume B-field is 0.5G
    mag_field_splitting_plus, mag_field_splitting_minus = B_field_detuning(1

    # absorption coefficient for sigma_plus and sigma_minus
    alpha_plus = susceptibility(detuning, mag_field_splitting_plus).imag
    alpha_minus = susceptibility(detuning, mag_field_splitting_minus).imag
```

```
    # refractive index for sigma_plus and sigma_minus
    n_plus = susceptibility(detuning, mag_field_splitting_plus).real
    n_minus = susceptibility(detuning, mag_field_splitting_minus).real

    # absorption terms for sigma_plus and sigma_minus
    absorption_plus = -(2*np.pi/wave_length)*cell_length * \
                      alpha_plus*alpha_scaling
    absorption_minus = -(2*np.pi/wave_length)*cell_length * \
                       alpha_minus*alpha_scaling

    # Faraday effect (difference of the refractive index)
    theta = (n_plus-n_minus)*cell_length*(2*np.pi/wave_length)*n_scaling

    # Effect of absorption on beam
    Efield_sigma_plus = E_sigma_plus -(E_sigma_plus *
                          np.exp(absorption_plus)*off_res)
    Efield_sigma_minus = (E_sigma_minus-(E_sigma_minus *
                         np.exp(absorption_minus))*off_res) \
                          * np.exp(1j * theta)
    return np.asarray([Efield_sigma_plus, Efield_sigma_minus])

def apply_polarisation(detuning_val, alpha_scaling, n_scaling,
                       offset_division=None, show_fig=None):
    # Calculate all atom beams at once
    atom_beams = atomic_interaction(detuning_val, E_plus_field,
                     E_minus_field, alpha_scaling, n_scaling)
    # Apply the polarisation structure to each beam
```

```
atom_plus = np.multiply(atom_beams[0, :, :], left_matrix)
atom_minus = np.multiply(atom_beams[1, :, :], right_matrix)
atom_beam = atom_plus - atom_minus

H_proj = projection(horizontal_matrix, atom_beam).astype('float64')
V_proj = projection(vertical_matrix, atom_beam).astype('float64')
R_proj = projection(right_matrix, atom_beam).astype('float64')
L_proj = projection(left_matrix, atom_beam).astype('float64')
D_proj = projection(diagonal_matrix, atom_beam).astype('float64')
A_proj = projection(antidiagonal_matrix, atom_beam).astype('float64')
total_proj = R_proj + L_proj
# off Resonance beam preparation for normalisation
off_resonance = atomic_interaction(-400e6, E_plus_field,
                                   E_minus_field, 1, 1, 0)
off_plus = np.multiply(off_resonance[0, :, :], left_matrix)
off_minus = np.multiply(off_resonance[1, :, :], right_matrix)
off_beam = off_plus - off_minus

H_proj_off = projection(horizontal_matrix, off_beam).astype('float64')
V_proj_off = projection(vertical_matrix, off_beam).astype('float64')
R_proj_off = projection(right_matrix, off_beam).astype('float64')
L_proj_off = projection(left_matrix, off_beam).astype('float64')
D_proj_off = projection(diagonal_matrix, off_beam).astype('float64')
A_proj_off = projection(antidiagonal_matrix, off_beam).astype('float64')
# Small epsilon value to avoid division by zero
epsilon = 1e-20
# Replace zero values in total_test with epsilon
```

```
# to avoid division by zero
H_off_safe = np.where(H_proj_off == 0, epsilon, H_proj_off)
V_off_safe = np.where(V_proj_off == 0, epsilon, V_proj_off)
R_off_safe = np.where(R_proj_off == 0, epsilon, R_proj_off)
L_off_safe = np.where(L_proj_off == 0, epsilon, L_proj_off)
D_off_safe = np.where(D_proj_off == 0, epsilon, D_proj_off)
A_off_safe = np.where(A_proj_off == 0, epsilon, A_proj_off)
Stokes_off_safe = np.stack((H_off_safe, V_off_safe, A_off_safe,
                  D_off_safe, R_off_safe, L_off_safe), axis=0)

if offset_division is None:
    stokes_projections = np.stack((H_proj, V_proj, A_proj, D_proj,
                                   R_proj, L_proj), axis=0)
else:
    stokes_projections = np.divide(np.stack((H_proj, V_proj, A_proj,
                                             D_proj, R_proj, L_proj),
                                            axis=0), Stokes_off_safe)

if show_fig is not None:
    fig = plt.figure(1)
    axes = [fig.add_subplot(1, 7, i + 1) for i in range(7)]
    axes[0].set_title('Total')
    axes[0].imshow(total_proj, cmap=plt.get_cmap('gray'))
    axes[3].set_title('R')
    axes[3].imshow(stokes_projections[4], cmap=plt.get_cmap('gray'))
    axes[4].set_title('L')
    axes[4].imshow(stokes_projections[5], cmap=plt.get_cmap('gray'))
```

```
        axes[1].set_title('H')
        axes[1].imshow(stokes_projections[0], cmap=plt.get_cmap('gray'))
        axes[2].set_title('V')
        axes[2].imshow(stokes_projections[1], cmap=plt.get_cmap('gray'))
        axes[5].set_title('D')
        axes[5].imshow(stokes_projections[3], cmap=plt.get_cmap('gray'))
        axes[6].set_title('A')
        axes[6].imshow(stokes_projections[2], cmap=plt.get_cmap('gray'))
        # remove axis from images
        for ax in axes:
            ax.axis('off')
        plt.show()
        plt.close()
        plt.clf()
    return stokes_projections


# this function imports the image and coordinates, and selects a
# region from the beam to unwrap into a polar plot
def unwrap_image(img, inner_rad, outer_rad, show_fig=None):
    # obtain image dimensions
    height, width = img.shape
    # determine image centre
    center = (int(height/2), int(width/2))

    # create a mask array of zeros equal to the image dimensions
    mask = np.zeros((height, width), dtype=np.uint8)
    # generate an image mask (order of drawn mask matter)
```

```
# sets all pixel up to outer_rad to white (255)
cv2.circle(mask, center, outer_rad, 255, -1)
# sets all pixel up to inner_rad to black (0),
# therefore only pixels between outer and inner are now white (255)
cv2.circle(mask, center, inner_rad, 0, -1)
# Apply the mask to the image
masked_image = cv2.bitwise_and(img, img, mask=mask)

# Unwrap the masked image
unwrapped_image = cv2.linearPolar(masked_image, center, outer_rad,
                                  cv2.INTER_LINEAR +
                                  cv2.WARP_FILL_OUTLIERS)
if show_fig is not None:
    # Create theta and rho values for the mesh plot
    # array is backwards to ensure data is correctly polar plotted
    theta_values = np.linspace(2*np.pi, 0, unwrapped_image.shape[1])
    rho_values = np.linspace(0, unwrapped_image.shape[0],
                             unwrapped_image.shape[0])
    # Create meshgrid for polar coordinates
    theta_mesh, rho_mesh = np.meshgrid(theta_values, rho_values)

    # identify the region of interest
    inner_circle_plt = plt.Circle(center, inner_rad, color='r',
                                  fill=False)
    outer_circle_plt = plt.Circle(center, outer_rad, color='r',
                                  fill=False)
    center_plt = plt.Circle(center, 7, color='r', fill=True)
```

```
        fig, axs = plt.subplots(1, 2, figsize=(14, 8))
        axs = axs.flatten()

        # Plot the mask region
        axs[0].imshow(img, cmap='gray')
        axs[0].add_patch(center_plt)
        axs[0].set_yticks([])
        axs[0].set_xticks([])
        axs[0].add_patch(inner_circle_plt)
        axs[0].add_patch(outer_circle_plt)

        # Plot the polar map
        axs[1].pcolor(rho_mesh, theta_mesh, unwrapped_image.transpose(),
                      cmap='gray')
        axs[1].set_ylabel('Polar angle $\Theta$')
        axs[1].set_ylim(max(theta_values), min(theta_values))
        axs[1].set_xlabel('Rho')
        axs[1].set_title('Polar plot')
        plt.tight_layout()
        plt.show()
        plt.close()
        plt.clf()
    return unwrapped_image.transpose()

# Function that generates the continuous polar plots
def sequential_polar_plot(cropped_array, show_fig=None):
```

```
x, y, _ = cropped_array.shape

# Concatenate all unwrapped images along the theta dimension
combined_unwrapped_image = np.concatenate(cropped_array, axis=0)

# Create theta and rho values for the mesh plot
# array is backwards to ensure data is correctly visualised
theta_values = np.linspace(2*np.pi, 0,
                           combined_unwrapped_image.shape[1])
rho_values = np.linspace(0, combined_unwrapped_image.shape[0],
                         combined_unwrapped_image.shape[0])
# Create meshgrid for polar coordinates
theta_mesh, rho_mesh = np.meshgrid(theta_values, rho_values)

x_ticks = [(combined_unwrapped_image.shape[0]/x)*
           i-y/2 for i in range(1,x+1)]
x_ticks_label = [(67 + i) for i in range(x)]
if show_fig is not None:
    plt.pcolor(rho_mesh, theta_mesh,
               combined_unwrapped_image, cmap='gray')
    plt.ylim(max(theta_values), min(theta_values))
    plt.ylabel('Polar angle (radians)', fontsize=11)
    plt.xlabel('Frequency range (MHz)', fontsize=11)
    plt.yticks([0, np.pi/2, np.pi, 3*np.pi/2, 2*np.pi],
               ["0", r"$\frac{\pi}{2}$", r"$\pi$",
                r"$\frac{3\pi}{2}$",
                r"$2\pi$"], fontsize=11)
```

```
        plt.xticks(x_ticks, x_ticks_label, fontsize=11)
        fig.savefig(f'polar_plot.jpg', dpi=300)
        plt.tight_layout()
        plt.show()
        plt.close()
        plt.clf()

def rotation_angle(cropped_array, show_fig=None):
    # sum of the horizontal pixel values of the polar image (unwrapped image
    sum_array = np.sum(cropped_array, axis=1)

    # define x-axis from 0 to 2pi
    # Theta values for y-axis
    theta_values = np.linspace(2*np.pi, 0, sum_array.shape[1])

    # arrays to save angle values
    angle_diff = []

    leg_label = ["67MHz", "85MHz"]
    leg_counter = 0

    for ind, freq_plot in enumerate(sum_array):
        freq_plot = freq_plot / np.amax(freq_plot)
        peaks = find_peaks(freq_plot, width=None, height=None,
                           distance=None, prominence=1e-4)[0]
        # if plot is not None:
        #     # Plot original data and fitted curve
```

```
    #      plt.plot(theta_values, freq_plot, label='Original Data')
    #      plt.plot(theta_values[peaks], freq_plot[peaks],
    #               "x", color="red")
    #      plt.xlabel('Polar angle (radians)')
    #      plt.ylabel('Normalised intensity (a.u.)')
    #      plt.show()

    if show_fig is not None:
        if ind == 0 or ind == len(sum_array) - 1:
            angle_diff.append(theta_values[peaks])
            col = ["blue", "green"]
            # Plot original data and fitted curve
            plt.plot(theta_values, freq_plot,
                     label=leg_label[leg_counter],
                     color=col[leg_counter])
            plt.xticks([0, np.pi/2, np.pi,3*np.pi/2, 2*np.pi],
                       ["0", r"$\frac{\pi}{2}$", r"$\pi$",
                        r"$\frac{3\pi}{2}$", r"$2\pi$"], fontsize=11)
            plt.yticks(fontsize=10)
            plt.xlabel('Polar angle (radians)', fontsize=11)
            plt.ylabel('Normalised intensity (a.u.)', fontsize=11)
            plt.legend(loc="lower right", ncol=1)
            leg_counter += 1
    plt.show()
    plt.close()
    plt.clf()
angle_diff = np.asarray(angle_diff)
```

```
    ang_diff_val = np.abs(angle_diff[0] - angle_diff[-1]) * 180/np.pi
    return ang_diff_val, np.mean(ang_diff_val), np.std(ang_diff_val)

# defined detuning range
detuning_range = np.arange(-18.3405e6, 18e6 + 1e6, 2e6)
projection_measurements = np.asarray([
    apply_polarisation(freq, 1, 1, offset_division=0, show_fig=None)
    for ind, freq in enumerate(detuning_range)])

# projection order: H, V, A, D, R, L
stokes_index = ["H", "V", "A", "D", "R", "L"]
for i in range(len(stokes_index)):
    # selects the projection
    select_projection = projection_measurements[:, i]
    # unwraps the beam and crops its out accordingly
    unwrapped_imgs = np.asarray([unwrap_image(beam, 10, 90, show_fig=None)
                                 for ind, beam in enumerate(select_projection
    unwrapped_imgs_cropped = unwrapped_imgs[:, 50:190]
    # generates the stacked polar plots
    sequential_polar_plot(unwrapped_imgs_cropped, show_fig=0)
    # generates the internsity plots vs polar angle for rotation
    # angle identification
    print(stokes_index[i], ":", rotation_angle(unwrapped_imgs_cropped,
                                               show_fig=None))
```